



TECHNISCHE UNIVERSITÄT MÜNCHEN

TUM School of Natural Sciences

Zeolite encapsulated transition metal sulfide clusters for catalytic hydrogenation

Roland Weindl

Vollständiger Abdruck der von der TUM School of Natural Sciences der
Technischen Universität München zur Erlangung eines

Doktors der Naturwissenschaften (Dr. rer. nat)

genehmigten Dissertation.

Vorsitz: Prof. Dr.-Ing. Kai-Olaf M. Hinrichsen

Prüfer der Dissertation: 1. Prof. Dr. Johannes A. Lercher

2. Prof. Dr. Roland A. Fischer

3. Prof. Dr. Karsten Reuter

Die Dissertation wurde am 03.06.2022 bei der Technischen Universität
München eingereicht und durch die TUM School of Natural Sciences am
13.09.2022 angenommen.

Für meine Familie

“If your life’s work can be accomplished in your lifetime, you’re not thinking big enough”

Wes Jackson
US-Biologist

Author's Declaration

I hereby declare that I have written this thesis independently only using the resources explicitly marked. Chapters 4 & 5 are reprinted with permission under the terms of the publishers. Edits have been made to the numbering and layout in order to improve the readability. All collaborators are acknowledged and the all contributions are declared at the end of the respective chapters.

Roland Weindl

Danksagung

Nach insgesamt über acht Jahren Studium und Promotion ist es nun endlich an der Zeit mich bei denjenigen Personen zu bedanken, die mich auf dieser Reise begleitet und unterstützt haben. Auch wenn mir eine vollständige Aufzählung aller Beteiligten wohl nicht gelingen wird, so hoffe ich doch, dass sich die meisten irgendwo in den folgenden Zeilen wiederfinden.

Zunächst einmal gilt mein Dank Prof. Dr. Johannes A. Lercher für die Gelegenheit meine Promotion an diesem Lehrstuhl anfertigen zu dürfen. Auch wenn du nie müde geworden bist zu betonen, dass man Doktoranden ja rein rechtlich nicht besitzen kann, so bin ich doch froh letztlich ein Teil „deiner“ Gruppe geworden zu sein. Die Gelegenheit wissenschaftlich selbstständig zu forschen habe ich ebenso genossen, wie die Möglichkeit die resultierenden Ergebnisse auf internationalen Konferenzen zu präsentieren. Das entgegengebrachte Vertrauen, deine klare und geradlinige Meinung zu wissenschaftlichen Fragen aller Art, aber auch deine überfachlichen Anekdoten haben jedes Meeting mit dir zu einem erfreulichen Erlebnis gemacht.

Speaking of scientific advice, I cannot give enough credit to my mentors Hui and Rachit. Your scientific rigor, your profound knowledge of previously published work, and your guidance in what to investigate next were crucial for the success of this thesis. Every time we were seemingly stuck in this project, which happened much more often than I would ever have imagined being honest, our symbiosis was the key for finding paths moving forward. I appreciated every single one of our countless discussions including, of course, the numerous shared trips to beamline across Europe with you, Rachit. Special thanks also to Axel Brait and Alexander Kuperman from Chevron and Oliver and Libor from PNNL for your collaboration and the fruitful discussions.

Ich möchte mich ebenfalls bei Apl. Prof. Dr. Andreas Jentys und Prof. Dr. Karsten Reuter bedanken. Eure Hilfe in der Interpretation von experimentellen und theoretischen Daten war eine zentrale Stütze für die beiden Publikationen. Andy, dir auch vielen Dank für die stets unterhaltsame und kurzweilige Zusammenarbeit.

Ein besonderer Dank gebührt natürlich auch allen Doktoranden und Post-Docs des Lehrstuhls, die meine Zeit am Lehrstuhl begleitet haben: Philipp, Fuli, Gianluca, Aimen, Mirjam, Wei Iris, Lingli, Lei, Laura, Tessi, Martina, Madita, Christoph, Lara, Guanhua, Xi, Ruixue, Takaaki, Yang & Edith. Nur die geteilten Kaffeepausen, Grillabende,

Abendessen, Sportveranstaltungen, und sonstigen Ausflüge machen aus einer Promotion ein echtes TCII-Erlebnis ;) Besonders hervorheben möchte ich an dieser Stelle die drei Doktoranden, die mich letztlich, durch die Betreuung meiner Arbeiten als Student am Lehrstuhl, dazu verleitet haben ebendort anzuheuern: Martina Braun, Daniel Melzer, und Ferdi. An dieser Stelle auch ein herzlicher Dank an die Kollegen aus der TCI, insbesondere an Thomas Burger für die experimentelle Hilfe.

Nicht zu vergessen gilt mein Dank auch der TC-Fußballcrew unter Leitung des Kapitäns a.D. Felix Kirchberger: Christian, Martl, Thomas Kleiner, Daniel Hirche, Ricardo, Philipp Donaubauer, Manuel Weber, Thomas Burger, Ehrmi, Ecki, Sebi, Stefan, Gregor, Christina, Marco, Simon, Kuba, Guoju, Peter und unzählige mehr. Unsere Trainingseinheiten und natürlich die jährlichen Fachschafts-Turniere hätten wohl so einige erfahrene Trainer neidisch (oder doch eher mitleidig?) gemacht.

Special thanks also to all former and current members of Hui's sulfur-crew: Manuel Wagenhofer, Sylvia, Ferdi, Christoph, Wanqiu, Yong, and Jie. If I were a sulfur atom, I would be scared as hell of this group ;)

Auch wenn manche Erinnerungen an gemeinsame Aktivitäten nur noch bruchstückhaft vorhanden sind, natürlich ein riesen Dank an alle „Desperate Sauf-Wives“: Niklas, Verena, Alex, Ferdi, Flo, Insu, Lennart, Christian und Christoph. Auf alle bisherigen und hoffentlich noch viele zukünftige (un)vergessliche Feiern und Ausflüge!

Ebenfalls möchte ich hier allen Studenten danken, die mit mir im Labor mit Rat und Tat zur Seite gestanden haben: Alisa, Anna-Lena, Christoph, Dennis, Hubert, Manuel, Mira, Svenja, Till und Vindy.

Nicht zu vergessen gilt mein Dank auch sämtlichen Angestellten des Lehrstuhls: Uli, Steffi und Katya für die Organisation und die gemeinsamen Unterhaltungen vor Johannes' Tür; Bettina für die bewundernswerte Geduld mit bürokratischen Schwächen und fehlerhaft ausgefüllten Formularen; und Xaver, Iqbal, Andreas und Martin für eure Hilfe im Labor.

Zu guter Letzt gebührt der größte Dank natürlich meiner Familie und meinen Freunden. Ohne eure unendlich Unterstützung und euer Verständnis wäre diese Arbeit sicherlich nicht möglich gewesen. Darauf, dass die verpassten Familienfeiern, Ausflüge und Fußballtrainings in Zukunft weniger werden mögen ;)

Abstract

Dimeric and tetrameric Mo_xS_y clusters have been synthesized inside NaY zeolites using chemical vapor deposition of $\text{Mo}(\text{CO})_6$ followed by sulfidation and reduction. In addition, also mixed metal sulfide catalysts with Ni, Co & Fe have been prepared *via* this approach. The materials are stable hydrogenation catalysts, but only in the absence of sulfur in the feed. Hydrogen is adsorbed in form of hydrides and is transferred to the competitively adsorbed alkene. The nature of adsorbed hydrogen is different from that on layered MoS_2 on which it is stabilized in form of acidic SH groups.

Kurzzusammenfassung

Zweikernige und vierkernige Mo_xS_y -Cluster wurden in NaY-Zeolithen mithilfe von chemischer Gasphasenabscheidung von $\text{Mo}(\text{CO})_6$ und nachfolgender Sulfidierung und Reduktion synthetisiert. Zusätzlich wurden auch Mischmetallsulfid-Katalysatoren mit Ni, Co & Fe auf diese Weise hergestellt. Diese Materialien sind stabile Hydrierkatalysatoren, allerdings ausschließlich in der Abwesenheit von Schwefel im Reaktionsstrom. Wasserstoff wird in der Form von Hydriden adsorbiert und auf das kompetitiv adsorbierte Alken transferiert. Die Art des adsorbierten Wasserstoffs unterscheidet sich von der auf geschichteten MoS_2 -Katalysatoren, auf denen er in Form von sauren SH-Gruppen stabilisiert wird.

Abbreviations and Explanations

AHM	Ammonium heptamolybdate
a.u.	Arbitrary unit
BAS	Brønsted acid site
bcc	body-centered cubic
BEA	Beta zeolite
B3LYP	Becke, 3-parameter, Lee-Yang-Parr
CN	Coordination number
CNT	Carbon nanotube
CVD	Chemical vapor deposition
d	(Interatomic) distance
DCM	Double crystal monochromator
DFT	Density functional theory
D3BJ	Becke-Johnson damping
EDS	Energy dispersive X-ray spectroscopy
EFAI	Extra-framework aluminum
<i>e.g.</i>	<i>exempli gratia/</i> for example
EPR	Electron paramagnetic resonance
ER	Eley-Rideal
<i>et al.</i>	<i>et alia/</i> and others
EXAFS	Extended X-ray absorption fine structure
FAU or Y	Faujasite zeolite
FT	Fourier-transformed
GC	Gas chromatography
HAADF	High-angle-annular dark field
HDM	Hydrodemetalation
HDN	Hydrodenitrogenation
HDO	Hydrodeoxygenation
HDS	Hydrodesulfurization
HER	Hydrogen evolution reaction
HERFD	High energy resolution fluorescence detected
i.d.	Inner diameter
<i>i.e.</i>	<i>id est/</i> that is to say
IR	Infrared
IWP	Incipient wetness impregnation
LAS	Lewis acid site
LH	Langmuir-Hinshelwood
MAS	Magic angle spinning
MFI	Zeolite Socony Mobil-5
MSI	Metal-support interaction

M _x S _y	Unspecified metal sulfide phase
n.d.	Not determined
NMR	Nuclear magnetic resonance
o.d.	Outer diameter
PBE	Perdew-Burke-Ernzerhof
PFR	Plug flow reactor
RDE	Rotating disc electrode
RHE	Reversible hydrogen electrode
RI	Resolution-of-identity
RIJCOSX	Resolution-of-identity approximation
RRHO	Rigid-rotor harmonic oscillator
SARC/J	Auxiliary basis set
SPE	Single-point-energy
STM	Scanning tunneling microscopy
TDDFT	Time-dependent density functional theory
TEM	Transmission electron microscopy
TFY	Total fluorescence yield
TMS	Transition metal sulfide
TPSSh	Functional (10% HF exchange) by Tao-Perdew-Staroverov-Scuseria
TZVP/TZVPP	Triple zeta polarization functions
UK	United Kingdom
UKS	Unrestricted Kohn Sham
U.S.	United States of America
VGO	Vacuum gas oil
<i>viz.</i>	<i>videre licet/</i> namely
VtC	Valence-to-core
wt%	Weight percent
XANES	X-ray absorption near edge structure
XAS	X-ray absorption spectroscopy
XES	X-ray emission spectroscopy
XPS	X-ray photoemission spectroscopy
XRD	X-ray diffraction
ZORA	Zeroth-order regular approximation
ZPE	Zero-point-energy
2D	Two-dimensional

Symbols

δ/Δ	Difference
δ^+/δ^-	Partial charge
θ	Diffraction angle
μ -bridging	Doubly bridging ligand
σ^2	Debye-Waller factor
$\chi(k)$	Oscillations as function of the circular wavenumber
ω	Spin-multiplicity
A	Amplitude
E	Energy
E_0	Absorption energy
G	(Gibbs) free energy
h	Planck constant
H	Enthalpy
k	Circular wavenumber
$K\alpha/K\beta$	Characteristic X-ray emission lines
k_B	Boltzmann constant
M_s	Spin quantum number
R	Radial distance or universal gas constant
S	Total spin or entropy
S_0^2	Amplitude reduction factor
U	Internal energy

Table of Contents

1 Introduction	1 -
1.1 Transition Metal Sulfide Catalysis in Past and Future	1 -
1.2 Enzymes as Blueprint for Catalyst Design	4 -
1.3 Scope of Thesis	6 -
1.4 References	8 -
2 Transition Metal Sulfides in Catalysis	9 -
2.1 Industrial Hydrotreating	10 -
2.1.1 Relevance	11 -
2.1.2 Chemical Background	13 -
2.1.2.1 Aromatics and Heteroatom-Containing Compounds.....	14 -
2.1.2.2 Mechanistic Aspects of Catalytic Hydrotreating	16 -
2.2 Upgrading of Renewable Resources	19 -
2.3 Electrochemistry	21 -
2.3.1 Electrocatalytic Hydrogen Production.....	21 -
2.3.2 Sulfide Phases as Electrode Materials	22 -
2.4 References	23 -
3 Structure and Reactivity of Transition Metal Sulfide Phases	27 -
3.1 Conventional Sulfide Catalysts	28 -
3.1.1 Synthesis Strategies	28 -
3.1.2 Structure and Morphology	30 -
3.1.3 Role of Support Materials	32 -
3.1.3.1 Self-Supported Sulfides	33 -
3.1.3.2 Metal Oxides, Mesoporous Materials and Zeolites	34 -
3.1.3.3 Carbonaceous Supports	35 -
3.1.4 Active Sites.....	36 -
3.1.4.1 Location of Active Sites.....	36 -
3.1.4.2 Sulfur Vacancies	37 -
3.1.4.3 Sulfhydryl Groups	39 -
3.1.5 Influence of Promoters	40 -
3.1.6 Catalyst Deactivation.....	43 -
3.2 Active Sites in Enzymes	45 -
3.2.1 Transition Metal Sulfide Structures in Nature	45 -
3.2.2 The Nitrogenase Enzyme Family.....	46 -
3.3 Molecular Clusters inside Zeolites	48 -
3.4 References	50 -

4 Zeolite-Stabilized Di- and Tetranuclear Molybdenum Sulfide Clusters Form Stable Catalytic Hydrogenation Sites	- 55 -
Abstract	- 56 -
4.1 Main Article.....	- 57 -
4.2 Acknowledgements	- 66 -
4.3 References.....	- 67 -
4.4 Supporting Information	- 69 -
4.4.1 Experimental Details.....	- 69 -
4.4.1.1 Catalyst Precursor Preparation	- 69 -
4.4.1.2 X-ray Absorption Spectroscopy (XAS) and X-ray Emission Spectroscopy (XES).....	- 69 -
4.4.1.3 Extended X-ray Absorption Fine Structure (EXAFS) Measurements	- 70 -
4.4.1.4 High Energy Resolution Fluorescence Detected X-ray Absorption Near Edge Structure (HERFD-XANES) and Valence-to-Core (VtC) XES Measurements	- 71 -
4.4.1.5 Computational Details	- 71 -
4.4.1.6 Electron Paramagnetic Resonance (EPR) Spectroscopy	- 72 -
4.4.1.7 Catalytic Reactions	- 72 -
4.4.2 ²⁷ Al Magic Angle Spinning-Nuclear Magnetic Resonance (MAS-NMR) Spectroscopy	- 73 -
4.4.3 High-Angle Annular Dark Field-Transmission Electron Microscopy (HAADF-TEM) & Energy Dispersive X-Ray Spectroscopy (EDS).....	- 73 -
4.4.4 Nitrogen Physisorption	- 75 -
4.4.5 Powder X-Ray Diffraction (XRD) Patterns	- 76 -
4.4.6 Relative Stability of Mo ₂ S ₄ and Mo ₄ S ₄ Clusters	- 77 -
4.4.7 Effect of Charge Transfer on the Optimized Mo ₂ S ₄ Structures	- 78 -
4.4.8 Location of Unpaired Electrons in Mo ₂ S ₄ and Mo ₄ S ₄ Clusters.....	- 79 -
4.4.9 X-Ray Emission Spectroscopy (XES) Measurements	- 82 -
4.4.10 High Energy-Resolution X-Ray Absorption Spectroscopy (XAS).....	- 85 -
4.4.11 ORCA Input Files.....	- 86 -
4.4.11.1 Typical ORCA Input File used for Geometry Optimization	- 86 -
4.4.11.2 Typical ORCA Input File used for Calculation of Thermochemical Properties and Hirshfeld Population Analysis	- 86 -
4.4.11.3 Typical ORCA Input File used for Simulation of X-ray Emission Spectra	- 87 -
4.4.11.4 Typical ORCA Input File used for Simulation of X-ray Absorption Spectra	- 87 -
4.4.12 Infrared (IR) Spectroscopy of Adsorbed Pyridine	- 88 -
4.5 References.....	- 89 -

5 Di- and Tetrameric Molybdenum Sulfide Clusters Activate and Stabilize Dihydrogen as Hydrides.....	- 91 -
Abstract	- 92 -
5.1 Introduction	- 93 -
5.2 Results and Discussion.....	- 95 -
5.2.1 Active Sites for CO Adsorption and Hydrogenation	- 95 -
5.2.2 Hydrogen Adsorption.....	- 98 -
5.2.3 Adsorption of Multiple H ₂	- 101 -
5.2.4 Ethene Adsorption	- 103 -
5.2.5 Competitive Adsorption Between Ethene and Hydrogen	- 105 -
5.3 Conclusions	- 107 -
5.4 Experimental and Computational Methods	- 108 -
5.4.1 Catalyst Precursor Preparation.....	- 108 -
5.4.2 Catalyst Preparation	- 108 -
5.4.3 Catalytic Reactions.....	- 109 -
5.4.4 Infrared (IR) Spectroscopy of Adsorbed Probe Molecules.....	- 109 -
5.4.5 Computational Details	- 110 -
5.5 Acknowledgements	- 111 -
5.6 References.....	- 112 -
5.7 Supporting Information	- 115 -
5.7.1 Methodology for the Calculation of Thermochemical Properties.....	- 115 -
5.7.2 Infrared (IR) Spectroscopy of Adsorbed CO	- 118 -
5.7.3 CO Adsorption on Mo _x S _y Clusters	- 122 -
5.7.4 Hydrogen Adsorption on Mo ₂ S ₄	- 123 -
5.7.5 Hydrogen Adsorption on Mo ₄ S ₄	- 128 -
5.7.6 Multiple Hydrogen Adsorption on Mo ₄ S ₄	- 133 -
5.7.7 Ethene Adsorption on Mo ₂ S ₄	- 137 -
5.7.8 Ethene Adsorption on Mo ₄ S ₄	- 140 -
5.7.9 Competitive Adsorption between Hydrogen and Ethene on Mo ₂ S ₄	- 145 -
5.7.10 Competitive Adsorption between Hydrogen and Ethene on Mo ₄ S ₄ ..	- 147 -
5.7.11 X-ray Absorption Spectroscopy (XAS) Measurements	- 149 -
5.7.12 Langmuir–Hinshelwood and Eley–Rideal Reaction Pathways on Mo ₂ S ₄	- 152 -
5.8 References.....	- 154 -

6 Catalytic Hydrogenation on Zeolite Supported Mixed Metal Sulfide Clusters	- 155 -
Abstract	- 156 -
6.1 Structures of Mixed Metal Sulfide Phases	- 157 -
6.2 Infrared Spectroscopy of Adsorbed Probe Molecules.....	- 158 -
6.3 Catalytic Hydrogenation Activity	- 160 -
6.4 Experimental Details.....	- 163 -
6.4.1 Catalyst Precursor Preparation.....	- 163 -
6.4.2 Infrared (IR) Spectroscopy of Adsorbed Probe Molecules.....	- 164 -
6.4.3 Catalytic Reactions.....	- 164 -
6.4.4 Transmission Electron Microscopy	- 165 -
6.5 Acknowledgements	- 166 -
6.6 References.....	- 167 -
6.7 Supporting Information	- 168 -
6.7.1 Elemental Compositions of Prepared Catalysts.....	- 168 -
6.7.2 Transmission Electron Microscopy of Spent Catalysts	- 170 -
6.7.3 Infrared Spectroscopy of Adsorbed Dimethyl Pyridine on NiNaY & CoNaY	- 171 -
6.7.4 Time on Stream Behavior of NiNaY Supported Catalysts	- 172 -
6.7.5 Kinetic Parameters of Ethene Hydrogenation on Mo _x S _y /CoNaY	- 173 -
7 Molecular Molybdenum Sulfide Clusters Supported on Carbon Nanotubes for Electrocatalysis	- 175 -
Abstract	- 176 -
7.1 Structures of Carbon Nanotube (CNT) Supported Molybdenum Sulfide Phases	- 177 -
7.2 Electrocatalytic Hydrogen Evolution Reaction.....	- 179 -
7.3 Experimental Details.....	- 181 -
7.3.1 Catalyst Precursor Preparation.....	- 181 -
7.3.2 X-ray Absorption/Emission Spectroscopy.....	- 181 -
7.3.3 Catalytic Reactions.....	- 182 -
7.4 Acknowledgements	- 183 -
7.5 References.....	- 184 -
8 Concluding Remarks.....	- 185 -
Scientific Contributions	- 187 -

1 Introduction

1.1 Transition Metal Sulfide Catalysis in Past and Future

Transition metal sulfides (TMS) have been a workhorse in industrial catalysis for about 100 years and there is good reason to believe that they will continue to play an important role in the future. Over the last decades their use became inevitable for the production of high-performance fuels in refineries and their unique catalytic properties make them an intriguing candidate for future applications towards the goal of a more sustainable energy supply.

The history of TMS and their application in catalysis was nicely reviewed multiple times, e.g., by Weisser and Landa,¹ Prins,² Topsøe,³ and Chianelli.⁴ This chapter only provides a brief excerpt of some major breakthroughs related to the synthesis, characterization and industrial application of TMS catalysts (presented in form of a timeline in Figure 1.1).

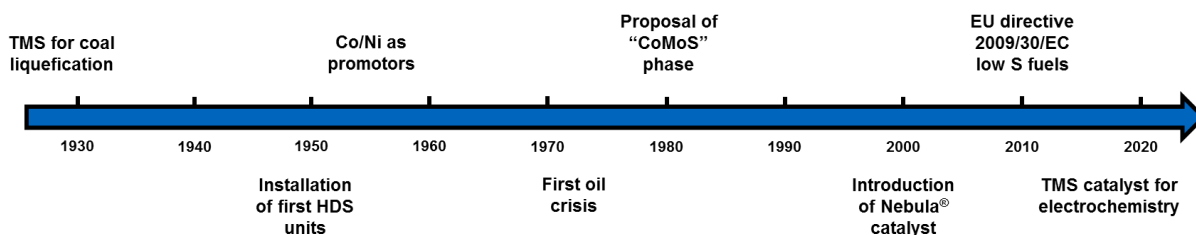


Figure 1.1 Timeline with selected milestones in the development of transition metal sulfide catalysts.

The rise of TMS materials as catalysts started in the 1920s and 1930s driven by the impressions of First World War. In order to circumvent the dependence of imported crude oil, German researchers at Badische Anilin und Sodafabrik (BASF) and I.G. Farben developed processes using coal as a resource for fuels. It turned out that the catalysts used in the high-pressure hydrogenation of coal and other fossil resources were poisoned by the presence of sulfur in these. Therefore, researchers systematically tested the different elements of the periodic table for the ones that remain active hydrogenation catalysts even in the presence of sulfur. As early as 1924 scientists at BASF were able to fully convert lignite tar into gasoline (at 200 bar and 450 °C) using catalysts based on molybdenum and tungsten.^{4,5}

In the 1940s refineries started to implement reforming units using catalysts based on platinum to improve the quality of produced fuels. The fact that these noble metal catalysts are highly sensitive towards the presence of sulfur in the feed is the foundation for the development of the first hydrodesulfurization (HDS) units. Enabling the use of sulfur sensitive downstream catalysts still is one of the most important achievements of TMS catalysis. Interestingly, these early TMS catalysts already were based on Ni/Co promoted Mo/W sulfides supported on alumina; a composition that is still the predominant one as of now. This shows the impressive diligence of the researchers at BASF and I.G. Farben, who developed these systems in a trial-and-error approach without the help of state-of-the-art characterization tools. These researchers reportedly tested over 6000 catalysts within a decade.^{3,4,6}

Even though the general composition of TMS catalysts hardly changed over the next decades, an optimum ratio of promotor (Ni/Co) and base metal (Mo/W) was established.⁷ Besides that these decades were relatively quiet in terms of hydrotreating research due to the abundant availability of crude oil. This changed dramatically with the oil crises of the 1970s, the sudden shortage of crude oil generated the necessity to use heavier crude oil fractions that have higher contents of polycyclic aromatics as well as heteroatom-containing molecules. To convert these feeds into high-quality fuels, improved hydrotreating processes were required fueling the research and development of novel catalytic materials in this field.^{3,8}

In order to develop new, more effective hydrotreating catalysts researchers intensified their efforts to understand how TMS phases are able to effectively catalyze hydrotreating reactions. In particular the question how first-row transition metals promote the activity of MoS₂ and WS₂ became a center point of many studies. After many models have been proposed, which all had their shortcomings in explaining the structure and reactivity of mixed metal sulfide phases, in the 1980s, the group of Topsøe was able to come up with a convincing model based on studies of Co promoted MoS₂ catalysts; the so-called “CoMoS” model. They proposed that Co atoms decorating the edges of MoS₂ slabs are the origin of the promoting effect in TMS catalysis; a model that is nowadays widely accepted.⁹⁻¹¹

After this finding the activity of TMS based catalysts was slowly but steadily improved, mostly by modifying the structure and morphology of sulfide phases in ways that resulted in higher fractions of edge atoms. Nevertheless, the general composition

still remained the same: Ni/Co promoted Mo(W)S₂ supported on alumina. With the turn of the millennium, however, researchers from Exxon Mobil, Akzo Nobel Catalysts (now Albemarle Catalysts), and Nippon Ketjen jointly presented so-called self-supported TMS catalysts. These catalysts no longer require “inert” support materials, resulting in much higher activities on a volumetric basis.^{12,13}

Nowadays, TMS catalysts are inevitable for upgrading of crude oil and are used in virtually every refinery worldwide. Starting from the historic necessity of hydrotreating units to prevent downstream catalysts from poisoning, the focus has shifted over the last decades. Environmental concerns and, as a result, more and more stringent limitations for sulfur and nitrogen contents in transportation fuels require the steady improvement of hydrotreating units.¹⁴

Although the use of TMS in hydrotreating will most likely remain predominant over the next decades, one may ask about the necessity of these catalysts in a hypothetical carbon neutral future, where fossil energy sources are no longer exploited. But in fact, due to their outstanding catalytic properties, e.g., availability and comparatively low price, reasonably high activity for a multitude of reactions involving hydrogen, and stability under harsh reaction conditions, future is looking bright for TMS catalysts. Actually, the number of results in “web of science” for the keyword ‘molybdenum sulfide’ sharply increased over the last years (Figure 1.2; although of course also the overall number of publications increased drastically in the same time). Looking at the papers published over the last years, two topics emerge as the most probable future catalytic application of TMS in upgrading of renewable feedstocks and electrocatalysis (discussed in detail in chapters 2.2 & 2.3).^{15,16}

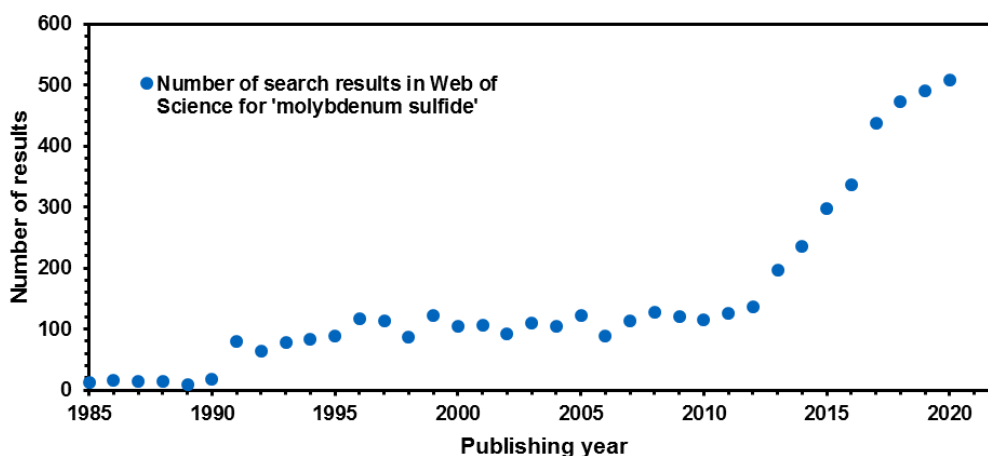


Figure 1.2 Number of search results for the keyword ‘molybdenum sulfide’ in Web of Science™ since 1985.¹⁷

1.2 Enzymes as Blueprint for Catalyst Design

Nature served as inspiration for scientists ever since, with the field of catalysis being no exception. Nature's catalysts, enzymes, are highly active and selective in catalyzing virtually all naturally occurring chemical transformations. In fact, the oldest use of enzymes as catalysts, although certainly unknowingly at that time, dates back approximately 10,000 years when the ancient Egyptians started to use fermentation. Nowadays, enzymes are widely used, *e.g.*, for the production of food and beverages, or in detergents. Chowdhury and Maranas nicely reviewed the history of using enzymes and discussed important milestones in their designed engineering (ref.¹⁸). As a pioneer in the field of enzyme engineering, Frances H. Arnold rightfully received the 2018 Nobel Prize in Chemistry "for the directed evolution of enzymes".¹⁹

What makes enzymes so intriguing for modern chemists is that they are enabling reaction pathways that are currently not accessible with classic catalysts and that they are able to do so under ambient conditions. In general, researchers focusing on enzymes as catalysts use different approaches: (i) whole cells as catalysts, (ii) extracted (and modified) enzymes as biocatalysts, and (iii) the design of novel catalysts using motifs from enzymes as a blueprint. Because all of these methods have their advantages and disadvantages, very prominently, combinations of different techniques are used, *e.g.*, the combined use of enzymatic and classic heterogeneous/homogeneous catalysts (reviewed on the example of biomass conversion in ref.²⁰). It is worth noting, that within the last two decades the dramatically increased computational power led to an improved understanding of structure and operation of enzymes fueling this field of research even more.²⁰⁻²²

Some of the most prominent examples for current research on enzymatic or enzyme inspired catalysis are biomass conversion to bioethanol,^{23,24} ammonia synthesis,²¹ hydrogen evolution,²⁵ hydrolysis,²⁶ and C-H bond activation (selective oxidation).²⁷⁻²⁹ While the production of bioethanol from biomass is already commercialized, some other concepts like ammonia synthesis or methane activation seem to be promising but have failed to yet reach the state of industrial application.

One example for the approach of using an enzyme as blueprint for designing a catalyst system for a challenging reaction is highlighted in Figure 1.3. The left side shows the tertiary structure of particulate methane monooxygenase together with the proposed active site for methane activation, a copper dimer. This enzyme is able to selectively oxidize methane to methanol, a process highly desirable in industry to

convert abundant methane from natural gas. Several groups have tried to mimic the structure of this enzyme in their effort to develop novel inorganic catalysts. The figure nicely demonstrates how two crucial properties were copied from the enzyme: (i) steric constraints, similar to the ones in enzyme pockets, were induced by using zeolites as host materials, and (ii) molecular, well-defined copper clusters serve as reactant adsorption site. Although the resulting material was able to selectively convert methane to methanol in a step-wise process, the activity of the enzyme still remains unmatched. Nevertheless, this is a nice example for a promising catalysts material being developed using Nature as a role model.²⁸⁻³⁰

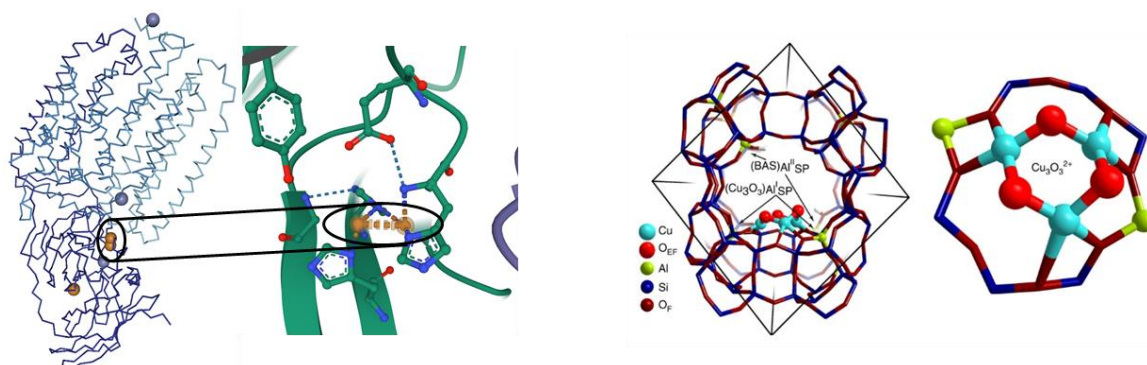


Figure 1.3 Structure of a particulate methane monooxygenase enzyme complex and its active Cu dimer (left). Brown (Cu), red (O), blue (N). Structures were obtained from the Research Collaboratory for Structural Bioinformatics Protein Data Bank (RCSB PDB; rcsb.org) of PDB ID 1YEW (particulate methane monooxygenase; ref. ³¹) and images were created using NGL viewer.³² Structure of copper oxygen cluster (Cu₃O₃²⁺) in mordenite-type zeolite active for methane oxidation to methanol (right; reproduced from ref. ²⁹ under the Creative Commons Attribution 4.0 International License; <http://creativecommons.org/licenses/by/4.0/>).

1.3 Scope of Thesis

The first chapter is a brief recap of the history of transition metal sulfide catalysis and introduces the concept of using naturally occurring enzymes as inspiration for the design of inorganic catalysts. This is followed by two chapters discussing in detail the use of transition metal sulfides in catalysis (chapter 2) and the structure and reactivity of sulfide phases (chapter 3). Besides reviewing the classic application of TMS in industrial hydrotreating, chapter 2 gives a perspective on the challenges and opportunities of using TMS catalysts for upgrading of renewable feedstocks and for electrocatalysis. Chapter 3 follows up with detailed discussions about structure and function of conventional sulfide catalysts including for example sections about synthesis, support materials, active sites and the role of promoters. In addition, other sulfide phases, namely sulfide based enzymes and molecular TMS clusters, are covered in this chapter.

These three chapters are the basis for the first published study presented in chapter 4. In there, synthesis and characterization of zeolite encapsulated TMS clusters are demonstrated. Molecular, well-defined molybdenum sulfide clusters were prepared inside faujasite-type zeolite as a host material *via* chemical vapor deposition (CVD). The resulting materials were extensively characterized using a multitude of state-of-the-art spectroscopic and microscopic tools in combination with density functional theory (DFT). The materials were also tested for catalytic hydrogenation, where they showed stable performance in contrast to a classic MoS₂ counterpart. Interestingly, this work was also able to unravel intriguing structural and electronic similarities between the clusters inside zeolites and the nitrogenase enzyme's active FeMo cofactor, *e.g.*, the local coordination geometry of Mo centers and the presence of unpaired electrons.

The second piece of published work (chapter 5) is following up by focusing on the reactivity of the above-mentioned clusters. Although their chemical composition was found to be very similar to classic TMS catalysts, the reactivity of molecular clusters turned out to significantly differ. For example, they stabilize adsorbed hydrogen in form of hydride species on their Mo atoms. This is in stark contrast to classic MoS₂ phases where hydrogen is commonly proposed to be stabilized in form of protons on S atoms. In contrast the presence of hydrides provides another striking resemblance to enzymatic TMS structures. This finding was jointly demonstrated by infrared (IR) spectroscopy of adsorbed probe molecules and DFT calculations. In addition, a

mechanistic model for the hydrogenation of ethene is presented in accordance with the observed kinetic parameters. The central finding in this model is that, under the tested conditions, active clusters with adsorbed hydrogen are a minority species due to the presence of more strongly bound ethene molecules.

In chapter 6 two synthesis strategies for incorporation of a second transition metal besides Mo are presented. Iron, cobalt, or nickel are introduced into NaY zeolite either by CVD or *via* ion exchange. In all cases, sulfidation of the materials leads to formation of small TMS clusters located inside the zeolite cages. Although, for FeMo catalysts a significant fraction of Fe is present on the outside of the zeolite crystals in form of larger FeS phases. The bimetallic catalysts were tested for the hydrogenation of ethene as a test reaction in a sulfided state. For catalysts prepared *via* sequential CVD of Mo and Co/Fe, the hydrogenation activity increases in the following order: FeMo < CoMo ≤ Mo. We therefore concluded that mixed metal clusters that are formed at least in parts are less active compared to pure Mo_xS_y clusters. Interestingly, Mo_xS_y/NiNaY and Mo_xS_y/CoNaY catalysts prepared *via* ion exchange were more active than pure Mo systems leading us to conclude that there is a beneficial effect of adjacent Mo_xS_y and Ni(Co)_xS_y phases present in close proximity inside the zeolite pores. We speculate, that this is due to the formation of bridging S atoms between both phases that are themselves able to stabilize adsorbed hydrogen in the form of sulfhydryl groups.

Lastly, a short proof-of-concept study is presented in chapter 7. The same synthesis strategy used for the preparation of zeolite encapsulated TMS clusters was used to incorporate TMS phases in a carbonaceous support. For this purpose, carbon nanotubes were used as a host material due to their porous structure similar to zeolite materials. It could be shown that conceptually it is possible *via* this route to produce carbon supported catalysts that are active for electrocatalytic hydrogen evolution reaction.

1.4 References

- (1) Weisser, O.; Landa, S. *Sulphide catalysts, their properties and applications*; Elsevier, 2013.
- (2) Prins, R. In *Handbook of Heterogeneous Catalysis*; Ertl, G., Knözinger, H., Schüth, F., Weitkamp, J., Eds.; John Wiley & Sons: 2008, p 2695.
- (3) Topsøe, H.; Clausen, B. S.; Massoth, F. E. In *Catalysis: Science and Technology*; Anderson, J. R., Boudart, M., Eds.; Springer Berlin Heidelberg: Berlin, Heidelberg, 1996, p 1.
- (4) Chianelli, R. R.; Berhault, G.; Torres, B. *Catalysis Today* **2009**, *147*, 275.
- (5) Krönig, W. *Die katalytische Druckhydrierung von Kohlen, Teeren und Mineralölen*; Springer, 1950.
- (6) Alfke, G.; Irion, W. W.; Neuwirth, O. S. In *Ullmann's Encyclopedia of Industrial Chemistry* 2007.
- (7) Beuther, H.; Flinn, R. A.; McKinley, J. B. *Industrial & Engineering Chemistry* **1959**, *51*, 1349.
- (8) Schuit, G.; Gates, B. C. *AIChE Journal* **1973**, *19*, 417.
- (9) Topsøe, H.; Clausen, B. S.; Candia, R.; Wivel, C.; Mørup, S. *Journal of Catalysis* **1981**, *68*, 433.
- (10) Sørensen, O.; Clausen, B. S.; Candia, R.; Topsøe, H. *Applied Catalysis* **1985**, *13*, 363.
- (11) Topsøe, H. *Applied Catalysis A: General* **2007**, *322*, 3.
- (12) Plantenga, F. L.; Cerfontain, R.; Eijsbouts, S.; van Houtert, F.; Anderson, G. H.; Miseo, S.; Soled, S.; Riley, K.; Fujita, K.; Inoue, Y. In *Studies in Surface Science and Catalysis*; Anpo, M., Onaka, M., Yamashita, H., Eds.; Elsevier: 2003; Vol. 145, p 407.
- (13) Eijsbouts, S.; Mayo, S. W.; Fujita, K. *Applied Catalysis A: General* **2007**, *322*, 58.
- (14) Union, E. *Official Journal of the European Union* **2009**, *5*, 2009.
- (15) Seh, Z. W.; Kibsgaard, J.; Dickens, C. F.; Chorkendorff, I.; Nørskov, J. K.; Jaramillo, T. F. *Science* **2017**, *355*, ead4998.
- (16) Wang, M.; Zhang, L.; He, Y.; Zhu, H. *Journal of Materials Chemistry A* **2021**, *9*, 5320.
- (17) Clarivate: *Results from Web of Science Core Collection for: molybdenum sulfide*. **2022**, <https://www.webofscience.com/wos/woscc/summary/09405c70-a2d9-407c-ac2a-c7ed4aaf8ab4-20099f22/relevance/1> (accessed 08.02.2022).
- (18) Chowdhury, R.; Maranas, C. D. *AIChE Journal* **2020**, *66*, e16847.
- (19) NobelPrize.org: *The Nobel Prize in Chemistry 2018*. **2022**, <https://www.nobelprize.org/prizes/chemistry/2018/summary/> (accessed 08.02.2022).
- (20) Marr, A. C.; Liu, S. *Trends in Biotechnology* **2011**, *29*, 199.
- (21) Hinnemann, B.; Nørskov, J. K. *Topics in Catalysis* **2006**, *37*, 55.
- (22) Chen, K.; Arnold, F. H. *Nature Catalysis* **2020**, *3*, 203.
- (23) Sheehan, J.; Himmel, M. *Biotechnology Progress* **1999**, *15*, 817.
- (24) Alvarado-Morales, M.; Terra, J.; Gernaey, K. V.; Woodley, J. M.; Gani, R. *Chemical Engineering Research and Design* **2009**, *87*, 1171.
- (25) Hinnemann, B.; Moses, P. G.; Bonde, J.; Jørgensen, K. P.; Nielsen, J. H.; Horch, S.; Chorkendorff, I.; Nørskov, J. K. *Journal of the American Chemical Society* **2005**, *127*, 5308.
- (26) Nothling, M. D.; Xiao, Z.; Bhaskaran, A.; Blyth, M. T.; Bennett, C. W.; Coote, M. L.; Connal, L. A. *ACS Catalysis* **2019**, *9*, 168.
- (27) Que, L.; Tolman, W. B. *Nature* **2008**, *455*, 333.
- (28) Bordeaux, M.; Galarneau, A.; Drone, J. *Angewandte Chemie International Edition* **2012**, *51*, 10712.
- (29) Grundner, S.; Markovits, M. A. C.; Li, G.; Tromp, M.; Pidko, E. A.; Hensen, E. J. M.; Jentys, A.; Sanchez-Sanchez, M.; Lercher, J. A. *Nature Communications* **2015**, *6*, 7546.
- (30) Jodts, R. J.; Ross, M. O.; Koo, C. W.; Doan, P. E.; Rosenzweig, A. C.; Hoffman, B. M. *Journal of the American Chemical Society* **2021**, *143*, 15358.
- (31) Lieberman, R. L.; Rosenzweig, A. C. *Nature* **2005**, *434*, 177.
- (32) Rose, A. S.; Bradley, A. R.; Valasatava, Y.; Duarte, J. M.; Prlić, A.; Rose, P. W. *Bioinformatics* **2018**, *34*, 3755.

2 Transition Metal Sulfides in Catalysis

“[H]ydrotreating is the largest application of industrial catalysis on the basis of the amount of material [...] processed per year. Based on the amount of catalyst sold per year, hydrotreating catalysts constitute the third largest catalyst business after exhaust gas catalysts and fluid cracking catalysts.”

Roel Prins

In Handbook of Heterogeneous Catalysis;
Ertl, G., Knözinger, H., Schüth, F., Weitkamp, J.,
Eds.; John Wiley & Sons: 2008

2.1 Industrial Hydrotreating

The term hydrotreating, in its broadest sense, describes a process in which hydrocarbon-containing feeds are reacted with hydrogen over a catalyst at elevated temperatures and pressures. The by far most prominent class of catalysts used for this process are based on transition metal sulfides as central component and are discussed in detail in chapter 3.

Under the reaction conditions commonly applied, the most dominant chemical transformations involve removal of heteroatoms, (partial) hydrogenation of olefins and (poly) aromatics and under harsher conditions to some extent also C-C bond cleavage. Depending on the heteroatom removed the first is usually referred to as hydrodesulfurization, hydrodenitrogenation (HDN), hydrodeoxygenation (HDO) or hydrodemetalation (HDM).¹⁻³

Despite the fact, that all reactions usually are taking place simultaneously, their relative rates are strongly dependent on external process parameters, *i.e.*, catalyst type, temperature, pressure, H₂/hydrocarbon ratio, and space velocity. In turn, to effectively adapt to the different demands, *e.g.*, production of low S/N content fuels requires high HDS/HDN rates; high polyaromatic content feeds require high H₂ partial pressures, in an industrial refining plant multiple hydrotreating units are applied at critical locations (Figure 2.1).

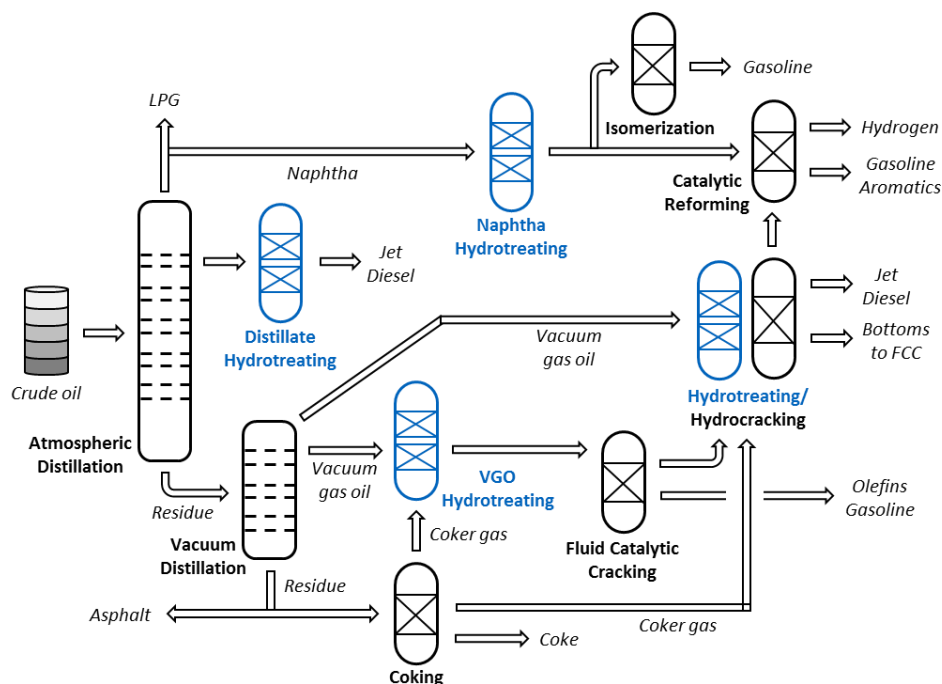


Figure 2.1 Simplified scheme of a modern refinery (adapted from ref. 4).

Commonly, at least one unit is used to treat Naphtha, middle distillates and vacuum gas oil (VGO), respectively. In addition, for most applications using reactor units consisting of multiple catalyst beds in a row with different catalyst formulations is beneficial to achieve high-quality products, e.g., stepwise reduction of S/N content to produce ultra-clean transportation fuels.⁴

In general, hydrotreating units for the upgrading of different refinery feeds are operated at ~300-400 °C and pressures of ~1-15 MPa, with the higher pressures and temperatures applied for treatment of vacuum gas oil and the lower ones for straight-run naphtha.^{3,5} Typically, these units are designed as continuous flow, trickle-bed reactors with hydrogen and liquid feed flowing in co-current mode. Trickle-bed operation in this case implies that reactions are taking place at a gas (hydrogen), liquid (hydrocarbon feed), solid (TMS catalyst) interface. To maintain high reaction rates and prevent formation of carbonaceous deposits, hydrotreating units are generally operated under excess hydrogen. Additional hydrogen is often introduced along the reactor profile to keep the H₂/liquid ratio high across the catalyst bed(s). For the same purpose hydrotreating units can also be operated in a counter-current flow mode of hydrogen and liquid phase.^{6,7} While excess hydrogen is recycled, H₂S, NH₃ and H₂O produced as byproducts from heteroatom removal are separated at the reactor outlet using a scrubber. Much more problematic in this regard are residuals like metal salts and organometallics resulting from metal impurities, especially in heavier feedstocks, as they can hardly be separated under reaction conditions and therefore partly deposit on the active TMS phases causing their deactivation.^{8,9}

It is important to note, that, due to the significantly different composition compared to crude oil, incorporation of renewable feedstocks will force industry to completely rethink the layout and process condition of hydrotreating units. This challenge is discussed in more detail in chapter 2.2.

2.1.1 Relevance

The necessity of installing multiple units in a modern refinery, each adapted to the treated hydrocarbon feed, makes hydrotreating the most important secondary refining process in terms of overall capacity. In fact, on a worldwide scale as of 2004, the installed hydrotreating capacity is about half the installed crude oil distillation capacity with the tendency to increase.^{4,10}

In the U.S. for example, the cumulated capacity of installed desulfurization units doubled since the 1980s (Figure 2.2).

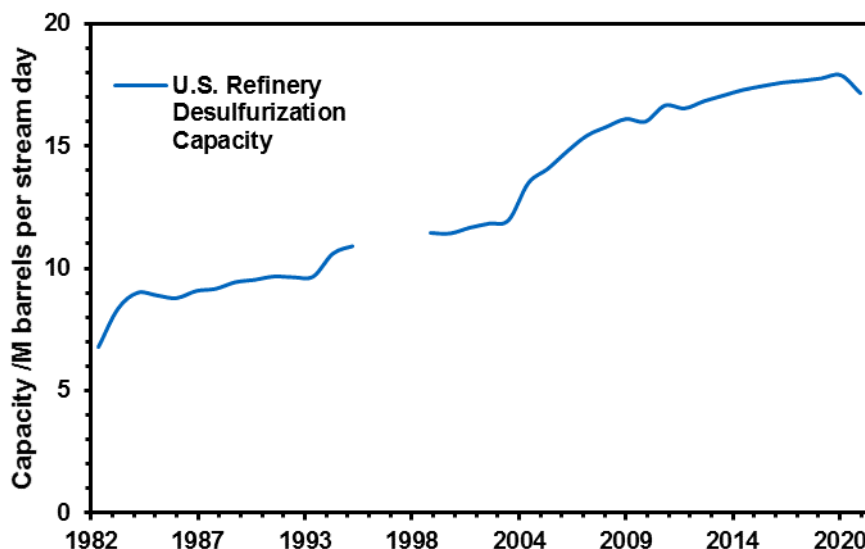


Figure 2.2 Desulfurization downstream charge capacity (in million barrels per stream day) installed in U.S. refineries over the last four decades (Source: U.S. Energy Information Administration).¹¹

Over the last decades, hydrotreating has been a cornerstone in the industrial refining of crude oil for production of transportation fuels mostly for two different reasons. The original intention, removing heteroatoms from crude oil to prevent deactivation (“poisoning”) of downstream (noble metal) catalyst, still is of utmost importance in modern-day refineries.^{1,4} Poisoning hereby describes the, under the given reaction conditions, irreversible blocking of catalytically active sites even by trace amounts of heteroatom-containing molecules present in reactant feeds. This is a result of the high affinity of heteroatom-containing molecules to group 8 and group 10 metals like Pt, Pd, Re and Ru, that are typically used in downstream catalytic processes. Two prime examples for downstream systems prone to poisoning by heteroatoms are catalytic reforming units in refineries and (car) exhaust catalysts, both using Pt and other (noble) metals as active components.¹²⁻¹⁵ Therefore, it is not a coincidence that hydrotreating units were first applied in refineries after the establishment of catalytic reforming in the 1940s/50s.¹⁶ It is worth noting that not only heteroatom removal but also hydrogenation of (poly) aromatic compounds is significantly improving the feed quality, as aromatics in general and polycyclic aromatics even more so are widely considered as potential precursors for coke formation in downstream processing units (e.g., fluid catalytic cracking and).^{4,17,18}

However, nowadays a second, even more powerful source is driving the development of industrial hydrotreating: an increasing environmental awareness and, in turn, more stringent governmental restriction for the chemical compositions of transportation fuels and energy carriers. A prime example in this regard are specifications regarding the sulfur content of combustion fuels (Figure 2.3).

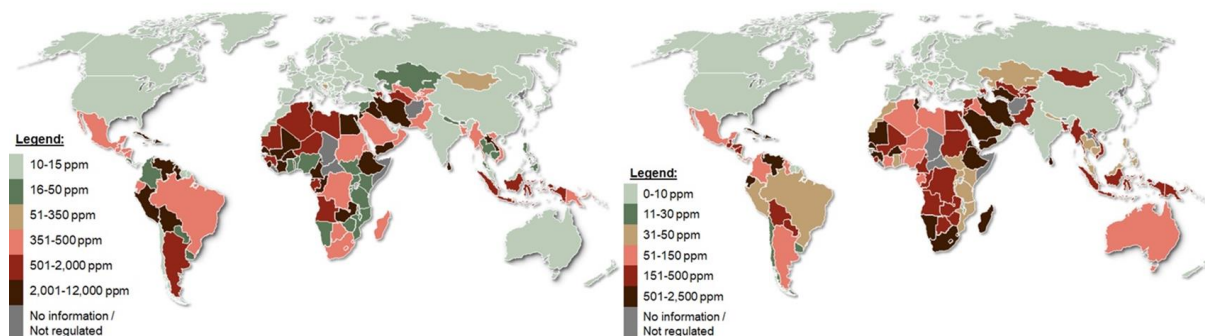


Figure 2.3 World map with maximum sulfur limits for on-road diesel (left) and gasoline (right) as of 2021 (Source: Stratias Advisors, reprinted with permission from refs. ^{19,20}).

As of 2021, almost every country worldwide has imposed limitations for the maximum S content in road fuels and more recently also in maritime fuels.²¹ Although there still are some countries with no/very low limits, these are exclusively found in less-developed parts of the world and therefore are not of major influence with respect to the total volume of fossil fuels consumed.

Up to now, the relevance of hydrotreating applications was strongly coupled to the overall use of fossil fuels. But looking into the future, hydrotreating almost certainly will remain a key process in the transition from fossil towards renewable energy carriers. The same way hydrotreating became inevitable in crude oil refineries for turning fossil resources into efficient energy carriers, it will play a major role in making use of renewable biomass feedstocks (chapter 2.2).

2.1.2 Chemical Background

As introduced before the main emphasis of industrial hydrotreating is the removal of heteroatoms as well as aromatic compounds from refinery flows. However, the content of these compounds widely varies within different crude feedstocks (*i.e.*, the oil field) as well as different refining fractions (Table 2.1).

Table 2.1 Sulfur, nitrogen and oxygen contents in different crude oils as well as different refinery fractions.

Refinery fraction	S content /wt%	N content /wt%	O content /wt%
Heavy crude oil (Turkey)	6.5 ^a	~1 ^a	~4 ^a
Brent crude oil (UK)	0.39 ^b	0.09 ^b	n.d.
Petroleum coke	0.8 ^c	2.0 ^c	12.6 ^c
VGO	2.45 ^d	0.17 ^d	n.d.
Naphtha	~0.04 ^e	> 0.01 ^e	n.d.

^a (ref. ²²), ^b (ref. ²³), ^c (ref. ²⁴), ^d (ref. ²⁵), ^e (ref. ²⁶), n.d.: not determined;

The heteroatom content by weight of these exemplary crudes varies by more than an order of magnitude forcing refiners to adapt to the respective feed. In addition, the sulfur and nitrogen contents of different refinery streams (e.g., naphtha & VGO) are significantly variant. A large fraction of sulfur and nitrogen present in crude oil is due to heteroatom-containing aromatics (see next section for detailed information). Due to the relatively high boiling points of S/N-containing molecules compared to pure hydrocarbons, the heavy distillate fractions in refineries generally contain higher heteroatom contents, making them more challenging for hydrotreating.^{25,26}

Different flows having vastly different contents of S/N/O and aromatics nicely demonstrates the necessity of different hydrotreating units meeting specific requirements at a refinery as already mentioned before in chapter 2.1. It is also obvious that for efficient operation some process parameters (e.g., temperature, pressure, H₂/liquid ratio) must be adapted to the crude oil feed that is processed.²⁷ Comparing the sulfur contents in crude oil feedstocks with the sulfur limits in transportation fuels shows the overall effectiveness required for hydrotreating units. In order to bring the sulfur content of a crude oil (~1 wt%) down to a level meeting the limitations for transportation fuels (maximum of 10 ppm by weight) 99.999% of the overall S atoms have to be removed *via* hydrodesulfurization.

2.1.2.1 Aromatics and Heteroatom-Containing Compounds

To effectively design hydrotreating units meeting the requirements determined by the hydrocarbon feed that is to be processed, it is insufficient to only focus on the content of compounds that are transformed. Within both classes, heteroatom-

containing molecules as well as aromatics, individual compounds show significantly different reactivities in hydrotreating reactions. An exemplary overview of the most prominent types of S/N/O-containing compounds found in hydrotreating feedstock is shown in Figure 2.4.

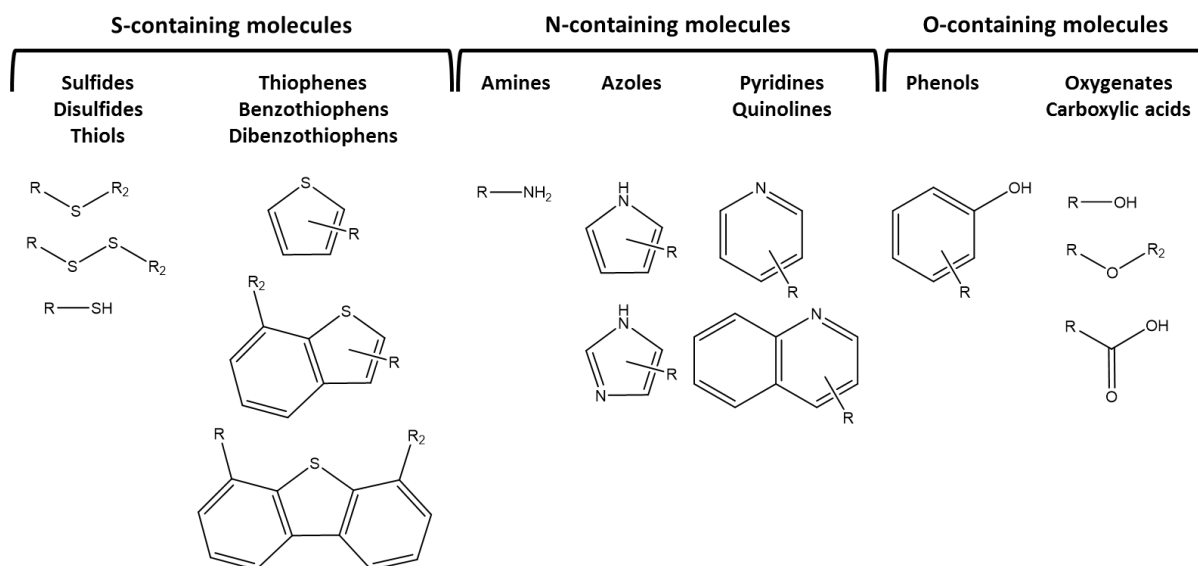


Figure 2.4 Excerpt of heteroatom-containing molecules typically present in crude oil. Randomly attached side chains are represented by R_x .²⁷

As already mentioned a significant fraction of heteroatoms is present in form of a wide variety of aromatic compounds. For catalytic hydrotreating this is challenging because substitutions of these compounds, especially in the proximity of the heteroatom to be removed, significantly influences the reactivities of the compounds for HDS, HDN and HDO reactions. In general, the reactivity for heteroatom removal decreases with increasing number and chain length of substituents. To a lesser extent, this is also true for the hydrogenation of (poly) aromatics. Substitutions increase the steric demand and thus hinder the adsorption of reactants on the active sites for catalytic conversion resulting in lower reaction rates.²⁷⁻³⁰

This is illustrated by the following examples: for substituted dibenzothiophenes, the relative HDS rate decreases by about an order of magnitude in the following series: dibenzothiophene (relative rate of 1) > 4-methyl dibenzothiophene (0.5) > 4-ethyl, 6-methyl dibenzothiophene (0.1);²⁸ for quinolines, only substitutions on the nitrogen-containing ring decrease the rate for HDN;²⁹ and for phenol HDO, the rate decreases with substitutions present in adjacency of the OH group.³⁰ For aromatics not only the degree of substitution is of importance, their reactivity also depends on the number of

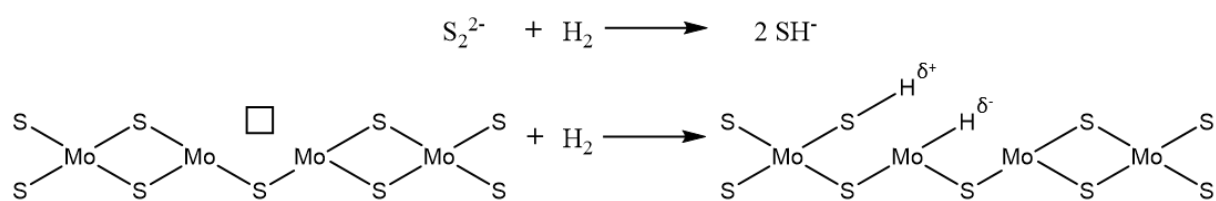
rings with polycyclic aromatics generally showing higher hydrogenation rates compared to benzene.²⁷

2.1.2.2 Mechanistic Aspects of Catalytic Hydrotreating

Although the individual compounds converted in hydrotreating reactions are very different in chemical nature, all reaction pathways involve a couple of basic steps that are virtually identical: (i) reactant molecules adsorb at the catalyst surface, (ii) H₂ is dissociatively adsorbed and stabilized at the sulfide phase, and (iii) dissociated hydrogen reacts with adsorbed reactant molecules in a surface reaction.³¹

On transition metal sulfide catalysts two types of sites are widely considered as crucial for the above-mentioned reactions: coordinatively unsaturated sites (CUS) and sulfhydryl (SH) groups. In essence, CUS are metal cations exposed by missing sulfur anions (S vacancies) whereas SH groups are formed by dissociative adsorption of hydrogen on TMS surfaces. Both types of active sites are discussed in more detail in section 3.1.4.

Scheme 2.1 depicts the formation of SH groups on an exemplary MoS₂ catalyst during hydrogen adsorption according to the two most prominent proposals: in the upper pathway a molecule of H₂ homolytically adsorbs on a bridging disulfide (S₂²⁻) group forming two SH groups, and in the bottom pathway H₂ is heterogeneously dissociated at a CUS forming one SH group and an adjacent hydride on the metal cation.^{32,33}

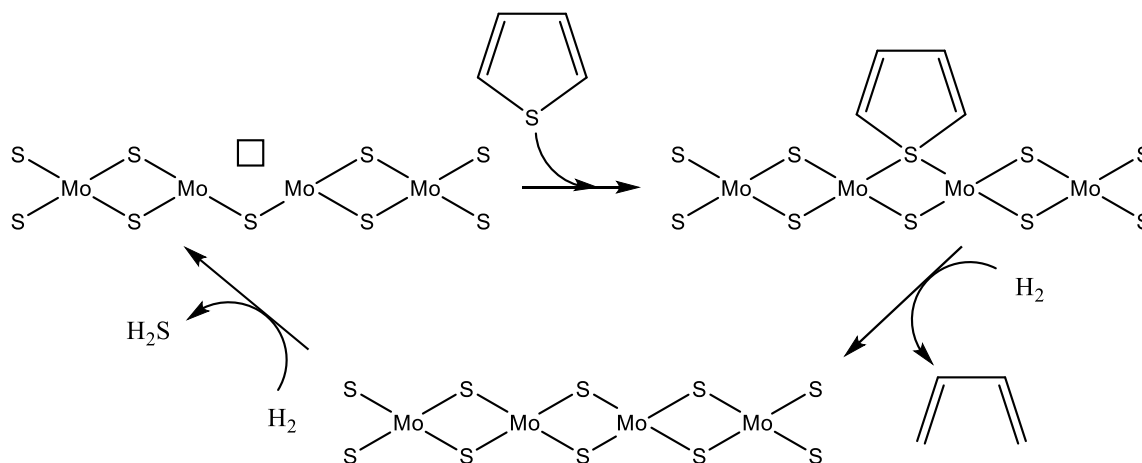


Scheme 2.1 Homolytic (top)³³ and heterolytic (bottom)³² hydrogen adsorption pathways at a schematic MoS₂ catalyst.

The second pathway, heterolytic splitting of H₂, leads to the formation of negatively charged hydride species on the metal sites. The fact that, up to now, these species have not been detected on classic TMS catalysts might at first disfavor the heterolytic adsorption pathway. But it is still possible that a transiently formed hydride is immediately scavenged by a neighboring S atom to form a second SH group. The excess electron density in this case is delocalized by distribution across the

semiconducting TMS phase. Interestingly, the mode of H₂ adsorption and stabilization is very sensitive to the composition and the structure of the TMS phase, a more detailed contemplation of this phenomenon can be found in chapter 5.^{32,34}

In contrast to the pathways of H₂ dissociation on TMS catalysts, the adsorption of other reactant molecules is less under debate. In general, two types of adsorption modes are considered to play a role: S/N/O-containing molecules can adsorb *via* coordination of the heteroatom on CUS whereas large (polycyclic) aromatics can also adsorb on TMS surfaces *via* π-interaction of the aromatic system. The former case is assumed crucial for pathways involving the direct abstraction of heteroatoms and the latter case for pathways involving hydrogenation of aromatic rings. Irrespective of their adsorption mode, aromatic rings are hydrogenated on TMS surfaces according to a Langmuir-Hinshelwood-type mechanism by reacting with hydrogen present in form of SH groups. Reaction pathways involving the direct removal of heteroatoms can also be described by Langmuir-Hinshelwood-type equations but in this case they are often referred to as reverse Mars-van-Krevelen-type mechanisms (Scheme 2.2).^{31,35} The differences between the reaction mechanisms most commonly referred to in heterogeneous catalysis were recently summed up in a nice work by R. Prins.³⁶



Scheme 2.2 Schematic pathway of sulfur removal from thiophene according to a reverse Mars-van-Krevelen-type mechanism on a MoS₂ catalyst.³¹

Although this scheme only shows the direct desulfurization of thiophene, the elementary steps for nitrogen and oxygen removal are similar. In a first step a heteroatom-containing molecule coordinates to a CUS followed by cleavage of the heteroatom-carbon bond by hydrogenolysis with hydrogen coming from SH groups. The resulting hydrocarbon (here butadiene) can be further hydrogenated in subsequent steps. As a result of heteroatom abstraction, the CUS is now occupied and

can be regenerated by reaction with hydrogen, again in form of adjacent SH groups. The heteroatom ultimately is released in form of H₂S, NH₃ or H₂O. It must be noted that the formation of a CUS does not necessarily have to occur at the original position. Rather, the active edges of TMS catalysts dynamically change under typical reaction conditions.^{27,31}

2.2 Upgrading of Renewable Resources

To sustainably operate a modern-day refinery, it will be inevitable to perform the switch from crude oil to renewable feedstocks. This is the only way to combine the advantages of an already existing, well-established industry with the goal of a future circular carbon environment. Given the current usage of primary energy sources in the global picture (Figure 2.5), this transformation will be one of the major challenges of the coming decades.

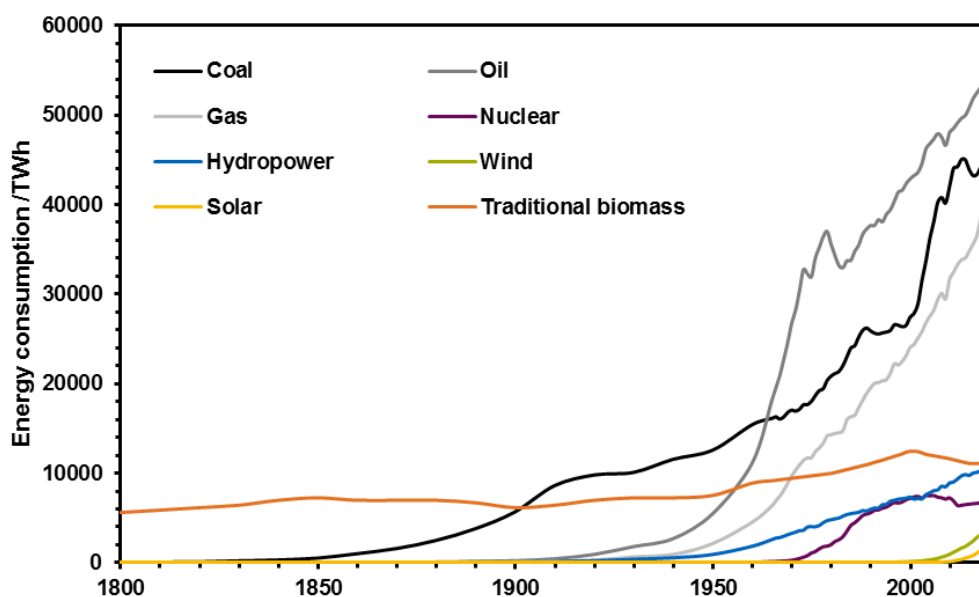


Figure 2.5 Global primary energy consumption by source between 1800 and 2019 measured by the “substitution” method taking account of the inefficiencies of fossil fuel production (Source: Vaclav Smil (2017) & BP Statistical Review of World Energy, adopted from ref. ³⁷ under the Creative Commons BY license; <https://creativecommons.org/licenses/by/4.0/>).

The distribution nicely illustrates the enormous amount of energy that is currently produced from fossil sources. This immediately raises the question if renewable hydrocarbon feedstocks will be available in the future in the quantities needed to replace fossil ones. Besides their availability, even only partly substituting crude oil by renewable feedstocks is accompanied with enormous hurdles to overcome for refiners. This is mostly due to the significantly different chemical compositions of these feeds. Table 2.2 is giving an overview of some potential renewable feedstocks that could be converted to energy carriers and their respective chemical composition.

Table 2.2 Elementary composition of various renewable hydrocarbon feedstocks.

Renewable feedstock	S content /wt%	N content /wt%	O content /wt%
Microalgae biomass	0.5-1.5 ^a	5-10 ^a	25-40 ^a
Lignocellulose (rice straw)	0.24 ^b	0.89 ^b	54 ^b
Waste chicken fat	n.d.	0.43 ^c	17 ^c
Waste water sludge	1-2 ^d	4-8 ^d	~35 ^d

^a (ref. ³⁸), ^b (ref. ³⁹), ^c (ref. ⁴⁰), ^d (ref. ⁴¹), n.d.: not determined;

Comparing the S/N/O contents of these alternative, renewable feedstocks with crude oil (Table 2.1) distinct differences are obvious: (i) the sulfur content in all renewable feeds is less problematic compared to heavy crude oil; (ii) the nitrogen content of microalgae and waste water sludge is significantly higher; (iii) the most dramatic difference is the very high oxygen content in renewable feeds. As a result, catalyst manufacturers have to design materials that are resistant against high contents of N/O as well as against formed ammonia and water. In addition, much like for refining of crude oils, catalysts have to work efficiently under varying feed compositions.

TMS have been studied under similarly harsh conditions for decades and new generations of sulfide catalysts were developed overcoming the challenges of more stringent fuel specifications as well as more demanding crudes.³ The longstanding and successful use in refining makes TMS a prime candidate for future applications in upgrading of renewable hydrocarbon sources (e.g., reviewed in refs. ⁴²⁻⁴⁴).

Lastly, it is important to also consider the effective H/C ratios of fossil and renewable feedstocks as well as the targeted products. Lignin (H/C ~0.6) and lignocellulose (H/C ~0.2) for example, are especially poor in effective hydrogen content compared to crude oil and therefore require the addition of more H₂ during hydrotreating in order to upgrade these feedstocks into valuable fuels (diesel H/C = 2).⁴⁵ In turn, using these feeds is economically less favorable under the current circumstances. Therefore, although the incorporation of renewable feeds into existing infrastructure is technically challenging but possible, it requires adapted political preconditions to make their use economically feasible.

2.3 Electrochemistry

The previous chapter briefly introduced the concept of replacing fossil by renewable hydrocarbon sources for the production of energy carriers in order to achieve a circular carbon economy. As already mentioned, due to the comparably low effective H/C ratios of biomass derived feeds, this transformation requires an enormous amount of hydrogen. Currently, hydrogen is produced almost exclusively by steam reforming of fossil fuels.^{46,47}

Although there exist ideas to reduce CO₂ emissions from steam reforming units (e.g., by electrified reactor heating),⁴⁸ in order to produce hydrogen without formation of CO₂ at all, so-called “green” hydrogen, alternative routes are required.⁴⁹ One of the most promising concepts in this regard is the production of H₂ by electrochemical water splitting (e.g., reviewed in refs. ⁵⁰⁻⁵²). In order for this process to produce green H₂ without emitting CO₂, the energy used has to be generated from renewable resources. How electrocatalysis can become a key tool for the world energy transformation and why TMS based catalyst emerge as promising candidates for this purpose will be discussed in the following sections.

2.3.1 Electrocatalytic Hydrogen Production

Electrocatalytic production of hydrogen is considered key to reduce the global CO₂ emissions for multiple reasons. First, as the combustion of hydrogen only produces water as product, H₂ can be directly used as an energy carrier for transportation,^{53,54} home heating⁵⁵ or in industrial plants (e.g., for the production of iron and steel⁵⁶). In all three cases hydrogen can replace the current energy carriers derived from fossil fuels.

In addition, hydrogen, as well as secondary energy carriers synthesized from H₂ in combination with other renewable resources, can be used as an energy storage. This is of utmost importance for the future switch from fossil energy production (coal, oil & gas power plants) to renewable energy production (solar, wind, hydropower) mentioned in chapter 2.2. This switch involves changing from large-scale, steady energy suppliers in form of power plants to a decentralized supply of energy from a multitude of smaller sources. As the energy supplied for example by photovoltaic or wind power plants heavily fluctuates, huge quantities of energy have to be stored. The general concept of transforming renewable energy into chemical energy for storage (power-to-X) is schematically depicted in Figure 2.6.

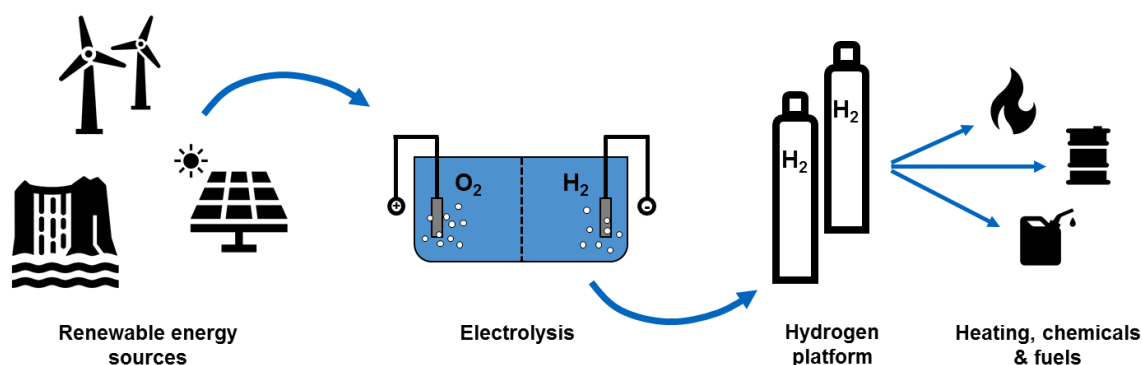


Figure 2.6 Production of hydrogen and secondary products *via* electrolysis using renewable energy sources (power-to-X concept).⁵⁷

Power-to-X in general describes a process in which renewable energy (“power”) is transformed into a chemical energy carrier of any kind (“X”; e.g., hydrogen, ammonia, hydrocarbons). The key step in this process is the electrolytic splitting of water into oxygen and hydrogen. As mentioned above, the formed hydrogen can be used either directly as an energy carrier or as a platform for the subsequent production of secondary energy carriers.^{50-52,57}

2.3.2 Sulfide Phases as Electrode Materials

Electrocatalytic water splitting has been studied for decades and in the majority of reports group 9 & 10 noble metals turned out to be the most efficient electrode materials (reviewed in refs. ^{47,51,58}). However, in order to upscale from lab-scale to industrial-scale production of hydrogen, there is a central problem accompanied with the use of noble metals: their low abundance and in turn their high price. Therefore, researchers focused on developing alternative catalyst materials with transition metal sulfide based materials emerging as one of the most promising classes. In analogy to their use as hydrogenation catalyst, TMS can be manufactured into effective catalyst materials for electrocatalytic hydrogen evolution. It should be noted, that in both cases it is essential to design TMS exposing a maximum number of exposed sites in order to end up with effective catalyst materials (see also section 3.1.4).⁵⁹⁻⁶¹

It is important mentioning, that the use of electrocatalysis in general and the use of TMS in particular is not limited to water splitting.⁶² TMS have been proposed as electrocatalysts for CO₂ reduction⁶³ and ammonia synthesis from N₂,⁶⁴ or as support materials in methanol oxidation fuel cells.⁶⁵

2.4 References

- (1) Prins, R. In *Handbook of Heterogeneous Catalysis*; Ertl, G., Knözinger, H., Schüth, F., Weitkamp, J., Eds.; John Wiley & Sons: 2008, p 2695.
- (2) Weisser, O.; Landa, S. *Sulphide catalysts, their properties and applications*; Elsevier, 2013.
- (3) Chianelli, R. R.; Berhault, G.; Torres, B. *Catalysis Today* **2009**, *147*, 275.
- (4) Robinson, P. R.; Dolbear, G. E. In *Practical Advances in Petroleum Processing*; Hsu, C. S., Robinson, P. R., Eds.; Springer New York: New York, NY, 2006, p 177.
- (5) Gruia, A. In *Handbook of Petroleum Processing*; Jones, D. S. J. S., Pujadó, P. R., Eds.; Springer Netherlands: Dordrecht, 2006, p 321.
- (6) Trambouze, P. In *Chemical Reactor Technology for Environmentally Safe Reactors and Products*; de Lasa, H. I., Doğu, G., Ravello, A., Eds.; Springer Netherlands: Dordrecht, 1992, p 425.
- (7) Mederos, F. S.; Ancheyta, J. *Applied Catalysis A: General* **2007**, *332*, 8.
- (8) Chen, H. J.; Massoth, F. E. *Industrial & Engineering Chemistry Research* **1988**, *27*, 1629.
- (9) Wei, J.; Zhao, X. *Chemical Engineering Science* **1992**, *47*, 2721.
- (10) Rabiei, Z. *Petroleum & Coal* **2012**, *54*.
- (11) U.S. Energy Information Administration: *U.S. Refinery Desulfurization (including Catalytic Hydrotreating) Downstream Charge Capacity as of January 1. 2021*, <https://www.eia.gov/dnav/pet/hist/LeafHandler.ashx?n=PET&s=8 NA 8CD0 NUS 5&f=A> (accessed 26.01.2022).
- (12) Oudar, J. *Catalysis Reviews* **1980**, *22*, 171.
- (13) Nabgan, W.; Rashidzadeh, M.; Nabgan, B. *Environmental Chemistry Letters* **2018**, *16*, 507.
- (14) Matsumoto, S. i. *Catalysis Today* **2004**, *90*, 183.
- (15) Fishel, N. A.; Lee, R. K.; Wilhelm, F. C. *Environmental Science & Technology* **1974**, *8*, 260.
- (16) Alfke, G.; Irion, W. W.; Neuwirth, O. S. In *Ullmann's Encyclopedia of Industrial Chemistry* 2007.
- (17) Cerqueira, H. S.; Sievers, C.; Joly, G.; Magnoux, P.; Lercher, J. A. *Industrial & Engineering Chemistry Research* **2005**, *44*, 2069.
- (18) Barbier, J. *Applied Catalysis* **1986**, *23*, 225.
- (19) Stratas Advisors: *Seven Countries Move Up in Top 100 Ranking on Diesel Sulfur Limits. 2021*, <https://stratasadvisors.com/Insights/2021/04272021-Top-100-Diesel-Sulfur-Ranking> (accessed 26.01.2022).
- (20) Stratas Advisors: *Seven Countries Move Up in Top 100 Ranking on Gasoline Sulfur Limits. 2021*, <https://stratasadvisors.com/Insights/2021/07232021-Top-100-gasoline-sulfur-ranking> (accessed 26.01.2022).
- (21) International Maritime Organization: *IMO 2020 – cutting sulphur oxide emissions. 2020*, <https://www.imo.org/en/MediaCentre/HotTopics/Pages/Sulphur-2020.aspx> (accessed 26.01.2022).
- (22) Akmaz, S.; Iscan, O.; Gurkaynak, M. A.; Yasar, M. *Petroleum Science and Technology* **2011**, *29*, 160.
- (23) Clarivate: *Results from Web of Science Core Collection for: molybdenum sulfide. 2022*, <https://www.webofscience.com/wos/woscc/summary/09405c70-a2d9-407c-ac2a-c7ed4aaf8ab4-20099f22/relevance/1> (accessed 08.02.2022).
- (24) Jungbluth, N.; Meili, C.; Wenzel, P. *Life cycle inventories of oil refinery processing and products Final report*, 2018.
- (25) Ma, X.; Sakanishi, K.; Mochida, I. *Industrial & Engineering Chemistry Research* **1996**, *35*, 2487.
- (26) Lengyel, A.; Magyar, S.; Kalló, D.; Hancsók, J. *Petroleum Science and Technology* **2010**, *28*, 946.

- (27) Kokayeff, P.; Zink, S.; Roxas, P. In *Handbook of Petroleum Processing*; Treese, S. A., Jones, D. S., Pujado, P. R., Eds.; Springer International Publishing: Cham, 2015, p 1.
- (28) Robinson, W. R. A. M.; van Veen, J. A. R.; de Beer, V. H. J.; van Santen, R. A. *Fuel Processing Technology* **1999**, *61*, 89.
- (29) Kim, S. C.; Simons, J.; Massoth, F. E. *Journal of Catalysis* **2002**, *212*, 201.
- (30) Gevert, B. S.; Otterstedt, J. E.; Massoth, F. E. *Applied Catalysis* **1987**, *31*, 119.
- (31) Topsøe, H.; Clausen, B. S.; Massoth, F. E. In *Catalysis: Science and Technology*; Anderson, J. R., Boudart, M., Eds.; Springer Berlin Heidelberg: Berlin, Heidelberg, 1996, p 1.
- (32) Breysse, M.; Furimsky, E.; Kasztelan, S.; Lacroix, M.; Perot, G. *Catalysis Reviews* **2002**, *44*, 651.
- (33) Thomas, C.; Vivier, L.; Lemberon, J. L.; Kasztelan, S.; Pérot, G. *Journal of Catalysis* **1997**, *167*, 1.
- (34) Schachtl, E.; Kondratieva, E.; Gutiérrez, O. Y.; Lercher, J. A. *The Journal of Physical Chemistry Letters* **2015**, *6*, 2929.
- (35) Mars, P.; van Krevelen, D. W. *Chemical Engineering Science* **1954**, *3*, 41.
- (36) Prins, R. *Topics in Catalysis* **2018**, *61*, 714.
- (37) Our World in Data: *Global primary energy consumption by source*. **2016**, https://ourworldindata.org/grapher/global-energy-consumption-source?country=~OWID_WRL (accessed 27.01.2022).
- (38) Yang, C.; Li, R.; Cui, C.; Liu, S.; Qiu, Q.; Ding, Y.; Wu, Y.; Zhang, B. *Green Chemistry* **2016**, *18*, 3684.
- (39) Li, B.; Yang, T.; Li, R.; Kai, X. *Energy* **2020**, *200*, 117524.
- (40) Suchamalawong, P.; Pengnarapat, S.; Reubroycharoen, P.; Vitidsant, T. *Journal of Environmental Chemical Engineering* **2019**, *7*, 103155.
- (41) Manara, P.; Zabaniotou, A. *Renewable and Sustainable Energy Reviews* **2012**, *16*, 2566.
- (42) Honkela, M. L.; Viljava, T.-R.; Gutierrez, A.; Krause, A. O. I. *Thermochemical Conversion of Biomass to Liquid Fuels and Chemicals* **2010**, *1*, 288.
- (43) Patel, M.; Kumar, A. *Renewable and Sustainable Energy Reviews* **2016**, *58*, 1293.
- (44) Gandarias, I.; Barrio, V. L.; Requies, J.; Arias, P. L.; Cambra, J. F.; Güemez, M. B. *International Journal of Hydrogen Energy* **2008**, *33*, 3485.
- (45) van Dyk, S.; Su, J.; Mcmillan, J. D.; Saddler, J. *Biofuels, Bioproducts and Biorefining* **2019**, *13*, 760.
- (46) Liu, K.; Song, C.; Subramani, V. *Hydrogen and syngas production and purification technologies*; John Wiley & Sons, 2010.
- (47) Dincer, I.; Acar, C. *International Journal of Hydrogen Energy* **2015**, *40*, 11094.
- (48) Wismann, S. T.; Engbæk, J. S.; Vendelbo, S. B.; Bendixen, F. B.; Eriksen, W. L.; Aasberg-Petersen, K.; Frandsen, C.; Chorkendorff, I.; Mortensen, P. M. *Science* **2019**, *364*, 756.
- (49) Turner, J. A. *Science* **2004**, *305*, 972.
- (50) You, B.; Sun, Y. *Accounts of Chemical Research* **2018**, *51*, 1571.
- (51) Shiva Kumar, S.; Himabindu, V. *Materials Science for Energy Technologies* **2019**, *2*, 442.
- (52) Tang, M. T.; Liu, X.; Ji, Y.; Norskov, J. K.; Chan, K. *The Journal of Physical Chemistry C* **2020**, *124*, 28083.
- (53) Candelaresi, D.; Valente, A.; Iribarren, D.; Dufour, J.; Spazzafumo, G. *International Journal of Hydrogen Energy* **2021**, *46*, 35961.
- (54) Evrin, R. A.; Dincer, I. *International Journal of Hydrogen Energy* **2019**, *44*, 6919.
- (55) Baldino, C.; O'Malley, J.; Searle, S.; Zhou, Y.; Christensen, A.; Retrieved from the International Council on Clean Transportation [https ...](https://www.icsct.org/): 2020.
- (56) Bhaskar, A.; Assadi, M.; Nikpey Somehsaraei, H. *Energies* **2020**, *13*, 758.
- (57) Ausfelder, F.; Dura, H. E. *DECHEMA, Gesellschaft für Chemische Technik und Biotechnologie* **2018**, *1*.

- (58) Rashid, M.; Al Mesfer, M. K.; Naseem, H.; Danish, M. *International Journal of Engineering and Advanced Technology* **2015**.
- (59) Sun, H.; Yan, Z.; Liu, F.; Xu, W.; Cheng, F.; Chen, J. *Advanced Materials* **2020**, *32*, 1806326.
- (60) Wang, M.; Zhang, L.; He, Y.; Zhu, H. *Journal of Materials Chemistry A* **2021**, *9*, 5320.
- (61) Merki, D.; Fierro, S.; Vrabel, H.; Hu, X. *Chemical Science* **2011**, *2*, 1262.
- (62) Seh, Z. W.; Kibsgaard, J.; Dickens, C. F.; Chorkendorff, I.; Nørskov, J. K.; Jaramillo, T. F. *Science* **2017**, *355*, eaad4998.
- (63) Chan, K.; Tsai, C.; Hansen, H. A.; Nørskov, J. K. *ChemCatChem* **2014**, *6*, 1899.
- (64) Xu, X.; Tian, X.; Sun, B.; Liang, Z.; Cui, H.; Tian, J.; Shao, M. *Applied Catalysis B: Environmental* **2020**, *272*, 118984.
- (65) Zhai, C.; Zhu, M.; Bin, D.; Ren, F.; Wang, C.; Yang, P.; Du, Y. *Journal of Power Sources* **2015**, *275*, 483.

3 Structure and Reactivity of Transition Metal Sulfide Phases

“The CoMo/Al₂O₃ and NiMo/Al₂O₃ catalysts have, for several decades, been the workhorses for hydrotreatment of a great variety of refinery feed stocks. The fundamental understanding of these catalyst systems has, however, constantly been lagging far behind. Consequently, the earlier developments of these catalysts have mainly occurred as a result of trial-and-error experiments and of extensive empirical knowledge. Despite intensive research efforts and numerous publications on the subject, it remained one of the most controversial topics within catalysis.”

Henrik Topsøe, Bjerne S. Clausen & Franklin E. Massoth

In Catalysis: Science and Technology;
Anderson, J. R., Boudart, M.,
Eds.; Springer Berlin Heidelberg: Berlin, Heidelberg, 1996

3.1 Conventional Sulfide Catalysts

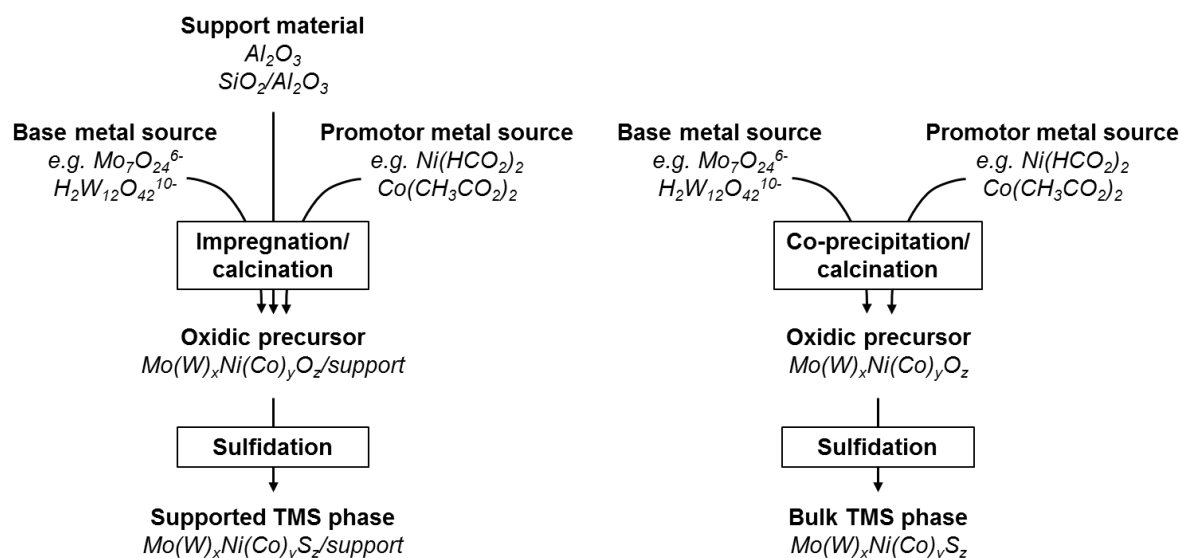
The successful implementation of hydrotreating units in virtually every modern refinery would not have been possible without the discovery and steady improvement of transition metal sulfide catalysts. Unlike most classic hydrogenation catalysts (*e.g.*, the most prominently used group 10 metals), transition metal sulfides, more specifically sulfides of molybdenum and tungsten, exhibit stable performance even under the presence of S/N/O contaminants in a reaction feed. In addition, they are economically affordable and available in the vast quantities needed for application in industrial refining. Interestingly, the fundamental concept of using MoS₂ and WS₂ for hydrogenation reactions in the presence of sulfur in the feed is still applied despite being developed almost 100 years ago.¹⁻³

Since the original discovery of TMS for hydrogenation reactions a lot of research activities have been devoted to improving their catalytic properties by optimizing for example the support materials, the exact chemical composition of the active sulfide phases, and the structure and morphology of the catalysts. Nevertheless, sulfides of Mo and W still serve as the basis for almost all hydrotreating catalysts. It is important to note that catalyst development in the field of TMS not only aims towards higher activities but also towards meeting the specific requirements needed to process the different feeds present in a refinery as mentioned earlier.^{1,4}

Their enormous versatility and resistance against poisoning/degradation even by challenging hydrocarbon feeds makes them an intriguing and promising candidate for a variety of modern-day and future applications as mentioned in chapter 2.

3.1.1 Synthesis Strategies

Although numerous strategies for the synthesis of transition metal sulfides have been reported in literature (*e.g.*, refs. ^{3,5-8}), the preparation of TMS catalysts on an industrial-scale mostly follows a very distinct route as seen in the patents of catalyst manufacturers.⁹⁻¹¹ First, an oxidic precursor is prepared which is then transformed into the desired sulfide phase by sulfidation inside the actual hydrotreating unit (Scheme 3.1).



Scheme 3.1 Simplified scheme of the preparation of supported (left) and bulk (right) TMS phases.

In the case of supported catalysts, the support material (e.g., alumina or silica-alumina) is impregnated with aqueous salt solutions of the base metals (Mo/W) and promoter metals (Co/Ni). Typically, incipient wetness impregnation (*i.e.*, the amount of metal salt solution is adjusted to the pore volume of the support) is used for better control over the final metal loadings. Virtually every combination of metals and a wide range of their respective loadings can be achieved by adding the different metals in the same impregnation step or sequentially and by applying repeated cycles of impregnation and drying. A more detailed discussion about the effect of promoting metals can be found in section 3.1.5. After impregnation these materials are usually dried and calcined in air to obtain the final oxidic precursors.^{6,7}

Self-supported catalysts (*i.e.*, bulk sulfide phases without primary oxide support) for industrial applications can also be prepared *via* oxidic precursors. In this case, co-precipitation out of a solution of the same metal salts mentioned above commonly is the method of choice. For modification of the catalyst structure and morphology chelating agents like organic molecules can be added to the precursor solution.^{9,12,13}

After preparation of oxidic precursors, the final catalysts are formed by sulfidation in the presence of hydrogen and a sulfiding agent at temperatures of up to 400 °C. In industry, this sulfidation step is done at the site of operation after installing the precursors using a conventional hydrotreating feed spiked with an additional sulfur source (e.g., dimethyl sulfide). This approach comes with the advantage of handling only the oxidic precursors (e.g., for extrusion and transport), which is significantly

easier due to their better mechanic properties. In addition, in liquid phase, heat dissipation during the highly exothermic sulfidation step is better controlled compared to sulfidation in gas phase as often applied on a lab-scale. It should be noted that the formation of precursor materials as well as the transformations occurring during sulfidation of these has been shown to play a critical role for the catalytic properties of the final TMS phases.^{7,14} This is, however, beyond the scope of this work.

On a lab-scale, several other routes have been presented especially for the synthesis of self-supported TMS phases, including sulfide phase preparation by thermal decomposition of thiosalts¹⁵, homogeneous sulfide precipitation,¹⁶ or co-maceration procedures.¹⁷

3.1.2 Structure and Morphology

Although the use of molybdenum sulfide as hydroprocessing catalyst and even the promoting effect of nickel and cobalt date back to the 1940s it was not until the beginning of the 1980s before the group of Topsøe *et al.* was able to come up with a convincing model describing the active phase in TMS catalysts; the so-called “CoMoS” or edge decoration model (Figure 3.1).^{18,19} A detailed review about the history of TMS catalyst design and application, including some alternative models that have been proposed for the structure of TMS phases, was prepared by Chianelli *et al.*³

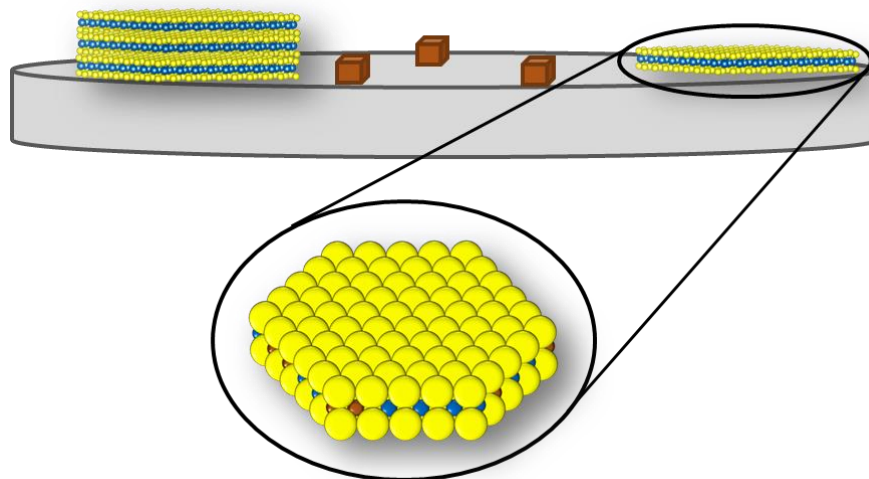


Figure 3.1 Simplified depiction of a typical TMS catalyst according to the “CoMoS” model composed of a bimetallic sulfide phase on a support.²⁰ Brown cubes (unspecified Co/Ni_xS_y phases), brown spheres (Co, Ni), blue (Mo, W), yellow (S), and gray (support). The sulfide slabs in the upper part were created using VESTA version 4.3.0. (based on ref. ²¹).

Figure 3.1 demonstrates that TMS catalysts actually consist of multiple, coexisting metal (sulfide) phases present on the support. While the base metals (Mo/W) are forming a two-dimensional, slab-like sulfide phase, Ni/Co are present in three different configurations: (i) as single metal atoms in strong interaction with the support (not shown in Figure 3.1), (ii) in form of segregated monometallic sulfide phases, and (iii) at the edges of the base metal slabs. While the former two are generally not considered to provide significant activity for hydrotreating reactions, Ni/Co decorating the edges of TMS slabs is nowadays widely accepted as the predominant origin of the promoting effect.^{6,20} How these promoting atoms are able to enhance the activity of TMS catalysts is discussed further in section 3.1.5.

The morphology of the active CoMoS phase is best described as a two-dimensional, layered slab consisting of a layer of metal cations sandwiched between two layers of sulfide anions. Note that, although the mixed metal phase is usually denoted as CoMoS in this work, virtually all permutations of base metals (Mo/W) in combination with promoters (Ni/Co) are possible. By the use of high-resolution electron microscopy, the 2D TMS phases have been shown to possess triangular or hexagonal shapes depending on their degree of promotion and the pretreatment conditions.²²⁻²⁴ Figure 3.2 is schematically showing the hexagonal structure of an ideal MoS₂ slab together with the corresponding local coordination of molybdenum and sulfur atoms.

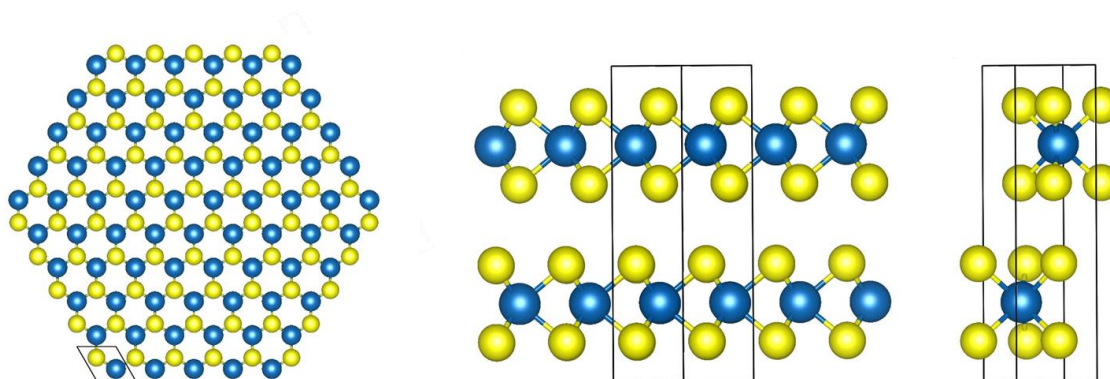


Figure 3.2 Structure of a representative MoS₂ slab in top view (left) and side view (middle, right). The black lines mark the unit cell. Blue (Mo), yellow (S). Drawings were created using VESTA version 4.3.0. (based on ref. ²¹).

From the top view of an ideal MoS₂ hexagon it can be seen that the edges of TMS slabs can be either terminated by sulfur or by metal atoms, hence denoted as sulfur and metal edges. For the metal edge it has been shown by STM in combination with theory that, due to perturbation of the electronic structure in close proximity to the edge,

the local electron density is higher compared to the bulk of the slab. These near-edge areas with enhanced electron density, sometimes referred to as “brim” sites, are proposed as additional adsorption sites especially important for the conversion of sterically demanding molecules.^{22,25,26}

Figure 3.2 also visualizes the local coordination of Mo and S atoms. Each metal atom is coordinated to six sulfur atoms as nearest neighbors (three from each of the two sandwiching S layers) and six metal atoms from the same metal layer. The side views demonstrate how several TMS slabs can be stacked over each other. Typically, the stacking of slabs as well as their size strongly depends on the synthesis method and conditions applied, *e.g.*, the support material,^{5,27} the sulfidation procedure,^{3,28} or the use of surfactants.^{8,29}

Lastly, it is worth mentioning that structure and morphology of TMS phases can be further manipulated during synthesis by the use of organic structure directing agents, like surfactants and swelling agents. The former usually are large-size organic molecules strongly coordinating to the metal cations and thus serving as a template able to tune slab size and stacking. In addition, by chelating Ni/Co atoms, they delay their sulfidation to higher temperatures. This is crucial for the incorporation of promoters into the TMS slabs because Ni/Co otherwise are sulfided at lower temperatures compared to Mo/W resulting in the increased formation of segregated metal sulfide phases. Swelling agents on the other hand control the porous structure (*e.g.*, pore size distribution) of the sulfide phases improving transport of reactants and products which is critical for their industrial application with real feeds.^{5,8,29}

3.1.3 Role of Support Materials

The choice of support materials is of utmost importance for almost every heterogeneous catalyst. Supports for industrial catalysts have to fulfill certain requirements in order to be technologically and economically feasible: (i) affordability and availability in the huge quantity they are needed, (ii) mechanical and thermal stability for catalyst preparation (*e.g.*, extrusion, filling of reactors) as well as during use, (iii) large surface area for dispersion of active phase. In addition, for hydrotreating catalysis, a moderate metal-support interaction is necessary for efficient sulfidation of loaded metals.^{5,7,27}

Although most commercial hydrotreating catalysts are still composed of TMS phases supported on alumina, more recently another promising class of sulfide catalysts emerged; so-called self-supported TMS.^{12,13} In the following section, the advantages and disadvantages of using self-supported sulfides and TMS supported on metal oxides, mesoporous materials or zeolites are discussed.

3.1.3.1 Self-Supported Sulfides

One of the breakthrough developments in hydrotreating catalysis over the last decades was the introduction of self-supported TMS phases as catalysts. The materials were developed in joint cooperation by ExxonMobil, Akzo Nobel Catalysts (now Albemarle Catalysts) and Nippon Ketjen Co. Ltd. under the trademark NEBULA[®] and first used in a commercial plant in 2001. The number of commercial hydrotreating units using NEBULA[®] catalysts quickly increased over the next years due to the significantly higher activity per volume of installed catalyst. The improved activity allowed refiners to upgrade existing units in a way to meet the more stringent requirements for sulfur limits in fuels (mentioned in chapter 2.1) without needing to build new reactors. On the other hand, for some units their activity is simply too high in order to be used efficiently.^{12,13}

In contrast to (commercial) alumina supported catalysts (e.g., NiMoS/Al₂O₃ & CoMoS/Al₂O₃) that show only very little stacking^{30,31} the slabs of self-supported TMS have been shown to be present in stacks of about three to four slabs on average.^{32,33} The same works report an average slab length of about 3-5 nm for both types of catalysts. While the slab length is crucial for the activity of TMS catalysts because of the increasing fraction of edge and corner metal atoms with decreasing slab length (discussed in more detail in section 3.1.4.1), the influence of stacking is under debate. On the one hand, there are reports claiming that adsorption of sterically demanding molecules is favored with higher stacking,^{34,35} but on the other hand Eijsbouts *et al.* showed that the absence of highly stacked sulfide slabs was not detrimental for commercial TMS catalysts used for the production of ultra-low sulfur diesel.³⁰ Regardless of whether the degree of stacking is of importance for their performance, the fact that self-supported TMS can be synthesized with similar slab lengths is supposedly the reason for their enhanced activity on a volumetric base. For supported catalysts, a significant volume is occupied by “inert” support phases, whereas for self-supported systems the whole catalyst particles consist of active sulfide phases.

3.1.3.2 Metal Oxides, Mesoporous Materials and Zeolites

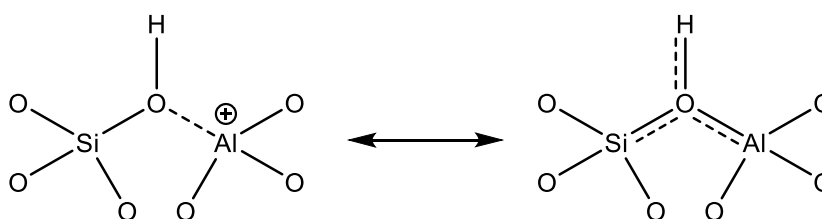
As already mentioned above, in most cases alumina is the support of choice for industrial hydrotreating catalysts. This is due to its excellent material properties in handling and processing (*e.g.*, mechanical strength, texture) and comparably low cost.³⁶ Nevertheless, a wide variety of different oxidic supports (*e.g.*, modified alumina, other (mixed) metal oxides, mesoporous materials, and zeolites) were tested for hydrotreating catalysis (reviewed in refs. ^{5,37}).

The main disadvantage of using alumina as a support for TMS is its strong interaction with Co/Ni cations and molybdates. Co/Ni cations strongly interacting with the support are generally considered inactive (as discussed in section 3.1.2) and the strong interaction of alumina and molybdates (formed upon impregnation and calcination; section 3.1.1) hampers the formation of molybdenum sulfide phases.^{5,37} It has been shown that it is possible to modify alumina (*e.g.*, by addition of heteroatoms like Ga or P,⁵ or by addition of a chelating agent like nitrilotriacetic acid³⁵) in a way that decreases the metal-support interaction (MSI). TMS phases supported on these modified materials with reduced MSI showed a higher dispersion and in turn significantly enhanced activity for hydrotreating reactions. Looking at the results for TMS supported on other metal oxides (*e.g.*, TiO₂ and ZrO₂) and mixed metal oxides (*e.g.*, amorphous silica-alumina, alumina-titania, and zirconia-titania), it can be concluded that the main descriptor for their activity is the dispersion of the active sulfide phase and as a result the fraction of exposed edge/corner metal atoms. In order to achieve highly dispersed TMS phases in combination with high overall metal loadings it is inevitable to use oxides with sufficiently high surface areas.^{5,35,37}

Another class of materials considered as support for TMS are highly ordered mesoporous (*e.g.*, SBA-15) and microporous (zeolites) molecular sieves. Besides their outstanding surface areas, they are able to provide Brønsted acidity (Scheme 3.2). Acidity of the support in general is proposed to influence the dispersion of sulfide phases and to decrease the electron density of the sulfide phase. As mentioned above influencing the dispersion will directly influence the catalytic activity, while the decreased electron density leads to increasing acidity of the TMS phase. In addition, Brønsted acid sites from the support materials themselves can also actively play a role as hydrogen source for hydrotreating reactions. The resulting bi-functional catalysts

often show improved activity and, in some cases, also open new reaction pathways (e.g., cracking reactions).^{5,31,37,38}

The overall effect of changing support acidity is quite dramatic for some cases. For the hydrogenation of tetralin, the activity of MoS₂ supported on a series of different BEA-type zeolites increased by a factor of 40 with increasing support acidity.²⁷ On the negative side, a major drawback of using Brønsted acid supports is the deactivation of the acid function under typical hydrotreating conditions, although this factor can be partly overcome by finding suitable ratios of sulfide phase and support acidity.^{37,38}



Scheme 3.2 Resonance structures of a Brønsted acid site found in acid silica-alumina supports.³⁹

3.1.3.3 Carbonaceous Supports

The support materials so far all consisted of metal oxides. Beyond these, there is an additional class of supports that was considered for TMS catalyst already at a very early stage; the ones that are based on carbon. Carbon has several material properties that suit well for application as a catalyst support: (i) it is comparatively cheap, (ii) metals can be easily regenerated from the support by combustion, and (iii) it possesses high stability under typical hydrotreating conditions. On top, surface areas and pore structures can be easily tuned and carbon shows a lower MSI with sulfide phases compared to alumina.^{5,37,40}

Amongst the class of carbon supports many different materials have been tested for TMS catalysis, e.g., carbon black⁴¹, activated carbon,⁴¹⁻⁴³ or highly ordered carbon nanotubes.^{40,44} In cases where carbon materials were superior to oxides as support for TMS phases, this was assigned to the high dispersion of sulfide phases due to high surface areas and an improved sulfidation due to reduced MSI. In addition, coke formation is usually observed to be less on carbonaceous supports compared to metal oxides because of the much higher acidity of the latter.^{40,41,43}

More recently TMS catalysts have also gained interest as replacement for noble metals in electrochemistry (see section 2.3.2; reviewed e.g., in refs. ^{45,46}). Besides

using self-supported TMS as catalysts, there are reports showing that TMS supported on conductive carbon supports like modified graphene⁴⁷ or carbon nanotubes^{48,49} are suitable for electrochemical applications. They can be used either directly as electrode materials or as support materials helping to disperse noble metals. The high activity of these materials, for instance for electrocatalytic hydrogen evolution, is related to the formation of highly dispersed TMS phases on high surface area carbon supports.⁴⁷⁻⁴⁹

3.1.4 Active Sites

For a long time, monitoring the active sites of TMS catalyst *operando* during hydrotreating reactions was almost impossible due to challenging reaction conditions (high temperatures and pressures) as well as the physico-chemical properties of the mixed metal sulfide phases. Some techniques like XPS, STM or TEM could only probe the parent state of catalysts under model conditions which proved to be insufficient because of the dynamic reconstruction of TMS phases in reactive atmospheres.^{22,50,51} For bulk techniques like IR spectroscopy of adsorbed probe molecules, XAS, Mössbauer spectroscopy or XRD, the sulfide phase itself was problematic due to its low specific surface area (low number of adsorbed probes) and its heterogeneity of sites.^{18,52,53} Especially for mixed TMS phases, bulk techniques were often unable to distinguish between the different configurations of the individual metals (*e.g.*, promoted, and non-promoted sites). For this reason, the nature of active sites as well as the mechanisms of promotion on TMS catalysts remained under debate.^{6,50,51}

It lasted to the 1980s, until, due to improved spectroscopic (*e.g.*, EXAFS, Mössbauer and IR) and microscopic (*e.g.*, STM in reactive atmospheres) techniques, a more coherent picture of the structure of transition metal sulfides and the nature of their active sites evolved (see section 3.1.2). Nevertheless, the questions how these phases catalyze a multitude of different reactions is still much more under debate.^{6,54}

3.1.4.1 Location of Active Sites

A common feature for heterogeneous catalysts is that only a (small) fraction of the overall phase is catalytically active. This is because of the inaccessibility of (metal)atoms located at the inside of three-dimensional particles. As heterogeneous catalysis is driven by reactions at the solid-fluid interface, only these sites can participate in chemical transformations that are located at this interface, and in turn at the outer surface of the catalyst particles. This holds especially true for transition metal

sulfide phases as depicted in Figure 3.3. Under typical reaction conditions, significant amounts of exposed metal sites are only present at the edges of the sulfide slabs and not at their basal planes. Experimentally, this has been verified by showing that the activity of TMS phases for hydrogenation and hydrodesulfurization correlates with their edge fraction.⁵⁵⁻⁵⁷ On a lab-scale, it is however possible to create artificial defect sites also on the basal planes that can then act as adsorption sites.⁵⁸

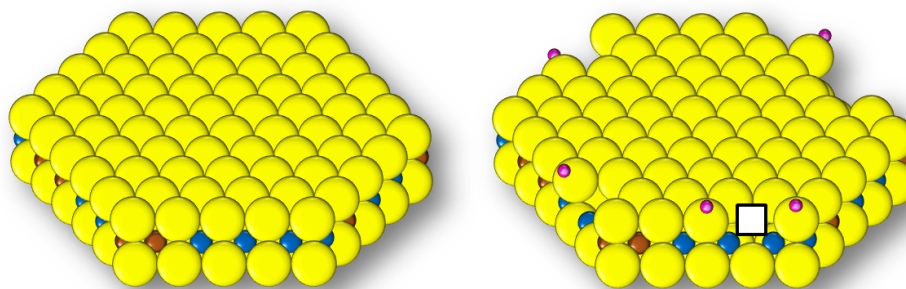


Figure 3.3 Schematic structure of a TMS slab in an ideal, fully sulfided state (left) and in a state representing the “working” state under reaction conditions (right). The white square emphasizes the location of one of the missing S atoms. Pink (H), brown (Co, Ni), blue (Mo, W), yellow (S).⁶

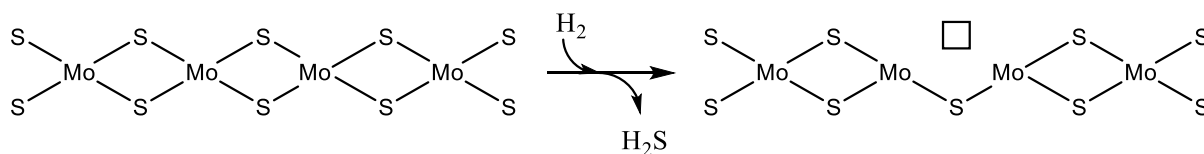
The simplified illustration shows SH groups and CUS, the two features mostly proposed to act as the active sites for catalyzed reactions. Their reactivity in hydrotreating will be discussed in the next sections. The most active sulfur atoms, required for the formation of CUS and SH, on TMS slabs are the ones terminating the edges due to their low coordination. Hence, highly active TMS catalysts are designed by minimizing the average slab size resulting in a higher fraction of edge atoms and in turn a higher density of active sites.^{6,7,56}

Interestingly, not only the terminating edge atoms but rather the whole near-edge area possesses special properties (as previously mentioned in section 3.1.2). Combining electron microscopy with density functional theory, the group of Topsøe was able to convincingly show that the near-edge areas have surprisingly high electron density due to restructured edge terminations. This discovery was used to develop improved hydrotreating catalysts introduced under the trademark BRIM[®].^{22,26,59,60}

3.1.4.2 Sulfur Vacancies

So-called defect sites, coordinatively unsaturated sites, or simply “missing” sulfur anions play a crucial role for the reactivity of all TMS phases irrespective of the

chemical composition of the sulfide phase. The formation of CUS from a fully sulfided/saturated TMS surface is schematically depicted in Scheme 3.3.



Scheme 3.3 Formation of a coordinatively unsaturated site on a schematic MoS₂ surface.⁶

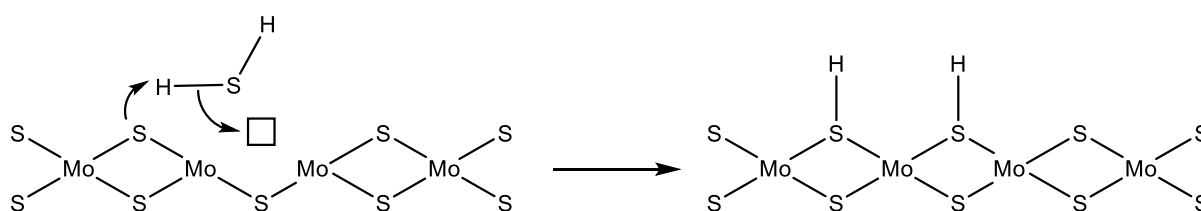
Surface hydrogen species interact with an edge sulfide anion to form H₂S resulting in a sulfur vacancy where now metal sites are exposed for reaction. Because this reaction is reversible under typical hydrotreating conditions (simultaneous presence of hydrogen and sulfide species in feed) a dynamic equilibrium, determining the amount of exposed metal centers, is established. The degree of saturation is depending on the partial pressure of hydrogen and the amount of S-containing molecules in the reaction feed and was found critical for the activity of TMS. The presence of neighboring CUS is also possible under reaction conditions and is claimed to influence the adsorption properties of sterically more demanding molecules.^{6,61-64}

At the resulting CUS one or more metal centers are accessible as adsorption sites for reactant molecules, in particular heteroatom-containing molecules. The exposed metal cations act as Lewis acids interacting with unpaired electrons at the heteroatom thereby weakening the carbon-heteroatom bonds.^{65,66} This is the first step of the direct heteroatom removal pathways according to the Mars-van-Krevelen-type mechanism (see section 2.1.2). As discussed earlier, CUS are also proposed to be involved in the activation of H₂ by (intermediate) formation of hydride species on the exposed metal cations.^{67,68}

In order to investigate the impact of CUS for the activity of TMS, many attempts have been made to quantify them. As CUS act as Lewis acid sites, the adsorption of Lewis basic molecular probes like CO, NO or nitrogen-containing bases can be used for their quantification. Prerequisite for this method is a well-established stoichiometry of adsorbed molecules and CUS. By far the most frequently used technique for monitoring the adsorption of molecular probes is IR spectroscopy,^{52,53,69} but other methods like (pulse) chemisorption^{33,70} and *in situ* titration⁷¹ have also been established.

3.1.4.3 Sulfhydryl Groups

The second feature determining the reactivity of TMS catalysts are sulfhydryl groups, in essence dissociatively adsorbed hydrogen stabilized on edge sulfide anions. Due to the significantly higher reactivity of terminating sulfide anions, SH groups are often found at the edges of TMS slabs in proximity to CUS. Besides formation by heterolytic dissociation of H_2 (as depicted in Scheme 2.1), SH groups are formed by dissociative adsorption of H_2S (Scheme 3.4)



Scheme 3.4 Formation of sulfhydryl groups by dissociative adsorption of H_2S on a schematic MoS_2 surface.⁷²

The first case results in the formation of a hydride species in addition to the SH group, whereas the latter case results in the formation of two SH groups. Interestingly, up to now, there exists no direct evidence for the formation of hydride species on MoS_2 phases as depicted in the heterolytic H_2 dissociation pathway. This is often rationalized by a rapid scavenging of the transiently formed hydride by a neighboring S atom to form an SH group as final state. In this case, the additional electron density must be compensated by the semiconducting sulfide phase.^{6,72} In addition, SH group formation has been explained by homolytic dissociation of H_2 on disulfide bridges present at the edges of TMS phases (as discussed in section 2.1.2.2).^{59,67,73}

In contrast to CUS that essentially act as adsorption sites, SH groups act as a reservoir of dissociated hydrogen on the surface of TMS. Therefore, they can participate in all types of reactions occurring in hydrotreating units. SH groups have been shown to be weak to moderate Brønsted acids depending on their formation and local electronic environment.^{51,74,75}

Similar to the quantification of CUS, SH groups can be quantified on sulfide materials using probe molecule adsorption. Owing to the Brønsted acidic character of SH groups, nitrogen-containing base molecules are usually chosen as probe. Although the possibility to use *in situ* titration for this purpose was recently shown in a proof-of-concept study,⁷¹ IR spectroscopy is still the most commonly used tool for monitoring. The protonated and non-protonated forms of pyridine as well as 2,6-dimethyl pyridine

for example have distinct vibration bands in turn allowing the differentiation between probe molecule adsorption on Brønsted and Lewis acid sites.^{72,76,77}

3.1.5 Influence of Promoters

A major reason for the versatility of TMS for heterogeneously catalyzed reactions is their tunability using promoters. As already mentioned in section 3.1.2, TMS catalysts generally consist of a base metal sulfide phase (Mo and/or W) in combination with 3d (most prominently Ni and Co) metals. Over the years multiple theories evolved to explain the mechanism of promotion by these elements. Some considered atomic Ni and Co as independent active sites,^{78,79} others favored small Ni_xS_y/Co_xS_y phases to dissociatively adsorb hydrogen which is subsequently “spilled-over” to the base metal sulfide phase for reaction.^{80,81} Although these theories cannot be fully discarded, nowadays a different model is widely accepted to be the predominant effect of promoting metals: the formation of mixed metal sulfide phases with promoting Ni/Co atoms decorating the edges of Mo(W)S₂ slabs. As this model was first proposed by Topsøe for a system containing Co and Mo these mixed phases are generally called CoMoS phases irrespective of their actual composition.¹⁸⁻²⁰

These mixed metal sulfide phases typically exceed the activity of monometallic sulfide phases by a wide margin. Interestingly, different mixtures of base and promoter metals result in a particular enhancement of individual reaction types (e.g., hydrogenation, HDS, HDN). For example, CoMoS phases show high activities for HDS reactions whereas NiMoS and NiWS phases have been reported to show superior hydrogenation activity. For industrial hydrotreating one makes use of this by designing catalysts with specific properties adapted to the processed feed and desired product specifications in each hydrotreating unit.^{1,6}

In contrast to many other heterogeneous catalysts, for preparation of TMS catalysts promoter metals are not only used in small doses but in significant fractions. The optimum fraction of promoter metal is around 0.3-0.5 in most reports (e.g., see Figure 3.4, right). This is mostly a result of the manufacturing process of TMS catalysts. As the final sulfide phases are generally formed at the site of operation, promoter metals are added already during synthesis of (oxidic) precursors. Because the transformation of oxide phases to sulfide phases is not topotactic it is hard to control the amount of promoter metals successfully incorporated in mixed metal sulfide phases. Therefore,

promotor metals are used in excess resulting in the formation of separate $\text{Ni}_x\text{S}_y/\text{Co}_x\text{S}_y$ phases in addition to the desired CoMoS phase (as mentioned in section 3.1.2).^{6,30,82}

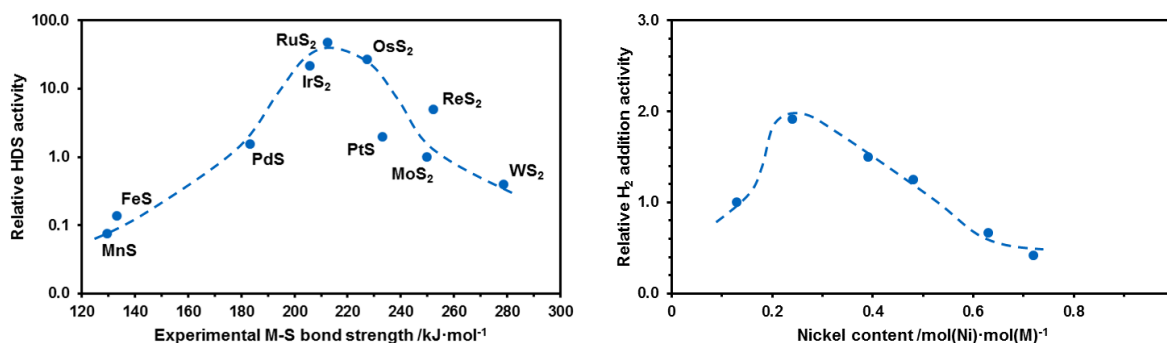


Figure 3.4 Relative HDS activities of various metal sulfides versus their experimental metal-sulfur bond strength (left; adopted from refs. ^{83,84}) and relative hydrogen addition activities of bulk $\text{Ni}_x\text{Mo}_y\text{S}_2$ catalysts with different Ni contents (right; adopted from ref. ³³).

A volcano shaped trend for catalytic activity of TMS versus their promotor metal content, as depicted above, was found for all sorts of bimetallic TMS catalysts applied in a wide variety of hydrotreating reactions.^{6,57} The increased activity at low promotor contents is understood by an increasing degree of promotor atoms decorating the edges of NiMoS phases. The negative influence of additional promotor was nicely demonstrated by Lercher *et al.* for NiMoS catalysts;⁸² at higher Ni contents more and more segregated Ni_xS_y phases are formed and these phases, being inactive themselves, block access to the active sites of the NiMoS phase. The authors showed that inert Ni_xS_y mass can be removed by post-synthetic treatment with HCl, leading to dramatically improved activities.⁸²

In order to understand how promotor atoms help increasing the activity of TMS, two properties have to be taken into account: (i) the quantity of active sites and (ii) their “quality”. As discussed previously, active sites, comprising of CUS and SH, are predominately found at the edges of TMS slabs. Consequently, the promoting effect has been explained for example by increased dispersion,^{15,85} and by increasing the probability for CUS creation. For sulfide phases, this probability is determined by the metal-sulfur bond strength.^{18,86}

This concept can be used to explain the activities of monometallic TMS phases (Figure 3.4, left) but it also applies for mixed metal sulfide phases. In essence, it is postulated that a decreased binding energy of sulfur increases the probability of CUS formation leading to more active catalysts. As seen in Figure 3.4., MoS_2 and WS_2 both

show too high M-S binding energies (right side of the volcano shaped curve), and in turn little propensity for CUS formation, to reach optimum activity. By incorporation of edge-decorating Co/Ni, new phases are formed that possess sulfides bridging Co(Ni) and Mo(W). The newly formed phases were shown to have sulfur binding energies close to the maximum of the volcano shaped curve and are therefore highly effective catalysts.^{8,57,83,86}

Based strictly on the concept of sulfur binding energy one would not expect the activity of TMS to be maximum at intermediate M-S bond strengths (as in Figure 3.4, left). Rather, TMS catalyst would be more active the lower the sulfur binding energy is due to the increased formation of active CUS. However, as this is not the case, one has to consider a second descriptor for the activity of TMS catalysts: the “quality” of each site, *i.e.*, the intrinsic activity of sites for a specific catalytic reaction. This is usually described in terms of the Sabatier principle. The interaction between reactant and active site has a maximum because very low interaction makes adsorption of reactants unlikely (adsorption is limiting) and very high interaction prevents desorption of formed products (desorption is limiting). For hydrotreating catalysis this is especially important because of the broad variety of different reactions occurring and reactants/products involved in them (see chapter 2.1). For every single reaction the optimum binding energy is slightly different, which is the reason for using different mixtures of base and promotor metals with adjusted electronic properties for hydrotreating of different feeds. It is worth noting, that Mo(W)S₂ phases have been electronically optimized by promotion with Ni and Co long before the development of volcano-type models.^{1,8,83,87}

More recently a distinctively different approach of promoting TMS catalysts by addition of group 10 metals was reported. In this case, small amounts of platinum added to an industrial CoMoS catalyst increased the activity by almost 50%. By a combination of XAS, electron microscopy and theory, the authors were able to show that atomically dispersed Pt is decorating the edges of the CoMoS phase. They concluded that Pt enhances the formation of active CUS by reducing the sulfur binding energy and thus increases the catalytic activity. Note that this explanation for the promoting effect of Pt falls in line with the previously mentioned sulfur binding energy model for promotion by other metals.⁸⁸

3.1.6 Catalyst Deactivation

Although the reasons for deactivation of TMS catalysts are manifold, most of them involve a loss of active sites accompanied by reduced activity. Under typical hydrotreating conditions these reasons include metal deposition during HDM reactions (as mentioned in chapter 2.1),^{89,90} changes in sulfide morphology (e.g., growing slab size, sintering),^{30,50} and coke formation.⁹¹⁻⁹³ Besides these factors influencing the activity of TMS by reducing the amount of accessible active sites, it has been shown that promoting metals are segregated under operation conditions further deteriorating the catalytic performance.^{12,91}

Severity and rate of deactivation depend on the catalyst composition as well as the process conditions. For example, segregation of promoters was reported to be more prominent in Ni promoted catalysts,^{12,91} metal deposition increases with increasing metal contents in heavier feeds, and structural changes of sulfide phases were found to depend on the severity (e.g., high temperatures) of sulfidation and hydrotreating conditions.^{30,50}

In terms of coke formation, the choice of promoters and support materials has been reported to have a major influence because of their ability to change the acidity of TMS catalysts. In general, higher acidity is proposed to lead to increased coke formation due to enhanced polymerization reactions. As these reactions predominantly start from polycyclic aromatics, their prevalence drastically increases catalyst deactivation. Overall, it becomes clear why heavier feeds (e.g., heavy crude oils, VGO) are much more demanding for hydrotreating processes. These feeds have very high contents of metals, polycyclic aromatics as well as sterically demanding heteroatom-containing molecules. The high contents of these compounds on the one hand directly lead to increased coke formation and metal deposition, and on the other hand require more severe process conditions in turn leading to enhanced morphological transformations further decreasing the catalytic activity.^{6,41,94,95}

In industrial applications very often a rapid initial deactivation is observed followed by a much slower deactivation in the long term. The initial fast deactivation is mostly assigned to coke formation whereas the following comparatively slow and gradual deactivation is explained by deposition of metals.⁶

For hydroprocessing of renewable feedstocks, like the ones discussed in chapter 2.2, developing adjusted catalyst (and support) systems will be critical because of the vastly different feed compositions. These feeds generally contain less sulfur but much higher contents of oxygen and water, leading to oxidation of the promotor atoms and therefore to a severe loss of activity.⁹⁶ In addition, the phosphorous content of renewable feeds was shown to be problematic due to polymerization/coke formation induced by developing phosphoric acid.⁹⁷

3.2 Active Sites in Enzymes

Fundamental research in science has always been inspired by Nature, with the field of catalysis being no exception. In Nature, countless chemical transformations are happening literally under “ambient” conditions, meaning at 1 bar and room temperature, which are only enabled by naturally occurring catalysts: enzymes. Therefore, it seems obvious to use these enzymes as a blueprint for development of catalysts. There are, however, major differences between industrial catalysts and enzymes, for example the use of metals. For the design of (heterogeneous) catalysts, there are virtually no limits in terms of metals that have been used (with a strong focus on noble metals) whereas enzymes, if at all, mostly rely on very few, naturally abundant metals like Cu and Fe. In addition, the active metal sites in enzymes typically consist of small, well-defined molecular clusters located in a very specific, constrained environment, the so-called enzyme pockets. On classic heterogeneous catalysts on the other hand, reactions are mostly occurring on the surface of nanoparticles. Nevertheless, nowadays, there exist quite a number of reactions where Nature served as a source of inspiration for catalyst development including nitrogen fixation, hydrolysis reactions, selective oxidation and electrocatalysis.⁹⁸⁻¹⁰⁰

3.2.1 Transition Metal Sulfide Structures in Nature

Interestingly, within the number of enzymes that use transition metals at their catalytically active sites, there are two very prominent examples using these metals in form of sulfide phases: hydrogenases and nitrogenases (Figure 3.5). While hydrogenases catalyze the conversion of H_2 into H^+ and *vice versa*, nitrogenases catalyze the biological reduction of N_2 to NH_3 . According to the metals found in their active sites, hydrogenases are divided into three groups: FeFe, NiFe, and Fe hydrogenases. Similarly, nitrogenases are categorized as Mo, V or Fe-only nitrogenases. It is important to note, that both enzymes contain secondary iron-sulfide clusters, most prominently Fe_4S_4 -type clusters with Fe^{2+}/Fe^{3+} as redox couple, which serve as electron carriers and are inevitable for their reactivity. These Fe_4S_4 clusters are workhorses for biological electron transport and are found in several other enzymes. The structures of the whole enzymes and the most important TMS clusters present in them as well as the reactions catalyzed by hydrogenases and nitrogenases are extensively discussed in the references corresponding to this paragraph.^{101,102}

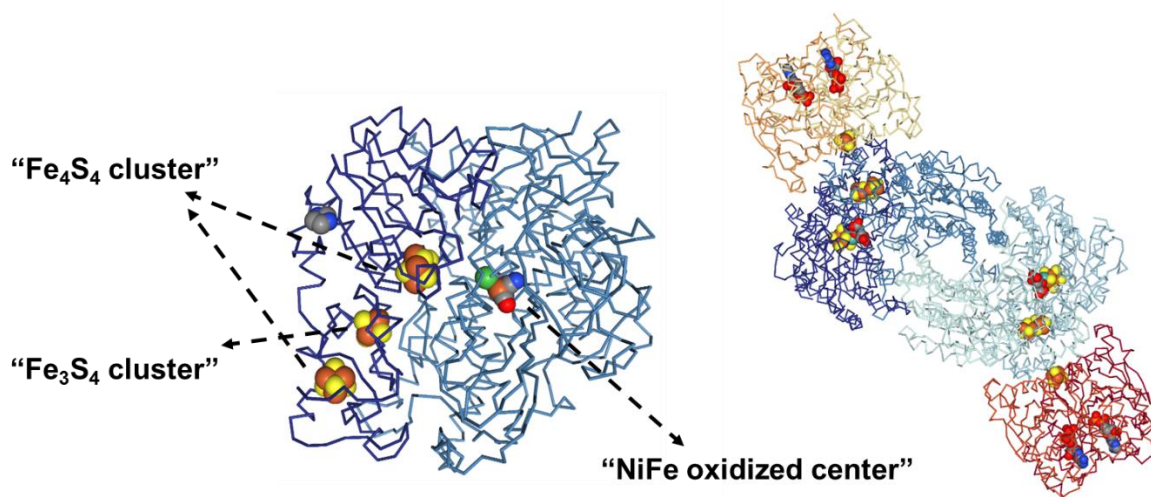


Figure 3.5 Structures of a NiFe-hydrogenase (left) and a Mo-nitrogenase (right) enzyme complex. The active clusters are depicted in spheres. Brown (Fe), cyan (Mo), green (Ni), carbon (grey), yellow (S), red (O), blue (N). Structures were obtained from the Research Collaboratory for Structural Bioinformatics Protein Data Bank (RCSB PDB; rcsb.org) of PDB ID 3MYR (hydrogenase; ref. ¹⁰³) and of PDB ID 1N2C (nitrogenase; ref. ¹⁰⁴) and images were created using NGL viewer.¹⁰⁵

Figure 3.5 shows the structures of exemplary hydrogenase and nitrogenase enzymes. In the former two different TMS clusters are found: a Fe_4S_4 and a Fe_3S_4 cluster. The TMS clusters present in the nitrogenase enzyme are assigned in the following chapter. The figure nicely demonstrates a major drawback of using whole enzymes for the synthesis of heterogeneous catalysts; on a mass and volume basis most of the enzyme consists of the protein backbone and only very little of active metal centers.^{101,102}

3.2.2 The Nitrogenase Enzyme Family

Nitrogenases are the only family of enzymes able to convert N_2 into a biocompatible nitrogen form: ammonia. As nitrogen is an essential building block in proteins and amino acids, this process is indispensable in Nature. This is in turn also the reason for the presence of significant fractions of nitrogen-containing molecules in crude oil as well as renewable feedstocks. Before the development of the Haber-Bosch process, N_2 fixation by nitrogenases was the predominant source of nitrogen available for living organisms. Interestingly, in both cases iron centers are crucial for the activation of N_2 , although the enzyme is using a sulfide cluster instead of the bare metal. For nitrogenases it should be mentioned that, besides a form only containing Fe at its active center, there exist other forms where one iron atom is replaced by either V

or Mo, with the Mo-dependent form of the enzyme (depicted in Figure 3.6) being the most prevalent one.^{101,106}

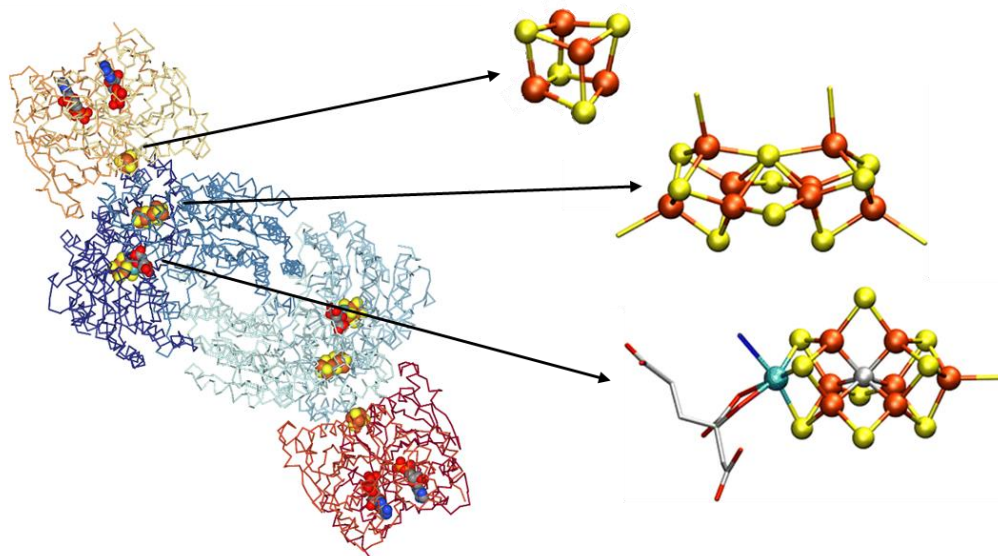


Figure 3.6 Structure of a nitrogenase enzyme (left; source see Figure 3.5) together with the incorporated TMS clusters (right; adapted from ref. ¹⁰⁷ under the Creative Commons BY license; <https://creativecommons.org/licenses/by/4.0/>). The active clusters are depicted in spheres. Brown (Fe), cyan (Mo), carbon (grey), yellow (S), red (O), blue (N).

Besides the already mentioned Fe_4S_4 cluster, the enzyme also includes a Fe_8S_7 cluster (so-called P-cluster; note that the cluster in the figure shows more than seven sulfur atoms; the additional S atoms are coming from S-containing amino acids coordinating to the cluster) and a Fe_7MoS_9 cluster with an interstitial carbon atom, the so-called FeMo cofactor. While the P-cluster is proposed to act as an electron shuttle, much like Fe_4S_4 , the FeMo cofactor is generally considered as the binding site for substrates. Due to its importance in Nature and its intriguingly complex structure, the nitrogenase FeMo cofactor has drawn a lot of attention in research.^{101,107-110}

The structure¹⁰¹ of the enzyme's active sites as well as the mechanism¹⁰⁸ for nitrogen fixation have been reviewed in the cited references. Some highlights include elucidation of the structure of the FeMo cofactor (high-resolution single-crystal XRD),¹¹¹ the nature of the interstitial atom (XES & EPR spectroscopy),^{112,113} and the oxidation/spin state of Mo (HERFD-XANES & time-dependent DFT calculations).¹¹⁴

3.3 Molecular Clusters inside Zeolites

As discussed in the previous chapter, there exist major differences between industrially applied heterogeneous catalysts and enzymes. The comparison of the nitrogenase enzyme and a classic hydrotreating catalyst is a prime example in this regard. Although both systems rely on TMS as catalytically active components, the former uses them in form of well-defined, molecular clusters in contrast to the latter where they are present in form of nanometer-sized slabs. In addition, the substrate binding sites in enzymes are located in sterically constrained enzyme pockets. To imitate this property, researchers used zeolites as host materials due to the nanostructured pore systems these materials provide. While this chapter will present a short overview of what has been done so far to mimic the nitrogenase enzyme's active site, chapter 4 shows our approach of synthesizing TMS clusters in the pores of NaY zeolite.^{107,115,116}

Simultaneous to the structural elucidation of naturally occurring, TMS-based enzymes, researchers tried to artificially recreate these TMS clusters and to test their catalytic performance. Most of these works focused on metal-organic synthesis to build up cubane-type TMS clusters, a feature that is found in all TMS clusters presented in Figures 3.5 and 3.6. Early on these synthetic approaches, especially by the groups of Holm and Coucouvanis, also focused on including Mo atoms in FeS clusters, just like in the most intriguing nitrogenase FeMo cofactor.¹¹⁷⁻¹¹⁹

In order to better understand the reactivity of the enzyme, the catalytic properties of the synthesized clusters were tested, *e.g.*, for the hydrogenation reactions of hydrazine to ammonia,¹¹⁹⁻¹²¹ acetylene to ethene,^{120,122} as well as for the reduction of diazene.¹²³ All of these reactions were carried out in organic solvents using auxiliary-reactants, *e.g.*, proton sources like 2,6-lutidine hydrochloride and reducing agents like CoCp₂.^{119,124}

Although these approaches nicely demonstrated the possibility of creating artificial TMS clusters that in a way mimic the reactivity of enzymes, there are two major disadvantages. First, the formation of TMS clusters *via* these routes is relatively elaborate and time intensive even on a lab-scale. And second, for catalysis in continuously operated reactors it would be preferable to have the catalyst immobilized on a stationary phase. In this regard, zeolites have been proposed to be an almost ideal host material because of the similarity of their pore structure and the substrate

binding pockets of enzymes. In addition, TMS clusters can be easily incorporated into zeolites by aqueous phase ion exchange with positively charged MoS and NiMoS clusters.¹²⁵⁻¹²⁷ Although, the resulting systems were shown to be active catalysts, e.g., for the formation of hydrocarbons from CO/H₂,¹²⁵ and HDS,¹²⁶ they were not stable under reaction conditions. The decomposition into MoS₂ slabs is most likely due to the inevitable presence of water during ion exchange.¹²⁸

A very promising concept for the facile synthesis of zeolite encapsulated TMS clusters developed by Okamoto *et al.* is shown in Figure 3.7.^{115,129}

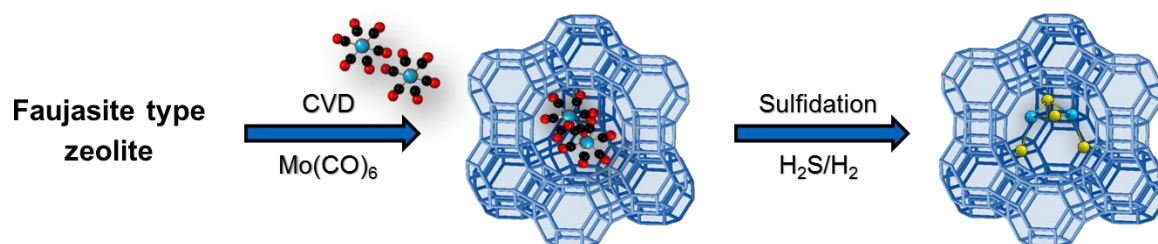


Figure 3.7 Synthesis of zeolite encapsulated Mo_xS_y clusters by chemical vapor deposition of Mo(CO)₆ followed by thermal treatment in sulfiding atmosphere.

In here, molybdenum is incorporated into a zeolite host *via* chemical vapor deposition. After thermal treatment in reactive gases two different MoS clusters could be stabilized: a dimeric (after treatment in H₂S/H₂) and a tetrameric (after treatment in H₂) one. The main advantages of this approach, compared to the multi-step syntheses presented before, are the simple preparation and the absence of water and ligands in the resulting catalysts. As long as an appropriate zeolite support is chosen, these systems only comprise of molecular MoS clusters inside the zeolite cavities allowing to relate the activity of the clusters directly to their structure. The group of Okamoto also showed the possibility to use CVD synthesis for preparation of bimetallic CoMoS clusters. Interestingly, the resulting tetrameric clusters in both cases, Mo-only and mixed Co/Mo, possess a similar cubane-type structure as the TMS clusters found in enzymes. The catalysts prepared *via* CVD and subsequent sulfidation were demonstrated to be active for hydrogenation and HDS reactions.¹²⁹⁻¹³²

3.4 References

- (1) Prins, R. In *Handbook of Heterogeneous Catalysis*; Ertl, G., Knözinger, H., Schüth, F., Weitkamp, J., Eds.; John Wiley & Sons: 2008, p 2695.
- (2) Weisser, O.; Landa, S. *Sulphide catalysts, their properties and applications*; Elsevier, 2013.
- (3) Chianelli, R. R.; Berhault, G.; Torres, B. *Catalysis Today* **2009**, *147*, 275.
- (4) Kokayeff, P.; Zink, S.; Roxas, P. In *Handbook of Petroleum Processing*; Treese, S. A., Jones, D. S., Pujado, P. R., Eds.; Springer International Publishing: Cham, 2015, p 1.
- (5) Tanimu, A.; Alhooshani, K. *Energy & Fuels* **2019**, *33*, 2810.
- (6) Topsøe, H.; Clausen, B. S.; Massoth, F. E. In *Catalysis: Science and Technology*; Anderson, J. R., Boudart, M., Eds.; Springer Berlin Heidelberg: Berlin, Heidelberg, 1996, p 1.
- (7) Breyse, M.; Geantet, C.; Afanasiev, P.; Blanchard, J.; Vrinat, M. *Catalysis Today* **2008**, *130*, 3.
- (8) Pascal, R.; Hervé, T. *Catalysis by transition metal sulphides: From molecular theory to industrial application*; Editions Technip, 2013.
- (9) Mironov, O.; Kuperman, A. E.; Lopez, J.; Brait, A.; Reynolds, B.; Chen, K. *Hydroprocessing bulk catalyst and uses thereof*, US 7,947,623 B2, 2010.
- (10) Riley, K. L.; Klein, D. P.; Hou, Z.; Soled, S. L.; Kerby, M. C.; McVicker, G. B.; Ellis, E. S.; Touvelle, M. S.; Miseo, S. *Hydrotreating using bulk multimetallic catalysts*, US 6,783,663 B1, 2004.
- (11) Bartholdy, J. *Hydrotreating catalyst particles*, US 6,667,271 B2, 2003.
- (12) Eijsbouts, S.; Mayo, S. W.; Fujita, K. *Applied Catalysis A: General* **2007**, *322*, 58.
- (13) Plantenga, F. L.; Cerfontain, R.; Eijsbouts, S.; van Houtert, F.; Anderson, G. H.; Miseo, S.; Soled, S.; Riley, K.; Fujita, K.; Inoue, Y. In *Studies in Surface Science and Catalysis*; Anpo, M., Onaka, M., Yamashita, H., Eds.; Elsevier: 2003; Vol. 145, p 407.
- (14) Texier, S.; Berhault, G.; Pérot, G.; Diehl, F. *Applied Catalysis A: General* **2005**, *293*, 105.
- (15) Inamura, K.; Prins, R. *Journal of Catalysis* **1994**, *147*, 515.
- (16) Candia, R.; Clausen, B. S.; Topsøe, H. *Bulletin des Sociétés Chimiques Belges* **1981**, *90*, 1225.
- (17) Hagenbach, G.; Courty, P.; Delmon, B. *Journal of Catalysis* **1971**, *23*, 295.
- (18) Topsøe, H.; Clausen, B. S.; Candia, R.; Wivel, C.; Mørup, S. *Journal of Catalysis* **1981**, *68*, 433.
- (19) Sørensen, O.; Clausen, B. S.; Candia, R.; Topsøe, H. *Applied Catalysis* **1985**, *13*, 363.
- (20) Topsøe, H.; Candia, R.; Topsøe, N.-Y.; Clausen, B. S.; Topsøe, H. *Bulletin des Sociétés Chimiques Belges* **1984**, *93*, 783.
- (21) Schönfeld, B.; Huang, J.; Moss, S. *Acta Crystallographica Section B: Structural Science* **1983**, *39*, 404.
- (22) Besenbacher, F.; Brorson, M.; Clausen, B. S.; Helveg, S.; Hinnemann, B.; Kibsgaard, J.; Lauritsen, J. V.; Moses, P. G.; Nørskov, J. K.; Topsøe, H. *Catalysis Today* **2008**, *130*, 86.
- (23) Helveg, S.; Lauritsen, J. V.; Lægsgaard, E.; Stensgaard, I.; Nørskov, J. K.; Clausen, B. S.; Topsøe, H.; Besenbacher, F. *Physical Review Letters* **2000**, *84*, 951.
- (24) Kisielowski, C.; Ramasse, Q. M.; Hansen, L. P.; Brorson, M.; Carlsson, A.; Molenbroek, A. M.; Topsøe, H.; Helveg, S. *Angewandte Chemie International Edition* **2010**, *49*, 2708.
- (25) Bollinger, M. V.; Lauritsen, J. V.; Jacobsen, K. W.; Nørskov, J. K.; Helveg, S.; Besenbacher, F. *Physical Review Letters* **2001**, *87*, 196803.
- (26) Topsøe, H.; Hinnemann, B.; Nørskov, J. K.; Lauritsen, J. V.; Besenbacher, F.; Hansen, P. L.; Hytoft, G.; Egeberg, R. G.; Knudsen, K. G. *Catalysis Today* **2005**, *107-108*, 12.

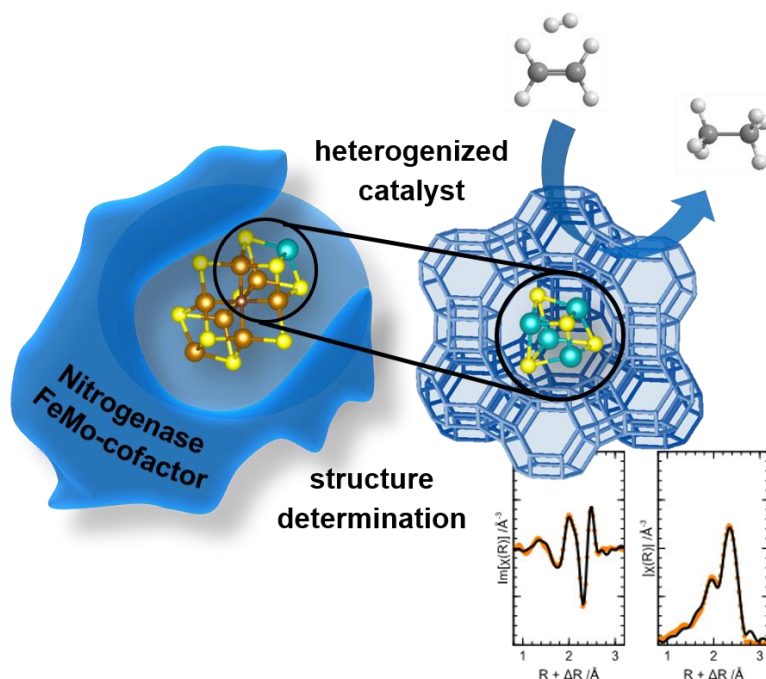
- (27) Hédoire, C.-E.; Louis, C.; Davidson, A.; Breysse, M.; Maugé, F.; Vrinat, M. *Journal of Catalysis* **2003**, *220*, 433.
- (28) Daage, M.; Chianelli, R. R. *Journal of Catalysis* **1994**, *149*, 414.
- (29) Afanasiev, P.; Xia, G.-F.; Berhault, G.; Jouguet, B.; Lacroix, M. *Chemistry of Materials* **1999**, *11*, 3216.
- (30) Eijsbouts, S.; van den Oetelaar, L. C. A.; van Puijenbroek, R. R. *Journal of Catalysis* **2005**, *229*, 352.
- (31) Gutiérrez, O. Y.; Singh, S.; Schachtl, E.; Kim, J.; Kondratieva, E.; Hein, J.; Lercher, J. A. *ACS Catalysis* **2014**, *4*, 1487.
- (32) Genuit, D.; Afanasiev, P.; Vrinat, M. *Journal of Catalysis* **2005**, *235*, 302.
- (33) Vogelgsang, F.; Ji, Y.; Shi, H.; Lercher, J. A. *Journal of Catalysis* **2020**, *391*, 212.
- (34) Qabazard, H.; Abu-Seedo, F.; Stanislaus, A.; Andari, M.; Absi-Halabi, M. *Fuel Science and Technology International* **1995**, *13*, 1135.
- (35) Hensen, E. J. M.; Kooyman, P. J.; van der Meer, Y.; van der Kraan, A. M.; de Beer, V. H. J.; van Veen, J. A. R.; van Santen, R. A. *Journal of Catalysis* **2001**, *199*, 224.
- (36) Euzen, P.; Raybaud, P.; Krokidis, X.; Toulhoat, H.; Le Loarer, J.-L.; Jolivet, J.-P.; Froidefond, C. In *Handbook of Porous Solids* 2002, p 1591.
- (37) Breysse, M.; Afanasiev, P.; Geantet, C.; Vrinat, M. *Catalysis Today* **2003**, *86*, 5.
- (38) Michaud, P.; Lemberton, J. L.; Pérot, G. *Applied Catalysis A: General* **1998**, *169*, 343.
- (39) Corma, A. *Journal of Catalysis* **2003**, *216*, 298.
- (40) Kazakov, M. O.; Kazakova, M. A.; Vatutina, Y. V.; Larina, T. V.; Chesalov, Y. A.; Gerasimov, E. Y.; Prosvirin, I. P.; Klimov, O. V.; Noskov, A. S. *Catalysis Today* **2020**, *357*, 221.
- (41) de Beer, V. H. J.; Derbyshire, F. J.; Groot, C. K.; Prins, R.; Scaroni, A. W.; Solar, J. M. *Fuel* **1984**, *63*, 1095.
- (42) Bouwens, S. M. A. M.; Prins, R.; De Beer, V. H. J.; Koningsberger, D. C. *The Journal of Physical Chemistry* **1990**, *94*, 3711.
- (43) Groot, C. K.; De Beer, V. H. J.; Prins, R.; Stolarski, M.; Niedzwiedz, W. S. *Industrial & Engineering Chemistry Product Research and Development* **1986**, *25*, 522.
- (44) Eswaramoorthi, I.; Sundaramurthy, V.; Das, N.; Dalai, A. K.; Adjaye, J. *Applied Catalysis A: General* **2008**, *339*, 187.
- (45) Seo, B.; Joo, S. H. *Nano Convergence* **2017**, *4*.
- (46) Wang, M.; Zhang, L.; He, Y.; Zhu, H. *Journal of Materials Chemistry A* **2021**, *9*, 5320.
- (47) Zhai, C.; Zhu, M.; Bin, D.; Ren, F.; Wang, C.; Yang, P.; Du, Y. *Journal of Power Sources* **2015**, *275*, 483.
- (48) Xie, S.; Sun, B.; Sun, H.; Zhan, K.; Zhao, B.; Yan, Y.; Xia, B. Y. *International Journal of Hydrogen Energy* **2019**, *44*, 15009.
- (49) Li, P.; Yang, Z.; Shen, J.; Nie, H.; Cai, Q.; Li, L.; Ge, M.; Gu, C.; Chen, X. a.; Yang, K.; Zhang, L.; Chen, Y.; Huang, S. *ACS Applied Materials & Interfaces* **2016**, *8*, 3543.
- (50) Topsøe, H.; Clausen, B. S. *Applied Catalysis* **1986**, *25*, 273.
- (51) Topsøe, H.; Clausen, B. S.; Topsøe, N.-Y.; Zeuthen, P. In *Studies in Surface Science and Catalysis*; Trimm, D. L., Akashah, S., Absi-Halabi, M., Bishara, A., Eds.; Elsevier: 1989; Vol. 53, p 77.
- (52) Dujardin, C.; Lélías, M. A.; van Gestel, J.; Travert, A.; Duchet, J. C.; Maugé, F. *Applied Catalysis A: General* **2007**, *322*, 46.
- (53) Travert, A.; Dujardin, C.; Maugé, F.; Cristol, S.; Paul, J. F.; Payen, E.; Bougeard, D. *Catalysis Today* **2001**, *70*, 255.
- (54) Topsøe, H.; Clausen, B. S. *Catalysis Reviews* **1984**, *26*, 395.
- (55) Salmeron, M.; Somorjai, G. A.; Wold, A.; Chianelli, R.; Liang, K. S. *Chemical Physics Letters* **1982**, *90*, 105.
- (56) Prins, R.; De Beer, V. H. J.; Somorjai, G. A. *Catalysis Reviews* **1989**, *31*, 1.
- (57) Chianelli, R. R.; Daage, M.; Ledoux, M. J. In *Advances in Catalysis*; Eley, D. D., Pines, H., Haag, W. O., Eds.; Academic Press: 1994; Vol. 40, p 177.
- (58) Farias, M. H.; Gellman, A. J.; Somorjai, G. A.; Chianelli, R. R.; Liang, K. S. *Surface Science* **1984**, *140*, 181.

- (59) Byskov, L. S.; Nørskov, J. K.; Clausen, B. S.; Topsøe, H. *Journal of Catalysis* **1999**, *187*, 109.
- (60) Topsøe, H. *Applied Catalysis A: General* **2007**, *322*, 3.
- (61) Kasztelan, S.; Wambeke, A.; Jalowiecki, L.; Grimblot, J.; Bonnelle, J. P. *Journal of Catalysis* **1990**, *124*, 12.
- (62) Lauritsen, J. V.; Bollinger, M. V.; Lægsgaard, E.; Jacobsen, K. W.; Nørskov, J. K.; Clausen, B. S.; Topsøe, H.; Besenbacher, F. *Journal of Catalysis* **2004**, *221*, 510.
- (63) Lauritsen, J. V.; Kibsgaard, J.; Helveg, S.; Topsøe, H.; Clausen, B. S.; Lægsgaard, E.; Besenbacher, F. *Nature Nanotechnology* **2007**, *2*, 53.
- (64) Cristol, S.; Paul, J.-F.; Payen, E.; Bougeard, D.; Hutschka, F.; Clémendot, S. *Journal of Catalysis* **2004**, *224*, 138.
- (65) Hensen, E. J. M.; Vissenberg, M. J.; de Beer, V. H. J.; van Veen, J. A. R.; van Santen, R. A. *Journal of Catalysis* **1996**, *163*, 429.
- (66) Šarić, M.; Rossmesl, J.; Moses, P. G. *Journal of Catalysis* **2018**, *358*, 131.
- (67) Travert, A.; Nakamura, H.; van Santen, R. A.; Cristol, S.; Paul, J.-F.; Payen, E. *Journal of the American Chemical Society* **2002**, *124*, 7084.
- (68) Breysse, M.; Furimsky, E.; Kasztelan, S.; Lacroix, M.; Perot, G. *Catalysis Reviews* **2002**, *44*, 651.
- (69) Oliviero, L.; Travert, A.; Garcia, E. D.; Chen, J.; Maugé, F. *Journal of Catalysis* **2021**.
- (70) Topsøe, N.-Y.; Topsøe, H. *Journal of Catalysis* **1983**, *84*, 386.
- (71) Vogelgsang, F.; Shi, H.; Lercher, J. A. *Journal of Catalysis* **2021**.
- (72) Schachtl, E.; Kondratieva, E.; Gutiérrez, O. Y.; Lercher, J. A. *The Journal of Physical Chemistry Letters* **2015**, *6*, 2929.
- (73) Thomas, C.; Vivier, L.; Lemberon, J. L.; Kasztelan, S.; Pérot, G. *Journal of Catalysis* **1997**, *167*, 1.
- (74) Maternová, J. *Applied Catalysis* **1982**, *3*, 3.
- (75) Topsøe, H.; Clausen, B. S.; Topsøe, N.-Y.; Nørskov, J. K.; Ovesen, C. V.; Jacobsen, C. J. H. *Bulletin des Sociétés Chimiques Belges* **1995**, *104*, 283.
- (76) Travert, A.; Maugé, F. In *Studies in surface science and catalysis*; Elsevier: 1999; Vol. 127, p 269.
- (77) Luo, W.; Shi, H.; Schachtl, E.; Gutiérrez, O. Y.; Lercher, J. A. *Angewandte Chemie International Edition* **2018**, *57*, 14555.
- (78) De Beer, V. H.; Duchet, J.; Prins, R. *J. Catal.:(United States)* **1981**, *72*.
- (79) Van Der Kraan, A. M.; Crajé, M. W. J.; Gerkema, E.; Ramselaar, W. L. T. M.; De Beer, V. H. I. *Hyperfine Interactions* **1989**, *46*, 567.
- (80) Hagenbach, G.; Courty, P.; Delmon, B. *Journal of Catalysis* **1973**, *31*, 264.
- (81) Karroua, M.; Grange, P.; Delmon, B. *Applied Catalysis* **1989**, *50*, L5.
- (82) Wagenhofer, M. F.; Shi, H.; Gutiérrez, O. Y.; Jentys, A.; Lercher, J. A. *Science advances* **2020**, *6*, eaax5331.
- (83) Toulhoat, H.; Raybaud, P.; Kasztelan, S.; Kresse, G.; Hafner, J. *Catalysis Today* **1999**, *50*, 629.
- (84) Pecoraro, T. A.; Chianelli, R. R. *Journal of Catalysis* **1981**, *67*, 430.
- (85) Fuentes, S.; Avalos-Borja, M.; Acosta, D.; Pedraza, F.; Cruz, J. In *Studies in Surface Science and Catalysis*; Guzzi, L., Solymosi, F., TÉTÉNYi, P., Eds.; Elsevier: 1993; Vol. 75, p 611.
- (86) Nørskov, J. K.; Clausen, B. S.; Topsøe, H. *Catalysis Letters* **1992**, *13*, 1.
- (87) Chianelli, R. R.; Berhault, G.; Raybaud, P.; Kasztelan, S.; Hafner, J.; Toulhoat, H. *Applied Catalysis A: General* **2002**, *227*, 83.
- (88) Weise, C. F.; Falsig, H.; Moses, P. G.; Helveg, S.; Brorson, M.; Hansen, L. P. *Journal of Catalysis* **2021**, *403*, 74.
- (89) Chen, H. J.; Massoth, F. E. *Industrial & Engineering Chemistry Research* **1988**, *27*, 1629.
- (90) Wei, J.; Zhao, X. *Chemical Engineering Science* **1992**, *47*, 2721.
- (91) Guichard, B.; Roy-Auberger, M.; Devers, E.; Pichon, C.; Legens, C. *Applied Catalysis A: General* **2009**, *367*, 9.

- (92) Zhang, H.; Lin, H.; Zheng, Y. *Carbon Resources Conversion* **2020**, *3*, 60.
- (93) Thakur, D. S.; Thomas, M. G. *Applied Catalysis* **1985**, *15*, 197.
- (94) Van Doorn, J.; Barbolina, H. A. A.; Moulijn, J. A. *Industrial & Engineering Chemistry Research* **1992**, *31*, 101.
- (95) Scaroni, A. W.; Jenkins, R. G.; Utrilla, J. R.; Walker, P. L. *Fuel Processing Technology* **1984**, *9*, 103.
- (96) Kubička, D.; Horáček, J. *Applied Catalysis A: General* **2011**, *394*, 9.
- (97) Laurent, E.; Delmon, B. *Journal of Catalysis* **1994**, *146*, 281.
- (98) Bullock, R. M.; Chen, J. G.; Gagliardi, L.; Chirik, P. J.; Farha, O. K.; Hendon, C. H.; Jones, C. W.; Keith, J. A.; Klosin, J.; Minteer, S. D.; Morris, R. H.; Radosevich, A. T.; Rauchfuss, T. B.; Strotman, N. A.; Vojvodic, A.; Ward, T. R.; Yang, J. Y.; Surendranath, Y. *Science* **2020**, *369*, eabc3183.
- (99) Que, L.; Tolman, W. B. *Nature* **2008**, *455*, 333.
- (100) Cracknell, J. A.; Vincent, K. A.; Armstrong, F. A. *Chemical Reviews* **2008**, *108*, 2439.
- (101) Van Stappen, C.; Decamps, L.; Cutsail III, G. E.; Bjornsson, R.; Henthorn, J. T.; Birrell, J. A.; DeBeer, S. *Chemical Reviews* **2020**.
- (102) Britt, R. D.; Rao, G.; Tao, L. *Nature Reviews Chemistry* **2020**, *4*, 542.
- (103) Ogata, H.; Kellers, P.; Lubitz, W. *Journal of molecular biology* **2010**, *402*, 428.
- (104) Schindelin, H.; Kisker, C.; Schlessman, J. L.; Howard, J. B.; Rees, D. C. *Nature* **1997**, *387*, 370.
- (105) Rose, A. S.; Bradley, A. R.; Valasatava, Y.; Duarte, J. M.; Prić, A.; Rose, P. W. *Bioinformatics* **2018**, *34*, 3755.
- (106) BOYD, E. S.; ANBAR, A. D.; MILLER, S.; HAMILTON, T. L.; LAVIN, M.; PETERS, J. W. *Geobiology* **2011**, *9*, 221.
- (107) Bjornsson, R.; Neese, F.; Schrock, R. R.; Einsle, O.; DeBeer, S. *JBIC Journal of Biological Inorganic Chemistry* **2015**, *20*, 447.
- (108) Burgess, B. K.; Lowe, D. J. *Chemical Reviews* **1996**, *96*, 2983.
- (109) Kowalska, J.; DeBeer, S. *Biochimica et Biophysica Acta (BBA) - Molecular Cell Research* **2015**, *1853*, 1406.
- (110) Van Stappen, C.; Davydov, R.; Yang, Z.-Y.; Fan, R.; Guo, Y.; Bill, E.; Seefeldt, L. C.; Hoffman, B. M.; DeBeer, S. *Inorganic Chemistry* **2019**, *58*, 12365.
- (111) Einsle, O.; Tezcan, F. A.; Andrade, S. L.; Schmid, B.; Yoshida, M.; Howard, J. B.; Rees, D. C. *Science* **2002**, *297*, 1696.
- (112) Lancaster, K. M.; Roemelt, M.; Ettenhuber, P.; Hu, Y.; Ribbe, M. W.; Neese, F.; Bergmann, U.; DeBeer, S. *Science* **2011**, *334*, 974.
- (113) Spatzal, T.; Aksoyoglu, M.; Zhang, L.; Andrade, S. L. A.; Schleicher, E.; Weber, S.; Rees, D. C.; Einsle, O. *Science* **2011**, *334*, 940.
- (114) Bjornsson, R.; Lima, F. A.; Spatzal, T.; Weyhermüller, T.; Glatzel, P.; Bill, E.; Einsle, O.; Neese, F.; DeBeer, S. *Chemical Science* **2014**, *5*, 3096.
- (115) Weindl, R.; Khare, R.; Kovarik, L.; Jentys, A.; Reuter, K.; Shi, H.; Lercher, J. A. *Angewandte Chemie International Edition* **2021**, *60*, 9301.
- (116) Wang, C.-H.; DeBeer, S. *Chemical Society Reviews* **2021**.
- (117) Wolff, T. E.; Berg, J. M.; Warrick, K. O. H.; Holm, R. H. *Journal of the American Chemical Society* **1978**, *100*, 4630.
- (118) Palermo, R. E.; Holm, R. H. *Journal of the American Chemical Society* **1983**, *105*, 4310.
- (119) Coucouvanis, D.; Mosier, P. E.; Demadis, K. D.; Patton, S.; Malinak, S. M.; Kim, C. G.; Tyson, M. A. *Journal of the American Chemical Society* **1993**, *115*, 12193.
- (120) Coucouvanis, D.; Demadis, K. D.; Malinak, S. M.; Mosier, P. E.; Tyson, M. A.; Laughlin, L. J. *Journal of Molecular Catalysis A: Chemical* **1996**, *107*, 123.
- (121) Demadis, K. D.; Malinak, S. M.; Coucouvanis, D. *Inorganic chemistry* **1996**, *35*, 4038.
- (122) Laughlin, L. J.; Coucouvanis, D. *Journal of the American Chemical Society* **1995**, *117*, 3118.
- (123) Malinak, S. M.; Simeonov, A. M.; Mosier, P. E.; McKenna, C. E.; Coucouvanis, D. *Journal of the American Chemical Society* **1997**, *119*, 1662.

- (124) Seino, H.; Hidai, M. *Chemical Science* **2011**, *2*, 847.
- (125) Taniguchi, M.; Ishii, Y.; Murata, T.; Tatsumi, T.; Hidai, M. *Journal of the Chemical Society, Chemical Communications* **1995**, 2533.
- (126) Taniguchi, M.; Imamura, D.; Ishige, H.; Ishii, Y.; Murata, T.; Hidai, M.; Tatsumi, T. *Journal of Catalysis* **1999**, *187*, 139.
- (127) Hédoire, C.-E.; Cadot, E.; Villain, F.; Davidson, A.; Louis, C.; Breyse, M. *Applied Catalysis A: General* **2006**, *306*, 165.
- (128) Hensen, E. J. M.; van Veen, J. A. R. *Catalysis Today* **2003**, *86*, 87.
- (129) Okamoto, Y. *Bulletin of the Chemical Society of Japan* **2014**, *87*, 20.
- (130) Okamoto, Y.; Katsuyama, H.; Yoshida, K.; Nakai, K.; Matsuo, M.; Sakamoto, Y.; Yu, J.; Terasaki, O. *Journal of the Chemical Society, Faraday Transactions* **1996**, *92*, 4647.
- (131) Kadono, T.; Kubota, T.; Chatani, H.; Kawabata, T.; Okamoto, Y. In *Studies in surface science and catalysis*; Elsevier: 2006; Vol. 162, p 849.
- (132) Kadono, T.; Chatani, H.; Kubota, T.; Okamoto, Y. *Microporous and mesoporous materials* **2007**, *101*, 191.

4 Zeolite-Stabilized Di- and Tetranuclear Molybdenum Sulfide Clusters Form Stable Catalytic Hydrogenation Sites



Keywords: DFT • EPR spectroscopy • Hydrogenation • XES • XAS • Molybdenum sulfide clusters • Transition metal sulfides

This chapter is based on a previously published article.

Reprinted with permission from: R. Weindl, R. Khare, L. Kovarik, A. Jentys, K. Reuter, H. Shi, J. A. Lercher, *Angew. Chem. Int. Ed.* **2021**, 60, 9301.

<https://doi.org/10.1002/anie.202015769>

This is an open-access article under the Creative Commons Attribution-NonCommercial-NoDerivatives 4.0 International (CC BY-NC-ND 4.0) BY license (<https://creativecommons.org/licenses/by-nc-nd/4.0/>); minor changes were made to the formatting to improve the readability.

Abstract

Supercages of faujasite (FAU)-type zeolites serve as a robust scaffold for stabilizing dinuclear (Mo_2S_4) and tetranuclear (Mo_4S_4) molybdenum sulfide clusters. The FAU-encaged Mo_4S_4 clusters have a distorted cubane structure similar to the FeMo-cofactor in nitrogenase. Both clusters possess unpaired electrons on Mo atoms. Additionally, they show identical catalytic activity per sulfide cluster. Their catalytic activity is stable (> 150 h) for ethene hydrogenation, while layered MoS_2 structures deactivate significantly under the same reaction conditions.

4.1 Main Article

Sulfide-based enzymes and the success of transition metal sulfide (TMS) catalysts for hydrotreating reactions have spurred wide interests to understand their activity and selectivity and especially the impact of the cluster size and structure for reductive catalysis. For the nitrogenase family, three TMS clusters have been identified acting as catalytically active sites, *i.e.*, a Fe_4S_4 tetramer, the P-cluster (Fe_8S_7) and a third cluster $\text{Fe}_7\text{MS}_9\text{C}$ ($\text{M} = \text{Fe}, \text{Mo}, \text{V}$); the Mo form, the so-called FeMo-cofactor, is the most intensively studied one among the $\text{Fe}_7\text{MS}_9\text{C}$ family of clusters.¹⁻⁹

The structures of the active site in the layered TMS materials have been equally well investigated compared to those in enzyme-based catalysts. In addition to the use of the former as hydrogenation and hydrodefunctionalization catalysts for hydrotreating of refinery fractions and renewable feedstocks,¹⁰⁻¹² TMS have recently drawn major interest as cathode materials in electrocatalysis.¹³⁻¹⁷ Despite their similar chemical compositions, the TMS clusters in enzymes are well-defined entities, whereas TMS phases in industrial catalysts for hydrotreating predominantly form significantly larger slab-like structures.^{18,19}

To achieve greater catalytic efficiencies, enzyme TMS clusters served as inspirations for the synthesis of active hydrogenation sites.^{5,20,21} Most of the prior studies focused on multi-step syntheses of TMS clusters and on using them as homogeneous organometallic catalysts in liquid phase.²²⁻²⁷ A one-step synthesis could, in contrast, enable the use of such entities as potentially robust highly efficient catalysts. In this context, zeolites represent a promising group of porous supports that provide a stable and well-defined steric environment for the TMS clusters, mimicking partly the pockets of enzymes that host the active center.

Among the methods reported for immobilizing Mo and NiMo sulfide clusters on/in zeolites, ion exchange proves useful yet requires intricate synthesis of the cationic clusters.²⁸⁻³¹ Even worse, the groups of Tatsumi and Breyse reported that the zeolite-confined TMS clusters decomposed into MoS_2 slabs under reaction conditions.^{28,29} This structural degradation is likely caused by the presence of water after ion exchange.³²

Using leads from Okamoto *et al.*,³³⁻³⁵ we used chemical vapor deposition (CVD) and subsequent thermal treatments in reactive gases to incorporate homotopic size-

and structure-selective Mo_xS_y clusters into the pores of zeolite NaY. The (uniformity of the) geometric structure and the spin state of the Mo_xS_y clusters were acquired in the present study by combining X-ray absorption spectroscopy (XAS), X-ray emission spectroscopy (XES), electron paramagnetic resonance (EPR) spectroscopy, and density functional theory (DFT) calculations. A close similarity was revealed between the tetranuclear Mo_4S_4 cluster and the Mo site in nitrogenase enzymes. These NaY-encaged Mo_xS_y clusters displayed outstanding stability for ethene hydrogenation, much superior to that of a traditional slab- MoS_2 catalyst.

$\text{Mo}(\text{CO})_6$ encapsulated in a NaY zeolite was treated in $\text{H}_2\text{S}/\text{H}_2$ at 673 K for 2 h to form Mo_xS_y species within the zeolite ($\text{Mo}_x\text{S}_y/\text{NaY-sulf}$). The zeolite used was almost free of extra-framework Al (EFAl) and remained so after loading Mo and sulfidation (Figure S4.1). This catalyst was subsequently reduced in pure H_2 ($\text{Mo}_x\text{S}_y/\text{NaY-red}$) at 673 K for 2 h. Figure 4.1 shows the k^3 -weighted extended X-ray absorption fine structure (EXAFS) and Fourier-transformed (FT) EXAFS of these catalysts at Mo K-edge.

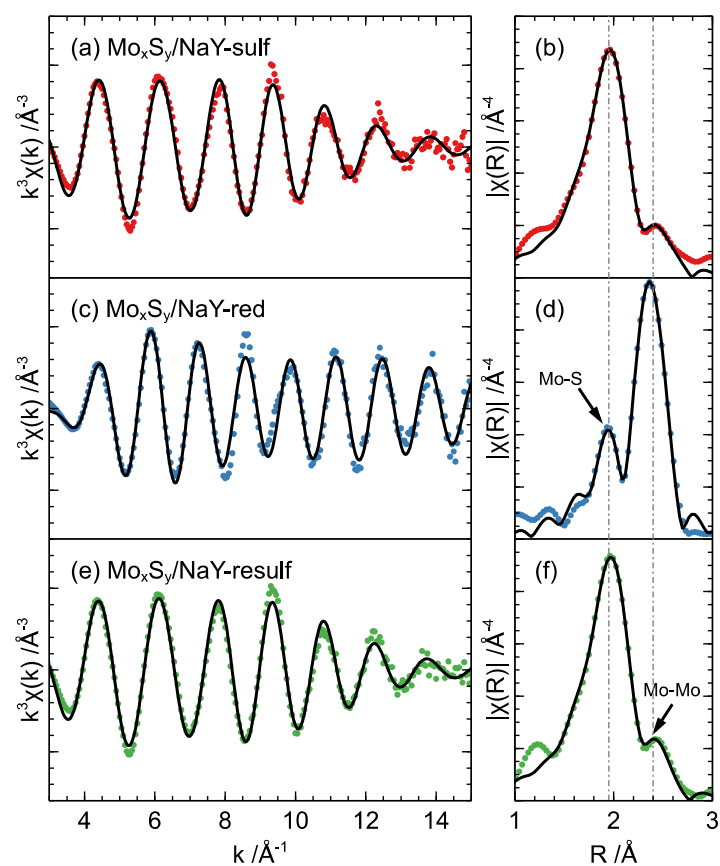


Figure 4.1 k^3 -weighted EXAFS and FT EXAFS of $\text{Mo}_x\text{S}_y/\text{NaY-sulf}$ (a, b), $\text{Mo}_x\text{S}_y/\text{NaY-red}$ (c, d), and $\text{Mo}_x\text{S}_y/\text{NaY-resulf}$ (e, f) catalysts. Experimental data is shown as closed symbols and the corresponding fits are shown as solid lines.

The corresponding fitted parameters are reported in Table 4.1. For $\text{Mo}_x\text{S}_y/\text{NaY}$ -sulf, the Mo-S and Mo-Mo coordination numbers (CN) and interatomic distances (d) together with the S/Mo ratio of ~ 2 (determined by elemental analysis) point to the overall cluster composition of Mo_2S_4 . We hypothesize that in this structure, each Mo atom is coordinated to two bridging S atoms and one terminal S atom (either in *cis* or in *trans* configuration), resulting in theoretical $\text{CN}_{\text{Mo-Mo}} \sim 1$ and $\text{CN}_{\text{Mo-S}} \sim 3$. Slightly higher measured coordination numbers ($\text{CN}_{\text{Mo-Mo}} \sim 3.9$; $\text{CN}_{\text{Mo-S}} \sim 1.3$) are attributed to a minor presence of higher nuclearity species (e.g., a few MoS_2 slabs on the external surface of the zeolite). For $\text{Mo}_x\text{S}_y/\text{NaY}$ -red, the observed $\text{CN}_{\text{Mo-Mo}}$ and $\text{CN}_{\text{Mo-S}}$ together with the S/Mo ratio of ~ 1 suggest the reduced state to be a Mo_4S_4 cluster. Additionally, based on similar values of $d_{\text{Mo-Mo}}$ and $d_{\text{Mo-S}}$, we hypothesize the Mo_4S_4 cluster to resemble a distorted Mo_4 -tetrahedron with an S atom sitting on each face. The composition and structure of this reduced state is different from a previously proposed Mo_4S_6 cluster with a cubane-like structure.³³⁻³⁵ Instead, we propose that the deduced structure has a close similarity with the $\text{MoFe}_3\text{S}_3\text{C}$ subunit of the nitrogenase FeMo-cofactor (Table 4.1).

Table 4.1 EXAFS fitting parameters: coordination numbers (CN), interatomic distances (d), E_0 , ΔE_0 , and Debye-Waller factors (σ^2), for Mo-Mo and Mo-S paths in $\text{Mo}_x\text{S}_y/\text{NaY}$ sulf/red catalysts. $\text{CN}_{\text{Mo-Fe}}$, $\text{CN}_{\text{Mo-S}}$, $d_{\text{Mo-Fe}}$ and $d_{\text{Mo-S}}$ of the nitrogenase FeMo-cofactor are added for comparison.

	Path	CN	d /Å	E_0 /eV	ΔE_0 /eV	$\sigma^2 \times 1000$ /Å ²	R-factor
$\text{Mo}_x\text{S}_y/\text{NaY}$ -sulf	Mo-S	3.9 ± 0.8	2.42 ± 0.01	19997	0.1 ± 2.4	6.6 ± 1.5	0.027
	Mo-Mo	1.3 ± 1.1	2.77 ± 0.03			10.3 ± 8.6	
$\text{Mo}_x\text{S}_y/\text{NaY}$ -red	Mo-S	2.6 ± 1.4	2.47 ± 0.05	19995	0.4 ± 5.0	5.5 ± 5.0	0.039
	Mo-Mo	3.3 ± 2.0	2.66 ± 0.03			6.3 ± 2.6	
$\text{Mo}_x\text{S}_y/\text{NaY}$ -resulf	Mo-S	4.1 ± 0.7	2.42 ± 0.01	19997	0.2 ± 2.1	6.4 ± 1.3	0.023
	Mo-Mo	1.0 ± 1.2	2.76 ± 0.03			8.2 ± 6.7	
Nitrogenase	Mo-S	$3^{[a,b]}$	$2.34^{[a]}, 2.32^{[b]}$				
FeMo-cofactor	Mo-Fe	$3^{[a,b]}$	$2.70^{[a]}, 2.61^{[b]}$				

[a] Data from ref.⁷; [b] Data from ref.⁶

The $\text{Mo}_x\text{S}_y/\text{NaY}$ -red catalyst was resulfided in $\text{H}_2\text{S}/\text{H}_2$ at 673 K for 2 h to form $\text{Mo}_x\text{S}_y/\text{NaY}$ -resulf. The observed Mo-Mo and Mo-S CN and interatomic distances in $\text{Mo}_x\text{S}_y/\text{NaY}$ -resulf were similar to those in $\text{Mo}_x\text{S}_y/\text{NaY}$ -sulf, suggesting that the

transformation between the sulfided and reduced structures is reversible by switching between pure H₂ and H₂S/H₂ (Table 4.1).³³⁻³⁵

Energy dispersive X-ray spectroscopy (EDS) mapping shows an even distribution of Mo across the zeolite particles (Figure S4.2), proving that Mo and S are not enriched at the outer surface of the crystallites. This indicates that Mo is initially evenly distributed and remains locally anchored as sulfide clusters with two different nuclearities. The decrease in zeolite micropore volume with increasing Mo loading also supports this conclusion (Figure S4.3). The absence of any larger particles in the high-angle-annular dark field-transmission electron microscopy (HAADF TEM; Figure S4.2) showed further that the di- and tetranuclear clusters are the predominant, if not the only, form of Mo_xS_y. X-ray diffraction patterns of the Mo_xS_y-containing samples and the parent NaY zeolite show a change in the relative intensities of several diffraction peaks (Figure S4.4), attributed to a redistribution of Na⁺ cations within the zeolite.^{36,37} This indicates a slight preference of the location of the TMS clusters, requiring, however, additional analysis.

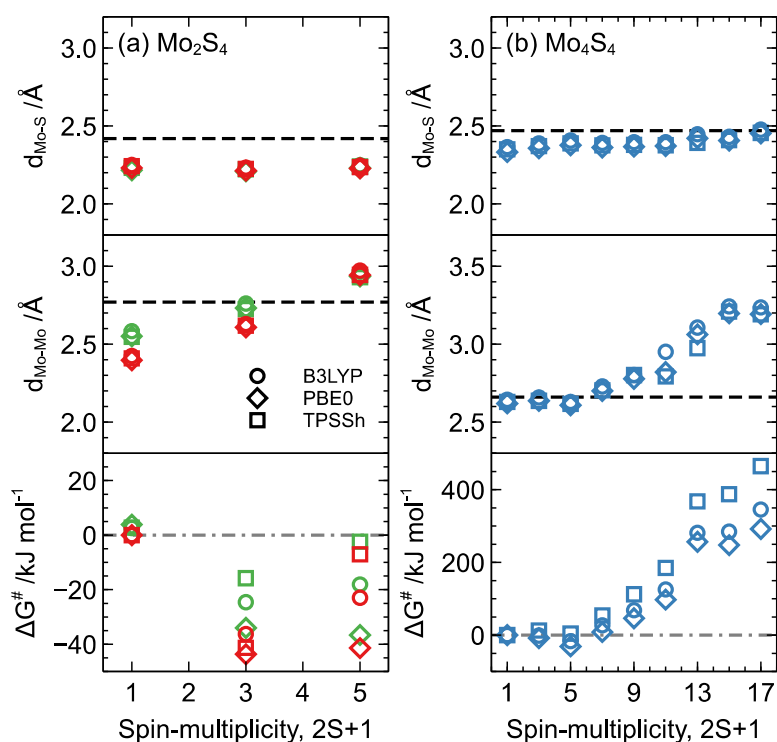


Figure 4.2 Average Mo-S ($d_{\text{Mo-S}}$) and Mo-Mo ($d_{\text{Mo-Mo}}$) interatomic distances, as well as the relative Gibbs free energies at 473 K ($\Delta G^\#$) of Mo₂S₄ (left) in *cis* (red) and *trans* (green) configurations, and Mo₄S₄ (right) clusters as a function of spin-multiplicity as calculated by DFT using B3LYP, PBE0, and TPSSh functionals. Experimentally observed $d_{\text{Mo-Mo}}$ and $d_{\text{Mo-S}}$ estimated from the EXAFS of Mo_xS_y/NaY-sulf/red catalysts are shown as dashed line.

The hypothesized structures of Mo₂S₄ and Mo₄S₄ clusters were optimized using DFT and the results were compared against the experimental data (EXAFS). Interestingly, variations in the number of unpaired electrons in the Mo d-orbitals correlated with the Mo-Mo bond distances, while the Mo-S interatomic distances were insensitive to these changes (Figure 4.2).

The DFT-computed $d_{\text{Mo-Mo}}$ (Table S4.3) obtained for the thermodynamically most stable configurations (spin-multiplicity of 3 for Mo₂S₄ and 5 for Mo₄S₄) matched excellently with the values obtained from EXAFS (Table 4.1). The computed $d_{\text{Mo-S}}$ however appear to be significantly lower than those observed experimentally, which we attribute to the fact that geometry optimization was performed in gas phase, while for the zeolite-encaged clusters, the terminal S atoms are likely to interact with sodium cations in the zeolite, which is expected to elongate the bonds. As these interactions could also lead to charge transfer to/from clusters, we investigated the influence of positive/negative charge on the optimized geometries (Figure S4.5). The calculations indicate that the structural parameters of these clusters are influenced more by the spin-multiplicity than by the net charge on the clusters. Based on computed Gibbs free energies (Figure 4.2 and Tables S4.1 & S4.2), the lowest-energy structures have a spin-multiplicity of 3 (two unpaired electrons) and 5 (four unpaired electrons) for Mo₂S₄ and Mo₄S₄ (Figure 4.3), respectively. For Mo₂S₄, the *cis* configuration was found to be more stable and is further examined.

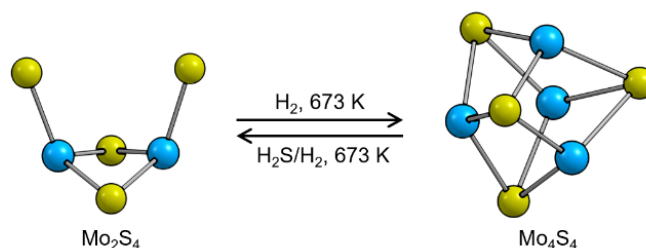


Figure 4.3 DFT-optimized Mo₂S₄ (*cis*) and Mo₄S₄ clusters. The depicted clusters were optimized with spin-multiplicity of 3 for Mo₂S₄ and 5 for Mo₄S₄ using B3LYP. Varying the functional did not result in a significant change in cluster geometry (Figure S4.6). S: yellow, Mo: blue.

As DFT calculations correspond to one unpaired electron per Mo for both clusters, the presence of unpaired electrons on Mo was also deduced from the EPR measurements (Figure 4.4 left). The EPR spectra show an intense central line with g-values ~ 2 , in close agreement with the g-values reported for unpaired electrons in Mo species of different formal oxidation states in nitrogenase, nitrate reductase, and

sulfur-bridged Mo dimer clusters.³⁸⁻⁴⁰ Although EPR signals with $g \sim 2$ are commonly assigned to $S = \frac{1}{2}$ systems, these signals may also be interpreted as $M_s \pm 1$ transitions of systems with higher spin-multiplicities, e.g., *cis*-Mo₂S₄ (spin-multiplicity = 3) and Mo₄S₄ (spin-multiplicity = 5), with a large zero field splitting.³⁸ Due to the lack of spin quantification, an in-depth electronic spin analysis of Mo_xS_y clusters proposed in this work is presently not achievable. It must also be noted that a mixture of clusters with different spin-multiplicities may be present as the DFT-computed Gibbs free energy difference between systems with slightly different multiplicities is relatively small (Figure 4.2 and Table S4.1 & S4.2).

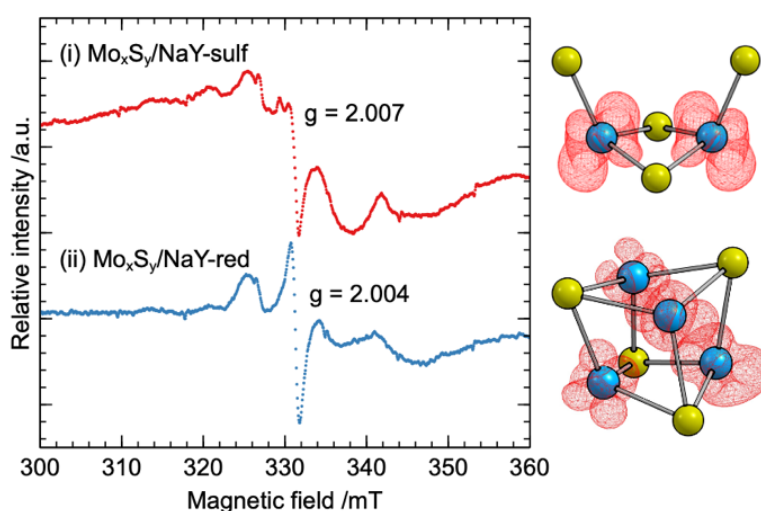


Figure 4.4 EPR spectra of Mo_xS_y/NaY-sulf/red catalysts (left) and the isosurface (0.02 a.u.) of the difference in alpha and beta electron densities (right) illustrating the location of unpaired electrons on *cis*-Mo₂S₄ (spin-multiplicity = 3) and Mo₄S₄ (spin-multiplicity = 5) clusters computed using DFT(B3LYP).

The DFT calculations unambiguously support our finding that the unpaired electrons are indeed located on the Mo atoms of both Mo_xS_y clusters (Figure 4.4, right and Figure S4.6). In this regard, it is important to note that ionic clusters would result in formal Mo oxidation states of +4/+2 (assuming neutral Mo₂S₄/Mo₄S₄ clusters) which could not possess single unpaired electrons due to their even number of total valence electrons. However, the Mo-S bonds in these nanoclusters are likely to be covalent in character, which is supported by Hirshfeld/Mulliken population analysis and Mayer bond orders computed using DFT (Tables S4.4 & S4.5).

Further confirmation of the hypothesized structures of NaY encapsulated Mo_xS_y clusters was deduced from Mo K α high energy resolution fluorescence detected X-ray absorption near edge structure (HERFD-XANES) and Mo K β valence-to-core (VtC)

XES. The VtC XES spectra of $\text{Mo}_x\text{S}_y/\text{NaY-sulf/red}$ catalysts are in close agreement with the simulated spectra of the optimized Mo_2S_4 and Mo_4S_4 structures (Figure S4.7 and Table S4.6) validating the structures suggested in this work. In addition, HERFD-XANES shows a shift towards lower absorption energies for the reduced catalyst supporting the proposed reduction of Mo centers in a pure H_2 atmosphere (Figure S4.10).

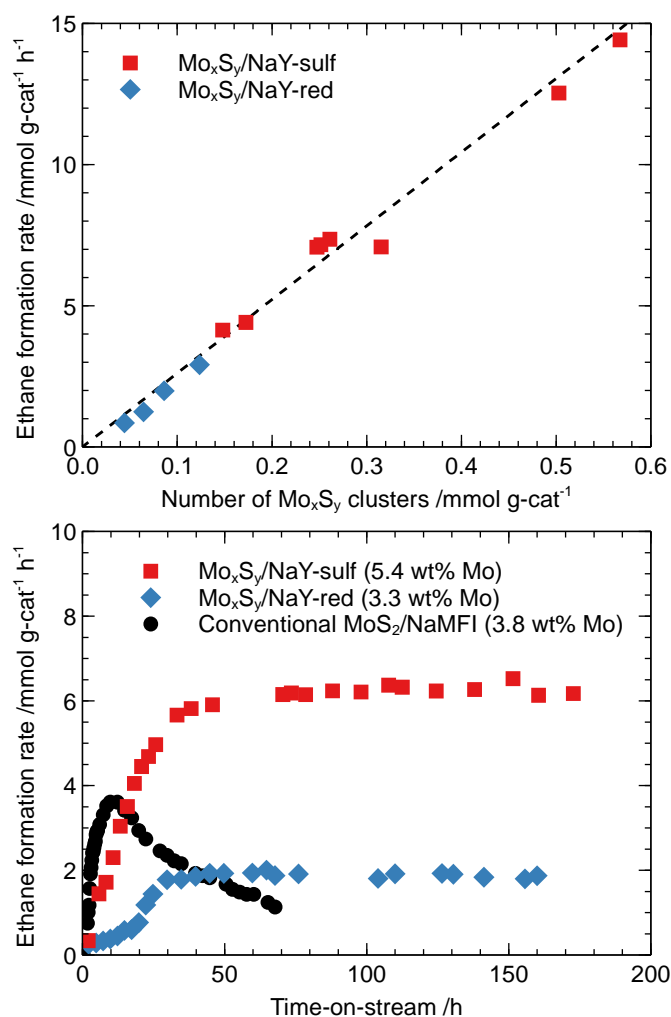


Figure 4.5 Steady-state ethane formation rates (top) at 473 K for cluster catalysts with different loadings and time-on-stream behavior (bottom) of representative $\text{Mo}_x\text{S}_y/\text{NaY-sulf/red}$ catalysts and $\text{MoS}_2/\text{NaMFI}$.

Interestingly, when subjecting the two cluster catalysts to a stream of ethene and H_2 , no activity was observed at the very beginning, but both catalysts gained activity and reached a steady-state over a time span of ~30 h (Figure 4.5). Elemental analysis of the spent $\text{Mo}_x\text{S}_y/\text{NaY-sulf}$ sample showed a loss of sulfur that corresponded to approximately one S per cluster. Thus, we hypothesize that partial sulfur loss from the fully sulfided Mo_2S_4 cluster may account for the generation of true active sites (S-

vacancies) while the original clusters are inactive. Given the high reduction temperature (673 K in pure H₂), further reduction and sulfur loss is rather unlikely for the Mo_xS_y/NaY red sample at the reaction temperature of 473 K and the induction period could be caused by restructuring.

While it would also be very important to understand a potential response of the Mo spin states to its local coordination environment, this is to be further investigated by *in situ* spectroscopy (EPR and XAS in particular) that monitors the dynamic evolution of the structure and chemical compositions of the active sites at reaction conditions.

For Mo_xS_y/NaY sulf/red catalysts, a linear increase of the steady-state ethane formation rate (per gram of catalyst) was observed with an increasing loading of clusters (Figure 4.5). The parent NaY zeolite itself (no EFAI species or Brønsted acid sites; Figures S4.1 & S4.11) did not exhibit hydrogenation activity. Therefore, we conclude that the measured activity stems solely from Mo_xS_y clusters that are homogeneous in nature. Surprisingly, the linear rate increase was identical for di- and tetramers indicating that each cluster forms the same number of equally active sites.

The cluster catalysts showed stable steady-state conversion rates (for at least 7 days), allowing to conclude that the active sulfide sites hosted in the zeolite cages remained stable, in contrast to previous studies that either lacked evaluation of the stability metric or clearly noted deactivation/degradation of the active structures.^{28,29,32} A traditional MoS₂/NaMFI catalyst that featured extended slabs, however, deactivated markedly after reaching the maximum activity (Figure 4.5). The NaMFI zeolite used as a support is free of Brønsted acid sites and did not show any activity under the probed conditions. We, therefore, conclude that deactivation results from degradation of the MoS₂ phase without supply of sulfur in the reactant stream.

In summary, we have shown that di- and tetrameric Mo_xS_y clusters can be stabilized in a homogeneous form by zeolite Na-FAU. The active clusters are homogeneously distributed in the zeolite and are essentially homotopic. The specific catalytic activity of these clusters for ethene hydrogenation is identical. The tetrameric cluster is structurally similar to the Mo site of the FeMo-cofactor in nitrogenase. DFT-based optimization of the cluster geometry and free energy calculations predict that both clusters contain a single unpaired electron at each Mo atom. While the intrinsic catalytic activity is similar to those of a conventional supported MoS₂ catalyst, the latter deactivates markedly during time on stream while both the di- and tetrameric Mo_xS_y

cluster-based catalysts are stable for days of operation. Thus, the zeolite-supported Mo_xS_y cluster catalysts are a promising new class of robust, bio-inspired hydrogenation catalysts that create exciting opportunities with respect to chemical and structural variability for catalysis.

4.2 Acknowledgements

This work was funded by the Chevron Energy Technology Company. The authors especially thank Dr. A. Kuperman and Dr. A. Brait (Chevron), and Prof. Takeshi Kubota (Shimane University, Japan) for fruitful discussions.

Conceptual work and structural determinations were supported by the U.S. Department of Energy (DOE), Office of Science, Office of Basic Energy Sciences (BES), Division of Chemical Sciences, Geosciences and Biosciences (Transdisciplinary Approaches to Realize Novel Catalytic Pathways to Energy Carriers, FWP 47319). Portions of the experiments were performed at the William R. Environmental Molecular Science Laboratory (EMSL), a national scientific user facility sponsored by the DOE Office of Biological and Environmental Research located at Pacific Northwest National Laboratory (PNNL). PNNL is a multiprogram national laboratory operated for DOE by Battelle Memorial Institute.

The authors gratefully acknowledge the Leibniz Supercomputing Center for funding this project by providing computing time on their Linux-Cluster. The X-ray absorption and emission spectroscopy measurements were performed on beamline ID26 at the European Synchrotron Radiation Facility (ESRF), Grenoble, France (Proposal CH 5641). We are grateful to Dr. Pieter Glatzel at the ESRF for his assistance. The authors also want to thank Dr. O. Storcheva (EPR spectroscopy), T. Schachtl & M. Aigner (NMR spectroscopy), and C. Gross (syntheses & reactions) for their help.

Contributions

R. Weindl and R. Khare contributed equally to this work. R. Weindl, H. Shi, and J. A. Lercher conceived the idea of this work. R. Weindl conducted synthesis, characterization and kinetic evaluation of the presented materials. R. Khare contributed XAS/XES measurements and interpretation as well as DFT calculations. L. Kovarik performed electron microscopy, A. Jentys assisted in interpretation of spectroscopic data, and K. Reuter assisted in evaluation of results obtained from DFT calculations. Experimental results were discussed by all authors and the manuscript was written and edited jointly.

4.3 References

- (1) Howard, J. B.; Rees, D. C. *Chemical Reviews* **1996**, *96*, 2965.
- (2) Burgess, B. K.; Lowe, D. J. *Chemical Reviews* **1996**, *96*, 2983.
- (3) Kowalska, J.; DeBeer, S. *Biochimica et Biophysica Acta (BBA) - Molecular Cell Research* **2015**, *1853*, 1406.
- (4) Lancaster, K. M.; Roemelt, M.; Ettenhuber, P.; Hu, Y.; Ribbe, M. W.; Neese, F.; Bergmann, U.; DeBeer, S. *Science* **2011**, *334*, 974.
- (5) Bjornsson, R.; Neese, F.; Schrock, R. R.; Einsle, O.; DeBeer, S. *JBIC Journal of Biological Inorganic Chemistry* **2015**, *20*, 447.
- (6) Bjornsson, R.; Lima, F. A.; Spatzal, T.; Weyhermüller, T.; Glatzel, P.; Bill, E.; Einsle, O.; Neese, F.; DeBeer, S. *Chemical Science* **2014**, *5*, 3096.
- (7) Einsle, O.; Tezcan, F. A.; Andrade, S. L.; Schmid, B.; Yoshida, M.; Howard, J. B.; Rees, D. C. *Science* **2002**, *297*, 1696.
- (8) George, S. J.; Barney, B. M.; Mitra, D.; Igarashi, R. Y.; Guo, Y.; Dean, D. R.; Cramer, S. P.; Seefeldt, L. C. *Journal of Inorganic Biochemistry* **2012**, *112*, 85.
- (9) George, S. J.; Hernandez, J. A.; Jimenez-Vicente, E.; Echavarri-Erasun, C.; Rubio, L. M. *Chemical Communications* **2016**, *52*, 11811.
- (10) Grilc, M.; Likozar, B.; Levec, J. *Applied Catalysis B: Environmental* **2014**, *150-151*, 275.
- (11) Liu, G.; Robertson, A. W.; Li, M. M.-J.; Kuo, W. C. H.; Darby, M. T.; Muhieddine, M. H.; Lin, Y.-C.; Suenaga, K.; Stamatakis, M.; Warner, J. H.; Tsang, S. C. E. *Nature Chemistry* **2017**, *9*, 810.
- (12) Eijsbouts, S.; Mayo, S. W.; Fujita, K. *Applied Catalysis A: General* **2007**, *322*, 58.
- (13) Tran, P. D.; Nguyen, M.; Pramana, S. S.; Bhattacharjee, A.; Chiam, S. Y.; Fize, J.; Field, M. J.; Artero, V.; Wong, L. H.; Loo, J.; Barber, J. *Energy & Environmental Science* **2012**, *5*, 8912.
- (14) Tran, P. D.; Tran, T. V.; Orio, M.; Torelli, S.; Truong, Q. D.; Nayuki, K.; Sasaki, Y.; Chiam, S. Y.; Yi, R.; Honma, I. *Nature materials* **2016**, *15*, 640.
- (15) Lu, A.-Y.; Yang, X.; Tseng, C.-C.; Min, S.; Lin, S.-H.; Hsu, C.-L.; Li, H.; Idriss, H.; Kuo, J.-L.; Huang, K.-W.; Li, L.-J. *Small* **2016**, *12*, 5530.
- (16) Voiry, D.; Fullon, R.; Yang, J.; de Carvalho Castro e Silva, C.; Koppera, R.; Bozkurt, I.; Kaplan, D.; Lagos, M. J.; Batson, P. E.; Gupta, G.; Mohite, Aditya D.; Dong, L.; Er, D.; Shenoy, V. B.; Asefa, T.; Chhowalla, M. *Nature Materials* **2016**, *15*, 1003.
- (17) Seo, B.; Joo, S. H. *Nano Convergence* **2017**, *4*.
- (18) Helveg, S.; Lauritsen, J. V.; Lægsgaard, E.; Stensgaard, I.; Nørskov, J. K.; Clausen, B. S.; Topsøe, H.; Besenbacher, F. *Physical Review Letters* **2000**, *84*, 951.
- (19) Topsøe, N.-Y.; Topsøe, H. *Journal of Catalysis* **1983**, *84*, 386.
- (20) Wolff, T. E.; Berg, J. M.; Warrick, K. O. H.; Holm, R. H. *Journal of the American Chemical Society* **1978**, *100*, 4630.
- (21) Seino, H.; Hidai, M. *Chemical Science* **2011**, *2*, 847.
- (22) Coucouvanis, D.; Demadis, K. D.; Malinak, S. M.; Mosier, P. E.; Tyson, M. A.; Laughlin, L. J. *Journal of Molecular Catalysis A: Chemical* **1996**, *107*, 123.
- (23) Coucouvanis, D.; Mosier, P. E.; Demadis, K. D.; Patton, S.; Malinak, S. M.; Kim, C. G.; Tyson, M. A. *Journal of the American Chemical Society* **1993**, *115*, 12193.
- (24) Demadis, K. D.; Malinak, S. M.; Coucouvanis, D. *Inorganic chemistry* **1996**, *35*, 4038.
- (25) Malinak, S. M.; Simeonov, A. M.; Mosier, P. E.; McKenna, C. E.; Coucouvanis, D. *Journal of the American Chemical Society* **1997**, *119*, 1662.
- (26) Herbst, K.; Monari, M.; Brorson, M. *Inorganic Chemistry* **2002**, *41*, 1336.
- (27) Laughlin, L. J.; Coucouvanis, D. *Journal of the American Chemical Society* **1995**, *117*, 3118.
- (28) Taniguchi, M.; Imamura, D.; Ishige, H.; Ishii, Y.; Murata, T.; Hidai, M.; Tatsumi, T. *Journal of Catalysis* **1999**, *187*, 139.
- (29) Hédoire, C.-E.; Cadot, E.; Villain, F.; Davidson, A.; Louis, C.; Breyse, M. *Applied Catalysis A: General* **2006**, *306*, 165.

- (30) Müller, A.; Sarkar, S.; Bhattacharyya, R. G.; Pohl, S.; Dartmann, M. *Angewandte Chemie International Edition in English* **1978**, *17*, 535.
- (31) Shibahara, T.; Yamasaki, M.; Sakane, G.; Minami, K.; Yabuki, T.; Ichimura, A. *Inorganic Chemistry* **1992**, *31*, 640.
- (32) Hensen, E. J. M.; van Veen, J. A. R. *Catalysis Today* **2003**, *86*, 87.
- (33) Kadono, T.; Chatani, H.; Kubota, T.; Okamoto, Y. *Microporous and mesoporous materials* **2007**, *101*, 191.
- (34) Kadono, T.; Kubota, T.; Chatani, H.; Kawabata, T.; Okamoto, Y. In *Studies in surface science and catalysis*; Elsevier: 2006; Vol. 162, p 849.
- (35) Okamoto, Y. *Bulletin of the Chemical Society of Japan* **2014**, *87*, 20.
- (36) Okamoto, Y.; Katsuyama, H.; Yoshida, K.; Nakai, K.; Matsuo, M.; Sakamoto, Y.; Yu, J.; Terasaki, O. *Journal of the Chemical Society, Faraday Transactions* **1996**, *92*, 4647.
- (37) Salama, T. M.; Othman, I.; Sirag, M.; El-Shobaky, G. A. *Microporous and Mesoporous Materials* **2006**, *95*, 312.
- (38) Van Stappen, C.; Decamps, L.; Cutsail III, G. E.; Bjornsson, R.; Henthorn, J. T.; Birrell, J. A.; DeBeer, S. *Chemical Reviews* **2020**.
- (39) Biaso, F.; Burlat, B.; Guigliarelli, B. *Inorganic Chemistry* **2012**, *51*, 3409.
- (40) Casewit, C. J.; DuBois, M. R. *Inorganic Chemistry* **1986**, *25*, 74.

4.4 Supporting Information

4.4.1 Experimental Details

4.4.1.1 Catalyst Precursor Preparation

The reference catalyst, MoS₂/NaMFI (3.8 wt% Mo), was prepared by incipient wetness impregnation (IWP) of a NaMFI zeolite support (Si/Al ~11) with an ammonium heptamolybdate (AHM, (NH₄)₆Mo₇O₂₄; 99.98% purity; Sigma-Aldrich) solution of appropriate concentration. The impregnated zeolite was dried at 383 K overnight followed by calcination in 100 mL min⁻¹ synthetic air (5 K min⁻¹ to 673 K, hold for 2 h).

Cluster catalyst precursors were prepared by chemical vapor deposition (CVD). A NaY zeolite (Zeolyst CBV 100 with Si/Al ~2.5; pelletized and sieved to 250 – 355 μm) was treated under reduced pressure (0.01 mbar) at elevated temperatures (5 K min⁻¹ to 408 K, hold for 2 h; 5 K min⁻¹ to 503 K, hold for 2 h; 5 K min⁻¹ to 653 K, hold for 1 h) to carefully remove adsorbed water without imposing steaming effects. The dried zeolite was loaded with Mo(CO)₆ (>99.9% purity; Sigma-Aldrich) at room temperature under static conditions for a predefined amount of time. Finally, the catalyst precursor was evacuated for 10 min to remove weakly physisorbed Mo(CO)₆ species. Carbonyl precursors were stored in a glovebox to avoid exposure to air/moisture at any time. For the same reason quartz tubes used for catalytic reactions as well as quartz capillaries used for X-ray spectroscopy measurements were packed in a glovebox.

4.4.1.2 X-ray Absorption Spectroscopy (XAS) and X-ray Emission Spectroscopy (XES)

XAS and XES spectra were collected at the ID26 beamline of the European Synchrotron Radiation Facility (ESRF) in Grenoble, France. The storage ring was operated at 6 GeV energy and 190 mA current. A flat Si311 double crystal monochromator (DCM) was used for obtaining monochromatic X-rays. A water cooled Rh-coated plane mirror was used to reject higher harmonics. The DCM was calibrated to Mo K-edge energy by measuring a Mo-foil and defining the first inflection point as 20000 eV. The beam spot-size was approximately 100 μm (vertical) x 500 μm (horizontal) at the sample position. The energy resolution of the incident X-rays is estimated to be ~0.6 eV at the Mo K-edge ($\Delta E/E \sim 0.3 \times 10^{-4}$). XAS data was collected using a photodiode detector while high-energy resolution XES data was collected using

a dead-time corrected silicon drift diode detector (Ketek). Possible attenuation in emission signal was reduced by placing a He-filled balloon inside the Rowland circle between the sample, the analyzer crystals, and the detector.

In situ XAS and XES spectra were measured in a quartz capillary micro-reactor setup. The $\text{Mo}(\text{CO})_6$ containing catalyst precursor was placed in a quartz capillary (WJM Glas, 1 mm o.d., 20 μm thickness) supported by two quartz wool plugs. The capillary was heated from below with a hot-air gas-blower (Oxford FMB). Gas flow rates were maintained using Bronkhorst electronic mass flow controllers and the pressure was monitored using a pressure gauge (Omega) placed upstream of the catalyst bed. All experiments were performed at ambient pressure. The $\text{Mo}(\text{CO})_6/\text{NaY}$ precursors were sulfided in a stream of 10 mL min^{-1} H_2S (10 vol% in H_2) at 673 K for 2 h (temperature ramp: 5 K min^{-1} to 673 K, hold for 2 h) to form the sulfided $\text{Mo}_x\text{S}_y/\text{NaY}$ -sulf sample. This sample was then treated in 10 mL min^{-1} H_2 at 673 K for 2 h (temperature ramp: 5 K min^{-1} to 673 K, hold for 2 h) to form the reduced $\text{Mo}_x\text{S}_y/\text{NaY}$ -red sample. The $\text{Mo}_x\text{S}_y/\text{NaY}$ -red sample was finally resulfided in 10 mL min^{-1} H_2S (10 vol% in H_2) at 673 K for 2 h (temperature ramp: 5 K min^{-1} to 673 K, hold for 2 h) to form resulfided $\text{Mo}_x\text{S}_y/\text{NaY}$ -resulf sample. After sulfidation/reduction of the Mo_xS_y phase, the capillary was cooled down to room temperature and placed on the sample stage for XAS or XES measurements. The data were monitored for any signs of X-ray beam damage. Several successive scans were averaged to reduce signal-to-noise ratio and improve the data quality.

4.4.1.3 Extended X-ray Absorption Fine Structure (EXAFS) Measurements

The spectra for EXAFS analysis were measured in total fluorescence yield (TFY) mode between 19700 and 21500 eV *via* continuous scanning. All spectra were corrected for self-absorption effects using the “Fluo” algorithm implemented in the Athena software package.¹ For EXAFS analyses, spectra were background subtracted, normalized, k^3 -weighted, and k^3 -weighted Fourier-transformed (FT) between $k = 3 \text{ \AA}^{-1}$ and $k = 15 \text{ \AA}^{-1}$. The EXAFS fitting was performed in k -space between 3 and 15 \AA^{-1} (uncorrected for phase shift) on the k^1 -, k^2 -, and k^3 -weighted data (corresponding the first Mo-Mo and Mo-S coordination shells). The fitting was performed using Artemis software package.¹ E_0 was set such that energy-shift (ΔE_0) obtained during the fit was less than 1 eV. A Mo-foil was first fitted to Mo bcc structure

and the Mo-Mo coordination number was set to 8 and 6 (theoretical values based on the bcc structure) for the first and second coordination shells, respectively, to obtain the amplitude reduction factor, $S_0^2 = 1.03$, which was then used in the subsequent fits.

4.4.1.4 High Energy Resolution Fluorescence Detected X-ray Absorption Near Edge Structure (HERFD-XANES) and Valence-to-Core (VtC) XES Measurements

Mo $K\alpha_1$ HERFD-XANES spectra were collected using a Johann-type XES spectrometer equipped with two Ge(999) crystals placed on a five-analyzer crystal XES spectrometer. The Ge(999) crystals were used to select the Mo $K\alpha_1$ emission line (~17480 eV). Spectra were then measured between 19950 eV and 20200 eV with a step size of 0.5 eV. Mo $K\beta$ VtC XES spectra were measured using three Si(12 12 0) crystals placed on the five-analyzer crystal XES spectrometer. Mo $K\beta$ VtC XES data were collected between 19920 eV and 20050 eV with a step-size of 0.2 eV and an incident energy of 20100 eV. VtC XES spectra were normalized to the maximum intensity of $K\beta_2$ peak.

4.4.1.5 Computational Details

Unrestricted Kohn Sham (UKS) density functional theory (DFT) calculations were performed using ORCA quantum chemistry package version 4.2.² Relativistic effects were taken into account by zeroth-order regular approximation (ZORA) and atom-pairwise dispersion correction with the Becke-Johnson damping scheme (D3BJ) were implemented.³ Relativistically recontracted versions of the all-electron Ahlrichs def2 basis sets with triple zeta polarization functions (ZORA-def2-TZVP for geometry optimization and ZORA-def2-TZVPP for other calculations),⁴ auxiliary basis sets SARC/J,^{5,6} and three different hybrid functionals: B3LYP, PBE0, and TPSSh, were used. The hybrid functionals were employed with RIJCOSX approximation to speed up the calculations.⁷⁻¹⁰ The RIJCOSX approach incorporates the resolution-of-identity (RI) approximation for the evaluation of the Coulomb matrices and the chain-of-spheres algorithm for the formation of the exchange-type matrices. The electron density based Hirshfeld charge and spin population analysis was performed on the optimized geometries. The isosurface (0.02 a.u.) depicting the difference in density of alpha and beta electrons was visualized using Chemcraft software to illustrate the location of unpaired electrons. XAS and XES spectra of the optimized structures were

simulated with time-dependent density functional theory (TDDFT) using Tamm-Dancoff approximation.¹¹ Up to 100 roots were calculated allowing for transitions only from Mo 1s orbitals. The calculated intensities include electric dipole, magnetic dipole and electric quadrupole contributions. Triplet states were not considered during TDDFT calculations. A Gaussian broadening of 4.5 eV was applied to XAS spectra and a Lorentzian broadening of 8.5 eV was applied to the XES spectra for comparison with the experimental data. Sample input files for geometry optimization, thermochemical property calculations, charge calculations, and XAS/XES simulations, are presented in Section 4.4.11 of the Supporting Information.

4.4.1.6 Electron Paramagnetic Resonance (EPR) Spectroscopy

Samples were packed in a glovebox and measured in airtight EPR tubes. EPR spectra were obtained on a JEOL JES-FA200 X-Band spectrometer at a frequency of 9.2 GHz and a microwave power of 5 mW. Spectra were recorded with a time constant of 0.1 s with a spectral width of ± 100 mT at a center field of 330 mT. For the determination of g-values, fourth absorption line of Mn^{2+} embedded in a MgO matrix (g-value of 1.981) was used as a standard.

4.4.1.7 Catalytic Reactions

All catalytic reactions were carried out in a lab-scale plug flow reactor (quartz tube with 4 mm inner diameter). Gas flow rates were maintained using Bronkhorst mass flow controllers. Catalyst precursors were diluted 1/10 in SiC (sieved to 500-1000 μm) and placed in the quartz tube supported with quartz wool. Impregnated precursors were sulfided in a stream of 20 mL min^{-1} H_2S (10 vol% in H_2) at ambient pressure (5 K min^{-1} to 673 K, hold for 16 h). Carbonyl precursors were sulfided in a stream of 20 mL min^{-1} H_2S (10 vol% in H_2) at ambient pressure (5 K min^{-1} to 673 K, hold for 2 h). Additionally, some carbonyl precursors were treated in a stream of pure H_2 (5 K min^{-1} to 673 K, hold for 2 h) after sulfidation. These samples are referred to as sulfided and reduced, respectively. After sulfidation, all catalysts were purged with N_2 for 30 min prior to catalytic reactions. Hydrogenation of ethene was performed at 473 K and ambient pressure with a typical $\text{H}_2/\text{C}_2\text{H}_4$ volumetric ratio of 20/1. Product composition was analyzed by online gas chromatography using an Agilent 7890B GC. Ethane was detected as the only product under all conditions and times-on-stream. Product formation rates were determined using space-time yields under differential conditions

(conversion less than 20%) after the catalysts reached a steady state (~24 h). Transport limitations have been excluded under the applied reaction conditions by varying the amount of loaded catalyst and its particle size.

4.4.2 ^{27}Al Magic Angle Spinning-Nuclear Magnetic Resonance (MAS-NMR) Spectroscopy

Solid state ^{27}Al MAS NMR spectra were recorded on a Bruker AV 500 MHz wide bore spectrometer with a magnetic field of 11.75 T corresponding to a Larmor frequency of 130.3 MHz. Samples were hydrated in a desiccator for at least 24 h before packing in ZrO_2 NMR rotors. For 1D single-pulse experiments the spinning frequency was 12 kHz and 2400 scans were recorded with a pulse width of 1.16 μs and a relaxation delay of 2 s. ^{27}Al MAS NMR results (Figure S4.1) confirm that the increase in extra framework aluminum (EFAI) content in $\text{Mo}_x\text{S}_y/\text{NaY}$ -sulf sample upon loading Mo and the subsequent sulfidation was negligible.

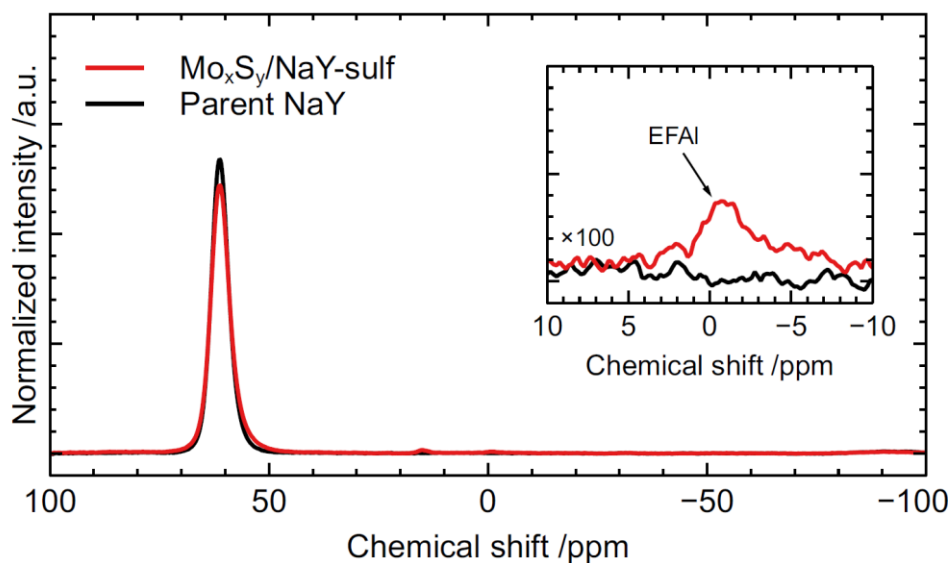


Figure S4.1 ^{27}Al MAS-NMR spectra of parent NaY zeolite (black) and a representative sulfided $\text{Mo}_x\text{S}_y/\text{NaY}$ -sulf catalyst (red).

4.4.3 High-Angle Annular Dark Field-Transmission Electron Microscopy (HAADF-TEM) & Energy Dispersive X-Ray Spectroscopy (EDS)

TEM sample preparation involved either embedding the zeolite-based powder into resin and microtoming thin sections using Leica microtome system, or alternatively crashing the powder in dry form between two glass slides and subsequently dispersing

the powder directly onto Cu 300 mesh lacey carbon TEM grids. The as prepared TEM grids were then transferred to TEM holder and loaded into the microscope for imaging. S/TEM analysis was performed with a probe-corrected FEI's Titan 80-300 operated at 300 kV. The observations were performed in scanning mode with a probe convergence angle of 18 mrad, and with the use of HAADF detector with inner detection angle set three times higher than the probe convergence angle. Compositional analysis was performed with EDS, using Oxford X-Max^N100TLE Solid Drift Detector SDD (100 mm²). The EDS data collection and processing were performed with Oxford's Aztec software package. EDS mapping (Figure S4.2 middle and right) showed that Mo and S are homogeneously distributed across the zeolite crystals on both sulfided Mo_xS_y/NaY-sulf and reduced Mo_xS_y/NaY-red catalysts. Additionally, HAADF-TEM micrographs (Figure S4.2 left) confirmed the absence of MoS₂ slabs outside the zeolite framework.

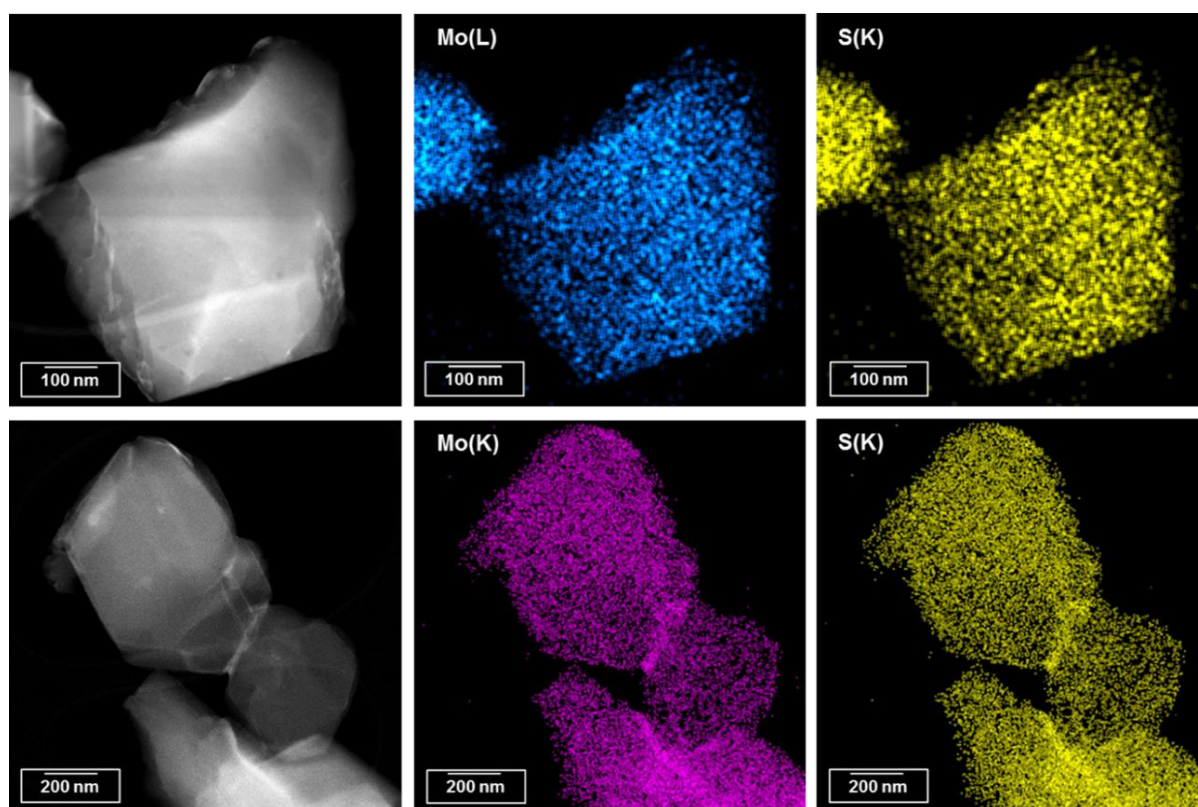


Figure S4.2 HAADF TEM micrographs (left) and EDS elemental mappings of molybdenum (middle) and sulfur (right) for Mo_xS_y/NaY-sulf (top row) and Mo_xS_y/NaY-red (bottom row) samples.

4.4.4 Nitrogen Physisorption

N_2 adsorption/desorption isotherms were measured on parent NaY zeolite, sulfided NaY zeolite, and three sulfided Mo_xS_y/NaY catalysts (with varying Mo content), at 77 K using a Thermo Finnigan Sorptomatic 1990 series instrument. Micropore volume (in $cm^3 g^{-1}$) was estimated with the t-plot method and the results are shown in Figure S4.3. The parent NaY zeolite showed no change in the micropore volume after sulfidation in H_2S (10 vol% in H_2) at 673 K for 2 h. The micropore volume decreased monotonically, with increasing Mo content, in the Mo-containing Mo_xS_y/NaY catalysts, suggesting incorporation of Mo_xS_y clusters in the micropores of the zeolite framework. All Mo species are considered to be encapsulated in the NaY supercages given that sodalite cages are too small to accommodate the carbonyl precursor or the sulfide cluster.

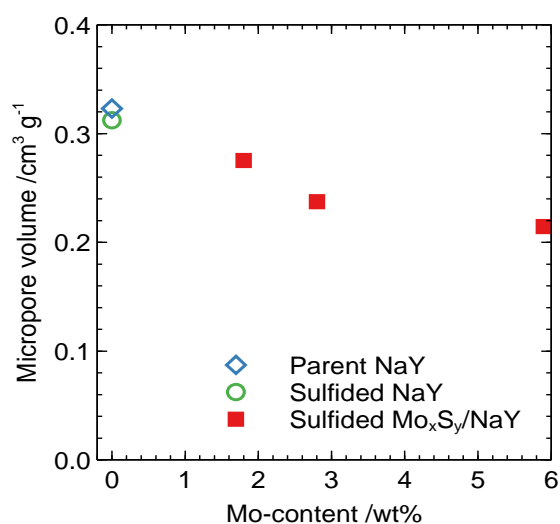


Figure S4.3 Micropore volume of the parent NaY, sulfided NaY, and three sulfided Mo_xS_y/NaY catalysts with varying Mo content, as determined from N_2 sorption isotherms.

4.4.5 Powder X-Ray Diffraction (XRD) Patterns

XRD patterns were obtained on a PANalytical Empyrean diffractometer equipped with a Cu K α source (0.154 nm, Ni K β filter) and a solid-state detector (PIXcel^{1D}). Patterns were recorded at 45 kV and 40 mA with a step size of 0.017 degrees and a scan time of 115 s per step. The zeolite framework was stable under sulfidation and reaction conditions. The relative intensities of the signals attributed to (111), (220), and (311) lattice planes change due to a redistribution of sodium cations in the zeolite framework caused by incorporation of transition metal sulfide (TMS) clusters.^{12,13}

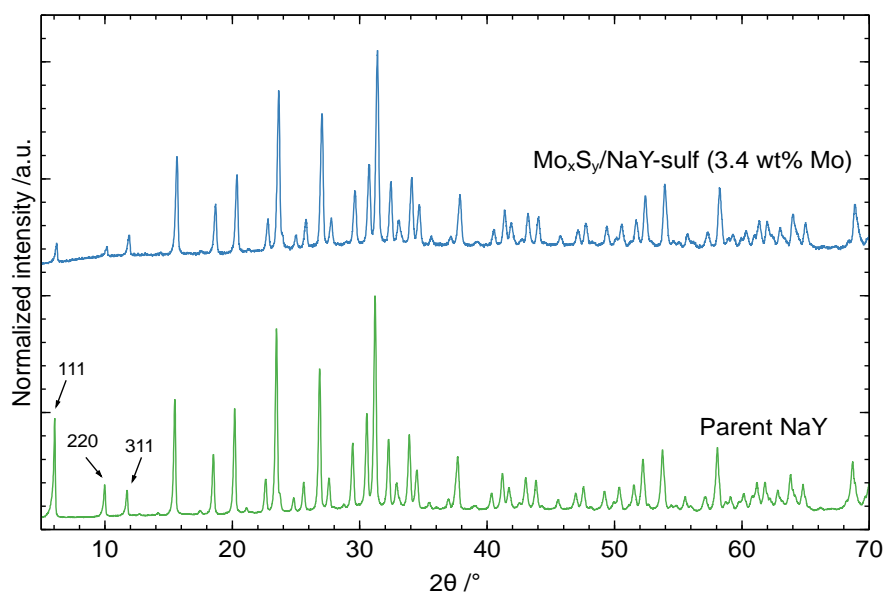


Figure S4.4 XRD patterns of the parent NaY zeolite used as catalyst support (bottom) and a representative Mo_xS_y/NaY-sulf catalyst (with 3.4 wt% Mo) after 24 h of ethene hydrogenation reaction (top).

4.4.6 Relative Stability of Mo₂S₄ and Mo₄S₄ Clusters

Table S4.1 Relative Gibbs free energies at 473 K ($\Delta G^\#$) of the *cis* and *trans* configurations of dinuclear Mo₂S₄ clusters with different spin-multiplicities computed using B3LYP, PBE0, and TPSSh functionals. The Gibbs free energy of the *cis*-Mo₂S₄ cluster with a spin-multiplicity of 1 (*i.e.*, no unpaired electrons) was used as the standard and was set to zero.

Configuration	Spin-Multiplicity (2S + 1)	Relative Gibbs Free Energy at 473 K, $\Delta G^\#$ /kJ mol ⁻¹		
		B3LYP	PBE0	TPSSh
<i>cis</i>	1	0.0	0.0	0.0
	3	-36.3	-43.7	-41.3
	5	-23.0	-41.4	-7.0
<i>trans</i>	1	2.6	3.9	2.8
	3	-24.6	-34.0	-15.8
	5	-18.1	-36.6	-2.4

Table S4.2 Relative Gibbs free energies at 473 K ($\Delta G^\#$) of tetranuclear Mo₄S₄ clusters with different spin-multiplicities computed using B3LYP, PBE0, and TPSSh functionals. The Gibbs free energy of Mo₄S₄ cluster with a spin-multiplicity of 1 (*i.e.*, no unpaired electrons) was used as the standard and was set to zero.

Spin-Multiplicity (2S + 1)	Relative Gibbs Free Energy at 473 K, $\Delta G^\#$ /kJ mol ⁻¹		
	B3LYP	PBE0	TPSSh
1	0.0	0.0	0.0
3	-1.4	-8.3	12.6
5	-16.6	-31.0	4.1
7	27.0	8.4	54.4
9	68.4	46.2	112.3
11	125.5	97.5	185.0
13	281.3	256.5	367.8
15	284.4	247.5	387.7
17	345.4	291.9	464.7

Table S4.3 Average Mo-Mo ($d_{\text{Mo-Mo}}$) and Mo-S ($d_{\text{Mo-S}}$) interatomic distances in the thermodynamically most stable dinuclear *cis*-Mo₂S₄ (spin-multiplicity = 3) and tetranuclear Mo₄S₄ (spin-multiplicity = 5) clusters, calculated after geometry optimization using B3LYP, PBE0, and TPSSH functionals.

Functional	<i>cis</i> -Mo ₂ S ₄		Mo ₄ S ₄	
	$d_{\text{Mo-S}}$	$d_{\text{Mo-Mo}}$	$d_{\text{Mo-S}}$	$d_{\text{Mo-Mo}}$
B3LYP	2.233	2.630	2.407	2.630
PBE0	2.214	2.608	2.376	2.608
TPSSH	2.225	2.619	2.389	2.617

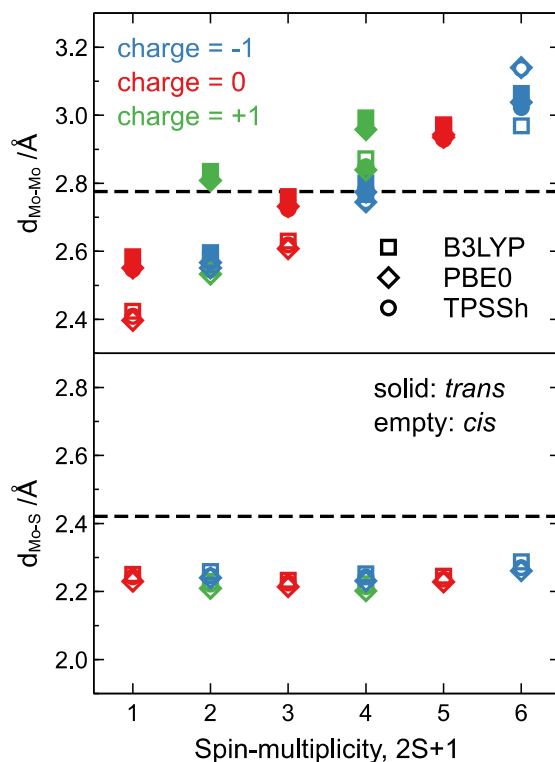
4.4.7 Effect of Charge Transfer on the Optimized Mo₂S₄ Structures

Figure S4.5 The Mo-Mo interatomic distances ($d_{\text{Mo-Mo}}$), and average Mo-S interatomic distances ($d_{\text{Mo-S}}$), of Mo₂S₄ cluster with terminal S-atoms in *cis* (empty symbols) or *trans* (solid symbols) configurations, as a function of spin-multiplicity ($2S + 1$) as estimated from DFT calculations using B3LYP, PBE0, and TPSSh functionals. Experimental $d_{\text{Mo-Mo}}$ and $d_{\text{Mo-S}}$ estimated from EXAFS analysis are shown as dashed lines. Effect of electron transfer from the zeolite to the cluster (blue; net charge = -1) or from the cluster to the zeolite (green; net charge = +1) is shown, in comparison to a neutral cluster (red).

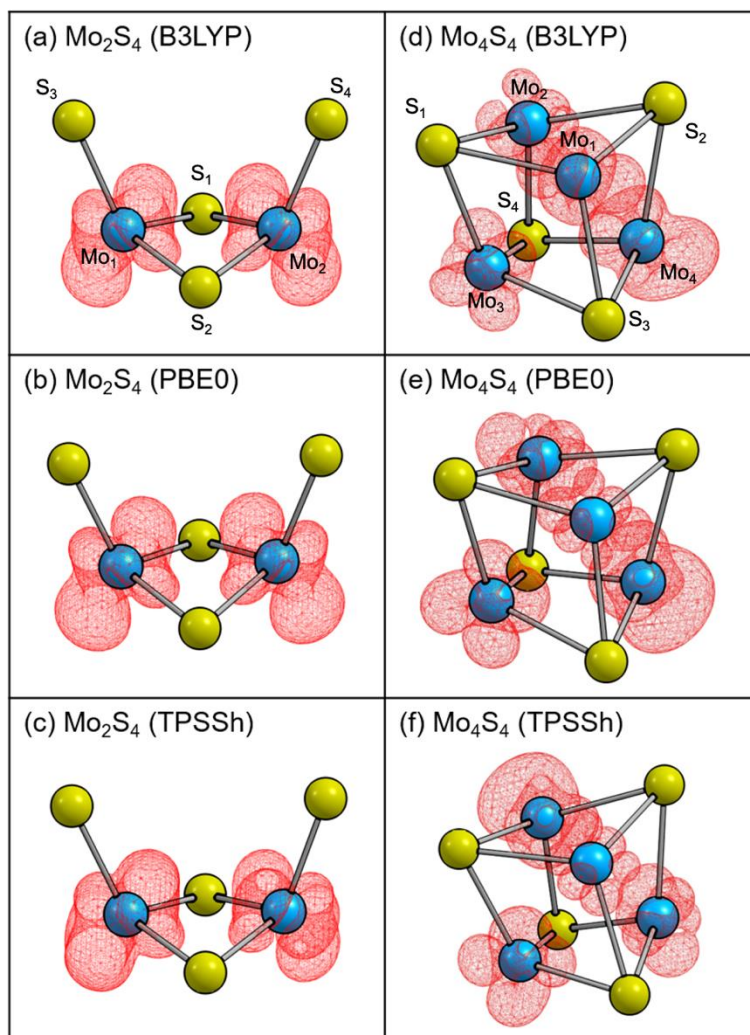
4.4.8 Location of Unpaired Electrons in Mo_2S_4 and Mo_4S_4 Clusters

Figure S4.6 Isosurface (0.02 a.u.) depicting the difference in the densities of alpha and beta electrons computed using B3LYP, PBE0, and TPSSh functionals, showing the location of unpaired electrons in *cis*- Mo_2S_4 (spin-multiplicity = 3), and Mo_4S_4 (spin-multiplicity = 5) clusters. S: yellow; Mo: blue.

Table S4.4 (a) Hirshfeld charge and spin population, (b) Mulliken charge and spin population, and (c) Mayer bond orders, in the thermodynamically most stable *cis*-Mo₂S₄ cluster (spin-multiplicity = 3) computed using B3LYP, PBE0, and TPSSh functionals. The nomenclature of atoms is shown in Figure S4.6(a).

Atom	Hirshfeld Charge Population			Hirshfeld Spin Population		
	B3LYP	PBE0	TPSSh	B3LYP	PBE0	TPSSh
Mo ₁	0.471	0.467	0.469	0.954	0.983	0.941
Mo ₂	0.471	0.467	0.469	0.949	0.978	0.937
S ₁	-0.243	-0.240	-0.243	-0.020	-0.032	-0.007
S ₂	-0.243	-0.240	-0.244	-0.021	-0.032	-0.006
S ₃	-0.228	-0.228	-0.226	0.069	0.052	0.068
S ₄	-0.228	-0.227	-0.225	0.069	0.052	0.068

Atom	Mulliken Charge Population			Mulliken Spin Population		
	B3LYP	PBE0	TPSSh	B3LYP	PBE0	TPSSh
Mo ₁	0.763	0.757	0.738	1.056	1.068	1.040
Mo ₂	0.765	0.757	0.738	1.046	1.063	1.072
S ₁	-0.395	-0.371	-0.397	-0.123	-0.148	-0.098
S ₂	-0.428	-0.450	-0.397	-0.080	-0.051	-0.099
S ₃	-0.352	-0.347	-0.339	0.051	0.034	0.042
S ₄	-0.352	-0.346	-0.343	0.049	0.034	0.044

Bond	Mayer Bond Orders		
	B3LYP	PBE0	TPSSh
Mo ₁ -Mo ₂	1.235	1.106	1.275
Mo ₁ -S ₁	1.126	1.147	1.126
Mo ₁ -S ₂	1.112	1.109	1.127
Mo ₁ -S ₃	2.099	2.120	2.080
Mo ₂ -S ₁	1.127	1.148	1.125
Mo ₂ -S ₂	1.112	1.109	1.127
Mo ₂ -S ₄	2.099	2.120	1.127

Table S4.5 (a) Hirshfeld charge and spin population, (b) Mulliken charge and spin population, and (c) Mayer bond orders, in the thermodynamically most stable Mo₄S₄ cluster (spin-multiplicity = 5) computed using B3LYP, PBE0, and TPSSh functionals. The nomenclature of atoms is shown in Figure S4.6(d).

Atom	Hirshfeld Charge Population			Hirshfeld Spin Population		
	B3LYP	PBE0	TPSSh	B3LYP	PBE0	TPSSh
Mo ₁	0.320	0.319	0.317	1.042	1.031	1.020
Mo ₂	0.320	0.319	0.317	1.038	1.034	1.020
Mo ₃	0.316	0.315	0.315	0.951	0.969	0.958
Mo ₄	0.317	0.315	0.315	0.946	0.968	0.958
S ₁	-0.318	-0.316	-0.316	0.019	0.011	0.027
S ₂	-0.318	-0.316	-0.316	0.019	0.011	0.027
S ₃	-0.319	-0.318	-0.316	-0.008	-0.012	-0.005
S ₄	-0.319	-0.319	-0.316	-0.008	-0.012	-0.005

Atom	Mulliken Charge Population			Mulliken Spin Population		
	B3LYP	PBE0	TPSSh	B3LYP	PBE0	TPSSh
Mo ₁	0.526	0.521	0.501	1.154	1.155	1.139
Mo ₂	0.526	0.521	0.501	1.149	1.159	1.140
Mo ₃	0.532	0.525	0.512	1.030	1.064	1.055
Mo ₄	0.532	0.525	0.512	1.024	1.062	1.055
S ₁	-0.522	-0.517	-0.502	-0.089	-0.112	-0.093
S ₂	-0.522	-0.517	-0.502	-0.089	-0.111	-0.093
S ₃	-0.536	-0.529	-0.512	-0.090	-0.109	-0.101
S ₄	-0.536	-0.529	-0.512	-0.090	-0.109	-0.101

Bond	Mayer Bond Orders			Bond	Mayer Bond Orders		
	B3LYP	PBE0	TPSSh		B3LYP	PBE0	TPSSh
Mo ₁ -Mo ₂	0.921	0.887	0.927	Mo ₂ -S ₁	0.785	0.806	0.790
Mo ₁ -Mo ₃	1.006	0.992	1.010	Mo ₂ -S ₂	0.785	0.806	0.790
Mo ₁ -Mo ₄	1.005	0.992	1.010	Mo ₂ -S ₄	0.784	0.805	0.796
Mo ₂ -Mo ₃	1.005	0.992	1.010	Mo ₃ -S ₁	0.841	0.851	0.862
Mo ₂ -Mo ₄	1.006	-0.992	1.010	Mo ₃ -S ₃	0.804	0.822	0.815
Mo ₃ -Mo ₄	0.711	-0.703	0.735	Mo ₃ -S ₄	0.804	0.822	0.815
Mo ₁ -S ₁	0.785	0.806	0.790	Mo ₄ -S ₂	0.841	0.852	0.862
Mo ₁ -S ₂	0.785	0.806	0.790	Mo ₄ -S ₃	0.805	0.822	0.815
Mo ₁ -S ₃	0.783	0.805	0.796	Mo ₄ -S ₄	0.805	0.822	0.815

4.4.9 X-Ray Emission Spectroscopy (XES) Measurements

The spectral feature at 19965.5 eV is assigned to $K\beta_2$ transition (Mo 4p \rightarrow Mo 1s). The less intense spectral features beyond the $K\beta_2$ peak are assigned to the $K\beta_4$ transition (Mo 4d \rightarrow Mo 1s and S 3p \rightarrow Mo 1s) at \sim 19998 eV and the valence-to-core $K\beta''$ transition (S 3s \rightarrow Mo 1s) at \sim 19988 eV. The positions and amplitudes of $K\beta''$ and $K\beta_4$ peaks (relative to the $K\beta_2$ peak) are reported in Table S4.6, together with the values simulated using TDDFT calculations. The positions of $K\beta''$ and $K\beta_4$ as well as the relative amplitude of $K\beta_4$ were not affected upon reduction of the catalyst. The relative energies obtained from DFT for the two less intense features are slightly higher than the experimental values which we again attribute to the shorter theoretical Mo-S bonds. This assumption is verified by additional calculations showing a closer agreement with experimental data if we artificially increase the Mo-S distance during theoretical simulations (Figures S4.8). The relative amplitude of the valence-to-core $K\beta''$ peak significantly decreased under reduction conditions suggesting a decrease in the intensity of S 3s \rightarrow Mo 1s transitions in the reduced catalyst. This decrease can be attributed to the fact the reduced catalyst contains less S atoms per Mo compared to sulfided catalyst. This decrease in relative intensity is also in agreement with the predictions from TDDFT.

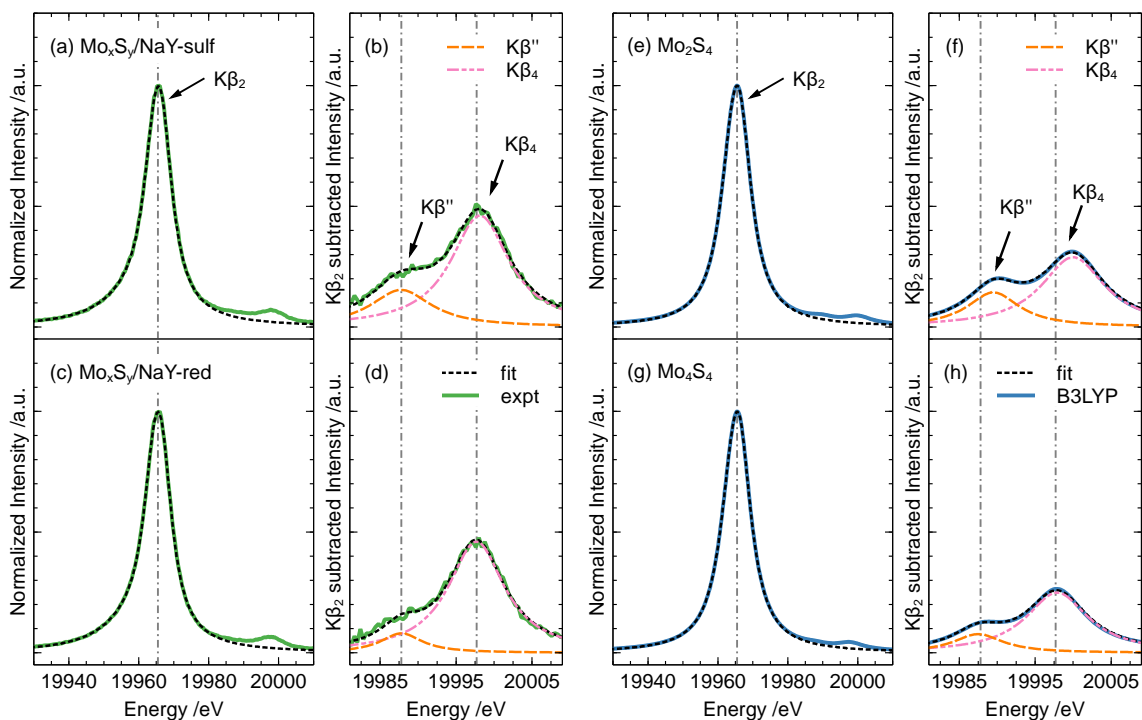


Figure S4.7 (a, c) High energy resolution Mo $K\beta$ VtC XES spectra, and (b, d) $K\beta_2$ -subtracted spectra of $\text{Mo}_x\text{S}_y/\text{NaY-sulf}$ (a, b) and $\text{Mo}_x\text{S}_y/\text{NaY-red}$ (c, d) catalysts. The $K\beta_4$ and $K\beta''$ spectral features fitted to Lorentzian peak forms are also shown. The spectra were normalized to the $K\beta_2$ maxima. (e, g) Simulated XES spectra (TDDFT/B3LYP) and (f, h) $K\beta_2$ -subtracted spectra, of the thermodynamically most stable *cis*- Mo_2S_4 (spin-multiplicity = 3) and Mo_4S_4 (spin-multiplicity = 5) clusters. A Lorentzian broadening of 8.5 eV was applied and the spectra were normalized to the $K\beta_2$ maxima. The $K\beta_4$ and $K\beta''$ peaks are also shown.

Table S4.6 Relative peak positions (δE) and amplitudes (A) of $K\beta''$ and $K\beta_4$ peaks in the experimentally measured XES spectra of $\text{Mo}_x\text{S}_y/\text{NaY-sulf}$ and $\text{Mo}_x\text{S}_y/\text{NaY-red}$ catalysts, and the theoretical spectra of *cis*- Mo_2S_4 (spin-multiplicity = 3) and Mo_4S_4 (spin-multiplicity = 5) clusters simulated with TDDFT using B3LYP, PBE0, and TPSSh functionals. The peak positions and amplitudes are reported relative to the $K\beta_2$ spectral feature.

	Functional	$K\beta''$		$K\beta_4$	
		δE /eV	A	δE /eV	A
$\text{Mo}_x\text{S}_y/\text{NaY-sulf}$ (experimental)		22.3	0.0152	32.7	0.0439
Mo_2S_4	B3LYP	24.1	0.0133	34.6	0.0268
	PBE0	24.4	0.0146	35.0	0.0290
	TPSSh	23.8	0.0133	34.0	0.0262
$\text{Mo}_x\text{S}_y/\text{NaY-red}$ (experimental)		22.4	0.0055	32.3	0.0426
Mo_4S_4	B3LYP	22.1	0.0072	32.5	0.0233
	PBE0	22.2	0.0085	32.7	0.0258
	TPSSh	21.8	0.0076	31.9	0.0237

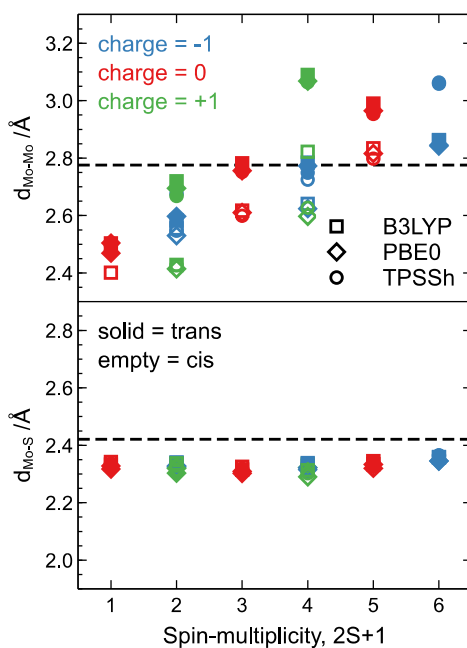


Figure S4.8 Mo-Mo interatomic distances ($d_{\text{Mo-Mo}}$) and average Mo-S interatomic distance ($d_{\text{Mo-S}}$), in Mo_2S_4 cluster with terminal S-atoms in *cis* (empty symbols) or *trans* (solid symbols) orientations, as a function of spin-multiplicity ($2S + 1$) as estimated from DFT calculations using B3LYP, PBE0, and TPSSh functionals. The bond length between Mo and terminal S-atom was extended to 2.42 Å and constrained during geometry optimization. Experimental $d_{\text{Mo-Mo}}$ and $d_{\text{Mo-S}}$ estimated experimentally from EXAFS are shown as dashed lines.

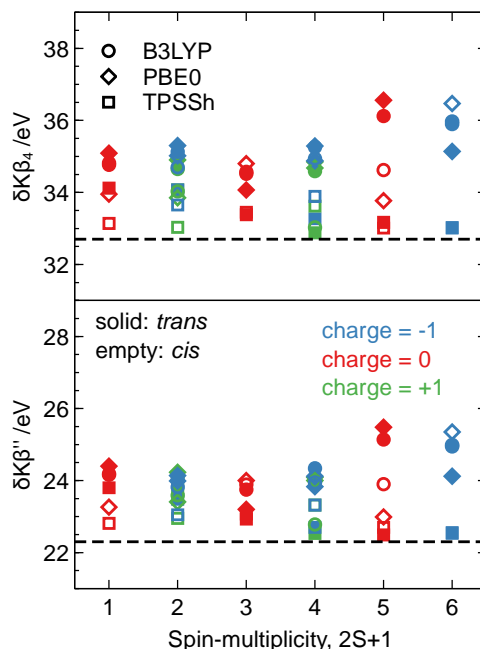


Figure S4.9 Relative peak positions (δE) of $\text{K}\beta''$ and $\text{K}\beta_4$ peaks, as a function of spin-multiplicities, in the theoretical XES spectra of the optimized Mo_2S_4 clusters (with Mo-S terminal bond length constrained at 2.42 Å) computed with TDDFT using B3LYP, PBE0, and TPSSh functionals. The peak positions are reported relative to the $\text{K}\beta_2$ spectral feature.

4.4.10 High Energy-Resolution X-Ray Absorption Spectroscopy (XAS)

TDDFT can also predict XAS spectra where the local electron structure and the oxidation state of the metal centers can strongly influence the energy of the absorption edge. The absorption edge of the reduced $\text{Mo}_x\text{S}_y/\text{NaY}$ -red catalyst shifted to a lower energy compared to that of the sulfided $\text{Mo}_x\text{S}_y/\text{NaY}$ -sulf catalyst (Figure S4.10a). This shift towards a lower absorption energy is in close agreement with theoretical predictions estimated from TDDFT using B3LYP, PBE0, and TPSSh functionals (Figure S10 b) and is evidence for a reduction of the Mo centers in a pure hydrogen atmosphere.

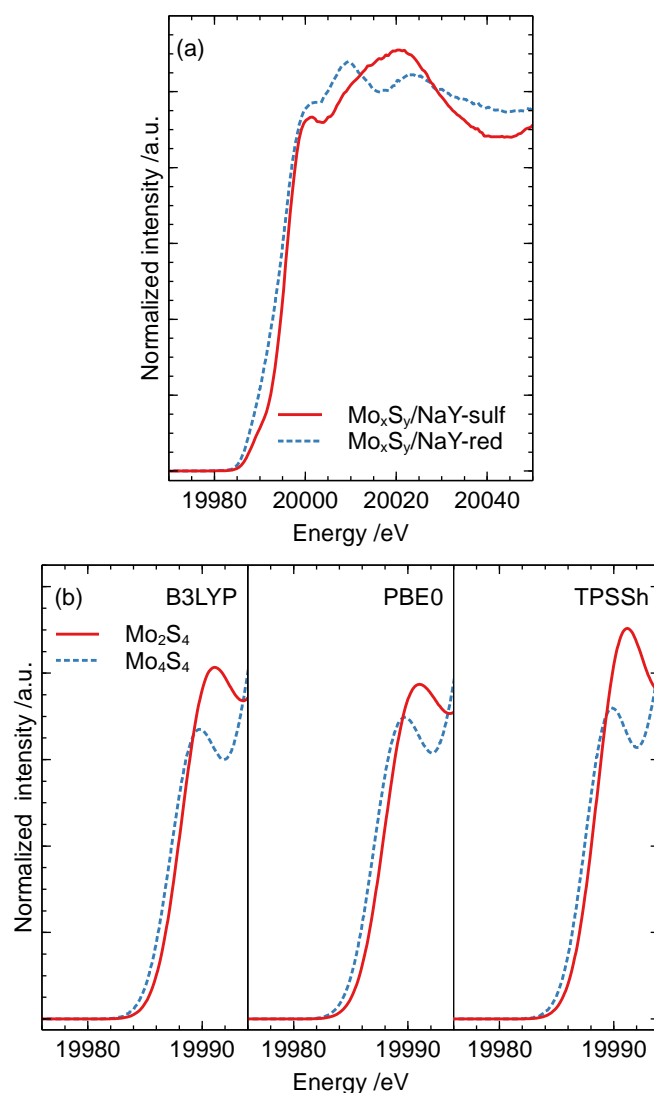


Figure S4.10 (a) Experimental Mo K α HERFD XAS spectra of $\text{Mo}_x\text{S}_y/\text{NaY}$ -sulf and $\text{Mo}_x\text{S}_y/\text{NaY}$ -red catalysts. (b) Theoretical X-ray absorption spectra of the optimized *cis*- Mo_2S_4 (spin-multiplicity = 3) and Mo_4S_4 (spin-multiplicity = 5) clusters simulated with TDDFT using B3LYP, PBE0, and TPSSh functionals.

4.4.11 ORCA Input Files

4.4.11.1 Typical ORCA Input File used for Geometry Optimization

```
! UKS B3LYP RIJCOSX ZORA ZORA-def2-TZVP SARC/J D3BJ TightOpt
! TightSCF SlowConv Grid5 FinalGrid7 GridX7 KDIIS XYZFile
```

```
%basis
  newGTO Mo "old-ZORA-TZVP" end
end
```

```
%method
  FrozenCore FC_ELECTRONS
  CheckFrozenCore True
end
```

```
%scf
  shift shift 0.1 erroff 0 end
  damp fac 0.8 erroff 0.001 end
end
```

```
*xyzfile charge multiplicity initial-coordinates.xyz
```

4.4.11.2 Typical ORCA Input File used for Calculation of Thermochemical Properties and Hirshfeld Population Analysis

```
! UKS B3LYP RIJCOSX ZORA ZORA-def2-TZVPP SARC/J D3BJ Freq
! VeryTightSCF SlowConv Grid7 FinalGrid7 GridX8 KDIIS
```

```
%basis
  newGTO Mo "old-ZORA-TZVPP" end
end
```

```
%scf
  shift shift 0.1 erroff 0 end
  damp fac 0.8 erroff 0.001 end
end
```

```
*xyzfile charge multiplicity optimized-coordinates.xyz
```

```
%output
  Print [P_Hirshfeld] 1
end
```

4.4.11.3 Typical ORCA Input File used for Simulation of X-ray Emission Spectra

```

! UKS B3LYP RIJCOSX ZORA ZORA-def2-TZVPP SARC/J D3BJ NoFrozenCore
! TightSCF SlowConv Grid7 FinalGrid7 GridX8 KDIIS

%basis
  newGTO Mo "old-ZORA-TZVPP" end
end

%scf
  shift shift 0.1 erroff 0 end
  damp fac 0.8 erroff 0.001 end
end

*xyzfile charge multiplicity optimized-coordinates.xyz

%xes
  CoreOrb 0,0
  OrbOp 0,1
  CoreOrbSOC 0,1
  DoSOC true
end

```

4.4.11.4 Typical ORCA Input File used for Simulation of X-ray Absorption Spectra

```

! UKS B3LYP RIJCOSX ZORA ZORA-def2-TZVPP SARC/J D3BJ NoFrozenCore
! TightSCF SlowConv Grid7 FinalGrid7 GridX8 KDIIS

%basis
  newGTO Mo "old-ZORA-TZVPP" end
end

%scf
  shift shift 0.1 erroff 0 end
  damp fac 0.8 erroff 0.001 end
end

*xyzfile charge multiplicity optimized-coordinates.xyz

%tddft
  OrbWin[0] = 0,0,-1,-1
  OrbWin[1] = 0,0,-1,-1
  DoQuad true
  Triplets true
  Nroots 100
  MaxDim 20
end

```

4.4.12 Infrared (IR) Spectroscopy of Adsorbed Pyridine

IR spectroscopy of adsorbed probe molecules was used to determine the acid properties of the synthesized catalysts. Experiments were performed on a Nicolet 6700 FTIR spectrometer (resolution = 4 cm^{-1}). All samples were sulfided in a plug flow reactor (PFR) setup prior to IR experiments. The sulfided catalysts were ground and pressed into self-supporting wafers ($\sim 5\text{ mg cm}^{-2}$). The wafers were resulfided in a stream of $20\text{ mL min}^{-1}\text{ H}_2\text{S}$ (10 vol% in H_2) at ambient pressure (5 K min^{-1} to 673 K , hold for 2 h). For activation, cycles of treatment in H_2 (4 cycles, total of 24 h) each followed by evacuation at 10^{-6} mbar for 30 min and 473 K were applied to all samples. Pyridine adsorption was performed on activated samples at 323 K by dosing 0.5 mbar pyridine into the IR cell and equilibrating for 0.5 h. Pyridine desorption was monitored by heating in steps of 50 K followed by equilibration for 0.5 h after each step. Spectra were background corrected using an OMNIC software package. All presented spectra are difference spectra against a reference spectrum at 10^{-7} mbar .

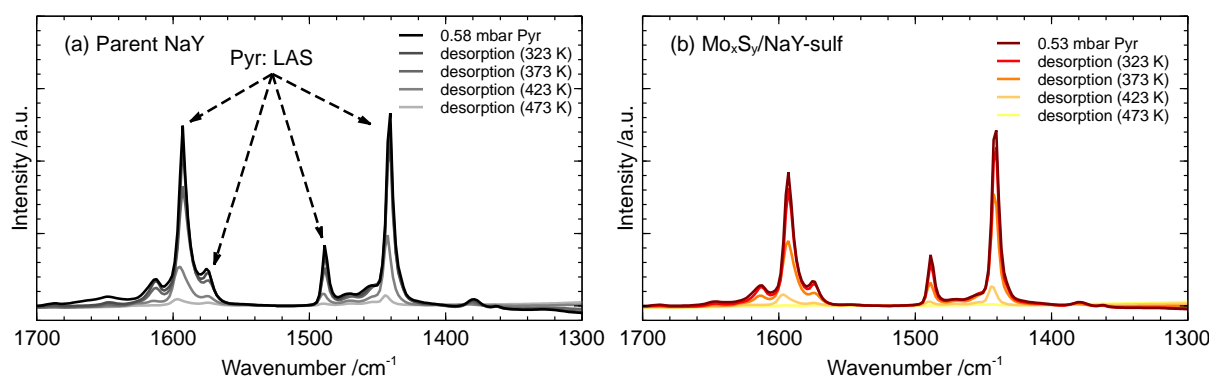
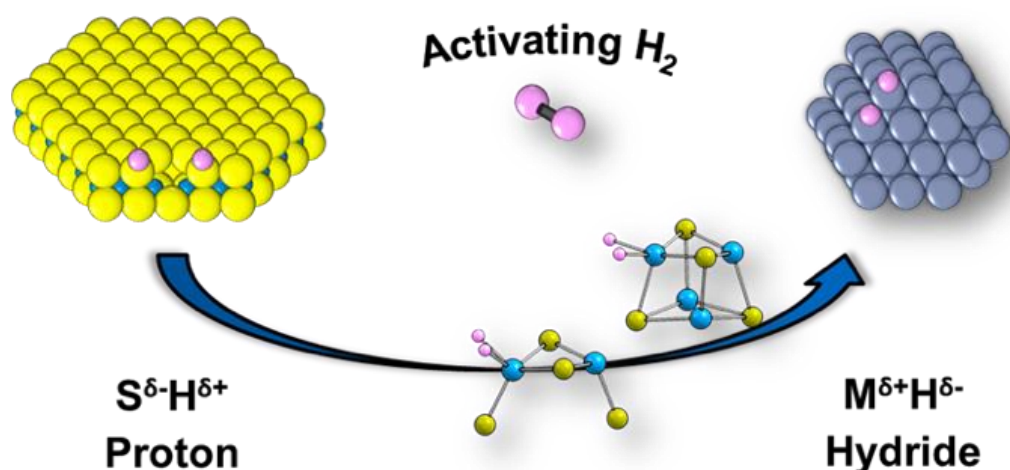


Figure S4.11 Pyridine adsorption on parent NaY zeolite (left) and a representative, sulfided and activated $\text{Mo}_x\text{S}_y/\text{NaY-sulf}$ catalyst (3.3 wt% Mo; right) monitored by IR spectroscopy. All bands are attributed to pyridine adsorbed on Lewis acid sites.¹⁴ No evidence was found for Brønsted acidity on zeolite support before or after incorporation of TMS clusters.

4.5 References

- (1) Ravel, B.; Newville, M. *Journal of Synchrotron Radiation* **2005**, *12*, 537.
- (2) Neese, F. *WIREs Computational Molecular Science* **2018**, *8*, e1327.
- (3) Wüllen, C. v. *The Journal of Chemical Physics* **1998**, *109*, 392.
- (4) Weigend, F.; Ahlrichs, R. *Physical chemistry chemical physics : PCCP* **2005**, *7*, 3297.
- (5) Weigend, F. *Physical Chemistry Chemical Physics* **2006**, *8*, 1057.
- (6) Rolfes, J. D.; Neese, F.; Pantazis, D. A. *Journal of Computational Chemistry* **2020**, *41*, 1842.
- (7) Petrenko, T.; Kossmann, S.; Neese, F. *The Journal of Chemical Physics* **2011**, *134*, 054116.
- (8) Izsák, R.; Neese, F. *The Journal of Chemical Physics* **2011**, *135*, 144105.
- (9) Neese, F.; Wennmohs, F.; Hansen, A.; Becker, U. *Chemical Physics* **2009**, *356*, 98.
- (10) Neese, F.; Olbrich, G. *Chemical Physics Letters* **2002**, *362*, 170.
- (11) Hirata, S.; Head-Gordon, M. *Chemical Physics Letters* **1999**, *314*, 291.
- (12) Okamoto, Y.; Katsuyama, H.; Yoshida, K.; Nakai, K.; Matsuo, M.; Sakamoto, Y.; Yu, J.; Terasaki, O. *Journal of the Chemical Society, Faraday Transactions* **1996**, *92*, 4647.
- (13) Salama, T. M.; Othman, I.; Sirag, M.; El-Shobaky, G. A. *Microporous and Mesoporous Materials* **2006**, *95*, 312.
- (14) Jacobs, P. A.; Heylen, C. *Journal of Catalysis* **1974**, *34*, 267.

5 Di- and Tetrameric Molybdenum Sulfide Clusters Activate and Stabilize Dihydrogen as Hydrides



Keywords: Molybdenum sulfide clusters • Hydrogen activation • Hydride • IR spectroscopy • Density functional theory

This chapter is based on a previously published article.

Reprinted with permission from: R. Khare, R. Weindl, A. Jentys, K. Reuter, H. Shi, J. A. Lercher, *JACS Au*. **2022**, 2, 3, 613-622.

<https://pubs.acs.org/doi/full/10.1021/jacsau.1c00507>

This is an open-access article under the Creative Commons Attribution-NonCommercial-NoDerivatives 4.0 International (CC BY-NC-ND 4.0) BY license (<https://creativecommons.org/licenses/by-nc-nd/4.0/>); minor changes were made to the formatting to improve the readability.

Abstract

NaY zeolite-encapsulated dimeric (Mo_2S_4) and tetrameric (Mo_4S_4) molybdenum sulfide clusters stabilize hydrogen as hydride binding to Mo atoms. Density functional theory (DFT) calculations and adsorption measurements suggest that stabilization of hydrogen as sulfhydryl (SH) groups, as typical for layered MoS_2 , is thermodynamically disfavored. Competitive adsorption of H_2 and ethene on Mo was probed by quantifying adsorbed CO on partly hydrogen and/or ethene covered samples with IR spectroscopy. During hydrogenation, experiment and theory suggest that Mo is covered predominately with ethene and sparsely with hydride. DFT calculations further predict that under reaction conditions, each Mo_xS_y cluster can activate only one H_2 , suggesting that the entire cluster (irrespective of its nuclearity) acts as one active site for hydrogenation. The nearly identical turnover frequencies ($24.7 \pm 3.3 \text{ mol}_{\text{ethane}} \cdot \text{h}^{-1} \cdot \text{mol}_{\text{cluster}}^{-1}$), apparent activation energies ($31\text{-}32 \text{ kJ} \cdot \text{mol}^{-1}$), and reaction orders (~ 0.5 in ethene and ~ 1.0 in H_2) show that the active sites in both clusters are catalytically indistinguishable.

5.1 Introduction

Two-dimensional, nanostructured transition metal sulfides (TMS) have a wide variety of applications in energy conversion.¹ Owing to their robust performance in the presence of heteroatoms, layered TMS materials, primarily based on Mo(W)S₂ promoted by Co/Ni, have long been used as hydrodefunctionalization catalysts in hydroprocessing.²⁻⁷ In addition, TMS catalysts show promise for a multitude of processes related to the production of fuels and chemicals¹, including the upgrading of bio-derived feedstocks (e.g., hydrodeoxygenation),⁸⁻¹⁰ (reverse) water gas shift (WGS/rWGS),^{11,12} and other synthetic approaches including syntheses from CO/CO₂.¹³⁻¹⁶ More recently, TMS have been studied as electrocatalysts.¹⁷⁻²¹

Most reactions studied on these catalysts involve H₂ as a reactant on sites that have been characterized by microscopy,^{22,23} spectroscopy,^{24,25} and adsorption of molecular probes,^{26,27} guided and aided by theory.²⁸⁻³⁰ The efforts have led to significantly improved catalytic properties, as well as to better atomistic understanding of local structures, and detailed mechanisms for hydrogenation/hydrogenolysis reactions. While the link between these catalysts and enzymes with sulfide based active sites seems intuitive, clear analogies have not been substantiated.^{2,6,31}

The impressive progress in the understanding of naturally occurring enzymes featuring metal-sulfur moieties in their active sites allows now to draw stronger analogies to inorganic materials containing atomistically defined sulfide clusters. The active sites in enzymes are the key to redox and hydrogenation catalysis, such as H⁺/H₂ conversion by hydrogenases and nitrogen fixation by nitrogenases.³²⁻³⁴ To translate this chemistry to non-enzyme systems, several supported (multinuclear) metal-sulfur clusters have been reported, some of which are known to mimic key structural motifs of sulfur-based enzyme cofactors.³⁵ To make them better accessible for catalytic hydrogenation, inorganic scaffolds are used for stabilization.^{14,36}

Activation of H₂ on sulfide materials occurs by dissociative adsorption, resulting in distinct final states for adsorbed hydrogen, e.g., SH groups on sulfide slabs or hydride species on metal sites.^{31,37-40} Interestingly, the nitrogenase enzyme's FeMo-cofactor was recently shown to stabilize hydrogen in the form of hydride species; in this case a fraction of adsorbed hydrogen is present as μ -bridging H^{δ-} on the Fe centers.^{34,41-43}

We recently reported Mo_xS_y clusters encapsulated in faujasite-type NaY zeolite with precisely defined nuclearity, geometry, and atomic connectivity.⁴⁴⁻⁴⁶ Using thermal treatment in sulfiding/reducing atmosphere, two different molecular cluster sizes were stabilized, *viz.* dimeric Mo_2S_4 and tetrameric Mo_4S_4 . The latter cluster structurally and electronically resembles the cubane motifs in nitrogenase enzyme, *i.e.*, the FeMo-cofactor.^{32,33} These catalysts exhibited remarkable stability for ethene hydrogenation in the absence of continuous sulfur supply to the reaction feed, while the classic layered MoS_2 catalyst deactivated significantly under the same conditions.⁴⁶ This deactivation behavior of conventional MoS_2 catalysts in the absence of sulfur in the feed has been reported extensively in literature.⁴⁷⁻⁴⁹

These promising results motivated us to address, how these Mo_xS_y clusters activate hydrogen and how their structures dynamically adapt to the reaction environment. Combining IR spectroscopy of adsorbed probe molecules with kinetic measurements and DFT calculations, employing ethene hydrogenation as a model reaction, we develop here the most plausible configurations of Mo_xS_y clusters and the changes in their geometric and electronic properties upon interactions with reactive gases (ethene, H_2 , and their mixtures) at low temperature (*i.e.*, 173 K; relevant for CO adsorption measurements) and high temperature (*i.e.*, 473 K; typical hydrogenation reaction temperature). The analyses provide insights into the similarities and differences in H_2 activation and the identity of surface hydrogen species among Mo_xS_y clusters, layered MoS_2 , and enzymes containing TMS-based structural motifs, and explains why it is justified to treat the entire cluster, rather than individual Mo atoms, as an active site for hydrogenation catalysis.

5.2 Results and Discussion

5.2.1 Active Sites for CO Adsorption and Hydrogenation

Direct spectroscopic evidence for the presence of hydrides on Mo atoms of Mo_xS_y phases has not been achieved so far and appears at present elusive. Thus, we turn to an indirect method to characterize the location and concentration of adsorbed hydrogen, using CO as a probe molecule. CO has been successfully used as a probe for Lewis acid sites (LAS) on TMS.^{26,50-52} In this case, CO appears to be an ideal probe. First, as long as CO molecules are not aligned, the wavenumbers of IR bands of CO adsorbed on LAS can be directly related to the electronic properties of the metal sites. Therefore, the observed shift in the band of adsorbed CO allows us to characterize the electronic state of Mo sites in the Mo_xS_y clusters compared to bulk MoS_2 . Second, a decrease in the intensity of bands after pre-exposing the catalyst to H_2 and/or ethene indicates blockage of Mo sites by adsorbed hydrogen/ethene. Third, the relative change in the intensity of IR bands (after pre-equilibrating with H_2 /ethene) allows to quantitatively estimate the fraction of Mo covered with hydrogen/ethene.

Figure 5.1 shows the IR spectra of CO adsorbed on $\text{Mo}_2\text{S}_4/\text{NaY}$, $\text{Mo}_4\text{S}_4/\text{NaY}$, and $\text{MoS}_2/\gamma\text{-Al}_2\text{O}_3$. In addition to the bands attributed to CO adsorbed on the acid sites of the support (*i.e.*, ~ 2175 and ~ 2125 cm^{-1} for NaY, ~ 2195 and ~ 2150 cm^{-1} for $\gamma\text{-Al}_2\text{O}_3$), all catalysts showed characteristic broad bands assigned to CO adsorbed on the Mo sites of Mo_xS_y at ~ 2035 cm^{-1} , ~ 2075 cm^{-1} , and 2085 cm^{-1} for the $\text{Mo}_x\text{S}_y/\text{NaY}$, and at ~ 2055 cm^{-1} , ~ 2095 cm^{-1} , and ~ 2105 cm^{-1} for $\text{MoS}_2/\gamma\text{-Al}_2\text{O}_3$.^{50,53}

In comparison to $\text{MoS}_2/\gamma\text{-Al}_2\text{O}_3$, the bands of CO adsorbed on Mo in $\text{Mo}_x\text{S}_y/\text{NaY}$ were red-shifted by ~ 20 cm^{-1} indicating an enhanced electron back-donation from Mo to CO in the case of cluster catalysts. This red-shift suggests a higher electron density in the Mo *d*-orbitals of Mo_xS_y clusters in comparison to the Mo atoms in MoS_2 slabs. It is interesting to note that the observed shift in the wavenumber was identical, suggesting the local electronic environment of Mo to be similar in both dimeric and tetrameric clusters. We also noticed that the amount of adsorbed CO, normalized to Mo content, on the two $\text{Mo}_x\text{S}_y/\text{NaY}$ catalysts (after quenching in vacuum) was comparable: 1455-1708 a.u. on $\text{Mo}_2\text{S}_4/\text{NaY}$ and 1730-1760 a.u. on $\text{Mo}_4\text{S}_4/\text{NaY}$ (Tables S5.1 and S5.2), suggesting that both dimeric and tetrameric clusters can accommodate similar number of CO molecules per Mo and that all Mo sites are accessible to CO adsorption.

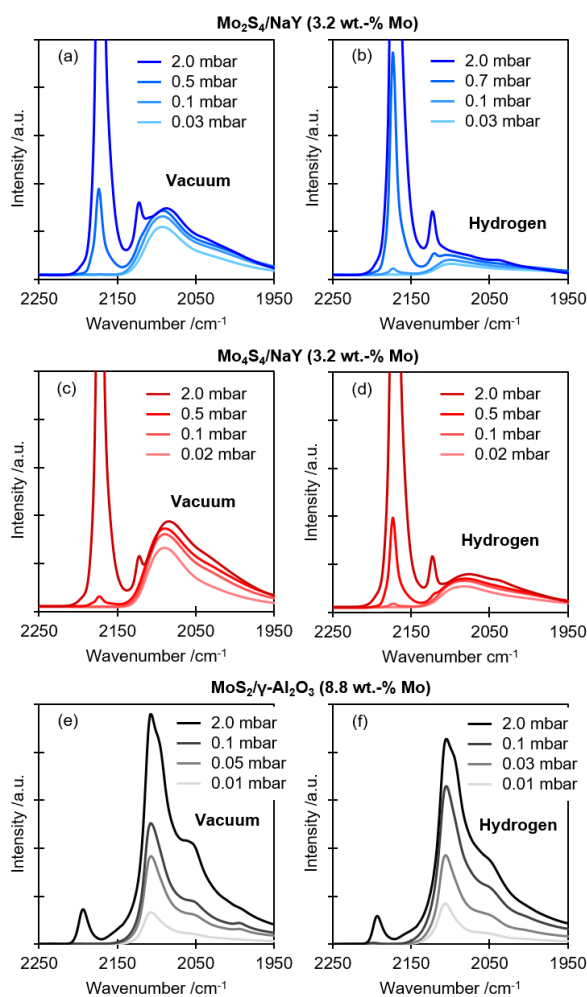


Figure 5.1 IR spectra of adsorbed CO on Mo₂S₄/NaY (top), Mo₄S₄/NaY (middle), and MoS₂/γ-Al₂O₃ (bottom) after quenching to 173 K in vacuum (left) or H₂ (right). All spectra are normalized to catalyst wafer thickness and mass.

We simulated the adsorption of CO on Mo₂S₄ and Mo₄S₄ clusters using DFT. Adsorption of three CO molecules per Mo atom resulted in an octahedral-like coordination environment around the Mo centers (Figure S5.3). This configuration was found to be thermodynamically stable on both clusters (Figure S5.4) thereby confirming the experimental observation that each Mo atom, irrespective of the nuclearity of the cluster it belongs to, can accommodate the same number of CO molecules.

CO binding to the Mo LAS on these NaY-encapsulated Mo_xS_y clusters shows pronounced similarities to CO binding to the nitrogenase enzyme's FeMo-cofactor.^{54,55} In both cases, CO is adsorbed on a metal atom (Mo in our case; Fe in FeMo-cofactor) that itself is coordinated to three non-metallic atoms (S only in our case; S and C in the FeMo-cofactor) in its first coordination shell. The similarity between these systems is especially intriguing, considering that the activity of nitrogenase enzyme for catalytic

hydrogenation of acetylene was shown to be almost completely lost in the presence of CO.⁵⁴ Thus, we hypothesize that the Mo centers are at least part of the active site for ethene hydrogenation on these cluster catalysts.

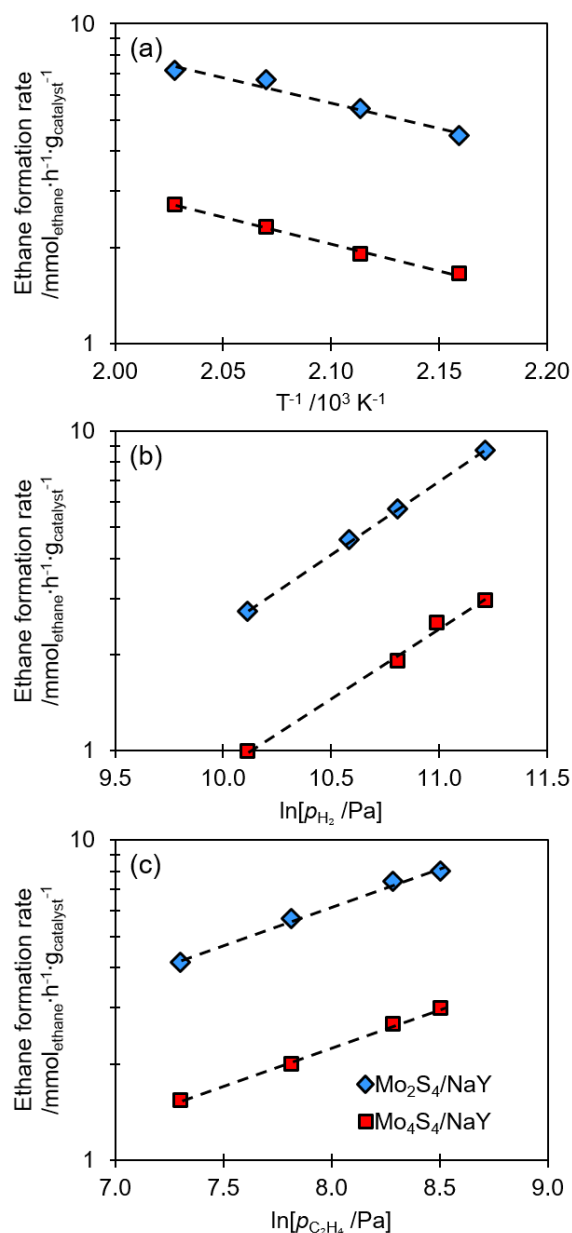


Figure 5.2 (a) Arrhenius-type plots ($T = 463\text{--}493 \text{ K}$, $p_{\text{H}_2} \approx 49 \text{ kPa}$, $p_{\text{C}_2\text{H}_4} \approx 2.5 \text{ kPa}$), and (b,c) steady-state ethane formation rates as a function of H₂ pressure ($T \approx 473 \text{ K}$, $p_{\text{H}_2} = 25\text{--}74 \text{ kPa}$, $p_{\text{C}_2\text{H}_4} \approx 2.5 \text{ kPa}$) and C₂H₄ pressure ($T \approx 473 \text{ K}$, $p_{\text{H}_2} \approx 49 \text{ kPa}$, and $p_{\text{C}_2\text{H}_4} = 1.5\text{--}5 \text{ kPa}$), on representative Mo₂S₄/NaY and Mo₄S₄/NaY catalysts with $\sim 3.2 \text{ wt.-% Mo}$.

For ethene hydrogenation, representative Mo₂S₄/NaY and Mo₄S₄/NaY catalysts (with $\sim 3.2 \text{ wt.-% Mo}$) showed similar apparent activation energies ($31 \pm 1 \text{ kJ}\cdot\text{mol}^{-1}$ on Mo₂S₄/NaY and $32 \pm 3 \text{ kJ}\cdot\text{mol}^{-1}$ on Mo₄S₄/NaY), similar reaction orders of ~ 1.0 in H₂ and ~ 0.5 in C₂H₄ (Figure 5.2), and virtually identical turnover frequencies (discussed

later) indicating that the active sites in both catalysts are catalytically indistinguishable despite different geometries and compositions of the two clusters. It is worth mentioning that X-ray absorption spectroscopy (XAS) measurements verify that the nuclearity of both clusters remains intact under reaction conditions (Section 5.7.11 of the Supplementary Information).

5.2.2 Hydrogen Adsorption

The amount of CO adsorbed on Mo_xS_y clusters, measured as the relative peak area of corresponding IR bands, decreased when either catalyst was exposed to H_2 (Figure 5.3). This suggests that hydrogen is adsorbed on the same site as CO, *i.e.*, the Mo atoms. In contrast, the intensity of the bands associated with CO adsorbed on $\text{MoS}_2/\gamma\text{-Al}_2\text{O}_3$ were unaffected by exposure to H_2 (decrease by only ~5%). This confirms that hydrogen does not bind to Mo but to sulfur atoms at the perimeter, forming SH groups, on the bulk MoS_2 catalysts.^{31,37,38,52}

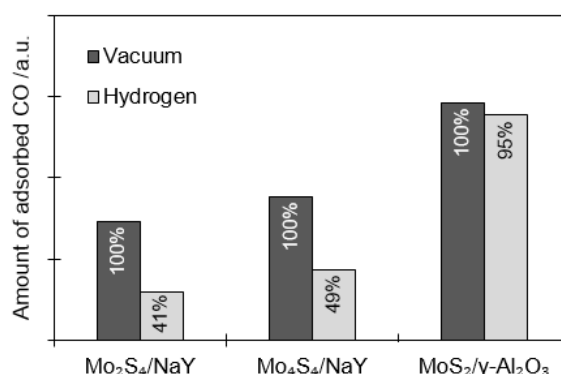


Figure 5.3 Amount of adsorbed CO (normalized to catalyst wafer thickness and mass), measured with IR spectroscopy, on $\text{Mo}_2\text{S}_4/\text{NaY}$, $\text{Mo}_4\text{S}_4/\text{NaY}$, and $\text{MoS}_2/\gamma\text{-Al}_2\text{O}_3$, after quenching in either vacuum or H_2 .

Using 4,6-dimethylpyridine (DMP) to probe weakly Brønsted acidic SH groups *via* IR bands at ~ 1650 and ~ 1625 cm^{-1} (attributed to protonated DMP)^{56,57} we had shown that for Al_2O_3 -supported MoS_2 , the concentration of SH groups increased after exposure to H_2 .⁵⁸ However, for $\text{Mo}_2\text{S}_4/\text{NaY}$ (Figure 5.4) we observed only bands of very low intensity and these bands did not increase after exposure to H_2 . Therefore, we conclude that these small bands result from residual Brønsted acid sites (BAS) of the zeolite support and that the Mo_xS_y nanoclusters do not form Brønsted acidic SH groups. In consequence, we conclude that hydrogen is indeed adsorbed on the Mo atoms of Mo_xS_y clusters.

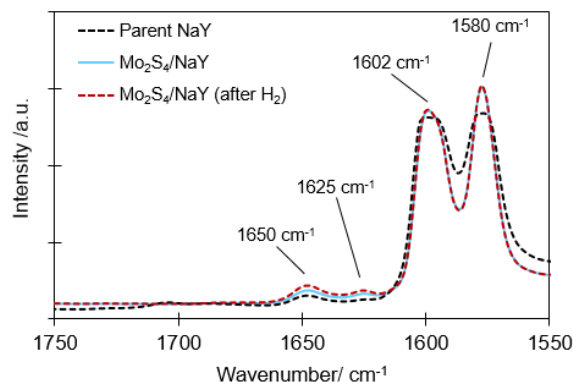


Figure 5.4 IR spectra of adsorbed 4,6-dimethylpyridine (DMP) on $\text{Mo}_2\text{S}_4/\text{NaY}$ (before and after admission of 1 bar H_2) and parent NaY zeolite. The bands at ~ 1650 & ~ 1625 cm^{-1} are assigned to ring vibrations of protonated DMP, the band at ~ 1602 cm^{-1} to weakly physisorbed DMP, and the band at ~ 1580 cm^{-1} to DMP physisorbed/adsorbed on zeolite Lewis acid sites.⁵⁶⁻⁵⁸

To investigate the adsorption structure further, we optimized (with DFT) the geometries of Mo_2S_4 and Mo_4S_4 clusters with hydrogen dissociatively adsorbed at five distinct locations: a single Mo atom, two different Mo atoms, one Mo and one bridging S atom, two bridging S atoms, and a single bridging S atom. The thermodynamically most-stable configuration for both clusters was found to be the one with H_2 dissociatively adsorbed on two different Mo atoms (Figure 5.5(e,f)). This configuration was thermodynamically more stable (Tables S5.3 and S5.6) than the configuration with hydrides stabilized on the same Mo atom (Figure 5.5(c,d)). However, the transition from the configuration with hydrides stabilized on a single Mo atom to separate Mo atoms involved a high free energy barrier on both dimeric and tetrameric Mo_xS_y clusters (Figures S5.6 and S5.8).

These high free energy barriers suggest that even though the thermodynamically most-stable configuration is the one with hydrides stabilized on separate Mo atoms, these states are kinetically not accessible at reaction conditions. Therefore, under typical reaction conditions, H_2 is likely dissociatively adsorbed on the same Mo atom for both Mo_2S_4 and Mo_4S_4 . This adsorbed hydrogen resembles the homolytic H_2 splitting on (noble) metal catalysts^{39,40} and points to the similarity to the FeMo cofactor, which similarly is able to stabilize hydrogen as hydride species.^{34,42,43,59} We speculate that electronic and structural similarities cause this analogous mode of interaction.

Interestingly, in contrast to the remarkable stability of structures that involved the formation of hydride species, configurations with hydrogen stabilized as SH groups (e.g., Figure 5.5 (g,h)) were much less stable (Tables S5.3 and S5.6). For the

tetrameric cluster, it was not even possible to stabilize hydrogen as SH groups without destroying the structural integrity of the cluster.

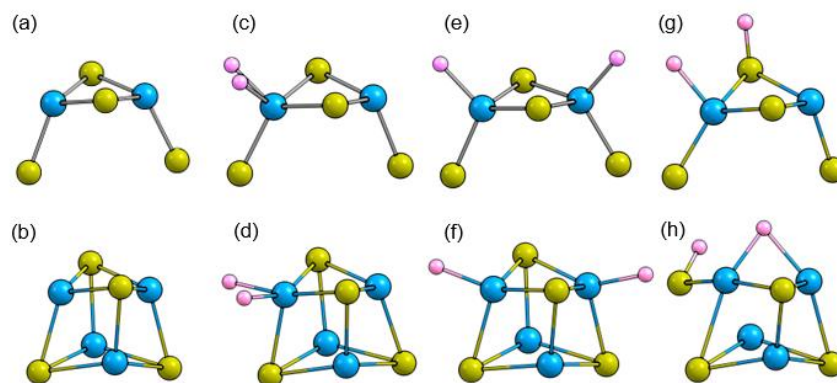


Figure 5.5 B3LYP/def2-TZVP-optimized geometries of bare Mo₂S₄ and Mo₄S₄ clusters (a,b), and configurations involving dissociatively adsorbed H₂ on same Mo atom (c,d), separate Mo atoms (e,f), or one Mo atom and one bridging S atom (g,h). Optimized geometries obtained using PBE0/def2-TZVP were similar. S: yellow; Mo: blue; H: pink.

The difference between hydrogen activation on Mo_xS_y clusters and bulk MoS₂ however cannot be directly linked to the dimension or the nuclearity of the transition metal sulfide phase as hydrogen was proven to be stabilized as SH groups on metal-organic S-bridged Mo dimers.⁶⁰ Therefore, the key difference has to lie within the electronic properties, and more specifically the electron density (or reducibility) of the involved Mo centers. Stabilization of hydrogen in the form of protons is formally an oxidation process and, therefore, requires reduction of the Mo centers.⁶¹ DFT calculations suggested that stabilization of hydrogen as SH groups resulted in electron density transfer from the H to the Mo_xS_y cluster. In contrast, stabilization of hydrogen as hydride species on Mo resulted in electron density transfer from the cluster to the H adatoms (Tables S5.5 and S5.8).

Our DFT models predict that a higher electron density on Mo should favor hydride formation, while a lower electron density on Mo atoms should favor sulfhydryl formation. In the case of extended MoS₂ slabs, upon formation of SH groups, the resulting electron density transfer from hydrogen is likely compensated by multiple Mo atoms and, thus, SH groups as a final state are thermodynamically feasible. DFT calculations additionally predict a barrier-less transfer of adsorbed hydrogen from Mo centers to the neighboring S atoms.^{31,37,38,62} In the case of zeolite-encapsulated Mo_xS_y nanoclusters, on the other hand, we hypothesize that the more covalent character of Mo-S bonds prevents reduction of these Mo centers perhaps due to a higher local

electron density on the Mo atoms.^{46,63} For this reason, stabilization of hydrogen as hydride species on these molecular clusters is thermodynamically favored over sulfhydryl group formation. It must be noted in passing that these findings are related to the difference between Molybdenum and Ruthenium sulfide phases for hydrogen binding using inelastic neutron scattering. Sulfhydryl groups were the single hydrogen species on MoS₂ slabs, while a mixture of SH groups and hydride species on the metal atoms of a more metallic RuS₂ phase were observed.⁶⁴

5.2.3 Adsorption of Multiple H₂

As both dimeric and tetrameric Mo_xS_y clusters comprise of multiple Mo atoms, which could potentially adsorb more than one H₂, we simulated the adsorption of multiple H₂ on both dimeric and tetrameric clusters (Section S5.7.6 of the Supplementary Information).

For Mo₂S₄, stable geometries for cases with two dissociatively adsorbed H₂ molecules could not be achieved. The second H₂ could only be stabilized as physisorbed species. For Mo₄S₄, on the other hand, stable geometries could be achieved for clusters accommodating more than one H₂ molecule (Figure S5.9). At 473 K, adsorption of more than one H₂, however, was thermodynamically unfavorable (Figure 5.6 and Table S5.9). We conclude, therefore, that, at typical reaction temperature, both clusters can only stabilize a single dissociatively adsorbed H₂, thereby acting as one hydrogenation site. Consequentially, the number of Mo_xS_y clusters must be the basis for calculating the turnover frequency for ethene hydrogenation. Applying this for a series of Mo_xS_y/NaY catalysts with varying Mo loading, we observed, as predicted, a constant turnover frequency of $24.7 \pm 3.3 \text{ mol}_{\text{ethane}} \cdot \text{h}^{-1} \cdot \text{mol}_{\text{cluster}}^{-1}$ (Figure 5.7). It must be noted that a Mo loading of ~9.7 wt.-% corresponds to ~1.6 Mo atoms or ~0.8 Mo₂S₄ clusters per NaY zeolite supercage.

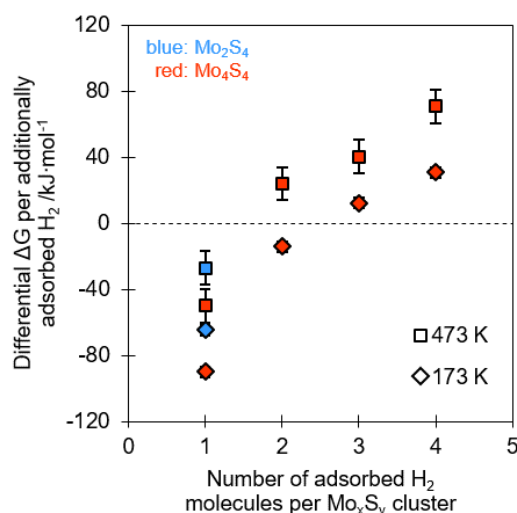


Figure 5.6 Differential free energy change per additionally adsorbed H₂ on Mo₂S₄ and Mo₄S₄ clusters, computed at T = 473 K and T = 173 K. The error bars correspond to $\pm\frac{1}{2}D$ gas-phase translational entropy of H₂.

Interestingly, the spin-multiplicity of (thermodynamically most-stable) Mo₄S₄ structure decreased from $\omega = 5$ (*i.e.*, four unpaired electrons) for the bare Mo₄S₄ cluster, to $\omega = 3$ (*i.e.*, two unpaired electrons) for the Mo₄S₄ cluster with one adsorbed H₂, and finally to $\omega = 1$ (*i.e.*, no unpaired electrons) for the Mo₄S₄ cluster with two adsorbed H₂ (Tables S5.9 and S5.10). Similarly, the spin-multiplicity of the dimeric cluster also decreased from $\omega = 3$ (*i.e.*, two unpaired electrons) for the bare Mo₂S₄ cluster, to $\omega = 1$ (*i.e.*, no unpaired electrons) for the Mo₂S₄ cluster with one adsorbed H₂ molecule (Table S5.3). Based on these observations we hypothesize that the unpaired electrons on Mo atoms likely interact with hydrogen species upon adsorption.

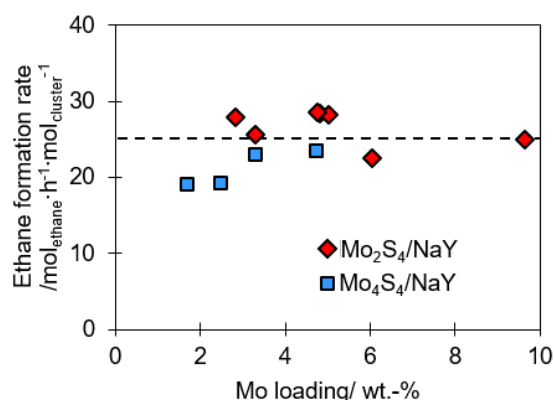


Figure 5.7 Steady-state ethane formation rates, normalized per cluster, on Mo₂S₄/NaY and Mo₄S₄/NaY catalysts with increasing Mo loading. Reaction conditions: T \approx 473 K, p_{H₂} \approx 96 kPa, and p_{C₂H₄} \approx 5 kPa.

5.2.4 Ethene Adsorption

Figure 5.8 shows the IR spectra of adsorbed CO on $\text{Mo}_x\text{S}_y/\text{NaY}$ catalysts after quenching to 173 K in ethene atmosphere. Quantitative analysis of the IR spectra shows that the concentration of CO adsorbed on Mo Lewis acid sites was reduced to ~14% on $\text{Mo}_2\text{S}_4/\text{NaY}$ and to ~11% on $\text{Mo}_4\text{S}_4/\text{NaY}$ after equilibration with ethene at 173 K (Figure 5.9 and Table S5.2). This suggests that in the presence of ethene a significantly higher fraction of Mo (as compared to the experiments with H_2 pretreatment) becomes inaccessible to CO, thereby suggesting that the coverage of ethene must be higher than that of hydrogen on Mo under the tested conditions.

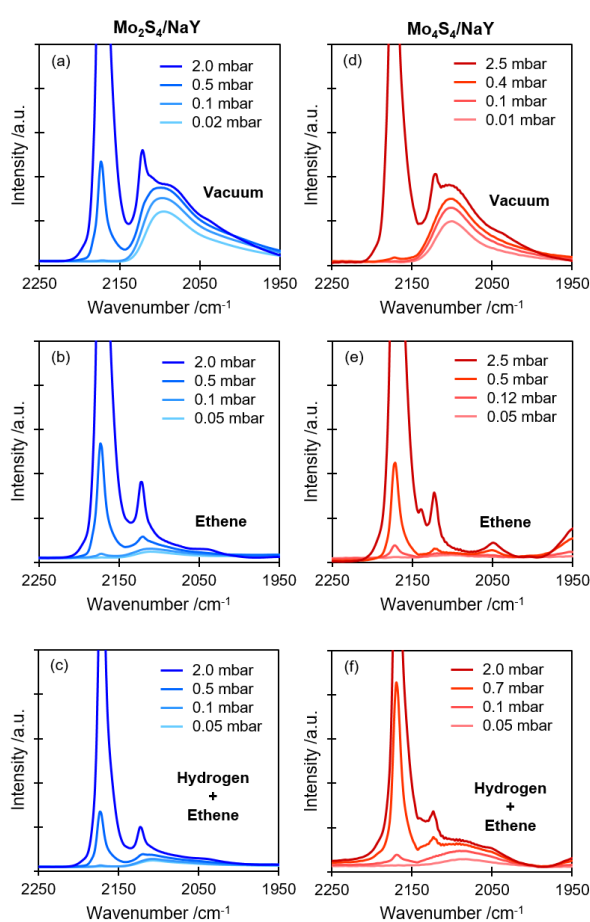


Figure 5.8 IR spectra of adsorbed CO on $\text{Mo}_2\text{S}_4/\text{NaY}$ (left) and $\text{Mo}_4\text{S}_4/\text{NaY}$ (right) after quenching to 173 K in vacuum (top), ethene (middle), or a mixture of hydrogen and ethene (bottom). All spectra are normalized to catalyst wafer thickness and mass.

DFT calculations of the adsorption of ethene on Mo_2S_4 and Mo_4S_4 (Sections 5.7.7 and 5.7.8 of the Supplementary Information) showed that ethene could not be stabilized on the S atoms of Mo_xS_y clusters, but only on Mo atoms. However, in contrast

to hydrogen adsorption, adsorption of multiple ethene molecules was thermodynamically favored on both Mo_2S_4 and Mo_4S_4 (Figure 5.10).

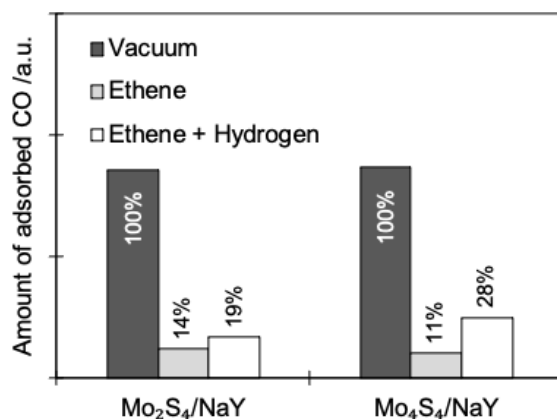


Figure 5.9 Amount of adsorbed CO (normalized to catalyst wafer thickness and mass), measured with IR spectroscopy, on $\text{Mo}_2\text{S}_4/\text{NaY}$ and $\text{Mo}_4\text{S}_4/\text{NaY}$, after quenching in vacuum, ethene, or a mixture of ethene and hydrogen.

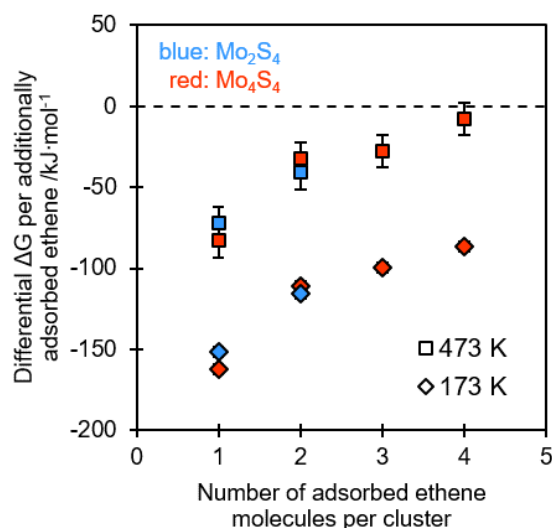


Figure 5.10 Differential free energy change per additionally adsorbed ethene molecule on Mo_2S_4 and Mo_4S_4 clusters, computed at $T = 473$ K and $T = 173$ K. The error bars correspond to $\pm 1/2 D$ gas-phase translational entropy of ethene.

Based on free energy calculations at 173 and 473 K, the configurations with two chemisorbed ethene molecules on Mo_2S_4 (Figure 5.11a), and four chemisorbed ethene molecules on Mo_4S_4 (Figure 5.11c), were thermodynamically most favored. The differential standard free energy change, however, decreased with the adsorption of each additional ethene molecule. DFT therefore predicts that, for CO adsorption experiments, a significant fraction of Mo atoms is expected to be covered by ethene. This prediction agrees with IR spectroscopy measurements that showed that $\sim 86\%$

and ~89% of Mo atoms were inaccessible to CO once the cluster had been in contact with ethene (Figure 5.9 and Table S5.2).

5.2.5 Competitive Adsorption Between Ethene and Hydrogen

Using IR spectroscopy and DFT calculations we showed above that both H₂ and ethene are adsorbed on the Mo atoms of the Mo_xS_y clusters. As both ethene and H₂ are simultaneously present during ethene hydrogenation and compete for the same sites, we turned to the IR spectra of adsorbed CO after quenching the samples to 173 K in a typical reaction mixture containing ~960 mbar bar H₂ and ~50 mbar ethene resulting in blocking of ~81% Mo sites for Mo₂S₄/NaY and ~72% Mo sites for Mo₄S₄/NaY (Figure 5.9 and Table S5.2).

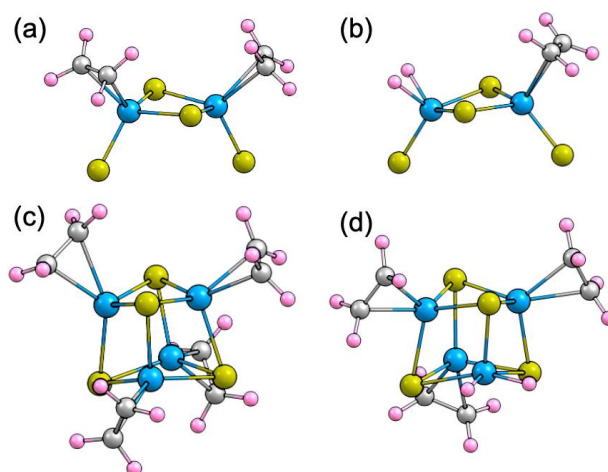


Figure 5.11 DFT/B3LYP/def2-TZVP-optimized geometries of Mo₂S₄ cluster with (a) two adsorbed ethene molecules, and (b) one ethene and one hydrogen molecule, and Mo₄S₄ cluster with (c) four adsorbed ethene molecules, and (d) one hydrogen and three ethene molecules. S: yellow; Mo: blue; C: grey; H: pink.

DFT (Sections S5.7.9 and S5.7.10 of the Supplementary Information) showed that the standard free energy of the Mo₂S₄ cluster with one ethene molecule and one H₂ molecule adsorbed on different Mo atoms (Figure 5.11b) was thermodynamically less stable than the thermodynamically most-stable configuration with two adsorbed ethene molecules (Figure 5.11a).

Similarly, for the tetrameric cluster, the configuration with one hydrogen and three ethene molecules adsorbed on separate Mo atoms (Figure 5.11d) was higher in free energy in comparison to the thermodynamically most-stable configuration with four adsorbed ethene molecules (Figure 5.11c). As this holds true at 173 K as well as at 473 K, we conclude that the clusters with at least one dissociatively adsorbed H₂ (*i.e.*,

the ones likely functioning as starting point for hydrogenation) are a minority species under reaction conditions. Note that this agrees well with the fact that ethene hydrogenation had a first order pressure dependence in H_2 on both Mo_2S_4/NaY and Mo_4S_4/NaY catalysts (Figure 5.2b).

Given the large distance between Mo atoms on Mo_xS_y clusters, and consequentially between the reactants adsorbed on these sites, (Figure 5.11 (b,d)), we hypothesize that the reaction between adsorbed ethene and adsorbed H_2 species to form ethane, *i.e.*, Langmuir-Hinshelwood (LH) type mechanism, is unlikely. We instead propose that the reaction proceeds *via* an Eley-Rideal (ER) type mechanism, wherein ethene weakly adsorbed in the zeolite pores reacts with an adsorbed hydrogen. The fractional reaction order in ethene (instead of unity as expected for ER type reactions), is attributed to the negative influence of the ethene partial pressure on the hydrogen coverage with both ethene and hydrogen competing for the same sites.

DFT simulations for LH-type (involving an adsorbed H_2 and an adsorbed ethene) and ER-type (involving as adsorbed H_2 and a gas-phase ethene) reaction pathways on the Mo_2S_4 cluster are presented in Section S5.7.12 of the Supplementary Information. The standard enthalpic barriers for the LH-type reaction pathway were computed to be higher than that for the ER-type reaction pathway (Figures S5.15 and S5.16). The DFT calculations, therefore, support our hypothesis that ER-type reaction mechanism (as opposed to LH-type reaction mechanism) likely proceeds on these zeolite pore stabilized molybdenum sulfide clusters.

5.3 Conclusions

NaY zeolite-encapsulated Mo_xS_y clusters adsorb H_2 dissociatively, binding both H atoms to a single Mo atom. DFT calculations suggest that this adsorption structure is caused by a high barrier to distribute the H atoms evenly among all Mo atoms of the cluster. Adsorption of hydrogen as hydrides contrasts the stabilization of hydrogen as sulfhydryl groups on the edge of conventional MoS_2 slabs. The difference is attributed to the easier reducibility of Mo in the larger MoS_2 slabs.

Both dimeric and tetrameric Mo_xS_y cluster catalysts show stable rates of hydrogenation scaling with the concentration of clusters in the catalyst, independent of the cluster nuclearity. This is also reflected by DFT calculations indicating that only one hydrogen can be dissociatively adsorbed per cluster under reaction conditions. The nature of the active site, is concluded to be identical for both clusters, *i.e.*, a single Mo center, as demonstrated by constant activation energies and reaction orders in H_2 and ethene on both $\text{Mo}_2\text{S}_4/\text{NaY}$ and $\text{Mo}_4\text{S}_4/\text{NaY}$ catalysts.

Thus, experiments and theory suggest jointly that active sites in both dimeric and tetrameric catalysts are catalytically indistinguishable for ethene hydrogenation. Theory and experiment also show that ethene, H_2 , and CO, competitively adsorb on Mo similarly to the situation reported for the FeMo sulfide cluster in nitrogenase. As ethene adsorbs more strongly than H_2 on both cluster catalysts, it is predicted to be the most abundant surface species under reaction conditions. Ethene hydrogenation is postulated to proceed *via* Eley-Rideal type mechanism, with a weakly adsorbed ethene in the zeolite pores reacting with an adsorbed hydrogen. The reaction between adsorbed ethene and adsorbed hydrogen, *i.e.*, the Langmuir-Hinshelwood type pathway, was found to have a high enthalpic barrier owing to large distance between the Mo atoms in these clusters.

5.4 Experimental and Computational Methods

5.4.1 Catalyst Precursor Preparation

MoS₂/γ-Al₂O₃ catalyst precursors were prepared by incipient wetness impregnation of γ-Al₂O₃ (provided by the Chevron company) with ammonium heptamolybdate (99.98% purity; Sigma-Aldrich) solution of appropriate concentration. The impregnated sample was dried at 383 K overnight followed by calcination in 100 mL·min⁻¹ synthetic air (temperature ramp: 5 K·min⁻¹ to 673 K, hold for 2 h).

Carbonyl-based catalyst precursors were prepared by chemical vapor deposition (CVD). Approximately 200 mg NaY (Zeolyst CBV100; Si/Al ~2.5; pelletized and sieved to 250-355 μm) were treated under reduced pressure (10⁻² mbar) at elevated temperatures (temperature ramp: 5 K·min⁻¹ to 408 K, held for 2 h; 5 K·min⁻¹ to 503 K, held for 2 h; 5 K·min⁻¹ to 653 K, held for 1 h) to carefully remove adsorbed water. Molybdenum hexacarbonyl (>99.9% purity; Sigma-Aldrich) was loaded on the dried zeolite at room temperature under static conditions for a defined amount of time. In the final step, the catalyst precursors were treated under reduced pressure (10⁻² mbar) for 10 min to remove physisorbed Mo(CO)₆. All carbonyl-based precursors were stored in a glovebox to avoid exposure to air/moisture at any time.

5.4.2 Catalyst Preparation

MoS₂/γ-Al₂O₃ and NaY-encapsulated cluster catalysts were prepared in a lab-scale plug flow reactor (quartz glass tube; 4 mm i.d.). Bronkhorst mass flow controllers were used to regulate gas flow rates. To avoid formation of hotspots, all precursors were diluted 1/10 in SiC (sieved to 500-1000 μm) and placed in the quartz tube supported with quartz wool on both sides. The precursors prepared *via* incipient wetness impregnation were sulfided in a stream of 20 mL·min⁻¹ H₂S (10% v/v in H₂) at ambient pressure (temperature ramp: 5 K·min⁻¹ to 673 K, held for 16 h). Precursors prepared *via* CVD were also sulfided in a flow of 20 mL·min⁻¹ H₂S (10% v/v in H₂) at ambient pressure (temperature ramp: 5 K·min⁻¹ to 673 K, held for 2 h) to form sulfided Mo_xS_y/NaY catalyst (previously shown to be primarily comprised of dimeric Mo₂S₄ clusters and denoted further as Mo₂S₄/NaY).⁴⁶ The Mo₂S₄/NaY catalyst was then treated in a stream of pure H₂ (temperature ramp: 5 K·min⁻¹ to 673 K, held for 2 h) to obtain the reduced Mo_xS_y/NaY catalyst (previously shown to be primarily comprised of

tetrameric Mo₄S₄ clusters and denoted further as Mo₄S₄/NaY).⁴⁶ After thermal treatments, all catalysts were purged with N₂ for 30 min prior to any catalytic reactions.

5.4.3 Catalytic Reactions

All catalytic reactions were also performed in the lab-scale plug flow reactor. Ethene hydrogenation was studied at ~473 K and ambient pressure with a H₂/ethene volumetric ratio of ~20. The product stream composition was analyzed by online gas chromatography using an Agilent 7890B GC. Ethane formation rates were determined using space-time yields under differential conditions after the catalysts reached a stable steady state (after ~24 h). External mass transport limitations have been excluded for the applied reaction conditions by varying the amount of loaded catalyst and its particle size. Limitations by internal mass transport were excluded owing to the small size of Mo_xS_y clusters (~5 Å for Mo₄S₄) and reactants/products in comparison to the diameter of the NaY zeolite supercages (~12 Å) and the pore openings (~7 Å).

5.4.4 Infrared (IR) Spectroscopy of Adsorbed Probe Molecules

IR spectroscopy of adsorbed probe molecules was performed using a Nicolet 6700 IR spectrometer with a resolution of 4 cm⁻¹. The catalyst materials were ground and pressed into self-supporting wafers (~5 mg·cm⁻²). The catalyst wafers were first sulfided/reduced in a stream of 20 mL·min⁻¹ H₂S (10% v/v in H₂) or 20 mL·min⁻¹ H₂ at ambient pressure (temperature ramp: 5 K·min⁻¹ to 673 K, held for 2 h). Then, for activation, a treatment in H₂ (4 cycles, total of 24 h) at 473 K each followed by evacuation at 10⁻⁶ mbar for 30 min was applied to all samples.

CO adsorption was performed on activated samples after cooling to 173 K using liquid nitrogen. The samples were examined after cooling in either H₂, ethene, a mixture of H₂ and ethene, or high vacuum. In a first run, after cooling to 173 K (by skipping the last evacuation cycle) in either H₂, ethene, or a mixture of H₂ and ethene, CO adsorption isotherms were obtained by applying controlled doses of CO ranging from 0.01 to 2 mbar. After this, CO and other adsorbed gases were desorbed at room temperature under high vacuum (10⁻⁷ mbar). Subsequently, the samples were thermally treated at 473 K for 1 h and cooled down to 173 K again under high vacuum (10⁻⁷ mbar) before the second run of CO adsorption. Possible errors caused by different thicknesses of the catalyst wafers are prevented in this procedure as multiple series of measurements are conducted on the same wafer. In lieu of molar extinction

coefficients for bands of CO adsorbed on cluster catalysts, we analyzed the areas normalized to wafer thickness for all experiments.

IR spectroscopy of adsorbed 4,6-dimethylpyridine (DMP) was performed on the activated samples at 323 K by applying small doses of DMP (up to 0.5 mbar) into the IR cell and equilibrating for 0.5 h. A second spectrum was taken after exposing the catalyst to an additional ~1 bar of H₂ and equilibrating for another 0.5 h.

All IR spectra were background corrected using OMNIC software package and are presented as difference spectra against the reference spectra at 10⁻⁷ mbar.

5.4.5 Computational Details

Unrestricted Kohn Sham (UKS) DFT calculations were performed on gas-phase Mo_xS_y clusters using the Orca quantum chemistry package version 4.2.⁶⁵⁻⁶⁷ The calculations were performed using two hybrid exchange-correlational functionals: B3LYP and PBE0. Relativistic effects were taken into account by zeroth-order regular relativistic approximations (ZORA), and Grimme's atom-pairwise dispersion correction with the Becke-Johnson damping scheme (D3BJ) was used for dispersion corrections.⁶⁸⁻⁷⁰ Relativistically recontracted versions of the all-electron Ahlrichs def2 basis sets with triple zeta polarization functions, ZORA-def2-TZVP, were employed for geometry optimization and vibrational frequency calculations, while ZORA-def2-TZVPP basis-sets were employed for single-point energy (SPE) calculations.⁷¹ The hybrid functionals were employed with RIJCOSX approximation to speed up the calculations and general auxiliary basis sets SARC/J were used for this purpose.⁷²⁻⁷⁷ The RIJCOSX approach incorporates the resolution-of-identity (RI) approximation for the evaluation of the Coulomb matrices and the chain-of-spheres algorithm for the formation of the exchange-type matrices.⁷⁸⁻⁸⁰ The core electrons (1s²2s²2p⁶3s²3p⁶3d¹⁰ for Mo, 1s²2s²2p⁶ for S, 1s² for C, and none for H) were kept frozen during geometry optimization and vibrational frequency calculations. The Hirshfeld charge populations and Mayer bond-orders were computed for the optimized geometries. Standard thermodynamics equations were used for computing the free energy and free enthalpy of different structures and the methodology is presented in detail in Section 5.7.1 of the Supplementary Information.

5.5 Acknowledgements

The authors thank Dr. A. Kuperman and Dr. A. Brait (Chevron), and Prof. Takeshi Kubota (Shimane University, Japan) for fruitful discussions. J. A. L. was supported by the U.S. Department of Energy (DOE), Office of Science, Office of Basic Energy Sciences, Division of Chemical Sciences, Geosciences and Biosciences (Transdisciplinary Approaches to Realize Novel Catalytic Pathways to Energy Carriers, FWP 47319). The authors gratefully acknowledge the Leibniz Supercomputing Center for funding this project by providing computing time on their Linux-Cluster. The XAS measurements were performed at the P65 beamline of DESY (Hamburg, Germany), a member of the Helmholtz Association HGF, as a part of the proposal I-20200919. The authors would like to acknowledge support from Dr. Edmund Welter and other staff from the P65 beamline.

Contributions

R. Khare and R. Weindl contributed equally. R. Weindl, R. Khare, H. Shi, and J. A. Lercher conceived the idea of this work. R. Weindl conducted synthesis, characterization and kinetic evaluation of the presented materials. R. Khare contributed XAS/XES measurements and interpretation as well as DFT calculations. A. Jentys assisted in interpretation of spectroscopic data, and K. Reuter assisted in evaluation of results obtained from DFT calculations. The manuscript was written through contributions of all authors. All authors have given approval to the final version of the manuscript.

5.6 References

- (1) Mao, J.; Wang, Y.; Zheng, Z.; Deng, D. *Frontiers of Physics* **2018**, *13*, 1.
- (2) Prins, R. In *Handbook of Heterogeneous Catalysis*; Ertl, G., Knözinger, H., Schüth, F., Weitkamp, J., Eds.; John Wiley & Sons: 2008, p 2695.
- (3) Weisser, O.; Landa, S. *Sulphide catalysts, their properties and applications*; Elsevier, 2013.
- (4) Topsøe, H.; Clausen, B. S. *Catalysis Reviews* **1984**, *26*, 395.
- (5) Chianelli, R. R.; Berhault, G.; Torres, B. *Catalysis Today* **2009**, *147*, 275.
- (6) Eijsbouts, S.; Mayo, S. W.; Fujita, K. *Applied Catalysis A: General* **2007**, *322*, 58.
- (7) Prins, R.; Egorova, M.; Röthlisberger, A.; Zhao, Y.; Sivasankar, N.; Kukula, P. *Catalysis Today* **2006**, *111*, 84.
- (8) Mortensen, P. M.; Grunwaldt, J.-D.; Jensen, P. A.; Knudsen, K. G.; Jensen, A. D. *Applied Catalysis A: General* **2011**, *407*, 1.
- (9) Wang, H.; Male, J.; Wang, Y. *Acs Catalysis* **2013**, *3*, 1047.
- (10) Laurenti, D.; Afanasiev, P.; Geantet, C. *Applied Catalysis B: Environmental* **2011**, *101*, 239.
- (11) Hou, P.; Meeker, D.; Wise, H. *Journal of Catalysis* **1983**, *80*, 280.
- (12) Lund, C. R. F. *Industrial & Engineering Chemistry Research* **1996**, *35*, 3067.
- (13) Hu, J.; Yu, L.; Deng, J.; Wang, Y.; Cheng, K.; Ma, C.; Zhang, Q.; Wen, W.; Yu, S.; Pan, Y. *Nature Catalysis* **2021**, *4*, 242.
- (14) Taniguchi, M.; Ishii, Y.; Murata, T.; Tatsumi, T.; Hidai, M. *Journal of the Chemical Society, Chemical Communications* **1995**, 2533.
- (15) Zhu, Q.; Wegener, S. L.; Xie, C.; Uche, O.; Neurock, M.; Marks, T. J. *Nature Chemistry* **2013**, *5*, 104.
- (16) Santos, V. P.; Van Der Linden, B.; Chojecki, A.; Budroni, G.; Corthals, S.; Shibata, H.; Meima, G. R.; Kapteijn, F.; Makkee, M.; Gascon, J. *ACS Catalysis* **2013**, *3*, 1634.
- (17) Hinnemann, B.; Moses, P. G.; Bonde, J.; Jørgensen, K. P.; Nielsen, J. H.; Horch, S.; Chorkendorff, I.; Nørskov, J. K. *Journal of the American Chemical Society* **2005**, *127*, 5308.
- (18) Jaramillo, T. F.; Jørgensen, K. P.; Bonde, J.; Nielsen, J. H.; Horch, S.; Chorkendorff, I. *science* **2007**, *317*, 100.
- (19) Li, P.; Yang, Z.; Shen, J.; Nie, H.; Cai, Q.; Li, L.; Ge, M.; Gu, C.; Chen, X. a.; Yang, K.; Zhang, L.; Chen, Y.; Huang, S. *ACS Applied Materials & Interfaces* **2016**, *8*, 3543.
- (20) Tran, P. D.; Tran, T. V.; Orto, M.; Torelli, S.; Truong, Q. D.; Nayuki, K.; Sasaki, Y.; Chiam, S. Y.; Yi, R.; Honma, I. *Nature materials* **2016**, *15*, 640.
- (21) Wang, H.; Tsai, C.; Kong, D.; Chan, K.; Abild-Pedersen, F.; Nørskov, J. K.; Cui, Y. *Nano Research* **2015**, *8*, 566.
- (22) Helveg, S.; Lauritsen, J. V.; Laegsgaard, E.; Stensgaard, I.; Nørskov, J. K.; Clausen, B. S.; Topsøe, H.; Besenbacher, F. *Physical Review Letters* **2000**, *84*, 951.
- (23) Kisielowski, C.; Ramasse, Q. M.; Hansen, L. P.; Brorson, M.; Carlsson, A.; Molenbroek, A. M.; Topsøe, H.; Helveg, S. *Angewandte Chemie International Edition* **2010**, *49*, 2708.
- (24) Bouwens, S. M. A. M.; Van Veen, J. A. R.; Koningsberger, D. C.; De Beer, V. H. J.; Prins, R. *The Journal of Physical Chemistry* **1991**, *95*, 123.
- (25) Wagenhofer, M. F.; Shi, H.; Gutiérrez, O. Y.; Jentys, A.; Lercher, J. A. *Science advances* **2020**, *6*, eaax5331.
- (26) Oliviero, L.; Travert, A.; Garcia, E. D.; Chen, J.; Maugé, F. *Journal of Catalysis* **2021**, Article ASAP.
- (27) Vogelgsang, F.; Shi, H.; Lercher, J. A. *Journal of Catalysis* **2021**, Article ASAP.
- (28) Casalongue, H. G. S.; Benck, J. D.; Tsai, C.; Karlsson, R. K. B.; Kaya, S.; Ng, M. L.; Pettersson, L. G. M.; Abild-Pedersen, F.; Nørskov, J. K.; Ogasawara, H. *The Journal of Physical Chemistry C* **2014**, *118*, 29252.
- (29) Gaur, A.; Hartmann Dabros, T. M.; Høj, M.; Boubnov, A.; Prüssmann, T.; Jelic, J.; Studt, F.; Jensen, A. D.; Grunwaldt, J.-D. *ACS Catalysis* **2019**, *9*, 2568.
- (30) Šarić, M.; Rossmeisl, J.; Moses, P. G. *Journal of Catalysis* **2018**, *358*, 131.

- (31) Byskov, L. S.; Bollinger, M.; Nørskov, J. K.; Clausen, B. S.; Topsøe, H. *Journal of Molecular Catalysis A: Chemical* **2000**, *163*, 117.
- (32) Einsle, O.; Tezcan, F. A.; Andrade, S. L.; Schmid, B.; Yoshida, M.; Howard, J. B.; Rees, D. C. *Science* **2002**, *297*, 1696.
- (33) Howard, J. B.; Rees, D. C. *Chemical reviews* **1996**, *96*, 2965.
- (34) Hoeke, V.; Tociu, L.; Case, D. A.; Seefeldt, L. C.; Raugei, S.; Hoffman, B. M. *Journal of the American Chemical Society* **2019**, *141*, 11984.
- (35) Weigand, W.; Schollhammer, P. *Bioinspired catalysis: metal-sulfur complexes*; John Wiley & Sons, 2014.
- (36) Taniguchi, M.; Imamura, D.; Ishige, H.; Ishii, Y.; Murata, T.; Hidai, M.; Tatsumi, T. *Journal of Catalysis* **1999**, *187*, 139.
- (37) Hensen, E. J. M.; Lardinois, G. M. H. J.; de Beer, V. H. J.; van Veen, J. A. R.; van Santen, R. A. *Journal of Catalysis* **1999**, *187*, 95.
- (38) Breyse, M.; Furimsky, E.; Kasztelan, S.; Lacroix, M.; Perot, G. *Catalysis Reviews* **2002**, *44*, 651.
- (39) Makolkin, N. V.; Kim, H. U.; Paukshtis, E. A.; Jae, J.; Bal'zhinimaev, B. S. *Catalysis in Industry* **2020**, *12*, 316.
- (40) Möbus, K.; Grünewald, E.; Wieland, S. D.; Parker, S. F.; Albers, P. W. *Journal of Catalysis* **2014**, *311*, 153.
- (41) Doan, P. E.; Telser, J.; Barney, B. M.; Igarashi, R. Y.; Dean, D. R.; Seefeldt, L. C.; Hoffman, B. M. *Journal of the American Chemical Society* **2011**, *133*, 17329.
- (42) Igarashi, R. Y.; Laryukhin, M.; Dos Santos, P. C.; Lee, H.-I.; Dean, D. R.; Seefeldt, L. C.; Hoffman, B. M. *Journal of the American Chemical Society* **2005**, *127*, 6231.
- (43) Van Stappen, C.; Davydov, R.; Yang, Z.-Y.; Fan, R.; Guo, Y.; Bill, E.; Seefeldt, L. C.; Hoffman, B. M.; DeBeer, S. *Inorganic Chemistry* **2019**, *58*, 12365.
- (44) Okamoto, Y. *Bulletin of the Chemical Society of Japan* **2014**, *87*, 20.
- (45) Okamoto, Y.; Katsuyama, H.; Yoshida, K.; Nakai, K.; Matsuo, M.; Sakamoto, Y.; Yu, J.; Terasaki, O. *Journal of the Chemical Society, Faraday Transactions* **1996**, *92*, 4647.
- (46) Weindl, R.; Khare, R.; Kovarik, L.; Jentys, A.; Reuter, K.; Shi, H.; Lercher, J. A. *Angewandte Chemie International Edition* **2021**, *60*, 9301.
- (47) Topsøe, H.; Clausen, B. S.; Massoth, F. E. In *Catalysis*; Springer: Berlin, 1996, p 1.
- (48) Guichard, B.; Roy-Auberger, M.; Devers, E.; Pichon, C.; Legens, C. *Applied Catalysis A: General* **2009**, *367*, 9.
- (49) Zhang, H.; Lin, H.; Zheng, Y. *Carbon Resources Conversion* **2020**, *3*, 60.
- (50) Travert, A.; Dujardin, C.; Maugé, F.; Cristol, S.; Paul, J. F.; Payen, E.; Bougeard, D. *Catalysis Today* **2001**, *70*, 255.
- (51) Dujardin, C.; Lérias, M. A.; van Gestel, J.; Travert, A.; Duchet, J. C.; Maugé, F. *Applied Catalysis A: General* **2007**, *322*, 46.
- (52) Schachtl, E.; Zhong, L.; Kondratieva, E.; Hein, J.; Gutiérrez, O. Y.; Jentys, A.; Lercher, J. A. *ChemCatChem* **2015**, *7*, 4118.
- (53) Hadjiivanov, K.; Knözinger, H. *Chemical physics letters* **1999**, *303*, 513.
- (54) Spatzal, T.; Perez, K. A.; Einsle, O.; Howard, J. B.; Rees, D. C. *Science* **2014**, *345*, 1620.
- (55) Buscagan, T. M.; Perez, K. A.; Maggiolo, A. O.; Rees, D. C.; Spatzal, T. *Angewandte Chemie International Edition* **2021**, *133*, 5768.
- (56) Travert, A.; Maugé, F. In *Studies in surface science and catalysis*; Elsevier: 1999; Vol. 127, p 269.
- (57) Oliviero, L.; Vimont, A.; Lavalley, J.-C.; Sarria, F. R.; Gaillard, M.; Maugé, F. *Physical Chemistry Chemical Physics* **2005**, *7*, 1861.
- (58) Schachtl, E.; Kondratieva, E.; Gutiérrez, O. Y.; Lercher, J. A. *The Journal of Physical Chemistry Letters* **2015**, *6*, 2929.
- (59) Lukoyanov, D. A.; Khadka, N.; Yang, Z.-Y.; Dean, D. R.; Seefeldt, L. C.; Hoffman, B. M. *Inorganic Chemistry* **2018**, *57*, 6847.
- (60) DuBois, M. R.; VanDerveer, M. C.; DuBois, D. L.; Haltiwanger, R. C.; Miller, W. K. *Journal of the American Chemical Society* **1980**, *102*, 7456.

- (61) Jones, L. O.; Mosquera, M. A.; Ratner, M. A.; Schatz, G. C. *ACS Applied Materials & Interfaces* **2020**, *12*, 4607.
- (62) Byskov, L. S.; Nørskov, J. K.; Clausen, B. S.; Topsøe, H. *Journal of Catalysis* **1999**, *187*, 109.
- (63) Singh, D. M. D. J.; Pradeep, T.; Bhattacharjee, J.; Waghmare, U. *The Journal of Physical Chemistry A* **2005**, *109*, 7339.
- (64) Lacroix, M.; Jobic, H.; Dumonteil, C.; Afanasiev, P.; Breysse, M.; Kasztelan, S. In *Studies in Surface Science and Catalysis*; Hightower, J. W., Nicholas Delgass, W., Iglesia, E., Bell, A. T., Eds.; Elsevier: 1996; Vol. 101, p 117.
- (65) Neese, F.; Wennmohs, F.; Becker, U.; Riplinger, C. *The Journal of Chemical Physics* **2020**, *152*, 224108.
- (66) Neese, F. *WIREs Computational Molecular Science* **2018**, *8*, e1327.
- (67) Neese, F. *WIREs Computational Molecular Science* **2012**, *2*, 73.
- (68) Grimme, S.; Ehrlich, S.; Goerigk, L. *Journal of Computational Chemistry* **2011**, *32*, 1456.
- (69) Grimme, S.; Antony, J.; Ehrlich, S.; Krieg, H. *The Journal of Chemical Physics* **2010**, *132*, 154104.
- (70) Wüllen, C. v. *The Journal of Chemical Physics* **1998**, *109*, 392.
- (71) Weigend, F.; Ahlrichs, R. *Physical Chemistry Chemical Physics* **2005**, *7*, 3297.
- (72) Weigend, F. *Physical Chemistry Chemical Physics* **2006**, *8*, 1057.
- (73) Pantazis, D. A.; Neese, F. *Theoretical Chemistry Accounts* **2012**, *131*, 1.
- (74) Pantazis, D. A.; Neese, F. *Journal of Chemical Theory and Computation* **2011**, *7*, 677.
- (75) Pantazis, D. A.; Neese, F. *Journal of Chemical Theory and Computation* **2009**, *5*, 2229.
- (76) Pantazis, D. A.; Chen, X.-Y.; Landis, C. R.; Neese, F. *Journal of Chemical Theory and Computation* **2008**, *4*, 908.
- (77) Rolfes, J. D.; Neese, F.; Pantazis, D. A. *Journal of Computational Chemistry* **2020**, *41*, 1842.
- (78) Petrenko, T.; Kossmann, S.; Neese, F. *The Journal of Chemical Physics* **2011**, *134*, 054116.
- (79) Izsák, R.; Neese, F. *The Journal of Chemical Physics* **2011**, *135*, 144105.
- (80) Neese, F.; Wennmohs, F.; Hansen, A.; Becker, U. *Chemical Physics* **2009**, *356*, 98.

5.7 Supporting Information

5.7.1 Methodology for the Calculation of Thermochemical Properties

Standard thermodynamics equations were used for computing the thermochemical properties of the system. The free energy of a system at any given temperature (T) is defined as:

$$G = H - TS, \quad (1)$$

where H is the enthalpy of the system and S is the total entropy of the system. The free energy of a gas-phase species at a non-standard partial pressure (p) was calculated according to the following relation:

$$G = G^0 + k_B T \ln p, \quad (2)$$

where G^0 is the standard free energy of the gas-phase species computed at 1 bar and k_B is the Boltzmann constant.

The enthalpy of a system is defined as:

$$H = U + k_B T, \quad (3)$$

where U is the internal energy of the system which was calculated according to the following equation:

$$U = E_{el} + E_{ZPE} + E_{vib} + E_{rot} + E_{tr}, \quad (4)$$

where E_{el} is the electronic energy of the system (obtained from single-point energy calculations), E_{ZPE} is the zero-point-energy (ZPE) correction to the internal energy of the system, and E_{vib} , E_{rot} , and E_{tr} are the contributions to internal energy of the system due to its vibrations, rotation, and translation, respectively.

The contribution to the internal energy of the system due to its translation at a finite temperature is:

$$E_{tr} = \frac{3}{2} RT \quad (5)$$

The contribution to the internal energy of the system due to its rotation at a finite temperature is:

$$E_{\text{rot}} = RT, \text{ for a linear molecule, and} \quad (6a)$$

$$E_{\text{rot}} = \frac{3}{2}RT, \text{ for a general polyatomic molecule.} \quad (6b)$$

Finally, the contribution to the internal energy of the system from zero-point vibrational energy and molecular vibrations at a finite temperature were calculated using the following equations:

$$E_{\text{ZPE}} = k_B \sum_k \frac{1}{2} \Theta_{v,k}, \text{ and} \quad (7)$$

$$E_{\text{vib}} = k_B \sum_k \frac{\Theta_{v,k}}{e^{\Theta_{v,k}/T} - 1}, \quad (8)$$

where $\Theta_{v,k} = hv_k/k_B$ is the characteristic temperature of a vibrational mode k (obtained from vibrational frequency calculations), v_k is the frequency of the vibrational mode, and h is the Planck's constant. Each of the $3N - 6$ vibrational modes for minima ($3N - 5$ vibrational modes for linear molecules and $3N - 7$ vibrational modes for transition states) were considered for calculating the E_{ZPE} and E_{vib} . The frequencies obtained from DFT calculations were not scaled and were used as computed.

The total entropy of a system is defined as:

$$S = S_{\text{el}} + E_{\text{vib}} + E_{\text{rot}} + E_{\text{tr}}, \quad (9)$$

where S_{el} , S_{vib} , S_{rot} , and S_{tr} are the contributions to the total entropy of the system from electronic, vibrational, rotational, and translational motions, respectively.

The entropy of a species due to its electronic degeneracy is defined as:

$$S_{\text{el}} = k_B \ln \omega, \quad (10)$$

where ω is the total electron spin-multiplicity of the system.

The entropy of a system due to its rotational motion can be obtained using the following equations:

$$S_{\text{rot}} = k_B \left(\ln \left(\frac{1}{\sigma_r} \left(\frac{T}{\Theta_r} \right) \right) + 1 \right), \text{ for a diatomic molecule, and} \quad (11a)$$

$$S_{\text{rot}} = k_B \left(\ln \left(\frac{\pi^{0.5}}{\sigma_r} \left(\frac{T^{1.5}}{(\Theta_{r,x}\Theta_{r,y}\Theta_{r,z})^{0.5}} \right) \right) + \frac{3}{2} \right), \text{ for a general polyatomic molecule,} \quad (11b)$$

where $\Theta_r = h^2/8\pi^2Ik_B$ is the characteristic rotational temperature of the system, σ_r is the rotational symmetry number, and I is the moment of inertia of the molecule.

The entropy of the system due to translational motion at a given temperature, T , and partial pressure, p , was obtained using the Sackur-Tetrode equation:

$$S_{tr} = k_B \left(\ln \left(\left(\frac{2\pi mk_B T}{h^2} \right)^{1.5} \frac{k_B T}{p} \right) + \frac{5}{2} \right). \quad (12)$$

Finally, the contribution to the entropy of a system due to its vibrational motion was determined using the rigid-rotor harmonic oscillator (RRHO) approximation:

$$S_{vib} = k_B \left(\sum_k \left(\frac{\Theta_{v,k}/T}{e^{\Theta_{v,k}/T} - 1} - \ln(1 - e^{-\Theta_{v,k}/T}) \right) \right), \quad (13)$$

Following the approach by Cramer and Truhlar,¹ all frequencies below the 100 cm⁻¹ were uniformly shifted up to the cut-off value for computing the vibrational entropy of the system.

5.7.2 Infrared (IR) Spectroscopy of Adsorbed CO

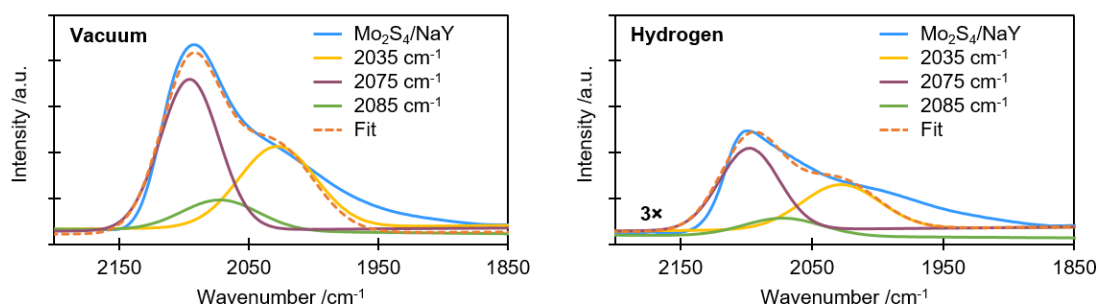
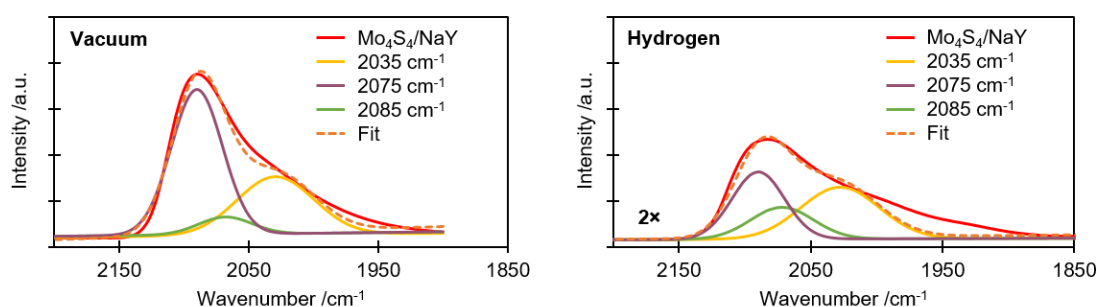
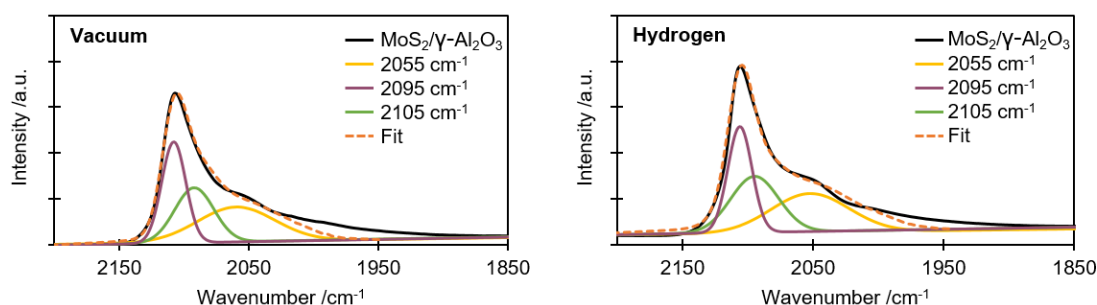
(a) Mo₂S₄/NaY (~3.2 wt.-% Mo)(b) Mo₄S₄/NaY (~3.2 wt.-% Mo)(c) MoS₂/γ-Al₂O₃ (~8.8 wt.-% Mo)

Figure S5.1 Example of peak deconvolution of IR spectra of adsorbed CO on (a) Mo₂S₄/NaY (~3.2 wt.-% Mo), (b) Mo₄S₄/NaY (~3.2 wt.-% Mo), and (c) MoS₂/γ-Al₂O₃ (~8.8 wt.-% Mo), after cooling to 173 K in either vacuum (left) or hydrogen (right). Background corrected difference spectra were deconvoluted to three Gaussian bands (~2105 cm⁻¹, ~2095 cm⁻¹, and ~2055 cm⁻¹ for MoS₂/γ-Al₂O₃ and ~2085 cm⁻¹, ~2075 cm⁻¹, and ~2035 cm⁻¹ for Mo_xS_y/NaY catalysts) using Origin 2020 software package. Half-widths of all peaks were kept constant within ±10% throughout the fitting process.

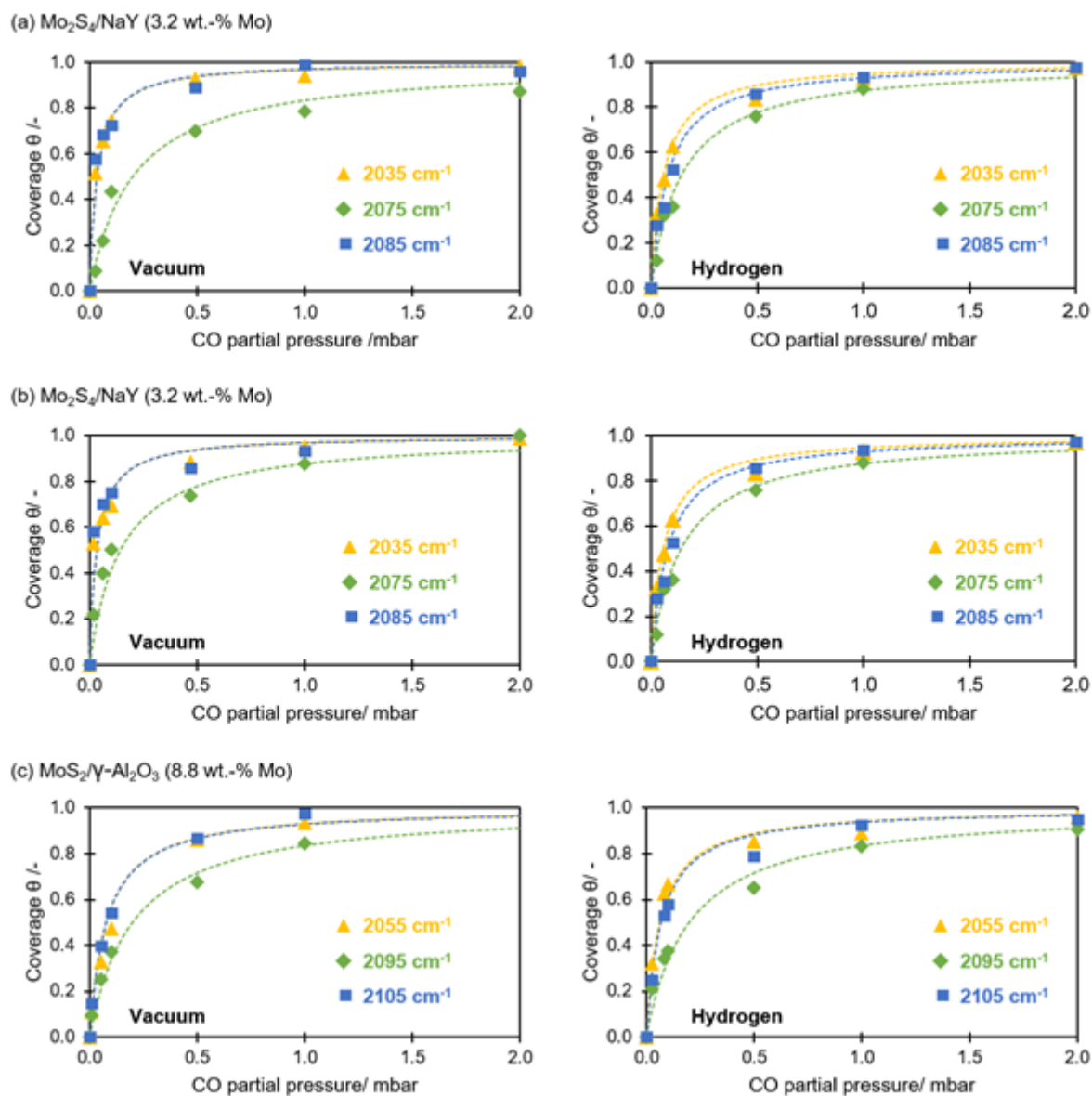


Figure S5.2 CO adsorption isotherms (between 0.01 mbar and 2 mbar) on (a) $\text{Mo}_2\text{S}_4/\text{NaY}$ (~3.2 wt.-% Mo), (b) $\text{Mo}_4\text{S}_4/\text{NaY}$ (~3.2 wt.-% Mo), and (c) $\text{MoS}_2/\gamma\text{-Al}_2\text{O}_3$ (~8.8 wt.-% Mo), after cooling to 173 K in vacuum (left) or hydrogen (right). The deconvoluted CO adsorption data were fitted to Langmuir-type isotherms.

Table S5.1 Adsorption constants (K) and maximum CO uptake (q_{\max} ; normalized to catalyst wafer mass and size) for the deconvoluted IR spectra of adsorbed CO on (a) Mo₂S₄/NaY (~3.2 wt.-% Mo), (b) Mo₄S₄/NaY (~3.2 wt.-% Mo), and (c) MoS₂/γ-Al₂O₃ (~8.8 wt.-% Mo), after cooling to 173 K in either vacuum or hydrogen.

(a) Mo ₂ S ₄ /NaY (~3.2 wt.-% Mo)								
Cooled in	Band position						Total CO adsorbed	
	2085 cm ⁻¹		2075 cm ⁻¹		2035 cm ⁻¹		[cm·g ⁻¹]	[%]
	K	q_{\max} [cm·g ⁻¹]	K	q_{\max} [cm·g ⁻¹]	K	q_{\max} [cm·g ⁻¹]		
Vacuum	30	920	5	115	30	420	1455	100
Hydrogen (1 bar)	13	430	7	25	17	140	595	41

(b) Mo ₄ S ₄ /NaY (~3.2 wt.-% Mo)								
Cooled in	Band position						Total CO adsorbed	
	2085 cm ⁻¹		2075 cm ⁻¹		2035 cm ⁻¹		[cm·g ⁻¹]	[%]
	K	q_{\max} [cm·g ⁻¹]	K	q_{\max} [cm·g ⁻¹]	K	q_{\max} [cm·g ⁻¹]		
Vacuum	30	900	7	200	30	660	1760	100
Hydrogen (1 bar)	15	445	7	100	15	320	865	49

(c) MoS ₂ /γ-Al ₂ O ₃ (~8.8 wt.-% Mo)								
Cooled in	Band position						Total CO adsorbed	
	2105 cm ⁻¹		2095 cm ⁻¹		2055 cm ⁻¹		[cm·g ⁻¹]	[%]
	K	q_{\max} [cm·g ⁻¹]	K	q_{\max} [cm·g ⁻¹]	K	q_{\max} [cm·g ⁻¹]		
Vacuum	13	740	5	950	13	1230	2920	100
Hydrogen (1 bar)	15	680	5	860	16	1240	2780	95

Table S5.2 Adsorption constants (K) and maximum CO uptake (q_{\max} ; normalized to catalyst wafer mass and size) for the deconvoluted IR spectra of adsorbed CO on (a) $\text{Mo}_2\text{S}_4/\text{NaY}$ (~3.2 wt.-% Mo), and (b) $\text{Mo}_4\text{S}_4/\text{NaY}$ (~3.2 wt.-% Mo), after cooling to 173 K in either vacuum, ethene, or a mixture of ethene and hydrogen.

(a) $\text{Mo}_2\text{S}_4/\text{NaY}$ (~3.2 wt.-% Mo)								
Cooled in (mbar)	Band position						Total CO adsorbed	
	2085 cm^{-1}		2075 cm^{-1}		2035 cm^{-1}		[$\text{cm}\cdot\text{g}^{-1}$]	[%]
	K	q_{\max} [$\text{cm}\cdot\text{g}^{-1}$]	K	q_{\max} [$\text{cm}\cdot\text{g}^{-1}$]	K	q_{\max} [$\text{cm}\cdot\text{g}^{-1}$]		
Vacuum	35	930	20	328	35	450	1708	100
C_2H_4 (100)	8	170	6	25	6	47	242	14
Vacuum	35	830	20	420	35	485	1735	100
H_2 (960) + C_2H_4 (50)	11	165	7	60	8	110	335	19

(a) $\text{Mo}_x\text{S}_y/\text{NaY}$ (~3.2 wt.-% Mo)								
Cooled in (mbar)	Band position						Total CO adsorbed	
	2085 cm^{-1}		2075 cm^{-1}		2035 cm^{-1}		[$\text{cm}\cdot\text{g}^{-1}$]	[%]
	K	q_{\max} [$\text{cm}\cdot\text{g}^{-1}$]	K	q_{\max} [$\text{cm}\cdot\text{g}^{-1}$]	K	q_{\max} [$\text{cm}\cdot\text{g}^{-1}$]		
Vacuum	16	970	22	440	28	320	1730	100
C_2H_4 (1000)	10	90	10	65	7	50	205	11
H_2 (960) + C_2H_4 (50)	14	285	7	100	8	110	495	28

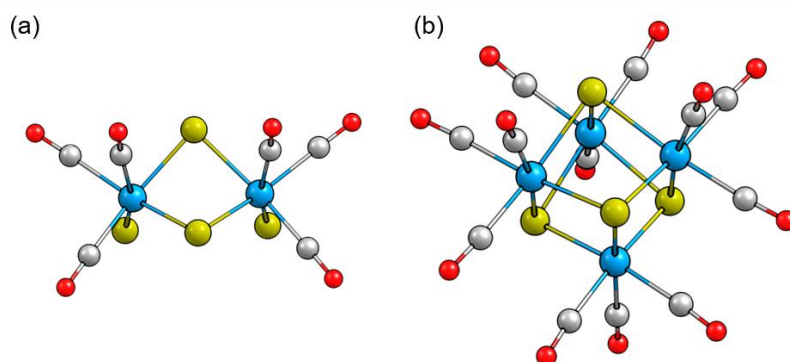
5.7.3 CO Adsorption on Mo_xS_y Clusters

Figure S5.3 DFT/B3LYP/def2-TZVP-optimized geometries of (a) Mo_2S_4 , and (b) Mo_4S_4 clusters, with multiple CO molecules (three per Mo) adsorbed on Mo atoms. The average C–O bond lengths in the adsorbed CO molecules were computed to be ~ 1.131 Å in the dimer and ~ 1.137 Å in the tetramer. The Mayer bond orders for the C–O bond were computed to be 2.31–2.40 in Mo_2S_4 and 2.27–2.34 in Mo_4S_4 . The C–O bond length and Mayer bond order for gas-phase CO species were computed to be ~ 1.125 Å and ~ 2.44 , respectively. Optimized geometries and structural parameters obtained using DFT/PBE0/def2-TZVP were similar. S: yellow; Mo: blue; C: gray; O: red.

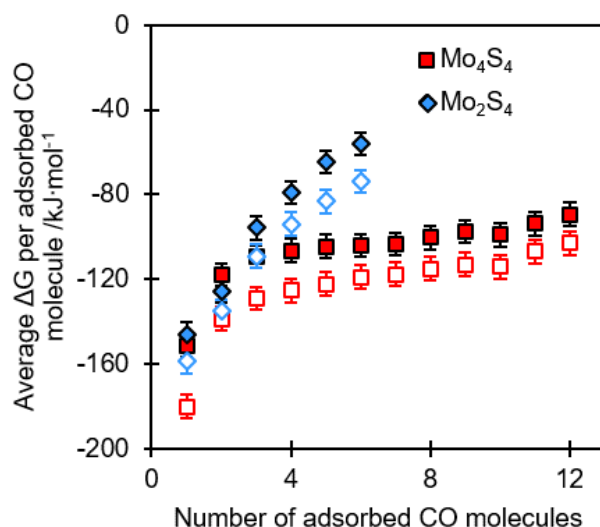


Figure S5.4 Average free energy change (ΔG) per adsorbed CO molecule on Mo_2S_4 and Mo_4S_4 clusters as a function of number of adsorbed CO molecules, computed at $T = 173$ K and $p_{\text{CO}} = 2$ mbar, with (i) DFT/B3LYP/def2-TZVPP (filled symbols), and (ii) DFT/PBE0/def2-TZVPP (open symbols). Error bars correspond to $\pm 1/2$ D gas-phase translational entropy of CO at 173 K.

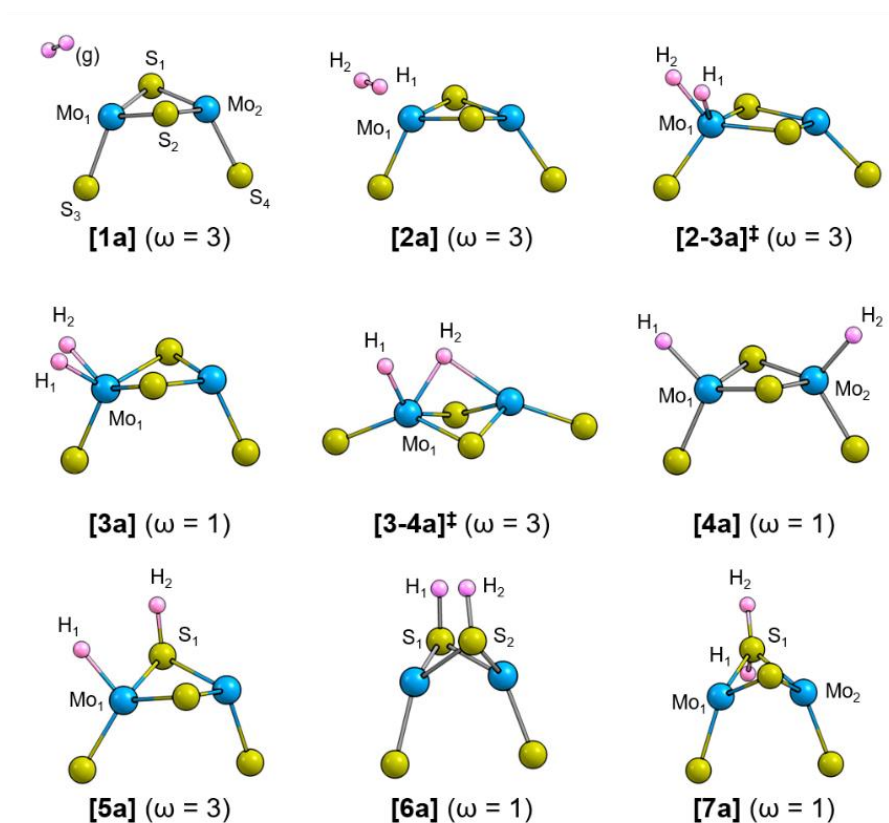
5.7.4 Hydrogen Adsorption on Mo₂S₄

Figure S5.5 DFT/B3LYP/def2-TZVP-optimized geometries of Mo₂S₄ clusters with gas-phase H₂ (**[1a]**) or physisorbed H₂ (**[2a]**) centered on Mo, and Mo₂S₄ clusters with dissociatively adsorbed H₂ (as hydride or sulfhydryl species) on (i) single Mo atom (**[3a]**), (ii) two Mo atoms (**[4a]**), (iii) one Mo atom and one bridging S atom (**[5a]**), (iv) two bridging S atoms (**[6a]**), and (v) single bridging S atom (**[7a]**). The optimized structures of the transition states between **[2a]** and **[3a]**, *i.e.*, **[2-3a][‡]**, and between **[3a]** and **[4a]**, *i.e.*, **[3-4a][‡]**, are also shown. The reported spin-multiplicities (ω) correspond to the thermodynamically most stable configurations (Table S5.3). Optimized geometries obtained using DFT/PBE0/def2-TZVP were similar. S: yellow; Mo: blue; H: pink.

Table S5.3 Relative enthalpies (ΔH) and free energies (ΔG) of Mo_2S_4 clusters with gas-phase, physisorbed, or dissociatively adsorbed H_2 , computed at $T = 473 \text{ K}$ and $p_{\text{H}_2} = 1 \text{ bar}$, using (a) DFT/B3LYP/def2-TZVPP and (b) DFT/PBE0/def2-TZVPP. The corresponding structures are depicted in Figure S5.5.

(a) DFT/B3LYP/def2-TZVPP						
Spin-multiplicity (ω)	$\Delta H^{473\text{K}} / \text{kJ}\cdot\text{mol}^{-1}$			$\Delta G^{473\text{K}} / \text{kJ}\cdot\text{mol}^{-1}$		
	1	3	5	1	3	5
[1a]	0.0 ^a	-32.2	-10.4	0.0 ^a	-35.1	-24.0
[2a]	-70.5	-90.9	-7.6 ^b	-15.3	-41.0	31.1 ^b
[2-3]‡	- ^d	-78.3	- ^e	- ^d	-26.9	- ^e
[3a]	-120.9	-81.2	- ^c	-61.0	-37.1	- ^c
[3-4]‡	79.6	34.2	- ^e	142.2	87.6	- ^e
[4a]	-156.5	-140.1	59.9	-100.8	-93.2	93.3
[5a]	-32.8	-52.5	-17.9 ^c	20.5	-4.3	22.4 ^c
[6a]	8.9	71.4	66.1	60.6	118.0	108.2
[7a]	109.6	134.2	150.0	163.5	184.3	195.6

(b) DFT/PBE0/def2-TZVPP						
Spin-multiplicity (ω)	$\Delta H^{473\text{K}} / \text{kJ}\cdot\text{mol}^{-1}$			$\Delta G^{473\text{K}} / \text{kJ}\cdot\text{mol}^{-1}$		
	1	3	5	1	3	5
[1a]	0.0 ^a	-39.9	-27.6	0.0 ^a	-42.9	-42.6
[2a]	-72.4	-109.4	-30.2 ^b	-19.5	-59.8	7.1 ^b
[2-3]‡	- ^d	-96.7	- ^e	- ^d	-46.1	- ^e
[3a]	-130.7	-89.1	- ^c	-71.6	-46.8	- ^c
[3-4]‡	73.6	28.5	- ^e	135.6	82.7	- ^e
[4a]	-162.5	-145.3	58.9	-106.9	-100.0	88.5
[5a]	-40.5	-69.8	-43.6 ^c	12.5	-22.4	-4.7 ^c
[6a]	-1.6	51.9	34.6	49.6	98.2	75.6
[7a]	95.0	107.6	114.7	149.0	160.7	159.5

^a The enthalpy and free energy of **[1a]** with spin-multiplicity, $\omega = 1$ (*i.e.*, no unpaired electrons) was used as the standard and was set to zero.

^b The lowest energy structure was the *trans* form with terminal S atoms pointing in opposite direction.

^c The optimized structure with non-imaginary vibrational frequency modes was not achieved.

^d No climbing image was found indicating a barrier-less transition.

^e Transition-state optimization was not performed for this structure.

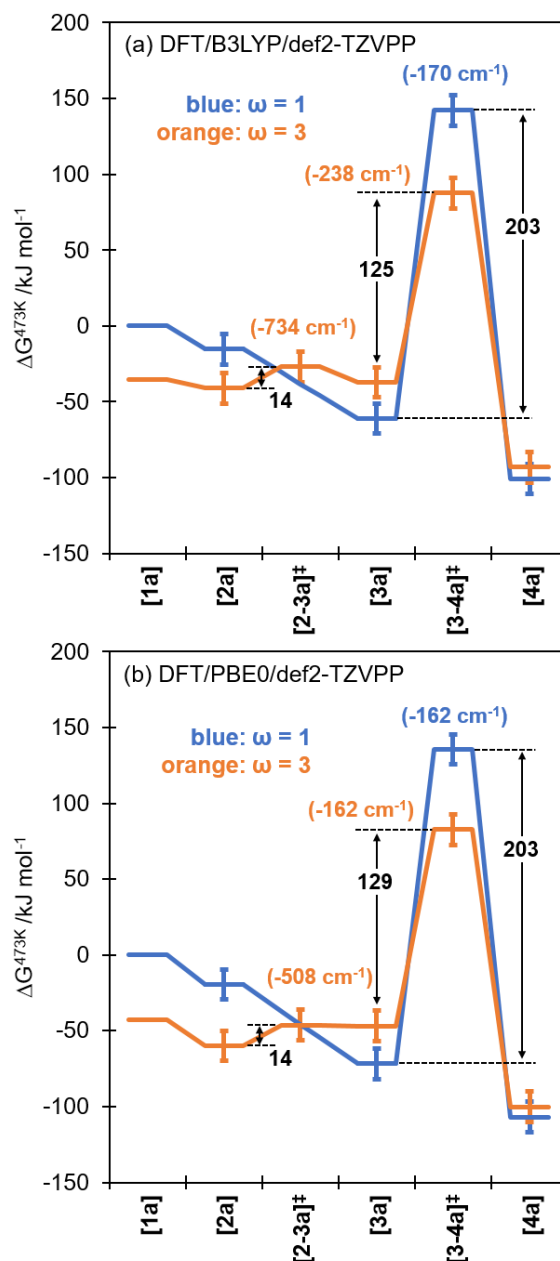


Figure S5.6 Free energy diagram of Mo₂S₄ configurations, with spin-multiplicity $\omega = 1$ and $\omega = 3$, showing the transitions from [2a] to [3a] and from [3a] to [4a], computed at $T = 473$ K and $p_{\text{H}_2} = 1$ bar, using (a) DFT/B3LYP/def2-TZVPP, and (b) DFT/PBE0/def2-TZVPP. The corresponding structures are shown in Figure S5.5. Error bars correspond to $\pm \frac{1}{2}D$ gas-phase translational entropy of the H₂ at 473 K. Values shown in the figure are in kJ·mol⁻¹. Values shown in parentheses are the imaginary frequencies of the corresponding transition state structures.

Table S5.4 Mayer bond orders and bond lengths of relevant bonds in the thermodynamically most-stable Mo₂S₄ configurations with gas-phase, physisorbed, or dissociatively adsorbed H₂, computed with (i) DFT/B3LYP/def2-TZVPP, and (ii) DFT/PBE0/def2-TZVPP. The nomenclature of atoms corresponds to the structures shown in Figure S5.5.

Structure (spin-multiplicity)	Bond	Mayer bond order		Bond length /Å	
		B3LYP	PBE0	B3LYP	PBE0
[1a] ($\omega = 3$)	H ₁ - H ₂	1.000	1.000	0.744	0.746
	Mo ₁ - H ₁	0.251	0.275	1.935	1.897
[2a] ($\omega = 3$)	Mo ₁ - H ₂	0.307	0.335	1.936	1.903
	H ₁ - H ₂	0.678	0.652	0.811	0.827
[2-3][‡] ($\omega = 3$)	Mo ₁ - H ₁	0.640	0.675	1.707	1.690
	Mo ₁ - H ₂	0.718	0.761	1.707	1.690
	H ₁ - H ₂	0.217	0.180	1.247	1.330
[3a] ($\omega = 1$)	Mo ₁ - H ₁	0.826	0.831	1.684	1.676
	Mo ₁ - H ₂	0.826	0.831	1.683	1.676
	H ₁ - H ₂	- ^a	- ^a	1.768	1.719
[3-4a][‡] ($\omega = 3$)	Mo ₁ - H ₁	0.850	0.854	1.684	1.685
	Mo ₁ - H ₂	0.596	0.553	1.803	1.840
	Mo ₂ - H ₂	0.259	0.293	2.171	2.120
[4a] ($\omega = 1$)	Mo ₁ - H ₁	0.868	0.877	1.713	1.705
	Mo ₂ - H ₂	0.868	0.877	1.713	1.705
[5a] ($\omega = 3$)	Mo ₁ - H ₁	0.883	0.895	1.708	1.701
	S ₁ - H ₂	0.957	0.953	1.354	1.353
[6a] ($\omega = 1$)	S ₁ - H ₁	0.961	0.956	1.358	1.358
	S ₂ - H ₂	0.961	0.956	1.358	1.358
[7a] ($\omega = 1$)	S ₁ - H ₁	0.948	0.942	1.345	1.346
	S ₁ - H ₂	0.848	0.856	1.382	1.381
	H ₁ - H ₂	- ^a	- ^a	1.982	1.978

^a The computed bond order was < 0.1.

Table S5.5 Net Hirshfeld charges in the thermodynamically most-stable Mo₂S₄ configurations with gas-phase, physisorbed, or dissociatively adsorbed H₂, computed using (a) DFT/B3LYP/def2-TZVPP, and (b) DFT/PBE0/def2-TZVPP. The nomenclature of atoms corresponds to the structures shown in Figure S5.5.

(a) DFT/B3LYP/def2-TZVPP

Structure	Net Hirshfeld charges								
	[1a]	[2a]	[2-3a]‡	[3a]	[3-4a]‡	[4a]	[5a]	[6a]	[7a]
Spin-multiplicity (ω)	3	3	3	1	3	1	3	1	1
Mo ₂ S ₄	0.000	-0.060	0.088	0.202	0.209	0.264	0.089	-0.098	-0.155
H ₁ H ₂	0.000	0.060	-0.088	-0.202	-0.209	-0.264	-0.089	0.098	0.155

(b) DFT/PBE0/def2-TZVPP

Structure	Net Hirshfeld charges								
	[1a]	[2a]	[2-3a]‡	[3a]	[3-4a]‡	[4a]	[5a]	[6a]	[7a]
Spin-multiplicity (ω)	3	3	3	1	3	1	3	1	1
Mo ₂ S ₄	0.000	-0.065	0.090	0.182	0.212	0.248	0.074	-0.112	-0.167
H ₁ H ₂	0.000	0.065	-0.090	-0.182	-0.212	-0.248	-0.074	0.112	0.167

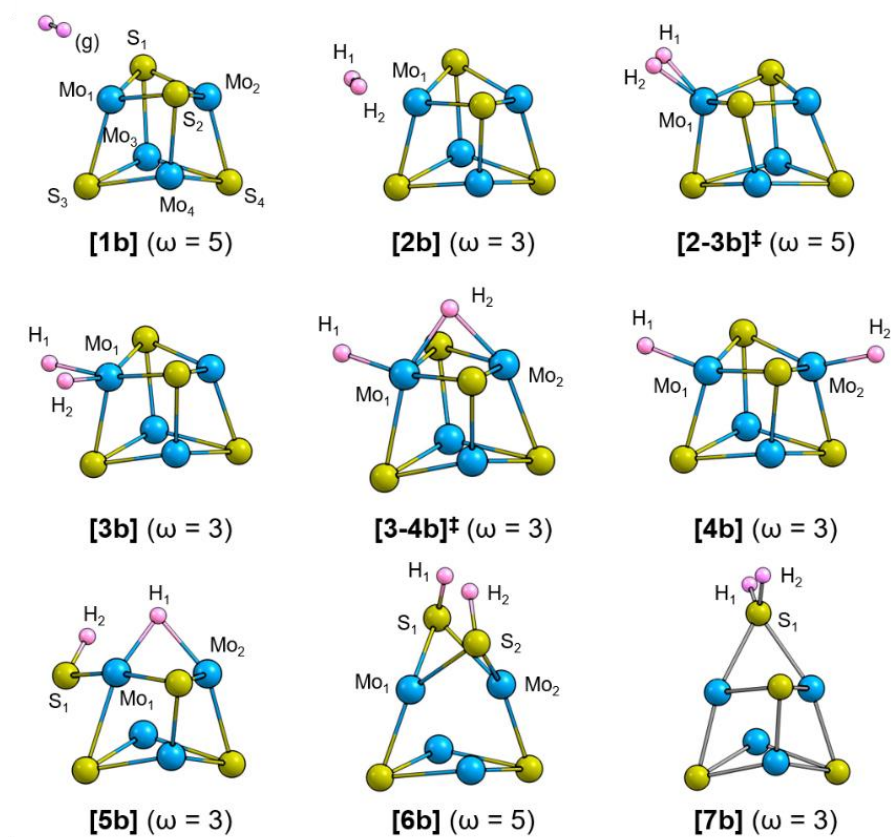
5.7.5 Hydrogen Adsorption on Mo₄S₄

Figure S5.7 DFT/B3LYP/def2-TZVP-optimized geometries of Mo₄S₄ clusters with gas-phase H₂ (**[1b]**) or physisorbed H₂ (**[2b]**) centered on Mo, and Mo₂S₄ clusters with dissociatively adsorbed H₂ (as hydride or sulfhydryl species) on (i) single Mo atom (**[3b]**), (ii) two Mo atoms (**[4b]**), (iii) one Mo atom and one bridging S atom (**[5b]**), (iv) two bridging S atoms (**[6b]**), and (v) single bridging S atom (**[7b]**). The optimized structures of transition states between **[2b]** and **[3b]**, *i.e.*, **[2-3b][‡]**, and between **[3b]** and **[4b]**, *i.e.*, **[3-4b][‡]**, are also shown. The reported spin-multiplicities (ω) correspond to the thermodynamically most stable configurations (Table S5.6). Optimized geometries obtained using DFT/PBE0/def2-TZVP were similar. S: yellow; Mo: blue; H: pink.

Table S5.6 Relative enthalpies (ΔH) and free energies (ΔG) of Mo_4S_4 clusters with gas-phase, physisorbed, or dissociatively adsorbed H_2 , computed at $T = 473 \text{ K}$ and $p_{\text{H}_2} = 1 \text{ bar}$, with (a) DFT/B3LYP/def2-TZVPP and (b) DFT/PBE0/def2-TZVPP. The corresponding structures are depicted in Figure S5.7.

(a) DFT/B3LYP/def2-TZVPP								
Multiplicity(ω)	$\Delta H^{473\text{K}} / \text{kJ}\cdot\text{mol}^{-1}$				$\Delta G^{473\text{K}} / \text{kJ}\cdot\text{mol}^{-1}$			
	1	3	5	7	1	3	5	7
[1b]	0.0 ^a	11.7	6.6	43.4	0.0 ^a	-4.1	-11.0	22.4
[2b]	-43.3	-70.5	-59.6	2.1	3.5	-31.5	-27.0	36.2
[2-3b]‡	-51.6	- ^b	-45.6	- ^c	0.4	- ^b	-7.2	- ^c
[3b]	-75.7	-108.3	-55.7	-2.7	-23.5	-61.0	-17.8	30.5
[3-4b]‡	54.9	49.3	54.6	- ^c	108.6	89.4	94.7	- ^c
[4b]	-99.7	-115.9	-69.9	-44.0	-47.6	-72.3	-32.9	-13.7
[5b]	81.9	-49.8	16.3	61.9	131.4	-15.4	49.4	83.6
[6b]	- ^d	156.5	145.9	- ^d	- ^d	188.2	177.3	- ^d
[7b]	- ^d	173.7	193.8	228.2	- ^d	202.4	228.2	254.3

(b) DFT/PBE0/def2-TZVPP								
Multiplicity (ω)	$\Delta H^{473\text{K}} / \text{kJ}\cdot\text{mol}^{-1}$				$\Delta G^{473\text{K}} / \text{kJ}\cdot\text{mol}^{-1}$			
	1	3	5	7	1	3	5	7
[1b]	0.0 ^a	5.0	-5.9	25.6	0.0 ^a	-7.2	-23.5	4.3
[2b]	-59.5	-83.6	-88.7	-31.2	-11.1	-47.7	-55.5	3.5
[2-3b]‡	-69.9	- ^b	-71.5	- ^c	-16.1	- ^b	-34.7	- ^c
[3b]	-90.5	-131.8	-76.4	-23.9	-37.5	-84.3	-38.3	8.9
[3-4b]‡	53.8	21.7	57.3	- ^c	109.1	64.9	98.2	- ^c
[4b]	-118.9	-140.1	-94.1	-52.1	-65.9	-96.4	-58.2	-20.5
[5b]	68.2	-61.0	29.5	52.9	119.8	-27.5	61.5	79.7
[6b]	- ^d	121.1	136.6	- ^d	- ^d	154.2	176.2	- ^b
[7b]	- ^d	173.2	182.4	218.8	- ^d	202.0	217.2	242.5

^a The enthalpy and free energy of **[1b]** with spin-multiplicity, $\omega = 1$ (*i.e.*, no unpaired electrons) was used as the standard and was set to zero.

^b No climbing image was found suggesting a barrier-less transition.

^c Transition-state optimization was not performed for this structure.

^d The optimized structure with non-imaginary vibrational frequency modes was not achieved.

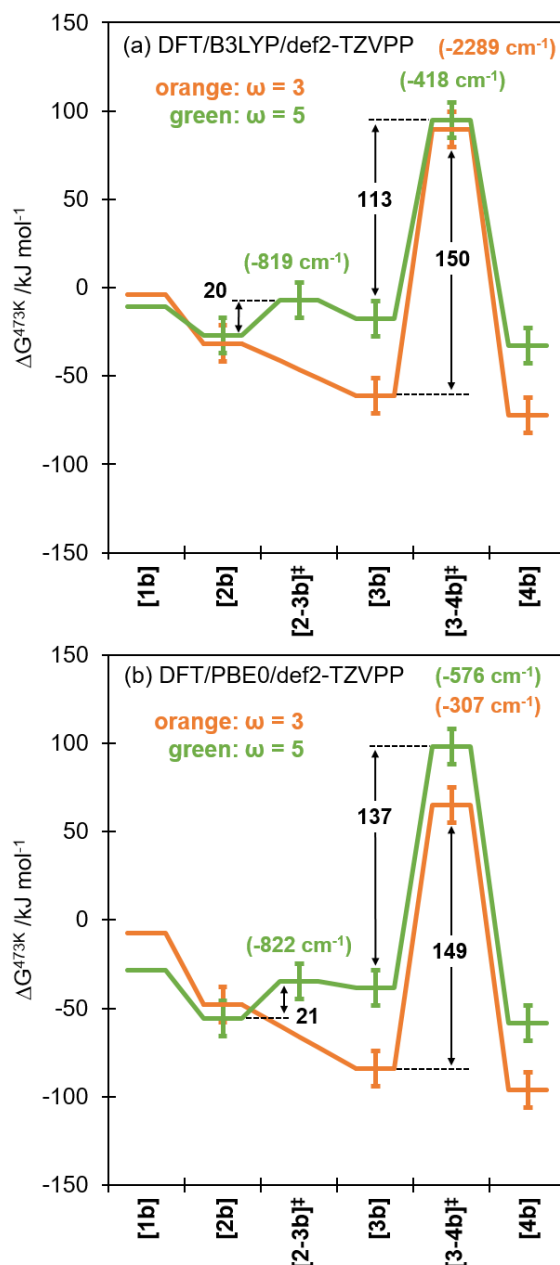


Figure S5.8 Free energy diagram of Mo₄S₄ configurations, with spin-multiplicity $\omega = 3$ and $\omega = 5$, showing the transition from [2b] to [3b] and from [3b] to [4b], computed at $T = 473$ K and $p_{\text{H}_2} = 1$ bar, with (a) DFT/B3LYP/def2-TZVPP, and (b) DFT/PBE0/def2-TZVPP. The corresponding structures are shown in Figure S5.7. Error bars correspond to $\pm \frac{1}{2}D$ gas-phase translational entropy of H₂ at 473 K. Values shown in the figure are in $\text{kJ}\cdot\text{mol}^{-1}$. Values shown in parentheses are the imaginary frequencies of the corresponding transition state structures.

Table S5.7 Mayer bond orders and bond lengths of relevant bonds in the thermodynamically most stable Mo₄S₄ configurations with gas-phase, physisorbed, or dissociatively adsorbed H₂, computed with (i) DFT/B3LYP/def2-TZVPP, and (ii) DFT/PBE0/def2-TZVPP. The nomenclature of atoms corresponds to the structures shown in Figure S5.7.

Structure (spin-multiplicity)	Bond	Mayer bond order		Bond length /Å	
		B3LYP	PBE0	B3LYP	PBE0
[1b] ($\omega = 5$)	H ₁ - H ₂	1.000	1.000	0.744	0.746
	Mo ₁ - H ₁	0.448	0.284 ^a	1.825	1.931 ^a
[2b] ($\omega = 3$)	Mo ₁ - H ₂	0.461	0.284 ^a	1.829	1.931 ^a
	H ₁ - H ₂	0.428	0.682 ^a	0.936	0.822 ^a
[2-3b]‡ ($\omega = 5$)	Mo ₁ - H ₁	0.654	0.647	1.734	1.732
	Mo ₁ - H ₂	0.654	0.666	1.734	1.721
	H ₁ - H ₂	0.229	0.228	1.225	1.227
[3b] ($\omega = 3$)	Mo ₁ - H ₁	0.836	0.849	1.719	1.712
	Mo ₁ - H ₂	0.836	0.849	1.719	1.712
	H ₁ - H ₂	- ^b	- ^b	1.980	1.948
[3-4b]‡ ($\omega = 3$)	Mo ₁ - H ₁	0.738	0.752	1.739	1.736
	Mo ₁ - H ₂	0.419	0.578	1.940	1.815
	Mo ₂ - H ₂	0.419	0.250	1.973	2.151
[4b] ($\omega = 3$)	Mo ₁ - H ₁	0.848	0.861	1.752	1.744
	Mo ₂ - H ₂	0.848	0.861	1.752	1.744
[5b] ($\omega = 3$)	Mo ₁ - H ₁	0.523	0.524	1.850	1.857
	Mo ₂ - H ₁	0.356	0.365	1.979	1.978
	S ₁ - H ₂	0.982	0.979	1.348	1.347
[6b] ($\omega = 5$)	S ₁ - H ₁	0.942	0.931 ^c	1.369	1.361 ^c
	S ₂ - H ₂	0.942	0.931 ^c	1.369	1.362 ^c
[7b] ($\omega = 3$)	S ₁ - H ₁	0.906	0.907	1.356	1.361
	S ₁ - H ₂	0.923	0.927	1.360	1.355
	H ₁ - H ₂	- ^b	- ^b	1.973	1.961

^a Data reported is for spin-multiplicity, $\omega = 5$.

^b The computed bond order was < 0.1 .

^c Data reported is for spin-multiplicity, $\omega = 3$.

Table S5.8 Net Hirshfeld charges in the thermodynamically most stable Mo₄S₄ configurations with gas-phase, physisorbed, or dissociatively adsorbed H₂, computed using (a) DFT/B3LYP/def2-TZVPP, and (b) DFT/PBE0/def2-TZVPP. The nomenclature of atoms corresponds to the structures shown in Figure S5.7.

(a) DFT/B3LYP/def2-TZVPP

Structure	Net Hirshfeld charges								
	[1b]	[2b]	[2-3b]‡	[3b]	[3-4b]‡	[4b]	[5b]	[6b]	[7b]
Multiplicity	5	3	5	3	3	3	3	5	3
Mo ₄ S ₄	0.000	0.100	0.310	0.328	0.305	0.402	0.123	-0.030	-0.127
H ₁ H ₂	0.000	-0.100	-0.310	-0.328	-0.305	-0.402	-0.123	0.030	0.127

(b) DFT/PBE0/def2-TZVPP

Structure	Net Hirshfeld charges								
	[1b]	[2b]	[2-3b]‡	[3b]	[3-4b]‡	[4b]	[5b]	[6b]	[7b]
Multiplicity	5	5	5	3	3	3	3	3	3
Mo ₄ S ₄	0.000	0.088	0.292	0.312	0.296	0.386	0.113	-0.053	-0.137
H ₁ H ₂	0.000	-0.088	-0.292	-0.312	-0.296	-0.386	-0.113	0.053	0.137

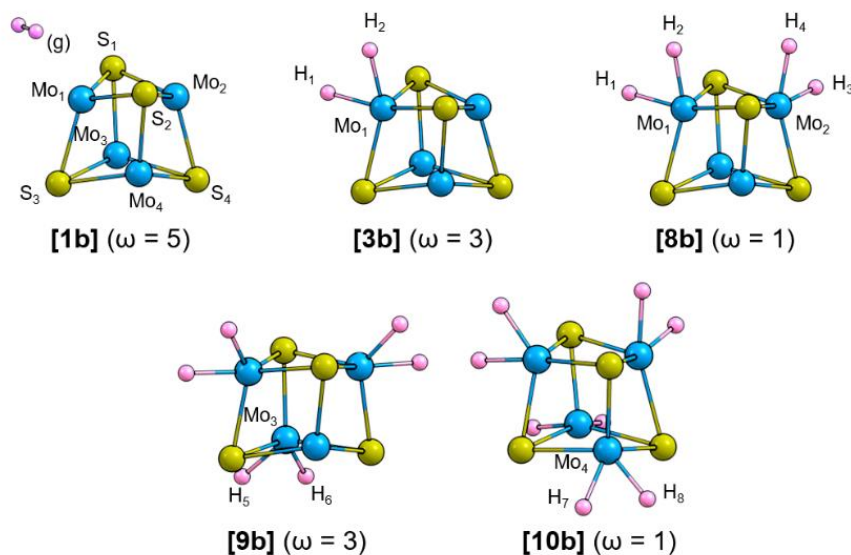
5.7.6 Multiple Hydrogen Adsorption on Mo₄S₄

Figure S5.9 DFT/B3LYP/def2-TZVP-optimized geometries of Mo₄S₄ clusters with one (**[3b]**), two (**[8b]**), three (**[9b]**), or four (**[10b]**) H₂ molecule(s) dissociatively adsorbed on Mo. The optimized geometry of bare Mo₄S₄ cluster with gas-phase ethene (**[1b]**) is also shown for comparison. The reported spin-multiplicities (ω) correspond to the thermodynamically most stable configurations (Tables S5.9 and S5.10). Optimized geometries obtained using DFT/PBE0/def2-TZVP were similar. S: yellow; Mo: blue; H: pink.

Table S5.9 Enthalpies (ΔH) and free energies (ΔG) of Mo_4S_4 clusters with (multiple) H_2 molecule(s) dissociatively adsorbed on Mo, computed at (a) $T = 473$ K and $p_{\text{H}_2} = 1$ bar, and (b) $T = 173$ K and $p_{\text{H}_2} = 1$ bar, with DFT/B3LYP/def2-TZVPP. The corresponding structures are shown in Figure S5.9.

(a) $T = 473$ K and $p_{\text{H}_2} = 1$ bar

Spin-multiplicity (ω)	$\Delta H^{473\text{K}} / \text{kJ}\cdot\text{mol}^{-1}$				$\Delta G^{473\text{K}} / \text{kJ}\cdot\text{mol}^{-1}$			
	1	3	5	7	1	3	5	7
[1b]	0.0 ^a	11.7	6.6	43.4	0.0 ^a	-4.1	-11.0	22.4
[3b]	-75.7	-108.3	-55.7	-2.7	-23.5	-61.0	-17.8	30.5
[8b]	-146.0	-127.3	-100.5	-38.1	-37.2	-28.1	-2.6	55.8
[9b]	-147.5	-150.4	-101.9	- ^b	16.8	3.2	43.6	- ^b
[10b]	-144.7	- ^b	- ^b	- ^b	74.2	- ^b	- ^b	- ^b

(b) $T = 173$ K and $p_{\text{H}_2} = 1$ bar

Spin-multiplicity (ω)	$\Delta H^{173\text{K}} / \text{kJ}\cdot\text{mol}^{-1}$				$\Delta G^{173\text{K}} / \text{kJ}\cdot\text{mol}^{-1}$			
	1	3	5	7	1	3	5	7
[1b]	0.0 ^a	10.4	5.1	41.8	0.0 ^a	5.5	-0.3	35.2
[3b]	-73.4	-106.2	-54.8	-2.3	-55.9	-90.3	-41.6	9.5
[8b]	-140.8	-123.1	-95.9	-33.4	-104.5	-89.7	-63.2	-2.1
[9b]	-139.3	-143.7	-97.1	- ^b	-84.7	-92.1	-47.3	- ^b
[10b]	-133.8	- ^b	- ^b	- ^b	-61.1	- ^b	- ^b	- ^b

^a The enthalpy and free energy of **[1b]** with spin-multiplicity, $\omega = 1$ (*i.e.*, no unpaired electrons) was used as the standard and was set to zero.

^b Optimized structure with only non-imaginary vibrational frequency modes was not achieved.

Table S5.10 Enthalpies (ΔH) and free energies (ΔG) of Mo_4S_4 clusters with (multiple) H_2 molecule(s) dissociatively adsorbed on Mo, computed at (a) $T = 473$ K and $p_{\text{H}_2} = 1$ bar, and (b) $T = 173$ K and $p_{\text{H}_2} = 1$ bar, with DFT/PBE0/def2-TZVPP. The corresponding structures are shown in Figure S5.9.

(a) $T = 473$ K and $p_{\text{H}_2} = 1$ bar

Spin-multiplicity (ω)	$\Delta H^{473\text{K}} / \text{kJ}\cdot\text{mol}^{-1}$				$\Delta G^{473\text{K}} / \text{kJ}\cdot\text{mol}^{-1}$			
	1	3	5	7	1	3	5	7
[1b]	0.0 ^a	5.0	-5.9	25.6	0.0 ^a	-7.2	-23.5	4.3
[3b]	-90.5	-131.8	-76.4	-23.9	-37.5	-84.3	-38.3	8.9
[8b]	-178.1	-160.9	-136.8	-70.3	-68.0	-59.9	-39.5	14.9
[9b]	-179.4	-195.8	-137.3	- ^b	-15.3	-33.9	8.3	- ^b
[10b]	-204.6	- ^b	- ^b	- ^b	18.1	- ^b	- ^b	- ^b

(b) $T = 173$ K and $p_{\text{H}_2} = 1$ bar

Spin-multiplicity (ω)	$\Delta H^{173\text{K}} / \text{kJ}\cdot\text{mol}^{-1}$				$\Delta G^{173\text{K}} / \text{kJ}\cdot\text{mol}^{-1}$			
	1	3	5	7	1	3	5	7
[1b]	0.0 ^a	4.0	-7.6	23.8	0.0 ^a	0.2	-12.9	17.2
[3b]	-88.2	-129.8	-75.6	-23.6	-70.3	-113.8	-62.3	-11.9
[8b]	-172.7	-156.4	-132.4	-68.4	-136.1	-122.5	-99.8	-38.7
[9b]	-171.4	-186.8	-132.6	- ^b	-116.8	-133.5	-82.7	- ^b
[10b]	-192.3	- ^b	- ^b	- ^b	-118.9	- ^b	- ^b	- ^b

^a The enthalpy and free energy of **[1b]** with spin-multiplicity, $\omega = 1$ (*i.e.*, no unpaired electrons) was used as the standard and was set to zero.

^b Optimized structure with only non-imaginary vibrational frequency modes was not achieved.

Table S5.11 Mayer bond orders and bond lengths of relevant bonds in the thermodynamically most-stable Mo₄S₄ configurations with (multiple) H₂ molecule(s) dissociatively adsorbed on Mo, computed with (i) DFT/B3LYP/def2-TZVPP, and (ii) DFT/PBE0/def2-TZVPP. The nomenclature of atoms corresponds to the structures shown in Figure S5.9.

Structure (spin-multiplicity)	Bond	Mayer bond order		Bond length /Å	
		B3LYP	PBE0	B3LYP	PBE0
[1b] ($\omega = 5$)	H ₁ - H ₂	1.000	1.000	0.744	0.746
	Mo ₁ - H ₁	0.836	0.849	1.719	1.712
[3b] ($\omega = 3$)	Mo ₁ - H ₂	0.836	0.849	1.719	1.712
	H ₁ - H ₂	- ^b	- ^b	1.980	1.948
[8b] ($\omega = 1$)	Mo ₁ - H ₁	0.837	0.850	1.722	1.715
	Mo ₁ - H ₂	0.847	0.856	1.710	1.704
	H ₁ - H ₂	- ^b	- ^b	1.986	1.949
	Mo ₂ - H ₃	0.837	0.850	1.721	1.705
	Mo ₂ - H ₄	0.847	0.856	1.710	1.704
	H ₃ - H ₄	- ^b	- ^b	1.984	1.949

^a The computed bond order was < 0.1.

Table S5.12 Net Hirshfeld charges in the thermodynamically most-stable Mo₄S₄ configurations with (multiple) H₂ molecule(s) dissociatively adsorbed on Mo, computed with (a) DFT/B3LYP/def2-TZVPP, and (b) DFT/PBE0/def2-TZVPP. The nomenclature of atoms corresponds to the structures shown in Figure S5.9.

(a) DFT/B3LYP/def2-TZVPP

Structure	Net Hirshfeld charges		
	[1b]	[3b]	[8b]
Spin-multiplicity (ω)	5	3	1
Mo ₄ S ₄	0.000	0.328	0.606
H ₁ H ₂	-	-0.328	-0.303
H ₃ H ₄	-	-	-0.303

(a) DFT/PBE0/def2-TZVPP

Structure	Net Hirshfeld charges		
	[1b]	[3b]	[8b]
Spin-multiplicity (ω)	5	3	1
Mo ₄ S ₄	0.000	0.312	0.575
H ₁ H ₂	-	-0.312	-0.287
H ₃ H ₄	-	-	-0.287

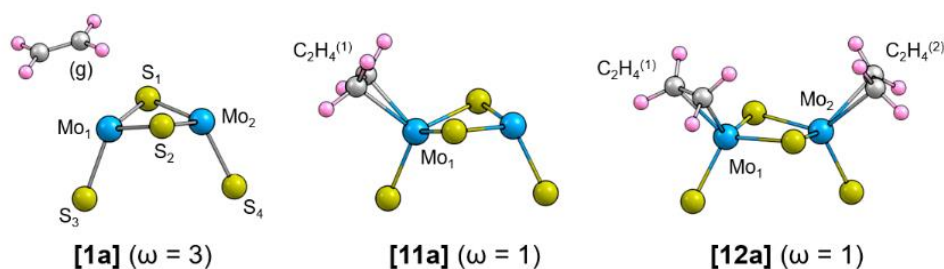
5.7.7 Ethene Adsorption on Mo₂S₄

Figure S5.10 DFT/B3LYP/def2-TZVP-optimized geometries of Mo₂S₄ clusters with one ([11a]) or two ([12a]) ethene molecules adsorbed on Mo. The optimized geometry of bare Mo₂S₄ cluster with gas-phase ethene [1a] is also shown for comparison. The reported spin-multiplicities (ω) correspond to the thermodynamically most stable configurations (Tables S5.13 and S5.14). Optimized geometries obtained using DFT/PBE0/def2-TZVP were similar. S: yellow; Mo: blue; H: pink; C: gray.

Table S5.13 Enthalpies (ΔH) and free energies (ΔG) of Mo₂S₄ clusters with (multiple) ethene molecule(s) adsorbed on Mo, computed at (a) T = 473 K and $p_{\text{C}_2\text{H}_4} = 50$ mbar, and (b) T = 173 K and $p_{\text{C}_2\text{H}_4} = 1$ bar, with DFT/B3LYP/def2-TZVP. The corresponding structures are shown in Figure S5.10.

(a) T = 473 K and $p_{\text{C}_2\text{H}_4} = 50$ mbar						
Spin-multiplicity (ω)	$\Delta H^{473\text{K}} / \text{kJ}\cdot\text{mol}^{-1}$			$\Delta G^{473\text{K}} / \text{kJ}\cdot\text{mol}^{-1}$		
	1	3	5	1	3	5
[1a]	0.0 ^a	-32.2	-10.4	0.0	-35.1	-24.0
[11a]	-213.6	-185.3	-113.0	-107.5	-89.0	-24.8
[12a]	-356.8	-311.0	-184.0	-148.6	-113.8	3.3

(b) T = 173 K and $p_{\text{C}_2\text{H}_4} = 1$ bar						
Spin-multiplicity (ω)	$\Delta H^{173\text{K}} / \text{kJ}\cdot\text{mol}^{-1}$			$\Delta G^{173\text{K}} / \text{kJ}\cdot\text{mol}^{-1}$		
	1	3	5	1	3	5
[1a]	0.0 ^a	-32.0	-11.0	0.0 ^a	-33.2	-15.6
[11a]	-216.0	-188.3	-116.9	-184.7	-160.2	-91.2
[12a]	-362.3	-317.5	-191.7	-300.7	-259.3	-136.4

^a The enthalpy and free energy of [1a] with spin-multiplicity, $\omega = 1$ (*i.e.*, no unpaired electrons) was used as the standard and was set to zero.

Table S5.14 Enthalpies (ΔH) and free energies (ΔG) of Mo_2S_4 clusters with (multiple) ethene molecule(s) adsorbed on Mo, computed at (a) $T = 473$ K and $p_{\text{C}_2\text{H}_4} = 50$ mbar, and (b) $T = 173$ K and $p_{\text{C}_2\text{H}_4} = 1$ bar, with DFT/PBE0/def2-TZVPP. The corresponding structures are shown in Figure S5.10.

(a) $T = 473$ K and $p_{\text{C}_2\text{H}_4} = 50$ mbar						
Spin-multiplicity (ω)	$\Delta H^{473\text{K}} / \text{kJ}\cdot\text{mol}^{-1}$			$\Delta G^{473\text{K}} / \text{kJ}\cdot\text{mol}^{-1}$		
	1	3	5	1	3	5
[1a]	0.0 ^a	-39.9	-27.6	0.0	-42.9	-42.6
[11a]	-236.6	-212.8	-143.5	-130.6	-116.7	-56.1
[12a]	-397.9	-353.1	-223.3	-188.9	-155.4	-36.3

(b) $T = 173$ K and $p_{\text{C}_2\text{H}_4} = 1$ bar						
Spin-multiplicity (ω)	$\Delta H^{173\text{K}} / \text{kJ}\cdot\text{mol}^{-1}$			$\Delta G^{173\text{K}} / \text{kJ}\cdot\text{mol}^{-1}$		
	1	3	5	1	3	5
[1a]	0.0 ^a	-39.7	-28.4	0.0 ^a	-40.9	-33.4
[11a]	-238.8	-215.7	-147.5	-207.7	-187.7	-122.0
[12a]	-403.2	-359.4	-231.0	-341.4	-301.1	-175.7

^a The enthalpy and free energy of **[1a]** with spin-multiplicity, $\omega = 1$ (*i.e.*, no unpaired electrons) was used as the standard and was set to zero.

Table S5.15 Mayer bond orders and bond lengths of relevant bonds in the thermodynamically most-stable Mo_2S_4 configurations with (multiple) ethene molecule(s) adsorbed on Mo computed with (i) DFT/B3LYP/def2-TZVPP, and (ii) DFT/PBE0/def2-TZVPP. The nomenclature of atoms corresponds to the structures shown in Figure S5.10.

Structure (spin-multiplicity)	Bond	Mayer bond order		Bond length / Å	
		B3LYP	PBE0	B3LYP	PBE0
[1a] ($\omega = 3$)	$\text{C}_1 - \text{C}_2$	1.910	1.946	1.325	1.323
	$\text{Mo}_1 - \text{C}_1^{(1)}$	0.683	0.707	2.203	2.174
[11a] ($\omega = 1$)	$\text{Mo}_1 - \text{C}_2^{(1)}$	0.683	0.707	2.202	2.174
	$\text{C}_1^{(1)} - \text{C}_2^{(1)}$	1.063	1.075	1.420	1.420
[12a] ($\omega = 1$)	$\text{Mo}_1 - \text{C}_1^{(1)}$	0.509	0.541	2.315	2.273
	$\text{Mo}_1 - \text{C}_2^{(1)}$	0.604	0.644	2.238	2.200
	$\text{C}_1^{(1)} - \text{C}_2^{(1)}$	1.172	1.177	1.397	1.400
	$\text{Mo}_2 - \text{C}_1^{(2)}$	0.604	0.645	2.237	2.199
	$\text{Mo}_2 - \text{C}_2^{(2)}$	0.510	0.543	2.314	2.271
	$\text{C}_1^{(2)} - \text{C}_2^{(2)}$	1.171	1.176	1.398	1.400

Table S5.16 Net Hirshfeld charges in the thermodynamically most-stable Mo₂S₄ configurations with (multiple) ethene molecule(s) adsorbed on Mo, computed with (a) DFT/B3LYP/def2-TZVPP, and (b) DFT/PBE0/def2-TZVPP. The nomenclature of atoms corresponds to the structures shown in Figure S5.10.

(a) DFT/B3LYP/def2-TZVPP			
Structure	Net Hirshfeld charges		
	[1a]	[11a]	[12a]
Spin-multiplicity (ω)	3	1	1
Mo ₂ S ₄	0.000	0.095	0.011
C ₂ H ₄ ⁽¹⁾	-	-0.095	-0.005
C ₂ H ₄ ⁽²⁾	-	-	-0.006

(b) DFT/PBE0/def2-TZVPP			
Structure	Net Hirshfeld charges		
	[1a]	[11a]	[12a]
Spin-multiplicity (ω)	3	1	1
Mo ₂ S ₄	0.000	0.098	0.018
C ₂ H ₄ ⁽¹⁾	-	-0.098	-0.009
C ₂ H ₄ ⁽²⁾	-	-	-0.010

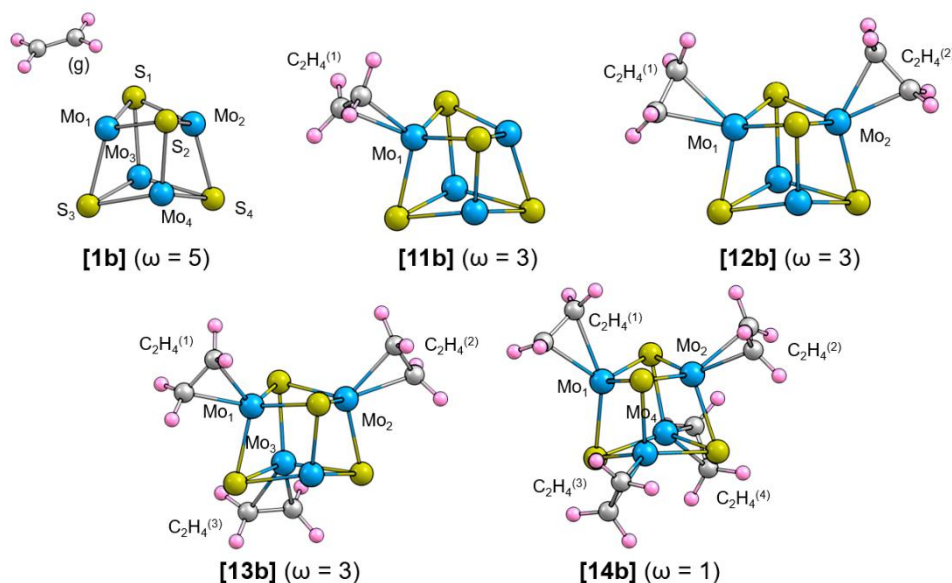
5.7.8 Ethene Adsorption on Mo₄S₄

Figure S5.11 DFT/B3LYP/def2-TZVP-optimized geometries of Mo₄S₄ clusters with one (**[11b]**), two (**[12b]**), three (**[13b]**), or four (**[14b]**) ethene molecule(s) adsorbed on Mo. The optimized geometry of bare Mo₄S₄ cluster with gas-phase ethene (**[1b]**) is also shown for comparison. The reported spin-multiplicities (ω) correspond to the thermodynamically most-stable configurations (Tables S5.17 and S5.18). Optimized geometries obtained using DFT/PBE0/def2-TZVP were similar. S: yellow; Mo: blue; H: pink; C: gray.

Table S5.17 Enthalpies (ΔH) and free energies (ΔG) of Mo_4S_4 clusters with (multiple) ethene molecule(s) adsorbed on Mo, computed with DFT/B3LYP/def2-TZVPP at (a) $T = 473$ K and $p_{\text{C}_2\text{H}_4} = 50$ mbar, and (b) $T = 173$ K and $p_{\text{C}_2\text{H}_4} = 1$ bar. The corresponding structures are shown in Figure S5.11.

(a) $T = 473$ K and $p_{\text{C}_2\text{H}_4} = 50$ mbar

Spin-multiplicity (ω)	$\Delta H^{473\text{K}} / \text{kJ}\cdot\text{mol}^{-1}$				$\Delta G^{473\text{K}} / \text{kJ}\cdot\text{mol}^{-1}$			
	1	3	5	7	1	3	5	7
[1b]	0.0 ^a	11.7	6.6	43.4	0.0	-4.1	-11.0	22.4
[11b]	-154.8	-185.4	-145.4	-87.5	-56.8	-94.2	-62.8	-1.5
[12b]	-325.4	-316.8	-278.2	-218.1	-126.8	-125.1	-93.9	-38.3
[13b]	-451.9	-450.1	-395.8	-372.5	-152.4	-154.6	-107.2	-88.5
[14b]	-567.1	-496.1	-531.5	-466.4	-162.8	-100.2	-139.4	-83.0

(b) $T = 173$ K and $p_{\text{C}_2\text{H}_4} = 1$ bar

Spin-multiplicity (ω)	$\Delta H^{173\text{K}} / \text{kJ}\cdot\text{mol}^{-1}$				$\Delta G^{173\text{K}} / \text{kJ}\cdot\text{mol}^{-1}$			
	1	3	5	7	1	3	5	7
[1b]	0.0 ^a	10.4	5.1	41.8	0.0 ^a	5.5	-0.3	35.2
[11b]	-158.6	-189.6	-150.3	-91.4	-129.4	-162.6	-126.0	-62.2
[12b]	-332.6	-324.3	-286.5	-226.6	-273.5	-267.5	-231.9	-164.9
[13b]	-462.5	-460.5	-406.9	-384.0	-373.4	-373.0	-321.5	-287.0
[14b]	-580.3	-510.1	-545.5	-481.8	-460.2	-392.6	-429.4	-350.7

^a The enthalpy and free energy of **[1b]** with spin-multiplicity, $\omega = 1$ (*i.e.*, no unpaired electrons) was used as the standard and was set to zero.

Table S5.18 Enthalpies (ΔH) and free energies (ΔG) of Mo_4S_4 clusters with (multiple) ethene molecule(s) adsorbed on Mo, computed with DFT/PBE0/def2-TZVPP at (a) $T = 473$ K and $p_{\text{C}_2\text{H}_4} = 50$ mbar, and (b) $T = 173$ K and $p_{\text{C}_2\text{H}_4} = 1$ bar. The corresponding structures are shown in Figure S5.11.

(a) $T = 473$ K and $p_{\text{C}_2\text{H}_4} = 50$ mbar

Spin-multiplicity (ω)	$\Delta H^{473\text{K}} / \text{kJ}\cdot\text{mol}^{-1}$				$\Delta G^{473\text{K}} / \text{kJ}\cdot\text{mol}^{-1}$			
	1	3	5	7	1	3	5	7
[1b]	0.0 ^a	5.0	-5.9	25.6	0.0	-7.2	-23.5	4.3
[11b]	-184.0	-225.6	-181.6	-130.9	-85.4	-125.9	-98.5	-48.9
[12b]	-381.4	-376.7	-343.1	-282.1	-181.9	-184.4	-157.5	-101.3
[13b]	-533.9	-531.6	-482.7	-464.8	-232.7	-235.3	-192.9	-179.5
[14b]	-673.7	-601.1	-641.4	-579.1	-267.3	-203.3	-247.8	-193.0

(b) $T = 173$ K and $p_{\text{C}_2\text{H}_4} = 1$ bar

Spin-multiplicity (ω)	$\Delta H^{173\text{K}} / \text{kJ}\cdot\text{mol}^{-1}$				$\Delta G^{173\text{K}} / \text{kJ}\cdot\text{mol}^{-1}$			
	1	3	5	7	1	3	5	7
[1b]	0.0 ^a	4.0	-7.6	23.8	0.0 ^a	0.2	-12.9	17.2
[11b]	-187.7	-227.4	-186.5	-135.5	-158.4	-198.7	-162.0	-107.3
[12b]	-388.6	-384.1	-351.2	-290.6	-329.2	-327.2	-296.3	-228.5
[13b]	-544.2	-541.8	-493.7	-476.2	-454.7	-454.1	-407.9	-378.8
[14b]	-686.4	-614.8	-655.2	-594.0	-565.9	-496.8	-538.7	-462.3

^a The enthalpy and free energy of **[1b]** with spin-multiplicity, $\omega = 1$ (*i.e.*, no unpaired electrons) was used as the standard and was set to zero.

Table S5.19 Mayer bond orders and bond lengths of relevant bonds in the thermodynamically most-stable Mo₄S₄ configurations with (multiple) ethene molecule(s) adsorbed on Mo, computed with (i) DFT/B3LYP/def2-TZVPP, and (ii) DFT/PBE0/def2-TZVPP. The nomenclature of atoms corresponds to the structures shown in Figure S5.11.

Structure (spin-multiplicity)	Bond	Mayer bond order		Bond length /Å	
		B3LYP	PBE0	B3LYP	PBE0
[1b] ($\omega = 5$)	C ₁ - C ₂	1.910	1.946	1.325	1.323
	Mo ₁ - C ₁ ⁽¹⁾	0.611	0.643	2.216	2.188
[11b] ($\omega = 3$)	Mo ₁ - C ₂ ⁽¹⁾	0.674	0.698	2.194	2.169
	C ₁ ⁽¹⁾ - C ₂ ⁽¹⁾	1.104	1.121	1.427	1.428
	Mo ₁ - C ₁ ⁽¹⁾	0.684	0.707	2.186	2.164
[12b] ($\omega = 3$)	Mo ₁ - C ₂ ⁽¹⁾	0.601	0.630	2.218	2.192
	C ₁ ⁽¹⁾ - C ₂ ⁽¹⁾	1.106	1.125	1.425	1.425
	Mo ₂ - C ₁ ⁽²⁾	0.600	0.630	2.219	2.192
	Mo ₂ - C ₂ ⁽²⁾	0.683	0.707	2.189	2.184
	C ₁ ⁽²⁾ - C ₂ ⁽²⁾	1.106	1.125	1.425	1.425
	Mo ₁ - C ₁ ⁽¹⁾	0.640	0.662	2.207	2.182
[13b] ($\omega = 3$)	Mo ₁ - C ₂ ⁽¹⁾	0.637	0.660	2.209	2.184
	C ₁ ⁽¹⁾ - C ₂ ⁽¹⁾	1.120	1.144	1.422	1.421
	Mo ₂ - C ₁ ⁽²⁾	0.639	0.662	2.207	2.182
	Mo ₂ - C ₂ ⁽²⁾	0.635	0.659	2.210	2.184
	C ₁ ⁽²⁾ - C ₂ ⁽²⁾	1.121	1.145	1.421	1.421
	Mo ₃ - C ₁ ⁽³⁾	0.594	0.620	2.238	2.208
	Mo ₃ - C ₂ ⁽³⁾	0.593	0.619	2.238	2.208
	C ₁ ⁽³⁾ - C ₂ ⁽³⁾	1.170	1.189	1.407	1.408
[14b] ($\omega = 1$)	Mo ₁ - C ₁ ⁽¹⁾	0.595	0.641	2.241	2.201
	Mo ₁ - C ₂ ⁽¹⁾	0.505	0.553	2.284	2.245
	C ₁ ⁽¹⁾ - C ₂ ⁽¹⁾	1.155	1.149	1.408	1.412
	Mo ₂ - C ₁ ⁽²⁾	0.670	0.704	2.181	2.153
	Mo ₂ - C ₂ ⁽²⁾	0.585	0.622	2.231	2.203
	C ₁ ⁽²⁾ - C ₂ ⁽²⁾	1.095	1.110	1.427	1.428
	Mo ₃ - C ₁ ⁽³⁾	0.640	0.665	2.217	2.190
	Mo ₃ - C ₂ ⁽³⁾	0.635	0.657	2.203	2.179
	C ₁ ⁽³⁾ - C ₂ ⁽³⁾	1.120	1.143	1.416	1.415
	Mo ₄ - C ₁ ⁽⁴⁾	0.622	0.638	2.216	2.193
	Mo ₄ - C ₂ ⁽⁴⁾	0.624	0.647	2.212	2.187
	C ₁ ⁽⁴⁾ - C ₂ ⁽⁴⁾	1.136	1.161	1.412	1.409

Table S5.20 Net Hirshfeld charges in the thermodynamically most-stable Mo₄S₄ configurations with (multiple) ethene molecule(s) adsorbed on Mo, computed with (a) DFT/B3LYP/def2-TZVPP, and (b) DFT/PBE0/def2-TZVPP. The nomenclature of atoms corresponds to the structures shown in Figure S5.11.

(a) DFT/B3LYP/def2-TZVPP					
Structure	Net Hirshfeld charges				
	[1b]	[11b]	[12b]	[13b]	[14b]
Spin-multiplicity (ω)	5	3	3	3	1
Mo ₂ S ₄	0.000	0.220	0.328	0.463	0.567
C ₂ H ₄ ⁽¹⁾	-	-0.220	-0.119	-0.170	-0.120
C ₂ H ₄ ⁽²⁾	-	-	-0.209	-0.169	-0.191
C ₂ H ₄ ⁽³⁾	-	-	-	-0.124	-0.137
C ₂ H ₄ ⁽⁴⁾	-	-	-	-	-0.119

(b) DFT/PBE0/def2-TZVPP					
Structure	Net Hirshfeld charges				
	[1b]	[11b]	[12b]	[13b]	[14b]
Spin-multiplicity (ω)	5	3	3	3	1
Mo ₂ S ₄	0.000	0.224	0.328	0.461	0.566
C ₂ H ₄ ⁽¹⁾	-	-0.224	-0.118	-0.169	-0.132
C ₂ H ₄ ⁽²⁾	-	-	-0.210	-0.169	-0.194
C ₂ H ₄ ⁽³⁾	-	-	-	-0.124	-0.132
C ₂ H ₄ ⁽⁴⁾	-	-	-	-	-0.108

5.7.9 Competitive Adsorption between Hydrogen and Ethene on Mo_2S_4

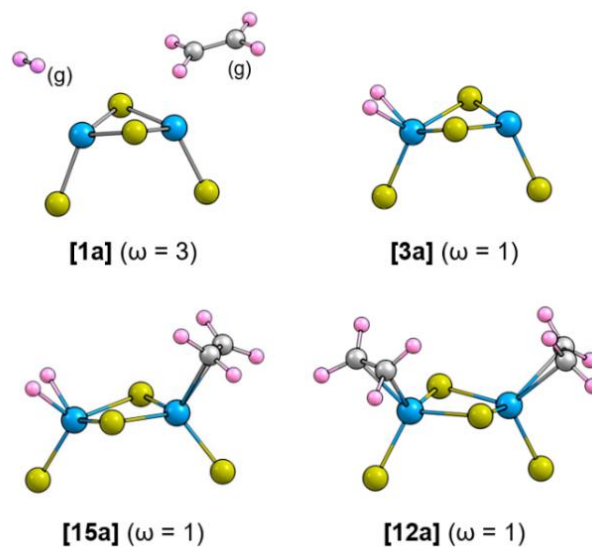


Figure S5.12 DFT/B3LYP/def2-TZVP-optimized geometries of Mo_2S_4 clusters with (simultaneously) adsorbed ethene and hydrogen. The reported spin-multiplicities (ω) correspond to the thermodynamically most stable configurations (Table S5.21). Optimized geometries obtained using DFT/PBE0/def2-TZVP were similar. S: yellow; Mo: blue; C: gray; H: pink.

Table S5.21 Enthalpies (ΔH) and free energies (ΔG) of Mo_2S_4 clusters with (simultaneously) adsorbed ethene and hydrogen, computed at $T = 473$ K, $p_{\text{C}_2\text{H}_4} = 50$ mbar, and $p_{\text{H}_2} = 1$ bar, with (a) DFT/B3LYP/def2-TZVPP, and (b) DFT/PBE0/def2-TZVPP. The corresponding structures are shown in Figure S5.12.

(a) DFT/B3LYP/def2-TZVPP						
Spin-multiplicity (ω)	$\Delta H^{473\text{K}} / \text{kJ}\cdot\text{mol}^{-1}$			$\Delta G^{473\text{K}} / \text{kJ}\cdot\text{mol}^{-1}$		
	1	3	5	1	3	5
[1a]	0.0 ^a	-32.2	-10.4	0.0	-35.1	-24.0
[3a]	-120.9	-81.2	-7.6	-61.0	-37.1	31.1
[15a]	-248.3	-207.4	- ^b	-87.4	-56.3	- ^b
[12a]	-356.8	-311.0	-184.0	-148.6	-113.8	3.3

(b) DFT/PBE0/def2-TZVPP						
Spin-multiplicity (ω)	$\Delta H^{473\text{K}} / \text{kJ}\cdot\text{mol}^{-1}$			$\Delta G^{473\text{K}} / \text{kJ}\cdot\text{mol}^{-1}$		
	1	3	5	1	3	5
[1a]	0.0 ^a	-39.9	-27.6	0.0	-42.9	-42.6
[3a]	-130.7	-97.4	-30.2	-71.6	-46.2	7.1
[15a]	-279.1	-236.0	- ^b	-119.2	-85.7	- ^b
[12a]	-397.9	-353.1	-223.3	-188.9	-155.4	-36.3

^a The enthalpy and free energy of **[1a]** with spin-multiplicity, $\omega = 1$ (*i.e.*, no unpaired electrons) was used as the standard and was set to zero.

^b The optimized structure with non-imaginary vibrational frequency modes was not achieved.

5.7.10 Competitive Adsorption between Hydrogen and Ethene on Mo_4S_4

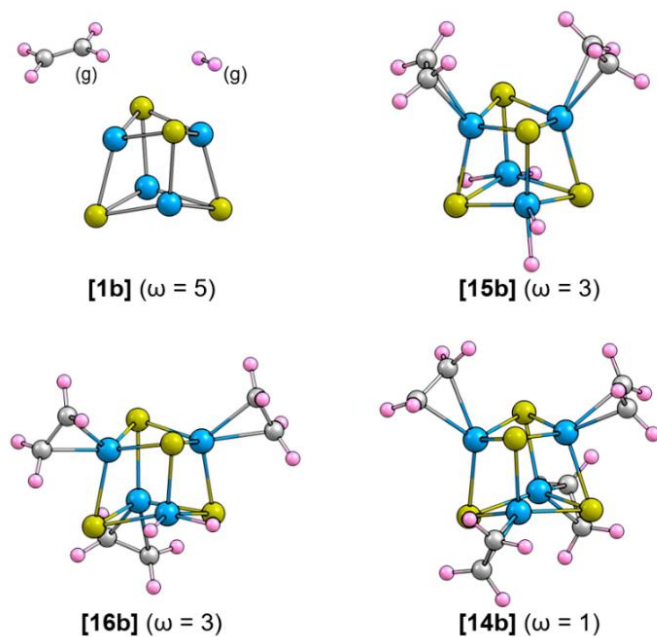


Figure S5.13 DFT/B3LYP/def2-TZVP-optimized geometries of Mo_4S_4 clusters with (simultaneously) adsorbed ethene and hydrogen. The reported spin-multiplicities (ω) correspond to the thermodynamically most stable configurations (Table S5.22). Optimized geometries obtained using DFT/PBE0/def2-TZVP were similar. S: yellow; Mo: blue; C: gray; H: pink.

Table S5.22 Enthalpies (ΔH) and free energies (ΔG) of Mo_4S_4 clusters with (simultaneously) adsorbed ethene and hydrogen, computed at $T = 473$ K, $p_{\text{C}_2\text{H}_4} = 50$ mbar, and $p_{\text{H}_2} = 1$ bar, with (a) DFT/B3LYP/def2-TZVPP, and (b) DFT/PBE0/def2-TZVPP. The corresponding structures are shown in Figure S5.13.

(a) DFT/B3LYP/def2-TZVPP								
Spin-multiplicity (ω)	$\Delta H^{473\text{K}} / \text{kJ}\cdot\text{mol}^{-1}$				$\Delta G^{473\text{K}} / \text{kJ}\cdot\text{mol}^{-1}$			
	1	3	5	7	1	3	5	7
[1b]	0.0 ^a	11.7	6.6	43.4	0.0	-4.1	-11.0	22.4
[15b]	-376.2	-375.6	-351.7	-271.3	-56.1	-75.5	-61.3	17.2
[16b]	-457.7	-465.0	-442.3	-381.1	-101.4	-113.5	-103.7	-45.4
[14b]	-567.1	-496.1	-531.5	-466.4	-162.8	-100.2	-139.4	-83.0

(b) DFT/PBE0/def2-TZVPP								
Spin-multiplicity (ω)	$\Delta H^{473\text{K}} / \text{kJ}\cdot\text{mol}^{-1}$				$\Delta G^{473\text{K}} / \text{kJ}\cdot\text{mol}^{-1}$			
	1	3	5	7	1	3	5	7
[1b]	0.0 ^a	5.0	-5.9	25.6	0.0	-7.2	-23.5	4.3
[15b]	-447.3	-450.8	-431.2	-348.7	-135.3	-150.3	-132.0	-59.7
[16b]	-546.6	-560.0	-535.3	-477.1	-187.8	-207.1	-195.8	-139.8
[14b]	-673.7	-601.1	-641.4	-579.1	-267.3	-203.3	-247.8	-193.0

^a The enthalpy and free energy of **[1b]** with spin-multiplicity, $\omega = 1$ (*i.e.*, no unpaired electrons) was used as the standard and was set to zero.

5.7.11 X-ray Absorption Spectroscopy (XAS) Measurements

XAS measurements were performed at the P65 beamline of the German Electron Synchrotron (DESY) in Hamburg, Germany.² The storage ring operated at 6 GeV energy and 100 mA current. A water-cooled Si311 double crystal monochromator (DCM) was used for obtaining monochromatic X-rays. Two Rh-coated plane mirrors were installed in front of the DCM to reject higher harmonics. The DCM was calibrated to Mo K-edge energy by measuring a reference Mo foil and setting the first major inflection point to 20 000 eV. The beam spot-size was 200 μm (vertical) \times 1.6 mm (horizontal) on the sample and the energy resolution of incident X-rays is estimated to be ~ 2 eV ($\Delta E/E \sim 1.0 \times 10^{-4}$) at Mo K-edge energy.

The carbonyl containing catalyst precursors were placed in a quartz capillary (WJM Glas, 1 mm outer diameter, 20 μm thickness) supported between two quartz wool plugs. The capillary was heated from below with a hot-air gas-blower (Oxford FMB). Gas flow rates were controlled using electronic mass flow controllers (Bronkhorst) and the pressure was monitored using a pressure gauge (Omega). All experiments were performed at ambient pressure. The catalyst precursors were sulfided *in situ* in a flow of 10 mL \cdot min⁻¹ H₂S (10 vol.-% in H₂) at 673 K for 2 h to form the sulfided Mo₂S₄/NaY catalyst. This sample was then treated in 10 mL \cdot min⁻¹ H₂ at 673 K for 2 h to form the reduced Mo₄S₄/NaY catalyst. After performing sulfidation/reduction, the catalysts were exposed to ethene hydrogenation reaction conditions ($T \approx 473$ K, $p_{\text{H}_2} \approx 950$ mbar, $p_{\text{C}_2\text{H}_4} \approx 50$ mbar) for at least 2 h. The capillary was then cooled down to room temperature and placed on the sample stage for XAS measurements, whilst maintaining the ethene/H₂ gas flow. The data were monitored for any signs of X-ray beam damage. Several successive scans were averaged to reduce signal-to-noise ratio and improve the data quality.

The XAS spectra were measured between 19 800 and 21 000 eV in total fluorescence yield (TFY) mode using a passivated implanted planar silicon (PIPS) detector. For extended X-ray absorption fine structure (EXAFS) analyses, spectra were background subtracted, normalized, k^3 -weighted, and Fourier-transformed (FT) between $k = 3$ and $k = 12$ \AA^{-1} . The EXAFS fitting was performed in k -space between 3 and 12 \AA^{-1} simultaneously on the k^1 -, k^2 -, and k^3 -weighted data. The fitting was performed using Artemis software package.³ E_0 was set such that energy shift (ΔE_0) obtained during the fit was less than 1 eV. A reference Mo foil was first fitted to Mo bcc

structure and the Mo–Mo coordination number was set to 8 and 6 (theoretical values based on the bcc structure) for the first and second coordination shells, respectively, to obtain the amplitude reduction factor (S_0^2) which was then used in the subsequent fits.

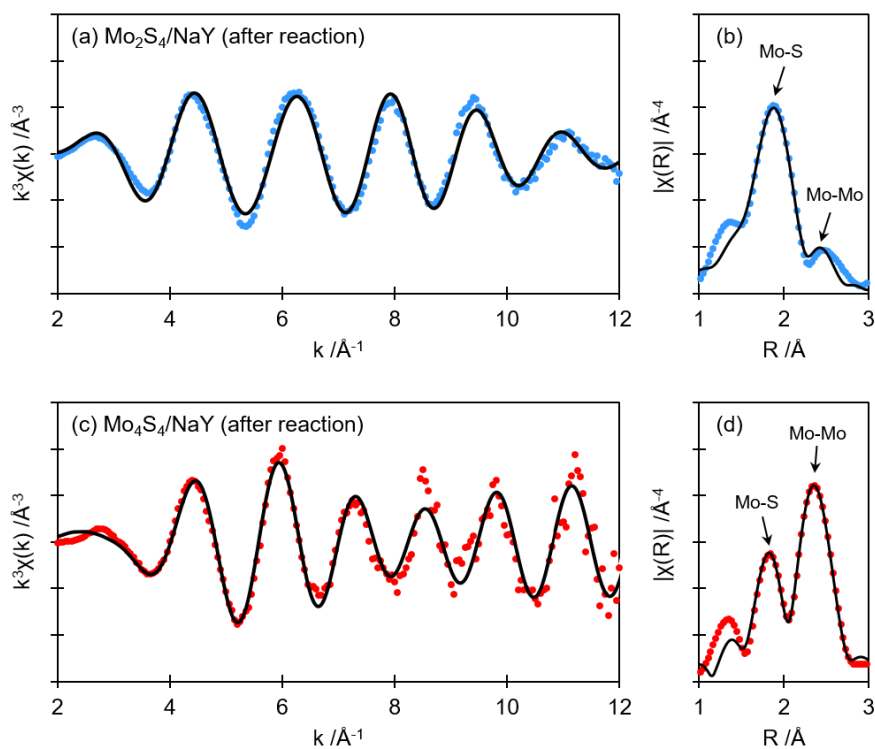


Figure S5.14 k^3 -weighted EXAFS (a, c) and Fourier-transformed EXAFS (b, d) of Mo₂S₄/NaY (blue) and Mo₄S₄/NaY (red), after 2 h time-on-stream under ethene hydrogenation reaction conditions ($T \approx 473$ K, $p_{\text{C}_2\text{H}_4} \approx 50$ mbar, and $p_{\text{H}_2} \approx 960$ mbar). Experimental data are shown as closed symbols and the fitted data are shown as solid black lines.

Table S5.23 EXAFS fitting parameters: coordination numbers (CN), interatomic distances (d), and Debye-Waller factors (σ^2), for Mo-S and Mo-Mo paths, in (a) Mo₂S₄/NaY, and (b) Mo₄S₄/NaY, after 2 h time-on-stream under ethene hydrogenation conditions ($T \approx 473$ K, $p_{\text{C}_2\text{H}_4} \approx 50$ mbar, and $p_{\text{H}_2} \approx 960$ mbar). The (previously reported) CN_{Mo-Mo}, CN_{Mo-S}, $d_{\text{Mo-Mo}}$, and $d_{\text{Mo-S}}$ for fresh Mo_xS_y/NaY catalysts are also shown for comparison.

(a) Mo ₂ S ₄ /NaY				
	Path	CN	$d/\text{\AA}$	$\sigma^2 \times 1000/\text{\AA}^2$
Fresh catalyst	Mo-S	3.9 ^a	2.42 ^a	
	Mo-Mo	1.3 ^a	2.77 ^a	
After reaction	Mo-S	3.1 ± 0.8	2.39 ± 0.02	8.1 ± 2.4
	Mo-Mo	1.3 ± 2.4	2.77 ± 0.04	13.7 ± 13
(b) Mo ₄ S ₄ /NaY				
	Path	CN	$d/\text{\AA}$	$\sigma^2 \times 1000/\text{\AA}^2$
Fresh catalyst	Mo-S	2.6 ^a	2.47 ^a	
	Mo-Mo	3.3 ^a	2.66 ^a	
After reaction	Mo-S	2.9 ± 2.3	2.44 ± 0.09	7.2 ± 9.1
	Mo-Mo	3.0 ± 3.2	2.66 ± 0.06	7.2 ± 5.3

^a Data from Weindl *et al.*⁴

5.7.12 Langmuir–Hinshelwood and Eley–Rideal Reaction Pathways on Mo₂S₄

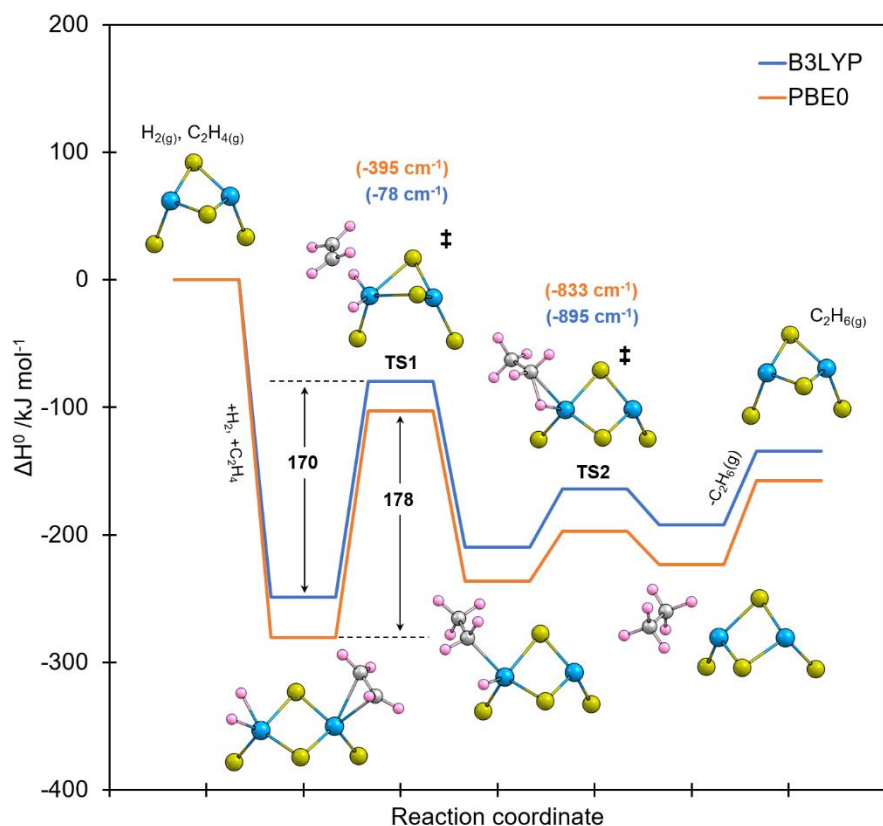


Figure S5.15 Standard enthalpy diagram of Langmuir–Hinshelwood (LH) type reaction pathway for ethene hydrogenation on Mo₂S₄ cluster with spin-multiplicity $\omega = 1$, showing the reaction between an adsorbed H₂ and an adsorbed ethene, computed with (i) DFT/B3LYP/def2-TZVP, and (ii) DFT/PBE0/def2-TZVP. Values shown in the figure are in kJ·mol⁻¹. Values shown in parentheses are the imaginary frequencies of the corresponding transition state structures. Displayed structures were optimized with B3LYP. Optimized transition state structures. Displayed structures were optimized with B3LYP. Optimized geometries obtained using PBE0 were similar. S: yellow; Mo: blue; H: pink; C: gray.

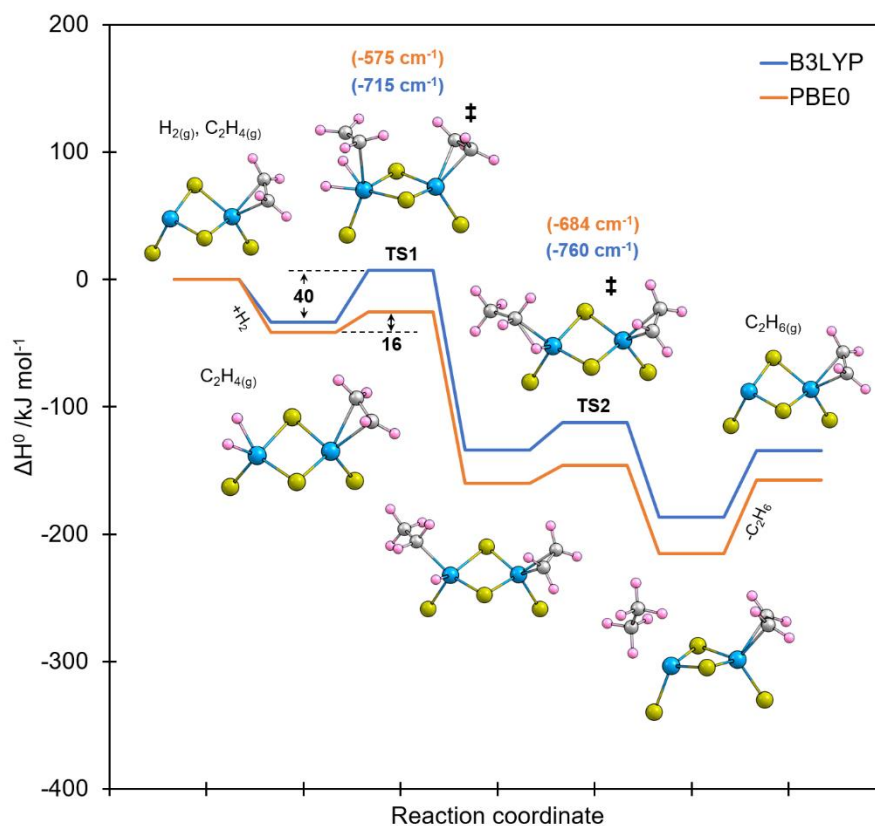
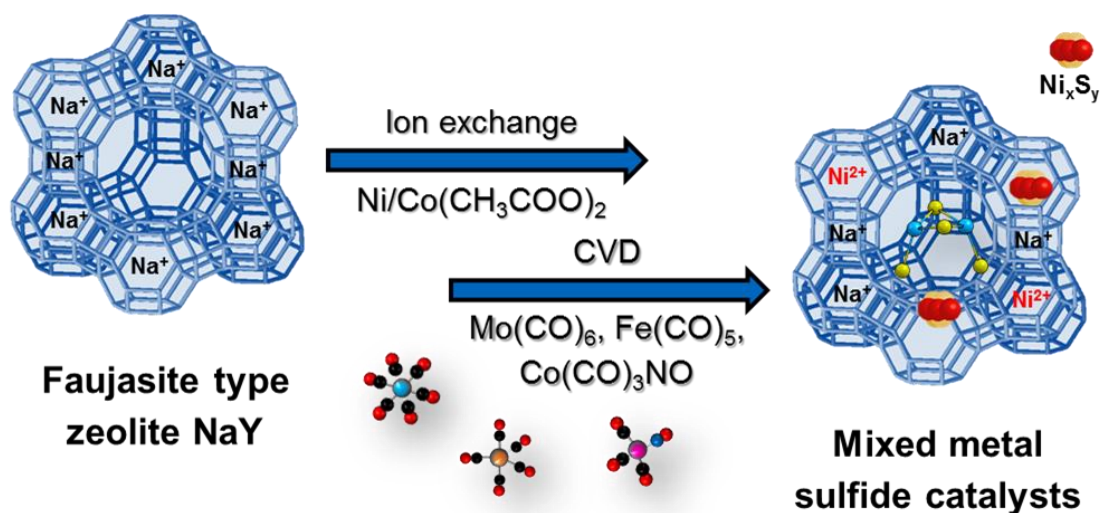


Figure S5.16 Standard enthalpy diagram of Eley-Rideal (ER) type reaction pathway for ethene hydrogenation on Mo_2S_4 cluster with spin-multiplicity $\omega = 1$, showing the reaction between an adsorbed H_2 and a gas-phase ethene, computed with (i) DFT/B3LYP/def2-TZVP, and (ii) DFT/PBE0/def2-TZVP. Values shown in the figure are in $\text{kJ}\cdot\text{mol}^{-1}$. Values shown in parentheses are the imaginary frequency of the corresponding transition state structures. Displayed structures were optimized with B3LYP. Optimized geometries obtained using PBE0 were similar. S: yellow; Mo: blue; H: pink; C: gray.

5.8 References

- (1) Ribeiro, R. F.; Marenich, A. V.; Cramer, C. J.; Truhlar, D. G. *The Journal of Physical Chemistry B* **2011**, *115*, 14556.
- (2) Welter, E.; Chernikov, R.; Herrmann, M.; Nemausat, R. *AIP Conference Proceedings* **2019**, *2054*, 040002.
- (3) Ravel, B.; Newville, M. *Journal of Synchrotron Radiation* **2005**, *12*, 537.
- (4) Weindl, R.; Khare, R.; Kovarik, L.; Jentys, A.; Reuter, K.; Shi, H.; Lercher, J. A. *Angewandte Chemie International Edition* **2021**, *60*, 9301.

6 Catalytic Hydrogenation on Zeolite Supported Mixed Metal Sulfide Clusters



Keywords: Transition metal sulfide clusters • Hydrogenation • IR spectroscopy • Density functional theory

Abstract

The catalytic hydrogenation activity of molecular Mo_xS_y clusters encapsulated in faujasite zeolites is significantly affected by the presence of a second transition metal. We introduced an additional transition metal either by ion exchange (Ni, Co) or by chemical vapor deposition (Fe, Co) leading to the formation of different mixed metal sulfide phases. In the former case, separate metal sulfide phases are formed in proximity resulting in an enhanced hydrogenation activity. We attribute that to an improved stabilization of adsorbed hydrogen in form of hydrides on the Mo centers and to the formation of sulfhydryl groups on S atoms bridging both sulfide phases. Both factors enhance the hydrogenation rate by increasing the overall availability of adsorbed hydrogen. Introduction of a second transition metal *via* chemical vapor deposition, on the other hand, partly results in formation of mixed metal sulfide clusters after sulfidation. These mixed metal clusters possess a significantly lower catalytic activity decreasing the overall hydrogenation rates.

6.1 Structures of Mixed Metal Sulfide Phases

Using transmission electron microscopy (TEM) and energy dispersive X-ray spectroscopy (EDX) we have shown previously that for $\text{Mo}_x\text{S}_y/\text{NaY-sulf}$ the majority of the metal sulfide phase is present in form of well-defined, molecular clusters inside the zeolite framework.¹ Similarly, we have analyzed bimetallic catalysts prepared *via* sequential chemical vapor deposition (CVD) of Co/Fe and Mo. The TEM images of spent $\text{Fe}_x\text{Mo}_y\text{S}_z/\text{NaY-sulf}$ and $\text{Co}_x\text{Mo}_y\text{S}_z/\text{NaY-sulf}$ catalysts are shown in Figure S6.1 of the Supporting Information. The catalysts containing Co and Mo do not show major fractions of sulfide phases located on the outer surface of the zeolite crystals. In contrast to that, external, nanometer-sized sulfide particles are visible on the $\text{Fe}_x\text{Mo}_y\text{S}_z/\text{NaY-sulf}$ samples. We conclude that during sulfidation a significant fraction of Fe migrates out of the zeolite framework ultimately leading to the formation of Fe_xS_y particles. For $\text{Co}_x\text{Mo}_y\text{S}_z/\text{NaY-sulf}$ catalysts, we assume that Co_xS_y , Mo_xS_y , and mixed $\text{Co}_x\text{Mo}_y\text{S}_z$ phases are all present inside the faujasite zeolite cages. Similarly, for $\text{Mo}_x\text{S}_y/\text{CoNaY}$ and $\text{Mo}_x\text{S}_y/\text{NiNaY}$, we suppose that all TMS phases formed after sulfidation are located inside the zeolite structure.

6.2 Infrared Spectroscopy of Adsorbed Probe Molecules

According to previous reports the sulfidation of Co and Ni ion exchanged zeolites leads to the formation of molecular Co_xS_y or Ni_xS_y clusters located inside the faujasite framework.²⁻⁴ Removal of Ni/Co cations that were coordinated to acidic functions of the zeolite framework should in turn lead to formation of Brønsted acid sites (BAS) upon formation of sulfide clusters. This proposal was corroborated for both, partly Ni and Co exchanged NaY monitoring the adsorption of pyridine using infrared (IR) spectroscopy (Figure 6.1).

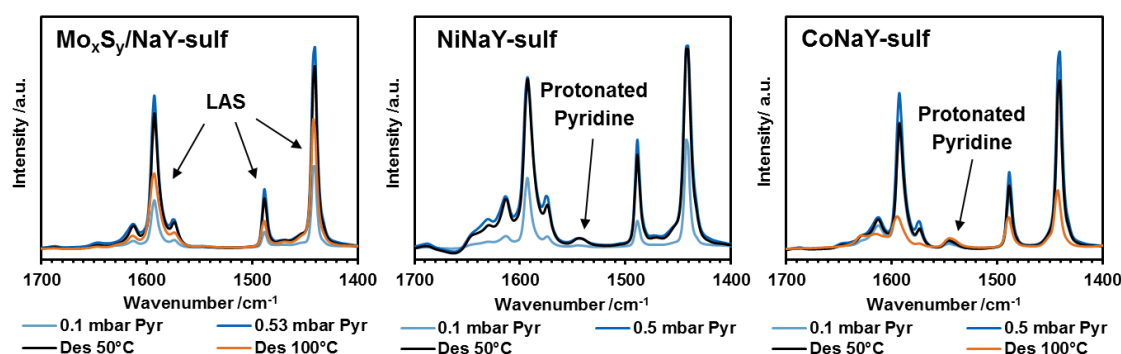


Figure 6.1 Pyridine adsorption on $\text{Mo}_x\text{S}_y/\text{NaY-sulf}$ (left; $342 \mu\text{mol}\cdot\text{g}^{-1}$ Mo; adapted from ref. ¹), NiNaY-sulf (middle), and CoNaY-sulf (right) at 323 K. Elemental compositions of the supports can be found in section 6.7.1 of the Supporting Information.

In contrast to parent NaY that only shows bands assigned to pyridine coordinated to zeolite Lewis acid sites (LAS), both ion exchanged supports additionally show a band at 1540 cm^{-1} assigned to protonated pyridine.⁵⁻⁷ This is in line with the above-mentioned formation of small Co_xS_y or Ni_xS_y clusters upon sulfidation. Using these ion exchanged materials as catalyst supports for the incorporation of Mo *via* chemical vapor deposition, we hypothesize that separate metal sulfide clusters are formed after sulfidation coexisting inside the zeolite framework and potentially interacting with each other.

For dimeric and tetrameric Mo_xS_y clusters in parent NaY zeolite we demonstrated that hydride species on the Mo centers are the active form of adsorbed hydrogen. SH groups, as found in classic, layered MoS_2 materials, were thermodynamically not favored and are therefore absent in this type of catalyst. In line with previous works, we showed the absence of Brønsted acidic SH groups using 2,6-dimethyl pyridine (DMP) as a probe molecule.⁸ Similarly, in this work we used DMP as a molecular probe for mixed metal sulfide phases. Figure 6.2 shows the adsorption of DMP on sulfided

Mo_xS_y clusters supported on partly ion exchanged NaY in comparison to the parent NaY supported catalyst.

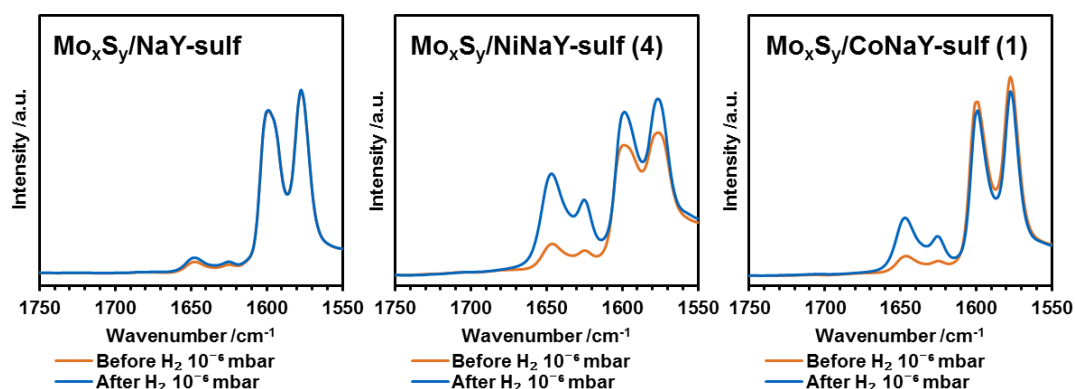


Figure 6.2 DMP adsorption on Mo_xS_y/NaY-sulf (left; 344 μmol·g⁻¹ Mo; adapted from ref. ⁸), Mo_xS_y/NiNaY-sulf (4) (middle), and Mo_xS_y/CoNaY-sulf (1) (right) before and after admission of 1 bar H₂ at 323 K. Elemental compositions of the catalysts can be found in section 6.7.1 of the Supporting Information. Spectra were collected after outgassing for 0.5 h.

For Mo_xS_y/NaY-sulf only two bands assigned to DMP coordinated to Lewis acidic sites (1575 cm⁻¹ and 1600 cm⁻¹) are present together with minor bands at 1625 cm⁻¹ and 1645 cm⁻¹ assigned to a negligible amount of protonated DMP. In contrast to that, the catalysts prepared using partly Co or Ni exchanged zeolites both show pronounced bands characteristic for protonated DMP after admission of hydrogen. This is commonly explained by the formation of SH groups upon adsorption of dihydrogen.^{6,7,9,10} Interestingly, the sulfided support materials NiNaY and CoNaY themselves did not show Brønsted acid sites before or after exposing them to H₂ (Figure S6.2). We therefore hypothesize that SH groups cannot be stabilized on monometallic Co/Ni_xS_y clusters and rather originate from S atoms bridging Co/Ni_xS_y clusters and Mo_xS_y clusters that are present in the zeolite host in close proximity.

6.3 Catalytic Hydrogenation Activity

To investigate the influence of the presence of a second transition metal, we tested all catalysts for the hydrogenation of ethene as a probe molecule. The ethane formation rates are presented in Figure 6.3 together with $\text{Mo}_x\text{S}_y/\text{NaY-sulf}$ catalysts as reference.

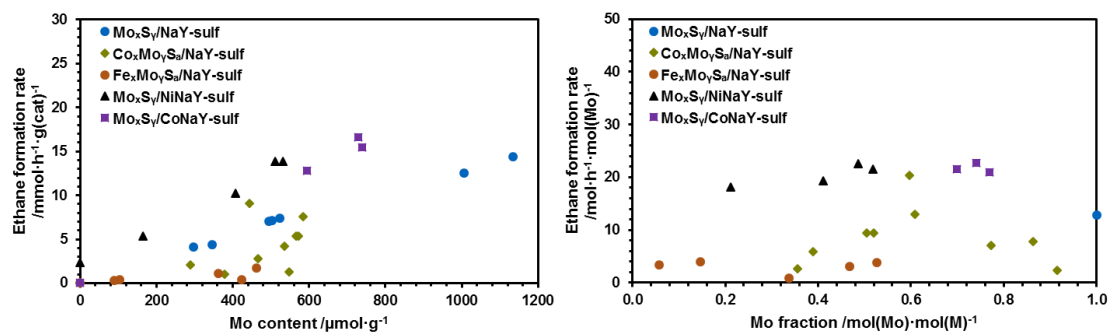


Figure 6.3 Ethane formation rates at 473 K of different bimetallic sulfide catalysts together with $\text{Mo}_x\text{S}_y/\text{NaY-sulf}$ catalysts as reference (previously reported in ref. ¹). Elemental compositions of the supports and catalysts can be found in section 6.7.1 of the Supporting Information. Activity is shown as mass-based rates plotted versus the Mo content (left) and as rates per mol of Mo plotted versus the molar fraction of Mo with respect to the total metal content (right).

We want to note, that $\text{W}_x\text{S}_y/\text{NaY-sulf}$ catalysts were also tested but did not show any hydrogenation activity under the tested conditions. Their structure and the reason for their inactivity remains unclear at this point. Similarly, monometallic $\text{Fe}_x\text{S}_y/\text{NaY-sulf}$ and $\text{Co}_x\text{S}_y/\text{NaY-sulf}$ systems showed negligible ethane formation rates at 473 K.

The $\text{Fe}_x\text{Mo}_y\text{S}_z/\text{NaY-sulf}$ catalysts, prepared from precursors synthesized *via* sequential CVD, also show only very little activity for hydrogenation irrespective of the Mo content and fraction of the catalysts. As mentioned before, we observed formation of a significant fraction of large-scale sulfide phases outside the zeolite framework with most likely only very little (or no) hydrogenation activity. Nevertheless, this cannot be the sole conformation of iron in these catalysts. If only separate Fe and Mo sulfide phases would be formed that do not directly interact with each other, the rates of $\text{Fe}_x\text{Mo}_y\text{S}_z/\text{NaY-sulf}$ catalysts should be equal to the rates of $\text{Mo}_x\text{S}_y/\text{NaY-sulf}$ catalysts with comparable Mo loadings. Based on the TEM images shown in Figure S6.1, physical blocking of the zeolite channels by external sulfide phases can be excluded. Therefore, we conclude that a fraction of Fe is forming catalytically inactive, mixed $\text{Fe}_x\text{Mo}_y\text{S}_z$ clusters most likely located inside the zeolite pores. We hypothesize that these mixed metal sulfide phases are inactive for hydrogenation because of their inability to stabilize hydrides as form of adsorbed hydrogen.

As we did not observe any evidence for the formation of external sulfide phases for $\text{Co}_x\text{Mo}_y\text{S}_z/\text{NaY}$ -sulf catalysts, we expect the majority of Co to be present in form of small, molecular Co_xS_y clusters. Supported by previous reports, we expect these clusters to be present inside the zeolite framework.²⁻⁴ Therefore, they co-exist in close proximity to encapsulated Mo_xS_y phases potentially influencing their activity. Similar to $\text{Fe}_x\text{Mo}_y\text{S}_z/\text{NaY}$ -sulf catalysts, in addition to the presence of separate Co_xS_y and Mo_xS_y clusters, we propose the formation of mixed $\text{Co}_x\text{Mo}_y\text{S}_z$ clusters for catalysts prepared *via* sequential CVD of Co and Mo. Interestingly, the ethane formation rates of $\text{Co}_x\text{Mo}_y\text{S}_z/\text{NaY}$ -sulf catalysts do not show a clear correlation, neither to the content of Mo nor to the molar Mo/Co ratio. As for $\text{Fe}_x\text{Mo}_y\text{S}_z/\text{NaY}$ -sulf we propose formed mixed metal sulfide clusters to be catalytically significantly less or even inactive for hydrogenation under the tested conditions. On the other hand, there are several $\text{Co}_x\text{Mo}_y\text{S}_z/\text{NaY}$ -sulf catalysts, especially with intermediate Mo fractions of around 0.5, which show activities per mol of Mo that are close to or even higher as the ones of pure $\text{Mo}_x\text{S}_y/\text{NaY}$ -sulf systems. We hence conclude that there exists a positive influence, most likely a synergetic effect between molecular Co_xS_y and Mo_xS_y clusters present in the cages of faujasite zeolite. As we were not able to control the distribution of Co and Mo phases using a sequential CVD approach, the fractions of Co with rate enhancing effect (co-existing clusters) and rate limiting effect (mixed $\text{Co}_x\text{Mo}_y\text{S}_z$ clusters) are essentially random for the prepared catalysts. Unfortunately, this prevents us from quantifying the rate enhancement.

To overcome this problem, we prepared samples with Co (and Ni) loaded in a more controlled way into NaY zeolite by partial ion exchange (denoted $\text{Mo}_x\text{S}_y/\text{CoNaY}$ and $\text{Mo}_x\text{S}_y/\text{NiNaY}$). For these catalysts we only expect the formation of separate $\text{Co}_x\text{S}_y/\text{Ni}_x\text{S}_y$ and Mo_xS_y clusters co-existing in the pores of the zeolite hosts. That way, we are able to decouple the ambivalent effects of a second transition metal on the activity of Mo_xS_y clusters. Indeed, both series of catalysts supported on partly ion exchanged NaY show ethane formation rates per mol of Mo almost doubled compared to a pure $\text{Mo}_x\text{S}_y/\text{NaY}$ -sulf reference. Assuming that hydrogenation on bimetallic catalysts proceeds according to a Langmuir-Hinshelwood type mechanism as we proposed for $\text{Mo}_x\text{S}_y/\text{NaY}$ -sulf catalysts,⁸ we speculate that this rate enhancement results from one of the two following effects or the mixture of both: (i) the formation of SH groups on S atoms bridging $\text{Co}_x\text{S}_y/\text{Ni}_x\text{S}_y$ and Mo_xS_y clusters (as discussed in the previous section) providing an additional source of adsorbed hydrogen, and/or (ii)

$\text{Co}_x\text{S}_y/\text{Ni}_x\text{S}_y$ inducing an increased electron density on Mo_xS_y clusters mitigating the dissociative adsorption of dihydrogen and in turn increasing the coverage of adsorbed hydrogen. In either case the overall coverage of adsorbed hydrogen is still low as the reaction shows first order dependency of H_2 on a representative $\text{Co}_x\text{Mo}_y\text{S}_z/\text{NaY-sulf}$ catalyst (Figure S6.4). The apparent energy of activation ($22 \text{ kJ}\cdot\text{mol}^{-1}$) is lower than the values we previously reported for $\text{Mo}_x\text{S}_y/\text{NaY-sulf/red}$ catalysts ($\sim 30 \text{ kJ}\cdot\text{mol}^{-1}$) in line with the observed increase in activity.⁸

6.4 Experimental Details

6.4.1 Catalyst Precursor Preparation

Mo-based precursors have been prepared by chemical vapor deposition as reported before.¹ In brief, about 200 mg NaY zeolite (Zeolyst CBV 100 with Si/Al 2.5; pelletized to 250 – 355 μm) were treated under reduced pressure (10^{-2} mbar) at elevated temperatures (5 K min^{-1} to 408 K, hold for 2 h; 5 K min^{-1} to 503 K, hold for 2 h; 5 K min^{-1} to 653 K, hold for 1 h) to carefully remove adsorbed water. $\text{Mo}(\text{CO})_6$ (>99.9% purity; Sigma Aldrich) was loaded on the dried zeolite at room temperature under static conditions for a defined time. In a last step, the catalyst precursors were treated under reduced pressure (10^{-2} mbar) for 10 min to remove physisorbed $\text{Mo}(\text{CO})_6$ species.

W-based precursors were prepared the same way starting from $\text{W}(\text{CO})_6$.

Similarly, Mo was loaded in partly Ni and Co ion exchanged supports. These supports were prepared as follows: about 1 g of NaY zeolite was suspended in 50 mL of a 10 – 20 mM cobalt/nickel acetate solution. The suspension was stirred at 80 °C overnight and the solid was filtered off, washed with excess water (3 \times 50 mL), and dried at 100 °C overnight. The samples were calcined in synthetic air (550 °C for 10 h).

Bimetallic $\text{Fe}_x\text{Mo}_y\text{S}_z/\text{NaY}$ and $\text{Co}_x\text{Mo}_y\text{S}_z/\text{NaY}$ precursors were prepared by sequential CVD steps. In a first step Fe or Co was introduced using $\text{Fe}(\text{CO})_5$ (>99.9% purity; Sigma Aldrich) or $\text{Co}(\text{CO})_3\text{NO}$ (>99.9% purity; Sigma Aldrich), respectively. After removal of physisorbed species under reduced pressure Mo was introduced as described above using $\text{Mo}(\text{CO})_6$.

All precursors are stored in a glovebox to avoid exposure to air/moisture at any time. For the same reason quartz glass tubes used for catalytic reactions were packed in a glovebox.

6.4.2 Infrared (IR) Spectroscopy of Adsorbed Probe Molecules

Infrared spectroscopy of adsorbed probe molecules was performed using a Nicolet 6700 FTIR spectrometer with a resolution of 4 cm^{-1} . Prior to IR experiments all catalyst samples were sulfided in the PFR set-up. After sulfidation catalysts were ground and pressed into self-supporting wafers of about 5 mg cm^{-2} . To remove water wafers were re-sulfided in a stream of $20\text{ ml min}^{-1}\text{ H}_2\text{S}$ (10% v/v in H_2) at ambient pressure (5 K min^{-1} to 673 K , hold for 2 h). For activation, a treatment in H_2 (4 cycles, total of 24 h) at 473 K each followed by evacuation at 10^{-6} mbar for 30 min was applied to all samples.

Pyridine adsorption was performed on activated samples at 323 K by applying small doses of pyridine up to 0.5 mbar into the IR cell and equilibration for 0.5 h. After adsorption the samples were outgassed at 323 K and 10^{-6} mbar for 0.5 h. Pyridine was desorbed by heating in steps of 50 K and equilibrating for 0.5 h after each step.

DMP adsorption was performed on activated samples at 323 K by applying small doses of DMP up to 1.0 mbar into the IR cell and equilibration for 0.5 h. After adsorption the samples were outgassed at 323 K and 10^{-6} mbar for 0.5 h. A second spectrum was taken after applying an additional 1013 mbar of H_2 , equilibration for 0.5 h and outgassing at 10^{-6} mbar for 0.5 h.

For all probe molecule adsorption experiments spectra were background corrected using an OMNIC software package. All spectra are difference spectra against reference spectra at 10^{-7} mbar .

6.4.3 Catalytic Reactions

Catalytic reactions were carried out in a lab-scale plug flow reactor (quartz glass tube of 4 mm inner diameter). Bronkhorst mass flow controllers were used to maintain gas flow rates. To avoid formation of hotspots all catalyst precursors were diluted 1/10 in SiC ($500 - 1000\text{ }\mu\text{m}$) and placed in a quartz tube supported with glass wool on both sides. Catalyst precursors were sulfided in a stream of $20\text{ ml min}^{-1}\text{ H}_2\text{S}$ (10 vol.% H_2) at ambient pressure (5 K min^{-1} to 673 K , hold for 2 h). After thermal treatment, all catalysts were purged with N_2 for 30 min prior to catalytic reactions. Ethene hydrogenation was performed at 473 K and ambient pressure in absence of H_2S in the feed with a $\text{H}_2/\text{C}_2\text{H}_4$ volumetric ratio of 20/1. The product stream composition was analyzed by online gas chromatography using an Agilent 7890B GC. Ethane formation rates were determined using space-time yields under differential conditions after the

catalysts reached a stable steady state (~24 h). For NiNaY supported catalysts the rates were determined as described in section 6.7.4 of the Supporting Information. Catalyst limitation by external mass transport has been excluded for the applied conditions by varying the amount of loaded catalyst.

6.4.4 Transmission Electron Microscopy

Transmission electron microscopy of the sulfide catalysts was performed with an XXXJEOL JEM-2011 instrument using an acceleration voltage of 120 keV. Samples were prepared by suspending the catalysts in ethanol ($\geq 99.5\%$) and deposit them on a carbon-film coated copper grid (QUANTIFOIL Multi A).

6.5 Acknowledgements

The author thanks Dr. A. Kuperman and Dr. A. Brait (Chevron) for fruitful discussions and C. Gross for his help in synthesis and kinetic evaluation. J. A. L. was supported by the U.S. Department of Energy (DOE), Office of Science, Office of Basic Energy Sciences, Division of Chemical Sciences, Geosciences and Biosciences (Transdisciplinary Approaches to Realize Novel Catalytic Pathways to Energy Carriers, FWP 47319).

Contributions

R. Weindl, R. Khare, H. Shi, and J. A. Lercher conceived the idea of this work. R. Weindl conducted synthesis, characterization and kinetic evaluation of the presented materials. A. Jentys assisted in interpretation of spectroscopic data. The manuscript was written by R. Weindl.

6.6 References

- (1) Weindl, R.; Khare, R.; Kovarik, L.; Jentys, A.; Reuter, K.; Shi, H.; Lercher, J. A. *Angewandte Chemie International Edition* **2021**, *60*, 9301.
- (2) Korányi, T. I.; Jentys, A.; Vinek, H. In *Studies in Surface Science and Catalysis*; Beyer, H. K., Karge, H. G., Kiricsi, I., Nagy, J. B., Eds.; Elsevier: 1995; Vol. 94, p 582.
- (3) Korányi, T. I.; Pham, N. H.; Jentys, A.; Vinek, H. In *Studies in Surface Science and Catalysis*; Froment, G. F., Delmon, B., Grange, P., Eds.; Elsevier: 1997; Vol. 106, p 509.
- (4) Kadono, T.; Kubota, T.; Hiromitsu, I.; Okamoto, Y. *Applied Catalysis A: General* **2006**, *312*, 125.
- (5) Topsoe, N.; Topsoe, H. *Journal of catalysis* **1993**, *139*, 641.
- (6) Berhault, G.; Lacroix, M.; Breysse, M.; Maugé, F.; Lavalley, J.-C.; Nie, H.; Qu, L. *Journal of Catalysis* **1998**, *178*, 555.
- (7) Luo, W.; Shi, H.; Schachtl, E.; Gutiérrez, O. Y.; Lercher, J. A. *Angewandte Chemie International Edition* **2018**, *57*, 14555.
- (8) Khare, R.; Weindl, R.; Jentys, A.; Reuter, K.; Shi, H.; Lercher, J. A. *JACS Au* **2022**, *2*, 613.
- (9) Travert, A.; Maugé, F. In *Studies in surface science and catalysis*; Elsevier: 1999; Vol. 127, p 269.
- (10) Oliviero, L.; Vimont, A.; Lavalley, J.-C.; Sarria, F. R.; Gaillard, M.; Maugé, F. *Physical Chemistry Chemical Physics* **2005**, *7*, 1861.

6.7 Supporting Information

6.7.1 Elemental Compositions of Prepared Catalysts

Table S6.1 Elemental compositions of all tested $\text{Fe}_x\text{Mo}_y\text{S}_z/\text{NaY-sulf}$ mixed metal sulfide catalysts prepared for this work.

	Metal content $\mu\text{mol}\cdot\text{g}^{-1}$		Mo fraction	Ethane formation rate	
	Mo	Fe		$\text{mmol}\cdot\text{h}^{-1}$ $\text{g}(\text{cat})^{-1}$	$\text{mol}\cdot\text{h}^{-1}$ $\text{mol}(\text{Mo})^{-1}$
$\text{Fe}_x\text{S}_y/\text{NaY-sulf}$	/	786	/	0.01	/
$\text{Fe}_x\text{Mo}_y\text{S}_z/\text{NaY-sulf}$ (1)	89	1446	0.06	0.30	3.43
$\text{Fe}_x\text{Mo}_y\text{S}_z/\text{NaY-sulf}$ (2)	104	607	0.15	0.41	3.89
$\text{Fe}_x\text{Mo}_y\text{S}_z/\text{NaY-sulf}$ (3)	423	834	0.34	0.35	0.84
$\text{Fe}_x\text{Mo}_y\text{S}_z/\text{NaY-sulf}$ (4)	361	411	0.47	1.09	3.01
$\text{Fe}_x\text{Mo}_y\text{S}_z/\text{NaY-sulf}$ (5)	461	414	0.53	1.73	3.76

Table S6.2 Elemental compositions of all tested $\text{Co}_x\text{Mo}_y\text{S}_z/\text{NaY-sulf}$ mixed metal sulfide catalysts prepared for this work.

	Metal content $\mu\text{mol}\cdot\text{g}^{-1}$		Mo fraction	Ethane formation rate	
	Mo	Co		$\text{mmol}\cdot\text{h}^{-1}$ $\text{g}(\text{cat})^{-1}$	$\text{mol}\cdot\text{h}^{-1}$ $\text{mol}(\text{Mo})^{-1}$
$\text{Co}_x\text{S}_y/\text{NaY-sulf}$	/	1237	/	0.06	/
$\text{Co}_x\text{Mo}_y\text{S}_z/\text{NaY-sulf}$ (1)	378	683	0.36	0.99	2.62
$\text{Co}_x\text{Mo}_y\text{S}_z/\text{NaY-sulf}$ (2)	466	729	0.39	2.76	5.92
$\text{Co}_x\text{Mo}_y\text{S}_z/\text{NaY-sulf}$ (3)	567	554	0.51	5.34	9.43
$\text{Co}_x\text{Mo}_y\text{S}_z/\text{NaY-sulf}$ (4)	572	527	0.52	5.39	9.42
$\text{Co}_x\text{Mo}_y\text{S}_z/\text{NaY-sulf}$ (5)	443	298	0.60	9.04	20.42
$\text{Co}_x\text{Mo}_y\text{S}_z/\text{NaY-sulf}$ (6)	583	376	0.61	7.54	12.92
$\text{Co}_x\text{Mo}_y\text{S}_z/\text{NaY-sulf}$ (7)	289	85	0.77	2.06	7.12
$\text{Co}_x\text{Mo}_y\text{S}_z/\text{NaY-sulf}$ (8)	535	85	0.86	4.17	7.80
$\text{Co}_x\text{Mo}_y\text{S}_z/\text{NaY-sulf}$ (9)	548	51	0.92	1.27	2.32

Table S6.3 Elemental compositions of all tested $\text{Mo}_x\text{S}_y/\text{CoNaY-sulf}$ mixed metal sulfide catalysts prepared for this work.

	Metal content $\mu\text{mol}\cdot\text{g}^{-1}$		Mo fraction	Ethane formation rate	
	Mo	Co		$\text{mmol}\cdot\text{h}^{-1}$ $\text{g}(\text{cat})^{-1}$	$\text{mol}\cdot\text{h}^{-1}$ $\text{mol}(\text{Mo})^{-1}$
<i>CoNaY-sulf</i>	/	288	/	0.02	/
<i>Mo_xS_y/CoNaY-sulf (1)</i>	594	255	0.70	12.81	21.58
<i>Mo_xS_y/CoNaY-sulf (2)</i>	729	255	0.74	16.58	22.74
<i>Mo_xS_y/CoNaY-sulf (3)</i>	740	221	0.77	15.45	20.90

Table S6.4 Elemental compositions of all tested $\text{Mo}_x\text{S}_y/\text{NiNaY-sulf}$ mixed metal sulfide catalysts prepared for this work.

	Metal content $\mu\text{mol}\cdot\text{g}^{-1}$		Mo fraction	Ethane formation rate	
	Mo	Ni		$\text{mmol}\cdot\text{h}^{-1}$ $\text{g}(\text{cat})^{-1}$	$\text{mol}\cdot\text{h}^{-1}$ $\text{mol}(\text{Mo})^{-1}$
<i>NiNaY-sulf</i>	/	665	/	2.38	/
<i>Mo_xS_y/NiNaY-sulf (1)</i>	164	612	0.21	5.34	18.08
<i>Mo_xS_y/NiNaY-sulf (2)</i>	406	582	0.41	10.25	19.35
<i>Mo_xS_y/NiNaY-sulf (3)</i>	510	540	0.49	13.88	22.53
<i>Mo_xS_y/NiNaY-sulf (4)</i>	531	494	0.52	13.83	21.54

6.7.2 Transmission Electron Microscopy of Spent Catalysts

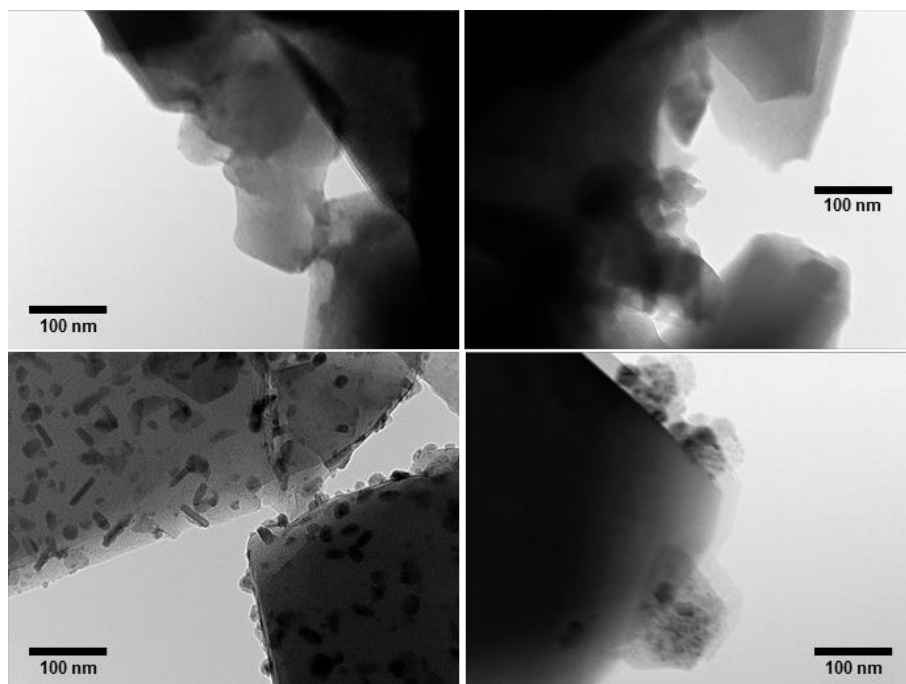


Figure S6.1 TEM images of representative Co_xMo_yS_z/NaY-sulf (top) and Fe_xMo_yS_z/NaY-sulf (bottom) catalysts after 24 h of ethene hydrogenation reaction. Elemental compositions of the catalysts can be found in section 6.7.1 of the Supporting Information. Co_xMo_yS_z/NaY-sulf (2) (top left), Co_xMo_yS_z/NaY-sulf (6) (top right), Fe_xMo_yS_z/NaY-sulf (3) (bottom left), and Fe_xMo_yS_z/NaY-sulf (5) (bottom right).

6.7.3 Infrared Spectroscopy of Adsorbed Dimethyl Pyridine on NiNaY & CoNaY

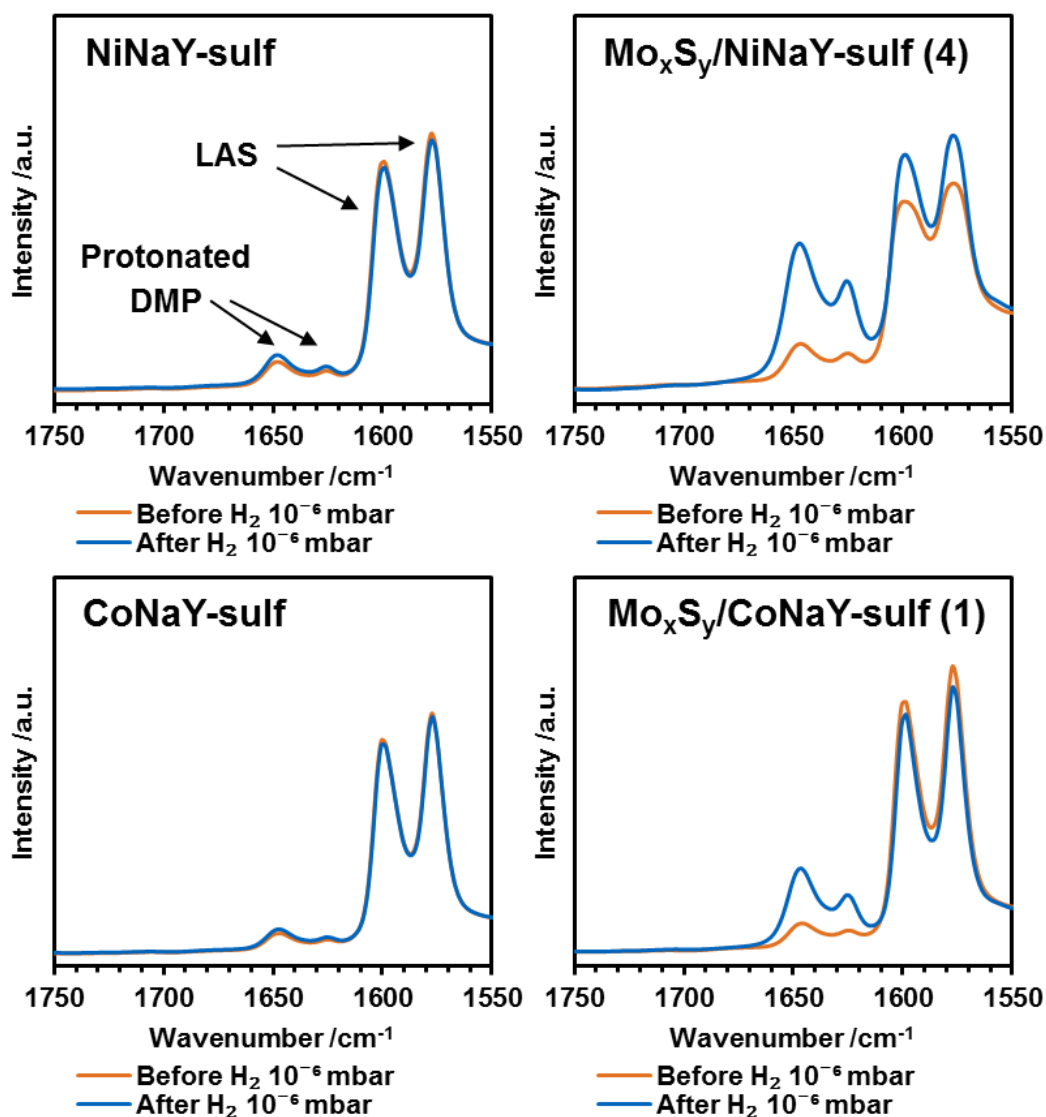


Figure S6.2 IR spectra of adsorbed DMP on NiNaY (top left) and CoNaY (bottom left) supports and Mo_xS_y/NiNaY-sulf (4) (top right) & Mo_xS_y/CoNaY-sulf (1) (bottom right) catalysts before and after admission of 1 bar H₂ at 323 K. Elemental compositions of the supports and catalysts can be found in section 6.7.1 of the Supporting Information. Spectra were collected after outgassing for 0.5 h.

6.7.4 Time on Stream Behavior of NiNaY Supported Catalysts

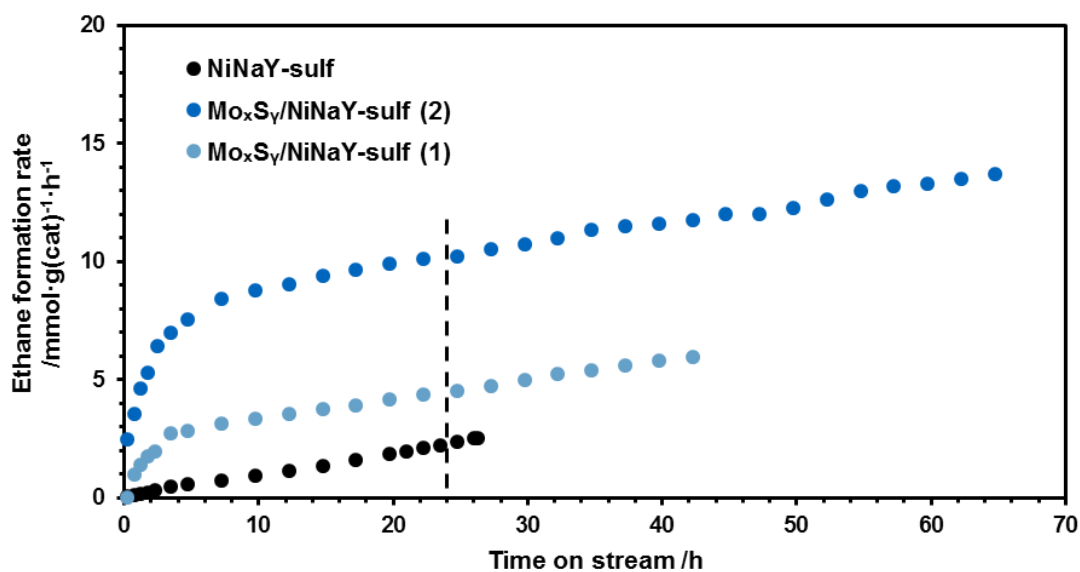


Figure S6.3 Ethane formation rates of representative NiNaY supported catalysts and the support material itself at 473 K. Elemental compositions of the supports and catalysts can be found in section 6.7.1 of the Supporting Information. As pure NiNaY-sulf is also active for hydrogenation, the rates attributed to the Mo_xS_y phases were determined by subtracting the activity of pure NiNaY (with same Ni loading as the catalysts) from the nominal rates of the catalysts after 24 h time on stream.

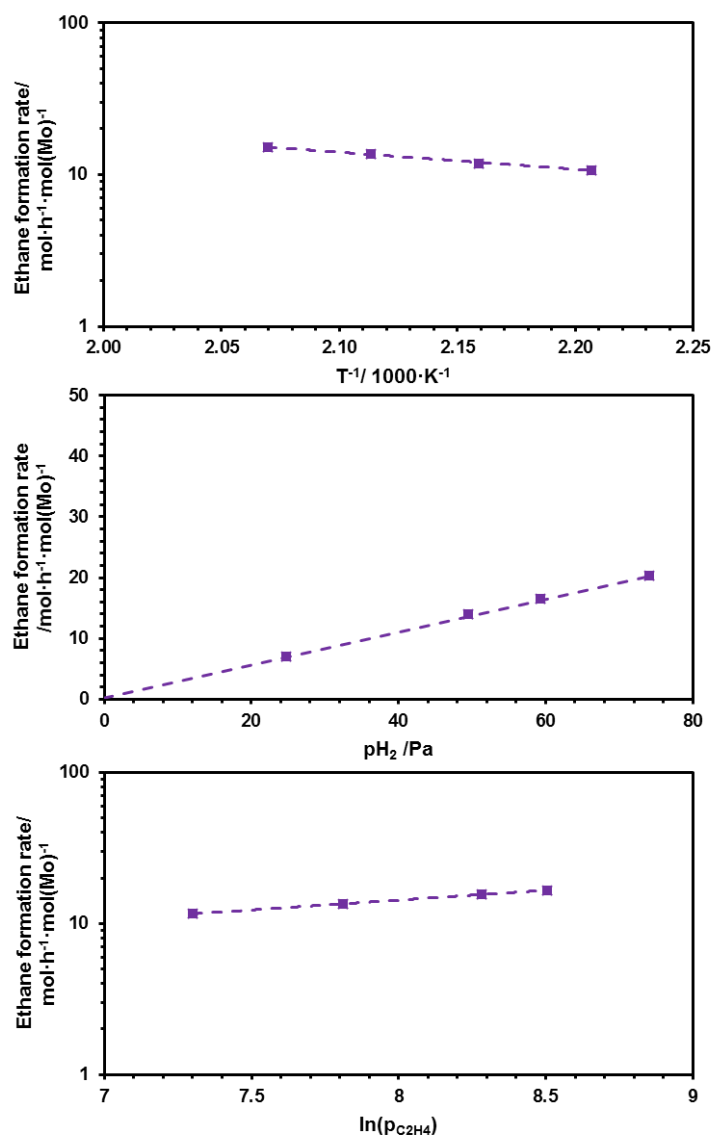
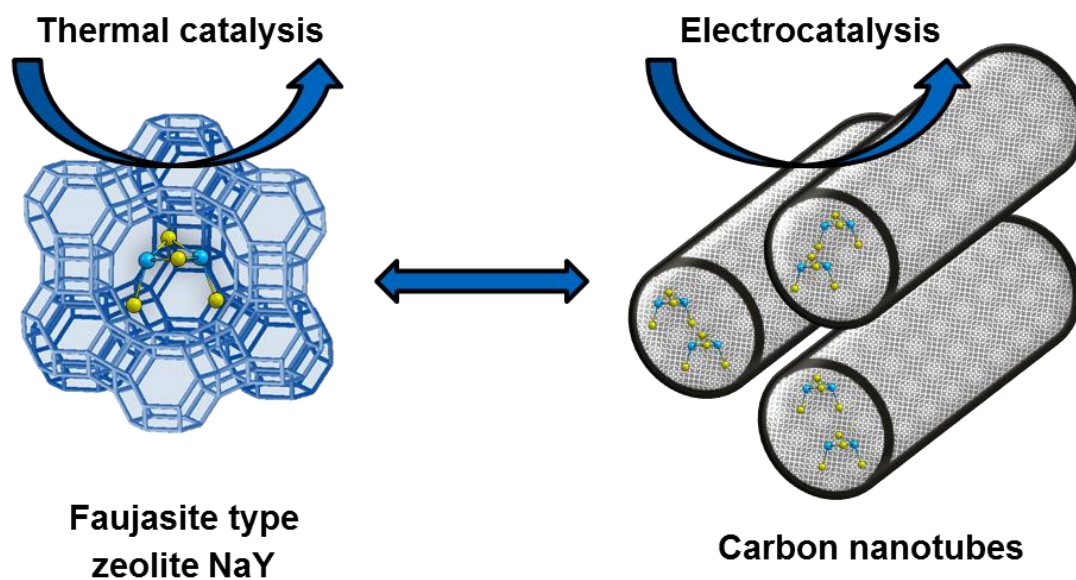
6.7.5 Kinetic Parameters of Ethene Hydrogenation on $\text{Mo}_x\text{S}_y/\text{CoNaY}$ 

Figure S6.4 Determination of kinetic parameters for ethene hydrogenation on $\text{Mo}_x\text{S}_y/\text{CoNaY}$ -sulf (1). Elemental composition of the catalyst can be found in section 6.7.1 of the Supporting Information. Arrhenius type plot for determination of energy of activation (top) and ethane formation rates in dependence of ethene and H_2 partial pressure for determination of reaction orders. The apparent energy of activation was $22 \pm 2 \text{ kJ} \cdot \text{mol}^{-1}$, and reaction orders were 1 ± 0.1 in H_2 and 0.3 ± 0.05 in ethene.

7 Molecular Molybdenum Sulfide Clusters Supported on Carbon Nanotubes for Electrocatalysis



Keywords: Molybdenum sulfide clusters • Hydrogen activation • Hydride • IR spectroscopy • Density functional theory

Abstract

Similar to the formation of molecular Mo_xS_y clusters in faujasite zeolites, molybdenum sulfide phases were incorporated within the confinement of carbon nanotubes *via* chemical vapor deposition followed by sulfidation. At low sulfidation temperatures well-defined dimers are formed that agglomerate at higher temperatures to form Mo_xS_y nanoclusters. Using carbon nanotubes as a conductive support, the resulting materials can be used as electrode materials in electrocatalysis. In this work we show that these materials are effective catalysts for the electrochemical evolution of hydrogen from water much superior to classic bulk MoS_2 . We attribute that to the significantly higher dispersion of active molybdenum sulfide phases on the one hand and to the improved stabilization of intermediately formed hydride species on the other hand.

7.1 Structures of Carbon Nanotube (CNT) Supported Molybdenum Sulfide Phases

Molybdenum sulfide nanoclusters supported on conductive carbon supports have been reported numerous times as efficient materials for electrocatalysis.¹⁻³ By using the same chemical vapor deposition (CVD) approach described in the previous chapters, we were able to successfully load molybdenum (~3 wt%) into multi-walled CNTs. In our case CNTs were chosen as a support because they provide a well-ordered channel structure in many ways similar to zeolites but in contrast to insulating zeolite supports, they possess reasonably good conductivity to serve as a support material for electrocatalysis. In order to be able to anchor molybdenum carbonyl species during CVD, CNT functionalized with COOH-groups were used.

To verify if sulfidation of carbonyl precursors leads to formation of molecular Mo_xS_y clusters hosted by CNTs, we monitored the temperature programmed sulfidation of an exemplary precursor *via* X-ray absorption spectroscopy (Figure 7.1).

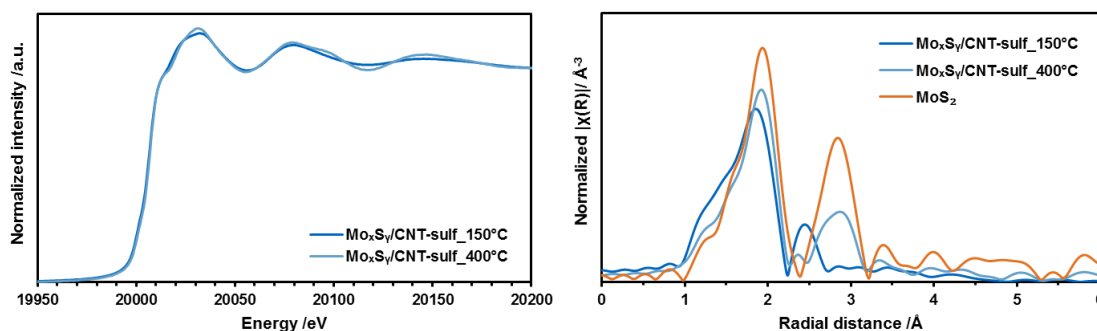


Figure 7.1 X-ray absorption near edge structure (XANES; left) and extended X-ray absorption fine structure (EXAFS; right) of $\text{Mo}_x\text{S}_y/\text{CNT-sulf}$ catalysts after sulfidation at different temperature together with bulk MoS_2 as a reference.

The identical absorption edges of both catalysts show that, although the structure of Mo_xS_y phases changes upon heating from 150 °C to 400 °C, the local electronic environment of Mo centers remains the same. Extended X-ray absorption fine structure analysis of $\text{Mo}_x\text{S}_y/\text{CNT-sulf}_{150^\circ\text{C}}$ resulted in coordination numbers (CN) of 4.3 for Mo-S and 1.1 for Mo-Mo at distances of about 2.40 Å and 2.76 Å, respectively. This is in reasonable agreement with the Mo_2S_4 structure we proposed for zeolite supported catalysts after sulfidation.⁴ For $\text{Mo}_x\text{S}_y/\text{CNT-sulf}_{400^\circ\text{C}}$ on the other hand, we obtained a $\text{CN}_{\text{Mo-S}}$ of 4.4 and a $\text{CN}_{\text{Mo-Mo}}$ of 3.0 at 2.40 Å and 3.16 Å. Although the coordination numbers are still lower compared to bulk MoS_2 , the bond distances are identical. We

7.1 Structures of Carbon Nanotube (CNT) Supported Molybdenum Sulfide Phases

hence conclude that upon sulfidation at higher temperatures the molecular structures, that have been initially formed, agglomerate to form Mo_xS_y nanoclusters. We attribute the fact that we did not observe this agglomeration on zeolite supported systems to the weaker interaction between the support and Mo_xS_y clusters.

7.2 Electrocatalytic Hydrogen Evolution Reaction

As discussed in chapter 2.3, electrochemical hydrogen evolution reaction (HER) is considered promising for the future production of H₂ from renewable resources. Therefore, the catalysts prepared using multi-walled carbon nanotubes as host material were tested for HER together with bulk MoS₂ and carbon supported platinum as references (Figure 7.2 & Table 7.1).

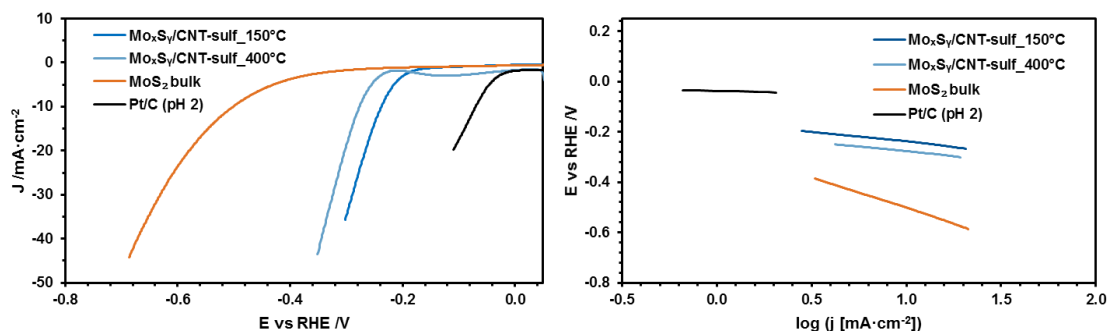


Figure 7.2 Linear polarization curves (left) and Tafel plots (right) for HER on tested electrocatalysts. The onset potentials and Tafel slopes are reported in Table 7.1.

Table 7.1 Onset potentials versus reversible hydrogen electrode (RHE) and Tafel slopes of Mo_xS_y/CNT catalysts and bulk MoS₂ and Pt/C as references.

Catalyst	Onset vs RHE /mV	Tafel slope /mV·dec ⁻¹
Pt reference	40	17
Mo _x S _y /CNT-sulf_150°C	160	80
Mo _x S _y /CNT-sulf_400°C	200	76
MoS ₂ bulk	260	245

The onset potentials as well as the Tafel slopes of both catalysts synthesized *via* CVD and subsequent sulfidation are significantly lower compared to a classic, layered bulk MoS₂ catalyst. Instead, the observed values are close to what has been previously reported for highly active molybdenum sulfide nanoclusters supported on CNTs or reduced graphene oxide.^{1,3} Nevertheless, Pt/C still remains the superior catalysts under the tested conditions.

Interestingly, the electrocatalytic properties of Mo_xS_y/CNT-sulf_150°C and Mo_xS_y/CNT-sulf_400°C are virtually identical. We speculate, that, at least for very small Mo_xS_y clusters exposing all Mo sites, the individual Mo centers are catalytically indistinguishable. However, we have to admit at this point that we lack *operando*

characterization data confirming that the structures of Mo_xS_y clusters are retained under reaction conditions.

The high activities of nano-sized Mo_xS_y phases for electrocatalytic hydrogen production reported in previous studies as well as in this work are often attributed to two main factors: (i) enhanced conductivity due to usage of carbon-based supports, and (ii) high density of active sites due to high dispersion of active Mo_xS_y phases.¹⁻³ In addition, we speculate that, in contrast to bulk MoS_2 , the ability of molecular Mo_xS_y clusters to effectively stabilize hydride species, intermediately formed in H_2 evolution, further contributes to their remarkable activity in HER. We recently confirmed the proposed formation of hydride species for a similar system of Mo_xS_y clusters encapsulated in faujasite zeolite as a host material using a combination of infrared spectroscopy and density functional theory.⁵

Overall, we have shown in here that by using CVD followed by thermal treatment in sulfiding atmosphere Mo_xS_y phases can be incorporated in CNTs as a conductive support. The resulting materials are efficient electrocatalysts for the noble metal free production of H_2 from water. Based on a related, zeolite-based catalyst system we propose the enhanced stabilization of hydride species as one of the reasons for the superior electrocatalytic performance of molecular transition metal sulfide clusters compared to classic, layered MoS_2 systems.

7.3 Experimental Details

7.3.1 Catalyst Precursor Preparation

Catalyst precursors have been prepared by chemical vapor deposition. About 200 mg COOH functionalized graphitized multi-walled carbon nanotubes (5 – 10 nm inner diameter; Cheap Tubes Inc.) were treated under reduced pressure (10^{-2} mbar) at elevated temperatures (5 K min^{-1} to 408 K, hold for 2 h; 5 K min^{-1} to 503 K, hold for 2 h; 5 K min^{-1} to 653 K, hold for 1 h) to carefully remove adsorbed water. $\text{Mo}(\text{CO})_6$ (>99.9% purity; Sigma Aldrich) was loaded on the dried support at room temperature under static conditions for 24 h. In a last step, the catalyst precursors were treated under reduced pressure (10^{-2} mbar) for 10 min to remove physisorbed $\text{Mo}(\text{CO})_6$ species.

These precursors are stored in a glovebox to avoid exposure to air/moisture at any time. For the same reason quartz glass tubes used for catalytic reactions were packed in a glovebox.

The bulk MoS_2 reference catalyst was prepared according to a method reported elsewhere.⁶⁻¹⁰

7.3.2 X-ray Absorption/Emission Spectroscopy

XAS were measured at the P65 beamline of the German Electron Synchrotron (DESY) in Hamburg, Germany. The storage ring operated at 6 GeV energy and 100 mA current in top-up mode. A water-cooled Si311 double crystal monochromator (DCM) was used for obtaining monochromatic X-rays. Two Rh-coated plane mirrors were installed in front of the DCM to reject higher harmonics. The DCM was calibrated to Mo K-edge energy by measuring a reference Mo foil and setting the first major inflection point to 20000 eV. The beam spot-size was 200 μm (vertical) \times 1.6 mm (horizontal) on the sample and the energy resolution of incident X-rays is estimated to be ~ 2 eV ($\Delta E/E \sim 1.0 \times 10^{-4}$) at Mo K-edge energy.

A carbonyl-form catalyst precursor was placed in a quartz glass capillary (WJM Glas, 1 mm o.d., 10-20 μm thickness) supported by two quartz wool plugs. The capillary was heated with a gas-blower (Oxford FMB). Gas flow rates were controlled using mass flow controllers (Bronkhorst) and the pressure was monitored using a pressure gauge (Omega). All experiments were performed at ambient pressure. The

precursor was sulfided in a flow of 10 mL min^{-1} H_2S (10 vol.-% in H_2) while ramping up the temperature from 373 K to 673 K. After reaching $\sim 423 \text{ K}$ and after reaching 673 K the sample was cooled to room temperature for collecting XAS. Several successive scans were averaged to reduce signal-to-noise ratio and improve the data quality.

7.3.3 Catalytic Reactions

Sulfidation of precursors was carried out in a lab-scale plug flow reactor (quartz glass tube of 4 mm inner diameter). Bronkhorst mass flow controllers were used to maintain gas flow rates. Catalyst precursors were sulfided in a stream of 20 ml min^{-1} H_2S (10 vol.% H_2) at ambient pressure (5 K min^{-1} to 423 K or 673 K, hold for 2 h). The bulk MoS_2 catalysts were re-sulfided according to the same procedure at 673 K to remove water. After thermal treatment, all catalysts were purged with N_2 for 30 min.

Linear polarization measurements were performed in a rotating disk electrode (RDE) setup using a Modulated Speed Rotator and an RDE glass cell with water jacket both from PINE research. The electric potential was controlled with an SP 300 potentiostat from BioLogic. In a three-electrode configuration, a glassy carbon RDE tip (5.0 mm o.d.) with catalyst coating (0.3 mg) was used as working electrode. For catalyst coating, 2.0 mg of catalyst was suspended in $190 \mu\text{L}$ ethanol and $10 \mu\text{L}$ Nafion 117 solution (5% in lower aliphatic alcohols and water; Sigma Aldrich) and sonicated for 30 min. $30 \mu\text{L}$ of the suspension were transferred to the glassy carbon disk and dried before immersion into the electrolyte. A Pt wire served as counter electrode and an Ag/AgCl electrode was used as reference electrode. The RDE tip as well as counter and reference electrode were purchased from PINE research. Before each experiment, the Ag/AgCl electrode was calibrated against a reversible hydrogen electrode. Therefore, its potential was measured against a Pt wire in a H_2 saturated electrolyte that was intended to be used in the linear polarization measurements, respectively. The RDE glass cell was stored in a potassium permanganate solution prior to use to remove any organic contaminations. Before filling with electrolyte, it was flushed with a 3% H_2O_2 / 1 M H_2SO_4 solution followed by rinsing with ultrapure water. All electrodes were immersed in 100 mL 0.5 M H_2SO_4 and the temperature (298 K) was adjusted with a FC 600s chiller from Julabo. The rotation speed of the RDE tip was set to 250 rpm and the external electric potential was scanned between -0.30 and 0.40 V vs. RHE. The scanning rate was 50 mV s^{-1} . Excess H_2 and O_2 were removed from the electrolyte solution *via* purging with He (20 mL min^{-1}) throughout the experiments.

7.4 Acknowledgements

The author thanks Dr. A. Kuperman and Dr. A. Brait (Chevron) for fruitful discussions. J. A. L. was supported by the U.S. Department of Energy (DOE), Office of Science, Office of Basic Energy Sciences, Division of Chemical Sciences, Geosciences and Biosciences (Transdisciplinary Approaches to Realize Novel Catalytic Pathways to Energy Carriers, FWP 47319).

Contributions

R. Weindl and J. A. Lercher conceived the idea of this work. R. Weindl conducted synthesis and characterization of the presented materials. P. Fischer conducted the electrochemical evaluation of all catalysts. The manuscript was written by R. Weindl.

7.5 References

- (1) Gao, X.; Qi, J.; Wan, S.; Zhang, W.; Wang, Q.; Cao, R. *Small* **2018**, *14*, 1803361.
- (2) Xie, S.; Sun, B.; Sun, H.; Zhan, K.; Zhao, B.; Yan, Y.; Xia, B. Y. *International Journal of Hydrogen Energy* **2019**, *44*, 15009.
- (3) Li, P.; Yang, Z.; Shen, J.; Nie, H.; Cai, Q.; Li, L.; Ge, M.; Gu, C.; Chen, X. a.; Yang, K.; Zhang, L.; Chen, Y.; Huang, S. *ACS Applied Materials & Interfaces* **2016**, *8*, 3543.
- (4) Weindl, R.; Khare, R.; Kovarik, L.; Jentys, A.; Reuter, K.; Shi, H.; Lercher, J. A. *Angewandte Chemie International Edition* **2021**, *60*, 9301.
- (5) Khare, R.; Weindl, R.; Jentys, A.; Reuter, K.; Shi, H.; Lercher, J. A. *JACS Au* **2022**, *2*, 613.
- (6) Vogelgsang, F.; Ji, Y.; Shi, H.; Lercher, J. A. *Journal of Catalysis* **2020**, *391*, 212.
- (7) Ruinart de Brimont, M.; Dupont, C.; Daudin, A.; Geantet, C.; Raybaud, P. *Journal of Catalysis* **2012**, *286*, 153.
- (8) Alonso, G.; Del Valle, M.; Cruz, J.; Petranovskii, V.; Licea-Claverie, A.; Fuentes, S. *Catalysis Today* **1998**, *43*, 117.
- (9) Alonso, G.; Siadati, M. H.; Berhault, G.; Aguilar, A.; Fuentes, S.; Chianelli, R. R. *Applied Catalysis A: General* **2004**, *263*, 109.
- (10) Yoosuk, B.; Kim, J. H.; Song, C.; Ngamcharussrivichai, C.; Prasassarakich, P. *Catalysis Today* **2008**, *130*, 14.

8 Concluding Remarks

Transition metal sulfides have for a long time been a crucial class of materials for industrial hydrotreating. Their remarkable catalytic activity under a wide range of harsh reaction conditions, *e.g.*, high temperatures/ pressures or high concentrations of heteroatom-containing molecules, made TMS the by far most widespread catalyst systems in this regard. Besides this “classic” application in hydrotreating of various refinery fractions, TMS are intriguing materials for example for upgrading of renewable resources or as electrode materials in electrocatalysis. These processes are described in detail in the first three chapters of this thesis together with the material properties that make TMS suitable catalysts for the above-mentioned applications.

In addition, the first chapter includes a discussion about the concept of using naturally occurring catalysts, *i.e.*, enzymes, as blueprint for the design of heterogeneous catalysts. In essence, that is the initial idea behind the work presented in the following chapters 4-6. In chapter 4 a synthesis strategy for dimeric Mo_2S_4 and tetrameric Mo_4S_4 clusters encapsulated in NaY zeolites is presented together with detailed physico-chemical characterization of both catalyst systems. XAS in combination with DFT calculations revealed the structures of the TMS clusters showing that the tetrameric one structurally resembles the FeMo cofactor that is commonly believed to act as active center in the nitrogenase enzyme family. Using EPR spectroscopy, again in combination with DFT, we were also able to confirm the presence of unpaired electrons on the Mo centers of Mo_xS_y clusters. The cluster catalysts show stable hydrogenation activity in sulfur-free reaction feeds while conventional MoS_2 strongly deactivates under the same conditions.

Despite their chemical composition being similar, molecular Mo_xS_y clusters show distinctively different catalytic properties compared to MoS_2 . One interesting example for this is presented in chapter 5. By combining probe molecule adsorption monitored *via* IR spectroscopy with DFT calculations we convincingly demonstrate that adsorbed hydrogen is stabilized in form of hydrides on Mo_xS_y clusters. This is contrary to the general consensus of adsorbed hydrogen being present as acidic sulfhydryl groups on MoS_2 catalysts. Most likely this is a result of the easier reducibility of Mo atoms in large, semiconducting MoS_2 slabs in contrast to Mo centers in molecular clusters. Additionally, we present a reasonable reaction pathway for the hydrogenation of

ethene on Mo_xS_y : hydride species adsorbed on Mo centers react in an Eley-Rideal type mechanism with ethene that is weakly adsorbed in the zeolite pores. Interestingly, we found both dimeric and tetrameric clusters to possess similar activities if the hydrogenation rates are normalized to the number of clusters present. This led us to two conclusions: (i) the whole clusters have to be considered as active sites rather than individual Mo atoms, and (ii) both clusters are catalytically indistinguishable for this particular reaction.

In chapter 6 the research is expanded to bimetallic systems containing either Co, Ni or Fe in addition to Mo. These materials, prepared either *via* sequential CVD of metal carbonyl precursors or *via* ion exchange followed by Mo CVD, are all catalytically active for the hydrogenation of ethene but their activities vary over a wide range. For materials prepared *via* sequential CVD the hydrogenation activity increases in the order of $\text{FeMo} < \text{CoMo} \leq \text{Mo}$. This leads to the conclusion that under the tested conditions mixed metal phases are less active compared to pure Mo_xS_y clusters. On the other hand, catalysts prepared *via* CVD of Mo on partly Co/Ni exchanged NaY zeolites show higher rates compared to the pure Mo reference system. This is speculated to be a result of the formation of separate Mo_xS_y and $\text{Ni}(\text{Co})_x\text{S}_y$ phases in close proximity. The presence of SH groups, verified *via* IR spectroscopy of adsorbed base molecules, leads to the conclusion, that these phases are connected *via* bridging sulfur atoms that are able to stabilize hydrogen as SH groups under hydrogenation conditions.

The last chapter 7 briefly demonstrates that it is possible to form Mo_xS_y clusters inside the channels of carbon nanotubes using CVD of $\text{Mo}(\text{CO})_6$ followed by a mild sulfidation. The usage of a conductive support could provide an intriguing option for the design of future electrocatalysts and indeed the resulting system shows promising electrocatalytic activity for hydrogen evolution reaction in this proof-of-concept study.

Scientific Contributions

R. Weindl, R. Khare, L. Kovarik, A. Jentys, K. Reuter, H. Shi, & J.A. Lercher;
Molybdenum Sulfide Clusters in Zeolite Resembling the Nitrogenase Enzyme's
FeMo-cofactor.

ESRF Highlights (to be published in **2022**).

R. Weindl, R. Khare, H. Shi, & J.A. Lercher;

Zeolite Encapsulated Molybdenum Sulfide Clusters Mimicking the Nitrogenase
Enzyme's Active Site.

Oral presentation, The 27th North American Catalysis Society Meeting 2022, New
York, USA.

R. Khare, R. Weindl, A. Jentys, K. Reuter, H. Shi, & J.A. Lercher;

Di- and tetrameric molybdenum sulfide clusters activate and stabilize hydrogen as
hydrides.

JACS Au **2022**, 2, 3, 613-622.

R. Khare, R. Weindl, A. Jentys, & J.A. Lercher;

Zeolite Stabilized Molybdenum Sulfide Clusters Activate Hydrogen as hydride
species and form stable catalytic hydrogenation sites.

Oral presentation, 8 th UK Catalysis Conference 2022, Loughborough, UK.

C. Zhu, O. Gutierrez, D. Santosa, M. Flake, R. Weindl, I. Kutnyakov, H. Shi, &
H. Wang;

Kinetics of nitrogen-, oxygen- and sulfur-containing compounds hydrotreating during
co-processing of bio-crude with petroleum stream.

Appl. Catal., B **2022**, 307, 121197.

R. Weindl, R. Khare, L. Kovarik, A. Jentys, K. Reuter, H. Shi, & J.A. Lercher; Zeolite-
Stabilized Di- and Tetranuclear Molybdenum Sulfide Clusters Form Stable Catalytic
Hydrogenation Sites.

Angew. Chem. **2021**, 60, 9301-9305.

R. Weindl, H. Shi, & J.A. Lercher;

Towards Structure-Activity Relationship in Hydrotreating Catalysis – Synthesis and
Characterization of Zeolite-Encapsulated Molybdenum Sulfide Clusters.

Poster presentation, Molecular Aspect of Catalysis by Sulfides 2019, Cabourg,
France.

R. Weindl, F. Vogelgsang, H. Shi, & J.A. Lercher;

Synthesis, Characterization and Catalytic Hydrogenation Activity of Intra-zeolite
Transition Metal Sulfide Clusters.

Poster presentation, 52. Jahrestreffen Deutscher Katalytiker 2019, Weimar,
Germany.